Experimental Insights of CZTS Thin Film as a Photovoltaic Absorber Deposited by RF Magnetron Sputtering and Spin Coating

By

Ashoke Kumar Sen Gupta
Student ID: 13PEE001P

A thesis submitted in partial fulfilment of the requirements for the degree of

DOCTOR of PHILOSOPHY

Department of Electrical and Electronic Engineering

CHITTAGONG UNIVERSITY OF ENGINEERING AND TECHNOLOGY

JULY 2023

Declaration

I hereby declare that the work contained in this thesis has not been previously submitted to meet requirements for an award at this or any other higher education institution. To the best of my knowledge and belief, the thesis contains no material previously published or written by another person except where due reference is cited.

Ashoke Kumar Sen Gupta
Student ID: 13PEE001P
Department of Electrical and Electronic Engineering
Chittagong University of Engineering and Technology (CUET)

Dedication

To my beloved son *Aninda Sen Gupta (**Adri**)*.

Epigraph

Remember to look up at the stars and not down at your feet. Try to make sense of what you see and wonder about what makes the universe exist. Be curious. And however difficult life may seem, there is always something you can do and succeed at. It matters that you don't just give up.

Stephen Hawking

List of Publications

Publications related to this thesis

Some of the research leading to this thesis has appeared previously in the following publications.

Journal Articles

[1] A.K. Sen Gupta, A. Adnan, S. Bhattacharjee, N. K. Das, M. A. Matin, and M. Quamruzzaman, "**SnapFib: An easy build Arduino based tabletop prototype for thin film deposition by Successive Ionic Layer Adsorption and Reaction method**,"*HardwareX*, vol. 12, p.e00347, Oct. 2022.
PubMed, Scopus, ESCI, Ei Compendex, DOAJ, INSPEC, IF: 2.2, Q2

[2] A.K. Sen Gupta, S.F.U. Farhad, M.S. Habib, M. R. Hossan, K. Hossain, N.K. Das, M. Quamruzzaman, M. A. Matin, and N. Amin, "**Characterizations of extrinsically doped CZTS thin films for solar cell absorbers fabricated by sol-gel spin coating method**,"*Applied Surface Science Advances*, vol. 13, p. 100352, Feb. 2023.
DOAJ, Scopus, ESCI, Web of Science, IF: 6.2, Q1

Conference Papers

[1] A.K. Sen Gupta, E. M. K. I. Ahamed, M. Quamruzzaman, M. A. Matin, K. S. Rahaman and N. Amin, "**Characterization of Intrinsic and Doped ZnO Thin-Films Deposited by RF Magnetron Sputtering for Chalcogenide Based Solar Cell Applications**,"in *4th International Conference on Electrical Information and Communication Technology (EICT)*, Dec. 2019, pp. 1-4.
Dr. Fatema Rashid Best Paper Award (2nd)

[2] A.K. Sen Gupta, E. M. K. I. Ahamed, M. Quamruzzaman, M. A. Matin, K. S. Rahaman and N. Amin, "**Structural properties of bi-layer Molybdenum Thin-film deposited by RF magnetron sputtering for CZTS solar cells**,"in *5th International Conference on Advances in Electrical Engineering (ICAEE)*, Sep. 2019, pp. 600-603.

[3] A.K. Sen Gupta, E. M. K. I. Ahamed, M. Quamruzzaman, M. A. Matin, and N. Amin, "**Throughout RF Magnetron Sputtering Route to Fabricate CZTS Thin-Film Solar Cell**,"in *37th European Photovoltaic Solar Energy Conference and Exhibition*, Sep. 2020, pp. 695-697.

[4] A.K. Sen Gupta, E. M. K. I. Ahamed, M. Quamruzzaman, M. A. Matin, K. S. Rahaman and N. Amin, "**Consequence on Optical Properties of ZnS Thin-Film Deposited by RF Magnetron Sputtering with Varying Substrate Temperatures**,"in *47th IEEE Photovoltaic Specialists Conference (PVSC)*, Jun. 2020, pp. 2646-2648.

Publications as a co-author

Some of the research works which are not mentioned in this thesis but have appeared previously in the following publications during PhD research period.

Journal Articles

[1] N.K. Das, J. Chakrabartty, M. Dey, A.K. Sen Gupta, and M.A. Matin, "**Present energy scenario and future energy mix of Bangladesh**," *Energy Strategy Reviews*, vol. 32, p. 100576, Nov. 2020.

[2] N.K. Das, J. Chakrabartty, S.F.U. Farhad, A.K. Sen Gupta, E.M.K.I. Ahamed, K.S. Rahman, A. Wafi, A.A. Alkhatani, M.A. Matin and N. Amin, "**Effect of substrate temperature on the properties of RF sputtered CdS thin films for solar cell applications**," *Results in Physics*, vol. 17, p. 103132, Jun. 2020.

[3] N.K. Das, S.F.U. Farhad, J. Chakrabartty, A.K. Sen Gupta, M. Dey, M. Al-Mamun, M.A. Matin and N. Amin, "**Structural and Optical Properties of RF-Sputtered CdTe Thin Films Grown on CdS:O/CdS Bilayers**," *Int.J. Renew. Energy Res.*, vol. 10, pp. 293-302, Mar. 2020.

[4] E.M.K.I. Ahamed, N.K. Das, A.K. Sen Gupta, M.N.I. Khan, M.A. Matin and N. Amin, "**Structural and Optical Characterization of As-grown and Annealed $Zn_xCd_{1-x}S$ Thin-films by CBD for Solar Cell Applications**," *Int.J. Renew. Energy Res.*, vol. 10, pp. 1464-1475, Mar. 2020.

Conference Papers

[1] N.K. Das, A.K. Sen Gupta, M. Dey, K.S. Rahman, M. A. Matin and N. Amin, "**Effect of $Cd_{1-x}Zn_xS$ Window Layer Incorporation in CdTe Solar Cell by Numerical Simulation**," in *2019 International Conference on Electrical, Computer and Communication Engineering (ECCE)*, Feb. 2019, pp. 1-5.

[2] N.K. Das, M. Dey, A.K. Sen Gupta and M. A. Matin, "**Present energy usage and future energy security of Bangladesh**," in *2nd Int. Conf. Phy. Sust. Deve. Tech.*, 2017.

[3] Maitry Dey, N.K. Das, A.K. Sen Gupta, Mrinmoy Dey, M.S. Hossain, M. A. Matin, and N. Amin, "**Deposition of CdS Thin Film by Thermal Evaporation**," in *2019 International Conference on Electrical, Computer and Communication Engineering (ECCE)*, Feb. 2019, pp. 1-5.

Approval by the Supervisor (s)

This is to certify that **Ashoke Kumar Sen Gupta** has carried out this research work under our supervision, and that he has fulfilled the relevant Academic Ordinance of the Chittagong University of Engineering and Technology, so that he is qualified to submit the following Thesis in the application for the degree of DOCTOR of PHILOSOPHY in Electrical and Electronic Engineering. Furthermore, the Thesis complies with the PLAGIARISM and ACADEMIC INTEGRITY regulation of CUET.

Prof. Dr. Muhammad Quamruzzaman

Principal Supervisor
Department of Electrical and Electronic Engineering
Chittagong University of Engineering and Technology (CUET)

Prof. Dr. Mahmud Abdul Matin Bhuiyan

Co-Supervisor
Department of Electrical and Electronic Engineering
Chittagong University of Engineering and Technology (CUET)

Prof. Dr. Nowshad Amin

Co-Supervisor
Institute of Sustainable Energy,
Universiti Tenaga Nasional, Malaysia

Board of Examiners

The thesis titled "**Experimental Insights of CZTS Thin Film as a Photovoltaic Absorber Deposited by RF Magnetron Sputtering and Spin Coating**" submitted by Ashoke Kumar Sen Gupta, Roll no. : 13PEE001P, Session: 2013-14 has been accepted as satisfactory in partial fulfillment of the requirement for the degree of Doctor of Philosophy on 04 March, 2023.

Acknowledgement

This doctoral thesis was delayed by the COVID-19 pandemic. I am grateful for the love, support, and direction of so many people who helped me to finish this dissertation.

First and foremost, I am deeply grateful for the continuous support, insight and patience of my supervisors: Prof. Dr. Muhammad Quamruzzaman, Prof. Dr. Nowshad Amin, and Prof. Dr. M. A. Matin. Without their constant trust and, sometimes, gentle prodding, this thesis would not have been completed. In particular, Prof. Nowshad Amin taught me to think from inquisitive, to design analyses that answer challenging questions and to present a compelling story with data. I'm honored to have been their student and grateful to collaborate with them as we publish this thesis' outcomes.

I would also like to thank my doctoral committee members: Head (Prof. Dr. Muhammad Ahsan Ullah, Prof. Dr. Mohammad Rubaiyat Tanvir Hossain, Prof. Dr. Nur Mohammad), Prof. Dr. Quazi Delwar Hossain, Prof. Dr. Muhammad Ibrahim Khan, Prof. Dr. Faruque-Uz-Zaman Chowdhury, and Prof. Dr. Md. Rafiqul Islam for generously giving time, expertise, and feedback to help to make this PhD work as good as it can be.

I am indebted to the *Renewable Energy Laboratory* at the Department of Electrical and Electronic Engineering, Chittagong University of Engineering and Technology, Chattogram, Bangladesh, which was funded by the World Bank and established by the University Grant Commission (UGC) of Bangladesh as part of the Higher Education Quality Enhancement Project (HEQEP), CP-3200. Sincere appreciation goes to my labmates and staffs of this laboratory.

Prof. Dr. Mohammad Rafiqul Alam, honorable vice-chancellor of CUET, my teacher who I first met at my job, Prof. Dr. Tofael Ahmed, my colleague, and Dr. Nilanjon Sen, my cousin; have been a never-ending source of love, encouragement and motivation.

Sincere gratitude to Dr. SFU Farhad, Principal officer, Industrial Physics Division, BCSIR Labs, Dhaka, Prof. Lee of Shenjeng University, PRC, and my colleague Prof. Dr. Murad Hasan, post-doctoral fellow at Starchlyde, UK for using their characterization facilities.

I would like to appreciate the invaluable assistance in characterizations provided by Dr. Mohammad Robiul Hossan, Associate Professor of Engineering and Physics, University of Central Oklahoma, USA and Dr. Khalid Hossain, JP Analytical LLC, USA.

Last, but not least, my wife and son had to grudgingly learn to accept my separation from them sometime and still gave me nothing but support. My special love and gratitude for my son, who can hardly be expressed his feelings in words, but his emotion make me understand everything. I dedicate this PhD thesis to him.

Abstract

This thesis investigates the impact of deposition procedures on the properties of Cu_2ZnSnS_4 (CZTS) thin films and the resultant characteristics of CZTS thin film solar cells. The present study investigated CZTS absorber layer deposited by two distinct techniques namely RF magnetron sputtering utilizing an off-stoichiometric single quaternary CZTS target and sol-gel spin coating. The focus of investigation pertains to buffer materials that are free from Cd and have the potential to improve band alignment. The present study also investigates the potential of ZnO:Ga (GZO) as a transparent conducting oxide (TCO) layer for CZTS solar cell applications as an alternative to the conventional ZnO:Al (AZO). Because of its longevity, microelectronic compatibility, and efficiency, Si-based PV technology dominates. Si with low indirect band gap absorption and sophisticated production methods like high temperature treatment and ion implantation are bottlenecks. Chalcogenide-based thin film PV technologies may lower PV costs. Because of their availability and non-toxicity, kesterite semiconductors containing copper, zinc, tin, sulfur, and selenium are attractive alternatives to CdTe and CIGS. Because of its 1.5 eV direct band gap, pure sulfide CZTS seems promising among the three kesterites. Vacuum-based sputtering produces clean, homogenous kesterite thin films, whereas non-vacuum spin-coating is appealing for component control and large-scale manufacturing. Irrespective of the two fabrication processes described in this thesis, in order to explore microstructural, morphological, optical, electrical, chemical oxidation states, and photovoltaic properties, numerous characterization tools were used at the film and device levels. These are X-ray Diffractometry (XRD), Raman spectroscopy, Field Emission Scanning Electron Microscopy (FESEM), 3D profilometry, Ultraviolet-Visible Near Infra Red (UV-Vis NIR) spectroscopy, X-Ray Photoelectron Spectroscopy (XPS), Hall-effect measurements, and I-V characteristics. Some numerical studies were carried out using SCAPS-1D simulation tools in accordance with experimental results to validate them. The process of sputtering thin films has traditionally included a two-step approach. The use of elemental sulfur in conjunction with vacuum deposition for the purpose of Rapid Thermal Annealing (RTA). Firstly, RF magnetron

sputtered CZTS thin films with a single off-stoichiometric quaternary target were examined for substrate temperature effects. It was found that, in-situ deposition may potentially replace the necessity of a high-temperature annealing stage. Research conducted on the literature pertaining to the alloying of CZTS with various elements such as Ag/Cu, Cd/Zn, Cd/Mg, and Ge/Sn has demonstrated the potential to enhance device efficiencies through the manipulation of band gap, control of defect size, mitigation of unwanted secondary phases, and modulation of carrier concentration. However, despite these advancements, the efficiencies achieved by these alloyed devices have not yet surpassed those of the devices currently in production. Previous research have successfully adjusted the partial replacement of Zn cation with Cd, leading to enhanced power conversion efficiency (PCE). Secondly, Ge-alloyed CZTS samples were fabricated and examined. This work hypothesized that Ge-alloying, in which Sn is partly replaced by Ge atoms, would minimize band gap fluctuations and band tailing, reducing the open-circuit voltage deficit and improving device performance. It was found that, alloyed films with $x = 0.38$ exhibited better morphology, crystallite size, microstrain, and dislocation density. Thirdly, a novel co-doped (Cd,Mg) CZTS thin films and superstrate structured thin film solar cells were fabricated and evaluated. Co-doped CZTS films and standard CdS heterointerface band alignments have been investigated. Numerical simulation verified both tasks. This task was predicted to lower the Cd content in the doped sample by adding Mg without compromising the benefits of Cd alone. Cadmium (Cd) and Magnesium (Mg) exhibit partial isoelectronic substitution at the Zn-site in kesterite CZTS. PCE increases significantly with 40% partial cation substitution of Zn by Cd and Mg. V_{oc} deficit was reduced by 23% and "cliff-like" CBO with a minimum energy of 0.12 eV was detected. In practical applications and in various academic papers, it is often observed that there is a discrepancy in the conduction band offsets between the absorber and buffer layers. Fourthly, in a study of the potential substitution of the traditional CdS buffer layer by ZnS fabricated by SILAR, results suggested that favorable "spike-like" CBO could be achieved. Finally, an alternative to the AZO window layer, GZO, was proposed, and encouraging results were found in film transmittance and resistivity.

বিমূর্ত

Cu_2ZnSnS_4 (CZTS) thin film এবং CZTS thin film সৌরকোষের বৈশিষ্ট্যসমূহ কিভাবে deposition প্রক্রিয়া দ্বারা প্রভাবিত হয়, মূলত সেটাই এই অভিসন্দর্ভের গবেষনার বিষয়। CZTS শোষক (absorber) স্তর দুটি পদ্ধতিতে গঠন করা হয়েছে : RF Magnetron Sputtering এবং Sol-gel Spin-coating. এছাড়াও Cd-মুক্ত buffer স্তর এবং বিকল্প TCO স্তর এর বিষয়েও এই থিসিসে নিরীক্ষণ করা হয়েছে। CdTe এবং CIGS, Chalcogenide-ভিত্তিক thin film PV প্রযুক্তিগুলির মধ্যে অন্যতম। CdTe এবং CIGS এর আকর্ষণীয় বিকল্প হিসাবে Kesterite crystal structure এর CZTS thin film নিয়ে বর্তমানে প্রচুর গবেষনা হচ্ছে। CZTS অর্ধপরিবাহীর মূল উপাদান হল তামা, দস্তা, টিন, সালফার এবং সেলেনিয়াম; যেগুলো খুবই সহজলভ্য । বিশুদ্ধ সালফাইড CZTS, Kesterite এর তিনটি প্রকারের মধ্যে প্রতিশ্রুতিশীল বলে মনে করা হচ্ছে, কেননা তার direct band gap হল 1.5 eV . Vacuum-ভিত্তিক Sputtering সুষম thin film তৈরী করে, অন্যদিকে Non-Vacuum based Sol-gel Spin-coating উপাদান নিয়ন্ত্রণ এবং বড় আকারের thin film তৈরীর জন্য আদর্শ। এই থিসিসে বর্ণিত দুটি প্রক্রিয়া নির্বিশেষে Microstructural, Morphological, Optical, বৈদ্যুতিক, রাসায়নিক জারণ অবস্থা এবং photovoltaic বৈশিষ্ট্য, film এবং device উভয়ক্ষেত্রেই অন্বেষণের জন্য অসংখ্য Characterizations ব্যবহার করা হয়েছে। ঐগুলি হলো: XRD, Raman, FESEM, ত্রিমাত্রিক profilometry, UV-Vis NIR, XPS, Hall effect এবং I-V. পরীক্ষামূলক ফলাফল যাচাই করতে কিছু সাংখ্যিক অধ্যয়নে SCAPS-1D Simulation tools ব্যবহৃত হয়েছে। প্রথমত, RF Magnetron Sputtering পদ্ধতিতে একটি off-stoichiometric CZTS target এর সাহায্যে CZTS thin film তৈরী করা হয়। প্রক্রিয়াজাত করনের সময় substrate এর তাপমাত্রা তৈয়ারীকৃত CZTS thin film এর বৈশিষ্ট্যের উপর কী প্রভাব ফেলে সেটা নিরীক্ষণই ছিল এই গবেষনার উদ্দেশ্য। RF Magnetron Sputtering একটি দুই ধাপের প্রক্রিয়া। Sputtering যন্ত্রে কাঁচের substrate এর উপর তৈরী করা thin film কে দ্বিতীয়ধাপে অধিকতর স্ফটিকরণের জন্য, সালফারের উপস্থিতিতে উচ্চ তাপমাত্রায় দাহন করা হয় । এই গবেষণায় এটা প্রতীয়মান হয় যে, sputtering পদ্ধতিতে CZTS thin film তৈরীতে, দ্বিতীয়ধাপের উচ্চ-তাপমাত্রা দাহনের প্রয়োজনীয়তা প্রক্রিয়াজাত করনের সময় substrate এ প্রায় দাহনের সমান তাপমাত্রা প্রয়োগের মাধ্যমে কার্যকরভাবে প্রতিস্থাপন করা যেতে পারে। দ্বিতীয়ত, একটি অভিনব co-sputtering প্রক্রিয়ায় Ge-alloyed CZTS thin film এর নমুনা তৈরী এবং নিরীক্ষণ করা হয়। যেখানে একটি ধাতব Ge এর target এবং একটি off-stoichiometric CZTS এর target একইসাথে প্রক্রিয়াজাতকরণে ব্যবহৃত হয় । CZTS thin film এ Ge-alloying এর কার্যকারিতা পূর্ববর্তী অনেক গবেষনাদ্বারা স্বীকৃত। এই নূতন পদ্ধতিতে তৈরি Ge-alloyed CZTS thin film এর নমুনার

গবেষনায় দেখা যায় যে, alloyed নমুনায় যখন CZTS এর ৩৮% Sn-atom, Ge-atom দ্বারা প্রতিস্থাপিত হয়, তখন alloyed thin-film এর উন্নত morphology, crystallite size, microstrain এবং dislocation density পাওয়া যায়। তৃতীয়ত, অপর এক অভিনব গবেষনায় Sol-gel spin coating প্রক্রিয়ায় (Cd,Mg) co-doping এর মাধ্যমে CZTS এর কিছু Zn-atom কে সফলভাবে যৌথভাবে Cd এবং Mg দ্বারা প্রতিস্থাপিত করা হয়। পূর্ববর্তী গবেষনায় শুধুমাত্র Cd-atom doping এর মাধ্যমে Zn-atom কে আংশিকভাবে প্রতিস্থাপিত করে CZTS thin film এবং device পর্যায়েও অত্যন্ত আশাব্যঞ্জক ফলাফল পাওয়া গিয়েছিল। কিন্তু, Cd এর বিষক্রিয়ার কথা মনে রেখে, co-doped thin film এ Cd এর পরিমান কমানোর জন্য এই গবেষনায় Cd এর সাথে Mg ও জুড়ে co-doping করা হয়, যেখানে atom-দ্বয় যৌথভাবে CZTS এর Zn atom গুলোকে আংশিকভাবে প্রতিস্থাপিত করে। Co-doped CZTS thin film এর বৈশিষ্ট্য নির্ণয়ের পাশাপাশি device পর্যায়ে তা কিরূপ আচরণ করে জানার জন্য superstrate structured CZTS (co-doped) সৌরকোষের I-V পরীক্ষাও করা হয় এবং সাথে hetero p-n junction এ band alignment এর অবস্থাও পরীক্ষা দ্বারা নির্ণয় করা হয়। এই গবেষনা হতে প্রাপ্ত উল্লেখযোগ্য ফলাফল এই যে, যখন, ৪০% Zn-atom, (Cd,Mg) দ্বারা যৌথভাবে প্রতিস্থাপিত হয়, তখন device efficiency বেড়ে যায়। শুধু তাই নয়, V_{oc} স্বল্পতা প্রায় ২৩% হ্রাস পায় এবং heterojunction এ কম মাত্রায় 0.12 eV এর “cliff-like” CBO সনাক্ত হয়। ফলাফলগুলো CZTS সৌরকোষের efficiency প্রতিবন্ধকতাকে অনেকাংশে লাঘব করার পক্ষে সমর্থন করে। চতুর্থত, ZnS দ্বারা ঐতিহ্যগতভাবে স্বীকৃত CdS buffer স্তরের সম্ভাব্য প্রতিস্থাপনের একটি গবেষণায় SILAR পদ্ধতিতে তৈরীকৃত ZnS thin film এর ফলাফল হতে দেখা যায় যে, CZTS শোষক এর সাথে এটি অনুকূল "spike-like" CBO সৃষ্টি করতে পারে। অবশেষে, AZO-window স্তরের একটি বিকল্প হিসেবে sputtering পদ্ধতিতে তৈরীকৃত GZO-window স্তরের প্রস্তাব করা হয়, এবং GZO thin film এর transmittance এবং resistivity এর আলোকে উদ্দীপনামূলক ফলাফল পাওয়া গিয়েছে।

Table of Contents

List of Figures

List of Tables

Acronyms and Abbreviations

AZO Al-doped Zinc Oxide 42

CBD Chemical Bath Deposition 10, 43, 45, 60, 69, 79
CBM Conduction Band Minimum 15, 16
CBO Conduction Band Offset 72
CCD Charge Coupled Device 64
CRM Critical Raw Materials 54

DFT Density Function Theory 38
DIW De-ionized Water 55
DMSO Dimethyl sulfoxide 35, 58, 68
DOS Density of States 38

EDS Energy Dispersive X-ray Spectroscopy 81
EMPA Swiss Federal Laboratories for Materials Science and Technology 34
EPBT Energy Pay Back Time 7
EQE External Quantum Efficiency 44

FESEM Field Emission Scanning Electron Microscopy ix
FOM Figure of Merit 147
FTO Fluorine doped Tin Oxide 55
FWHW Full Width at Half Maximum 89, 101, 137

GZO Ga-doped Zinc Oxide 11, 12, 136, 138

HZB Helmholtz Zentrum Berlin 34

IBM International Business Machines 34
IPES Inverse Photoelectron Spectroscopy 53
ITO Indium Tin Oxide 42, 53

JCPDS Joint Committee on Powder Diffraction Standards 75

LASER Light Amplification by Stimulated Emission of Radiation 18
LED Light Emitting Diode 18

MEM Maximum Entropy Method 92
MFC Mass Flow Converter 57

MJ Multi Junction 31

NJUPT Nanjing University of Posts and Telecommunications 35
NREL National Renewable Energy Laboratory 34

PCE Power Conversion Efficiency xviii, 18, 21, 27, 28
PTFE Polytetrafluoroethylene 68

QD Quantum Dot 31

RF Radio Frequency 57
RMS Root Mean Square 87, 99
RoHS Restriction of Hazardous Substances (like Toxicity) Directive 54
RT Room Temperature 73, 74
RTA Rapid Thermal Annealing ix

SCAPS Solar Cell Capacitance Simulator 65, 134
SCCM Standard Cubic Centimeters per Minute 57, 136
SILAR Successive Ionic Layer Adsorption and Reaction 10, 43, 62, 70
SLG Soda Lime Glass 55, 67

TCO Transparent Conducting Oxides 25, 53, 138, 147
TFSC Thin Film Solar Cell 74

UN United Nations 1
UNSW University of New South Wales 34
UPS Ultraviolet Photoelectron Spectroscopy 53, 152
UV-Vis NIR Ultraviolet-Visible Near Infra Red ix, 138, 142

VBM Valance Band Maximum xx, 16, 71, 126, 127
VBO Valance Band Offset 71

XPS X-Ray Photoelectron Spectroscopy ix, 53, 106, 134, 152
XRD X-ray Diffractometry ix, 74, 91, 114

ZSW Centre for Solar Energy and Hydrogen Research BadenWürttemberg 34

List of Symbols

α Absorption coefficient 20
D Average crystallite size 75

E_g Band gap 88
V_{bi} Built-in voltage 23

$L_{n,p}$ Diffusion lengths of minority carriers 22
δ Dislocation density 75

ε Electric field at the p-n junction 23
η Power Conversion Efficiency 18

FF Fill factor 29

$\tan\delta$ Loss factor 142

ϕ_{TC} Figure of merit (FOM) 147
ε Microstrain 75

σ_{opt} Optical conductivity 144
V_{oc} Open-circuit voltage, volt 27

ϕ Phototon flux, photons/sec 20

ρ Resistivity 147

$\rho(x)$ Space charge 23
J_{sc} Short-circuit current density, mA/cm^2 27

E_u Urbach energy 89

Chapter 1: INTRODUCTION

In light of the adverse effects of fossil fuel consumption, including climate change and energy scarcity, humanity has been compelled to shift towards renewable energy sources. The cost-effectiveness, adaptability to various locations, and zero carbon emissions of photovoltaic energy have resulted in superior performance compared to hydroelectric, wind, and nuclear energy sources.

This chapter provides an overview of the research's background and contextual factors, as well as its intended objectives. The following section delineates the importance and extent of this study while furnishing explications of the lexicons employed. Ultimately, this chapter comprises an outline of the subsequent chapters.

1.1. Global energy scenario

One of the greatest difficulties confronting humanity in the 21st century is finding solutions to the world's energy problems. The first obstacle is a supply and demand conundrum. Every 12 years since 1975, the world population has expanded by one billion. In 2011, it surpassed its final benchmark of 7 billion. In November 2022, one additional billion was added: 8 billion. The United Nations (UN) forecasts that the world's population will reach a peak of around 10.4 billion people in 2086, just before the end of the century[1]

This massive population's rising energy needs have elevated standards of living and economic ramifications as well. If energy supply does not change much, the price of the products will increase. Natural gas, coal, and oil are examples of fossil fuels that are being used extensively in the world's energy infrastructure. It's common knowledge that burning fossil fuels releases greenhouse gases (CO_2) into the environment and depletes limited fossil energy reserves. CO_2 is a primary contributor to global warming and consequent climate change. As the acquired value did not fall within the predetermined parameters. From October 31 to November 12, 2021, the COP26 international climate conference was held in Glasgow. The main goal was to reach 'net zero' by the middle of the century and keep warming to no more than 1.5°C. 'Net zero' means that the amount of pollution put into the environment is equal to or less than what is taken out. There were four clear goals set to reach global net zero and 1.5°C degrees by mid-century. First, speeding up the phase-out of coal, stopping

---

[1] This is based on its medium-fertility projection scenario. Its 'low' projection scenario peaks much earlier in 2054 at 8.9 billion people. Its 'high' projection scenario does not peak by the end of the century.

deforestation, speeding up the switch to electric vehicles, and encouraging investment in renewables. Second, adapt to protect communities and natural habitats. Third, get at least $100 billion a year for climate change. Last but not least, cooperation between individuals is essential for success. It is undeniable that achieving an international energy shift that is consistent with the world's climate objectives is a difficult task. Energy consumption in 2020 was significantly impacted by the COVID-19 pandemic, leading to a 5.2% decrease in worldwide CO_2 emissions. Since then, however, the global economy has recovered at an unparalleled rate, helped along by monetary and fiscal stimulus measures and the widespread distribution of vaccinations. Coal-fired power plants became increasingly prevalent when the economy recovered in 2021. As a consequence, both global CO_2 emissions from combustion of energy and natural gas prices spiked to all-time highs. Emissions dropped by 1.9 Gt in 2020 due to a pandemic, but made a strong comeback the following year (2021). Around 180 Mt of more CO_2 were released into the atmosphere in 2021 compared to 2019's pre-pandemic levels. Due to an increase in carbon dioxide emissions, energy-related GHG emissions reached a record high in 2021. With a 100-year horizon for global warming potential, total greenhouse gas emissions in 2021 totaled 40.8 Gt of CO_2 equivalent, surpassing the previous record set in 2019.

To achieve a goal of zero net CO_2 emissions from the energy industry by 2050, a dramatic shift is needed in technology. Mainstays include reducing energy waste and using renewable sources. One of the most important steps toward decarbonization is switching to clean power. Electrification has emerged as a critical instrument for cutting emissions throughout the economy as the energy industry gets cleaner. Key milestones and actions for rapid emission reductions are:

- Ramping up renewables, together with an aggressive energy efficiency strategy.
- The decarbonisation of end-uses needs to make much faster progress.
- A comprehensive set of policies is needed to achieve the necessary levels of deployment.

The world's consumption of energy and shares of global primary energy is shown in Figure 1.1.

Renewable energy made for 28.3% of global electricity in 2021. Solar and wind energy generated over 10% of global electricity for the first time. Figure 1.2 shows that renewable electricity is the most cost-effective in most places. As shown in Figure 1.3, renewable energy could cut power sector carbon emissions by 90% by 2050. 85 million sustainable energy jobs are expected by 2030. Expanding educational and training programs and promoting a diverse and fair workforce transition are necessary to fill newly created jobs.

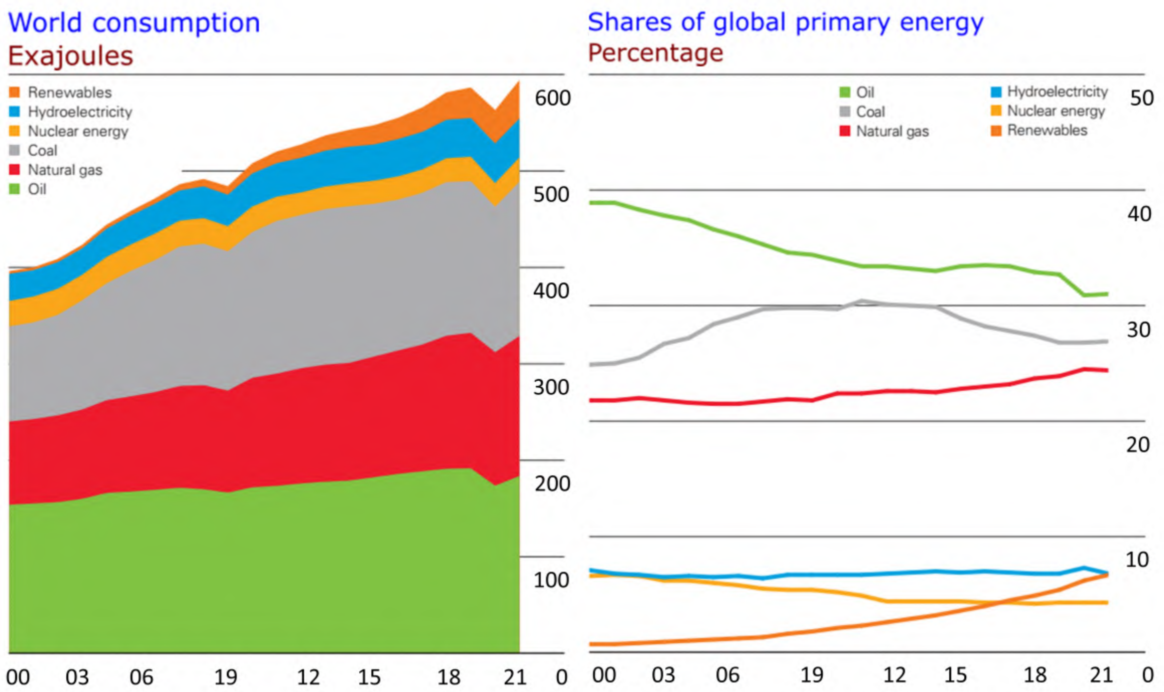

Figure 1.1: Consumption of energy worldwide
[**Source:** bp statistical review of world energy 2022, 71st edition]

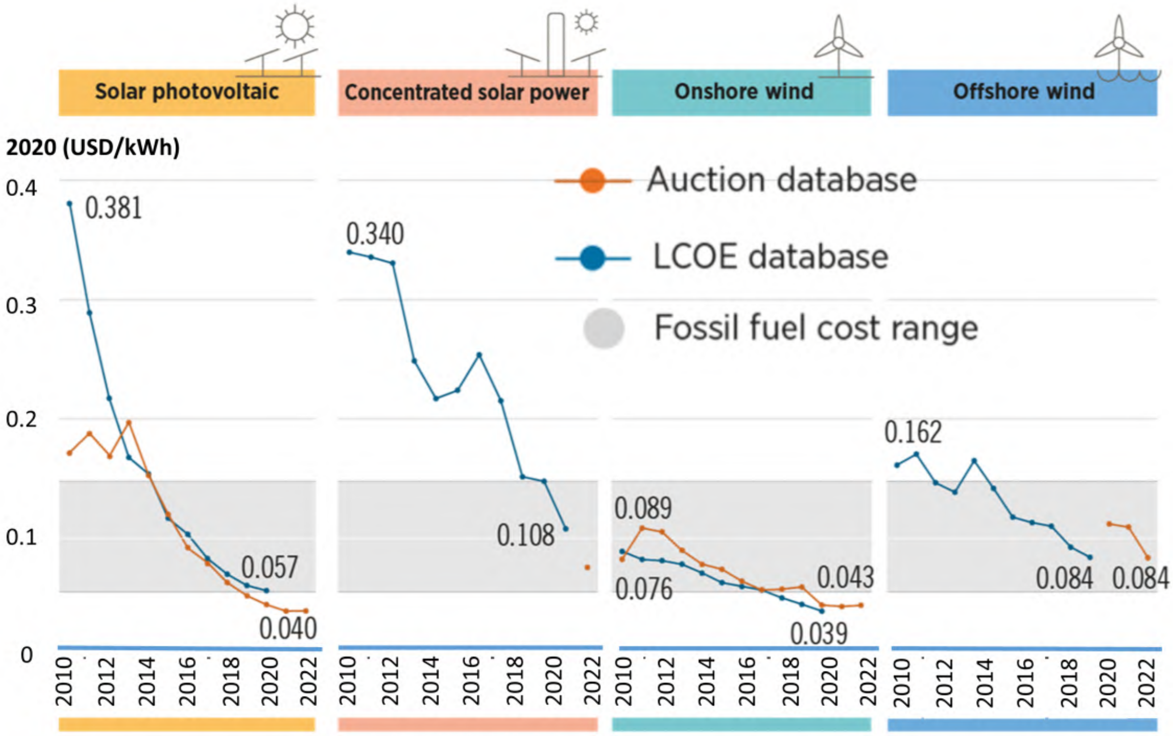

Figure 1.2: Utility-scale solar power levelized cost globally
[**Source:** IRENA 2022]

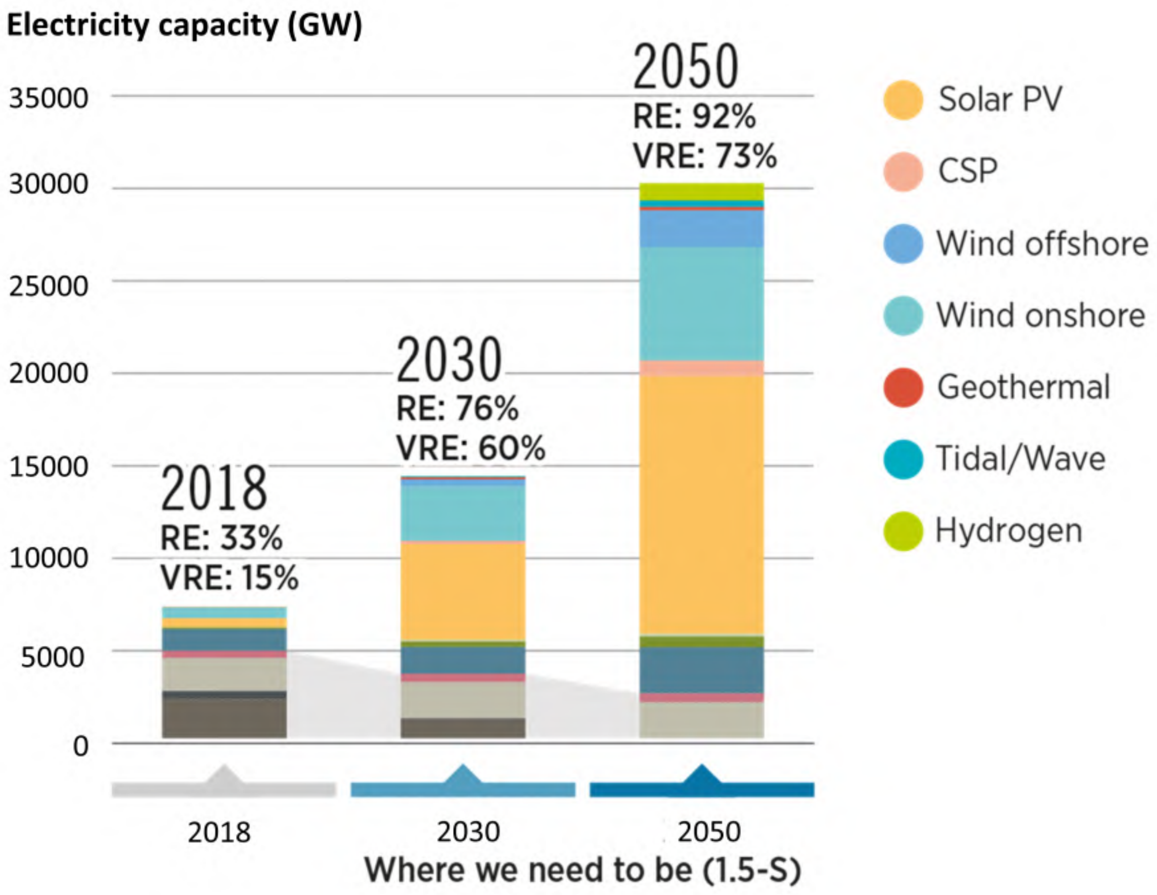

Figure 1.3: From 25% in 2018, renewables will supply 65% of electricity by 2030 [**Source:** IRENA 2022]

1.2. Motivation

The motivations of this study are in two folds: firstly, renewable energy as a solution for net-zero emission and secondly, solar energy in particular.

1.2.1. Renewable energy

Despite the COVID-19 pandemic, fresh financial inflows into renewable energy and fuels were USD 366 billion in 2021, a record high. China accounted for 37% of worldwide renewable energy and fuel investment in 2021. China, Europe, and the US have received almost two-thirds of worldwide renewable energy and fuel investment since 2011. South Australia, Scotland, and Denmark used 100% wind and solar energy as of April 2022.

Solar and wind power generated over 10% of global electricity in 2021, making renewable energy 28.3% of the global electricity mix. Solar and wind power installations increased renewable power capacity by 17% (314.5 GW) in 2021.

As energy markets revived, renewables made up 84% of net power increases. Industrial and agricultural sectors provide 25% of worldwide greenhouse gas emissions. So, renewable energy may replace fossil fuels for a wide spectrum of energy needs.

Over 1,100 municipalities have committed to net zero. Europe, Latin America, and the Caribbean have the highest net zero energy objectives, followed by East Asia and North America. Fifty-nine cities have banned or restricted non-renewable energy. Barcelona, Bristol, Shanghai, and Stuttgart are the only cities with vehicle bans.

According to the IEEFA, Bangladesh will need to invest $1.53 billion to $1.71 billion per year from 2024 to 2041 to meet its goal of generating 40% of its energy capacity from renewable sources. Although the electricity sector's subsidy burden is smaller than in fiscal year 2021–22, accelerating the switch to renewable energy will free up financial resources for subsidization. IEEFA also reported that rising fossil fuel prices have raised power generation costs, requiring more power sector subsidies. Thus, policymakers should incorporate sustainable energy goals into future Integrated Energy and Climate Plans (IECPs).

Energy security and financial resources may improve if the electrical business shifts faster to renewable energy. The research advises the government to embrace renewable energy policy changes. These changes remove the rooftop solar installation capacity restriction and exclude FRP walkways, imported inverters, mounting structures, and DC cable taxes. Bangladesh extended its 2020 goal of generating 10% of its energy from renewable sources to 2030. However, the nation has set a loftier goal of producing 40% of its energy by 2041.

1.2.2. Solar energy

Solar power seems to be the most auspicious advancement in the realm of renewable energy. Solar power constitutes the predominant share of newly installed power capacity on an annual basis and is increasingly being recognized as a reliable and sustainable energy option. The utilization of solar energy has the potential to significantly reduce greenhouse gas emissions within the power industry, enhance energy security through market expansion, and facilitate the worldwide transition towards a green economy.

According to the International Energy Agency (IEA), solar photovoltaic (PV) capacity experienced a 25-fold increase from 23 GW to 627 GW on a global scale between 2009 and 2019. The global solar photovoltaic industry receives financial and legal support from multiple governments. Furthermore, progress in this regard has been aided by the reduction in production costs, which can be attributed to the innovative efforts of Chinese panel

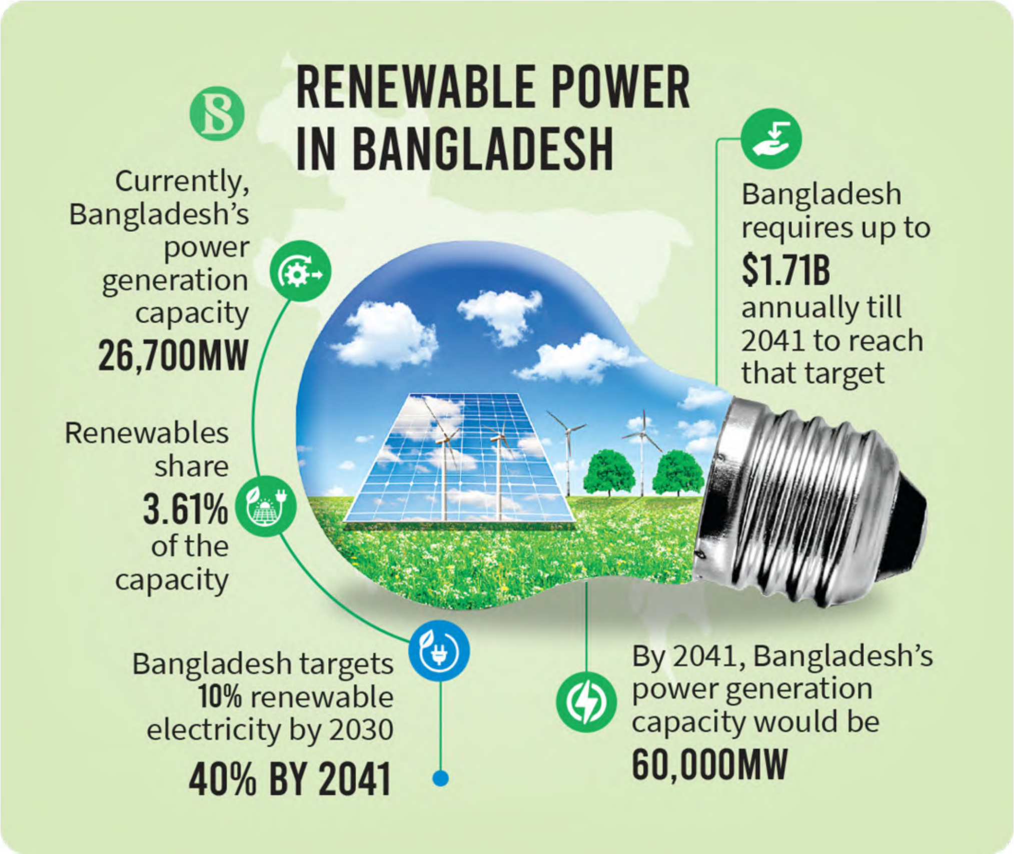

Figure 1.4: Renewable power in Bangladesh
[**Source:** Infogrphic report in The Business Standard, Bangladesh]

manufacturers.

Forecasts from the solar industry predict a 50% drop in the price of solar power by 2030. Modules with higher efficiency have the potential to produce 1.5 times the amount of power compared to modules of similar size. The solar industry additionally declares and monitors advancements that reduce the expenses associated with costly materials such as silver and silicon, which are utilized in the production of solar panels and double-surface modules that collect solar energy from both sides. Floating solar energy solutions are preferred in regions with limited land availability but ample water resources such as reservoirs, lakes, ponds, canals, and rivers due to their low maintenance and administrative costs.

Following the invasion of Ukraine by Russia, the food networks have exhibited increased susceptibility, potentially leading to a worldwide food crisis. Nations are currently seeking tactics to enhance their agricultural productivity. Prior to the recent past, the construction of a solar farm entailed the relinquishment of arable land. Recent technological advancements, particularly in the field of agrivoltaic systems, have rendered it possible to utilize land for both agricultural purposes and solar panel installation. The efficiency of harvesting is enhanced by the implementation of panel shadows and the capacity to collect rainwater in this system.

The utilization of digital technology for the purpose of enhancing the integration of solar energy into residential and commercial buildings, as well as power networks, is regarded as a noteworthy progression. The objective is to enhance the efficiency, promptness, and durability of solar energy.

Due to these advancements, it seems that solar energy is progressing towards attaining a cost benefit that will enable it to compete with and potentially exceed fossil fuels in numerous regions across the globe.

Currently, Si solar cells are the prevailing commercial photovoltaic (PV) technology. The Energy Pay Back Time (EPBT) is a significant methodology for evaluating and contrasting various categories of solar cells. Photovoltaic modules generate electricity that is environmentally friendly due to their lack of pollution, greenhouse gas emissions, and dependence on fossil fuels. Nevertheless, the production of the modules requires a significant amount of energy and resources. Time taken for solar cells to produce enough energy to run a photovoltaic system is included into the EPBT measure. Hence, the duration within which the module must operate to yield a return on investment that justifies its implementation is referred to as the payback period.

The efficacy of Si technology as a photovoltaic (PV) solution to steer the industry's growth is debatable. There exist several alternative PV materials, such as CdTe, CIGS, CZTS, organic, dye-sensitized, and the recently discovered perovskites, which could potentially serve as substitutes. In terms of resource preservation, thin film solar cells excel since they require a thickness of approximately 1 μm to achieve sufficient light absorption.

The focus of this research is on examining the quaternary compound copper-zinc-tin-sulfide, denoted as Cu_2ZnSnS_4 or CZTS, which is constituted by abundant and environmentally safe elements that are widely available on the planet. The subject matter has experienced a significant increase in attention in recent times.

The efficiency progression of CIGS and CZTSSe solar cells is depicted in Figure 1.5. It is apparent that CIGS solar cells have achieved an efficiency level of 23.4% after being introduced 40 years ago. In contrast, the solar cell technology based on CZTS is relatively recent. A comparison of a 12-year timeframe for both solar cell types reveals that CZTS achieves an efficiency of 13%, exhibiting a growth rate that is nearly identical to that of CIGS. It can be inferred that CZTS is expected to exhibit superior or comparable efficiency levels once it attains a 40-year lifespan.

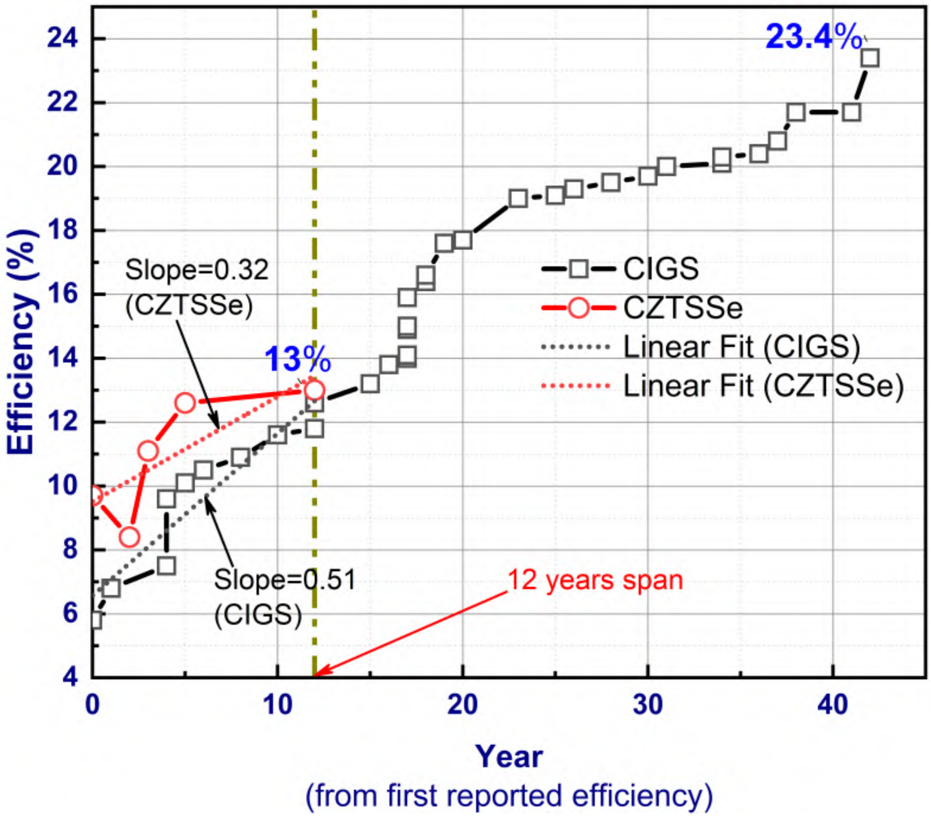

Figure 1.5: Efficiency evolution of CIGS and CZTSSe solar cells from the first recorded working cell at NREL. Year 0 is 1976 for CIGS and 2009 for CZTSSe

1.3. Problem statement

Since its inception in 1988 [1], advances in CZTS thin film research have remained a topic of great interest due to a number of promising qualities. Although the ongoing efforts to improve their performance, their efficiency is still far from the Shockley-Queisser theoritical limit [2]. Due to deposition process variability and interdependence, little is known about how absorber, buffer, and window layers affect CZTS-TFSC production. RF magnetron sputtering could assist to deposit all layers.

Studies reported that off-stoichiometric CZTS, preferably in the Cu-poor, Zn-rich regime outperformed stoichiometric CZTS in photovoltaic performance [3]. Due to this off-stoichiometric composition, there is the possibility to form various detrimental binary and ternary other than the CZTS phase, secondary phases. Thus, simply modifying the absorber stoichiometry is not sufficient to increase device performance to a level that is comparable to other thin film solar cells. Moreover, the CZTS compound may develop a variety of intrinsic defects and defect-clusters including vacancies, antisities, and interestrials [4]. Thus, the addition of extrinsic atoms in varying amounts to the Kesterite-type crystal matrix is being studied to attain the beneficial properties of absorber [5]. Germanium (Ge) is one of the best group IV dopants for Sn-sites. Study found, Ge doping has significantly reduced the V_{oc} deficit to 0.57 V. Several doping tactics are being investigated. Another potential solution could be RF magnetron co-sputtering.

While CIGS has attained excellent efficiency up to 23.35% [6], The performance of CZTS/CZTSSe is deemed inadequate due to the presence of an open circuit voltage deficit, $\left(\frac{E_g}{q} - V_{oc}\right)$ [7–9]. Several explanations, including strong band tail effects [10], secondary phases [11], and non-ideal interface [12], have been put forth. The issue of majority faults was frequently cited as one of the primary causes of the V_{oc} deficiency [10, 13, 14].

In CIGS and kesterite solar cells, the majority faults are of distinct types. $\mathrm{V_{Cu}}$ is a shallow defect and makes up the majority of defects in CIGS, according to theoretical calculations [15], whereas $\mathrm{Cu_{Zn}}$ antisite, which has a deeper defect level in the band gap, makes up the majority of defects in CZTS/CZTSSe. $\mathrm{Cu_{Zn}}$ antisite is a defect in which Cu replaces Zn in the lattice, whereas $\mathrm{V_{Cu}}$ is a defect in which Cu moves out of its lattice and leaves its spot unfilled. The stability of the defect is attributed to the cation disorder resulting from the comparable size and overlapping functions of Cu and Zn. In solar cells, deeper defects are undesirable because they serve as recombination hubs and produce band potential fluctuations and tailing effects. The creation of defects-complexes like ($\mathrm{V_{Cu}}$ + $\mathrm{Zn_{Cu}}$), ($\mathrm{V_{Zn}}$ + $\mathrm{Sn_{Zn}}$), ($\mathrm{Zn_{Sn}}$ + 2$\mathrm{Zn_{Cu}}$), and (2$\mathrm{Cu_{Zn}}$ + $\mathrm{Sn_{Sn}}$) that can serve as non-radiative recombination centers is similarly influenced by these point defects [15].

Therefore, one way to decrease the V_{oc} deficit is to partially replace Zn atoms with an extrinsically doped other atoms during the production of CZTS films. This will reduce the density of defects associated with the $\mathrm{Cu_{Zn}}$ antisite based on better carrier lifetime, sharp absorption edge and V_{oc} improvement. To minimize $\mathrm{Cu_{Zn}}$ antisite defects, the Cu-cationic site can also be substituted; however, in this thesis, Zn-cationic site was in focus. In selecting the dopant atoms for Zn-cationic sites, the size of the atom and its location in the periodic table are important. The band gaps in compound semiconductors get smaller when heavier atoms from belonging to the same cluster in the periodic chart are substituted [16]. The atoms having the same isoelectronic configuration as Zn, same valence electrons as Zn, and a larger atomic size than Zn are considered during the dopant selection [17].

In the same group II-B as Zn, Cd is regarded as a potential dopant for a probable partial Zn-cation substitution in the CZTS crystal. Since Cd and Zn atoms have the same electron structure, they are isoelectronic. The atomic radii of Zn and Cd, according to J.C. Slater [18], are

1.35Å and 1.55Å, respectively. Therefore, Cd atom is bigger than Zn atom. In addition, the Zn^{2+} and Cd^{2+} ions' respective ionic radii in tetrahedral coordination are 0.6Å and 0.78Å respectively. It has been discovered that Cd doping for partial Zn cation substitution helps reduce defects brought on by Cu_{Zn}, which lowers the V_{oc} deficit.

Toxic Cd doping in non-toxic CZTS, might, however, cause additional issues that can exceed the advantages. Taking this into account, the main aim behind this study, to reduce the Cd content by introducing another dopant atom at the same Zn-cationic site in such a way to get same benefit as Cd-dopant alone. It has been proposed that Cd concentration may be reduced by simultaneous doping with other elements. As a possible second dopant, we have hypothesized Mg as a non-toxic counterpart of Cd, which is a group II-A element having 1.50Å atomic radius [18], 0.57Å ionic radius, and same valence electrons as Zn atoms. The uniqueness of this work resides in the fact that co-doping in the same cationic site (such as the Zn-site) has not been studied previously.

Band synchronization at the hetero junction interface is another challenge for CZTS photovoltaic cells. For open circuit voltage enhancement, a lattice matched heterojunction partner with absorber CZTS is required [19]. Until now, Chemical Bath Deposition processed thin CdS layer has largely been reported as an n-type companion of p-type CZTS. In this sense, two difficulties might be addressed. First, there is the question of CdS toxicity. Second, with CZTS, lattice mismatch leads in a cliff-like conduction band offset. As a result, it has been predicted that a non-toxic, closely lattice matched substance with a reasonably simple fabrication method should be used. As an alternative to CdS buffer layer, a ZnS thin film was fabricated using a home built Successive Ionic Layer Adsorption and Reaction (SILAR) technique.

Thin-film solar cells composed of amorphous silicon or Cu(In,Ga)Se_2 have recently reached in-vitro power conversion efficiencies of over 22% [20], and Al-doped zinc oxide (AZO) is being extensively used as a top electrode in both research and industry for this purpose. Compared to ITO, AZO has lower production costs and more readily available raw materials. AZO thin film deposition method by RF- or DC magnetron sputtering is often employed in thin-film solar cell production [21, 22] because to its good film quality, relatively high deposition rate, and tolerance with large-area substrates. An alternative to AZO is Ga-doped zinc oxide (GZO). To accomplish this, extensive experiments of RF-sputtered GZO at various deposition pressures were conducted, looking at its electrical, structural inequality, morphological, and compositional properties.

1.4. Aims and objectives

1.4.1. Aims

This research aims to find out how co-doping a CZTS thin film with Cd and Mg affects its microstructural, morphological, optical, and photovoltaic properties when prepared by the sol-gel spin coating and treated with sulfur afterward. Furthermore, the aim of this effort is to look at the thin films made by using partial cation substitution of Sn with Ge in RF magnetron cosputtering. The study also wants to find out if the CZTS/ZnS heterointerface could be used instead of the usual CZTS/CdS interface. RF magnetron sputtering has been looked into as a way to make GZO, which could be used as a window layer.

1.4.2. Objectives

1. Fabrication and characterizations of CZTS thin-films deposited by RF magtnetron sputtering by varying substrate temperatures.
2. Fabrication and characterizations of Ge-alloyed CZTS thin films by RF magnetron co-sputtering.
3. Fabrication and characterizations of superstrate structured CZTS thin film solar cell by sol-gel spin coating: Effect of (Cd,Mg) co-doping.
4. Band alignment study at CZTS/CdS (fabricated by CBD) and CZTS/ZnS (fabricated by SILAR) heterojunction interfaces and validation with numerical simulation.
5. Fabrication and characterizations of Ga-doped Zinc Oxide (GZO) thin-films by RF magnetron sputtering to be used as a potential TCOs in CZTS thin-film solar cell.

1.5. Thesis organization

This section outlines the content of each chapter of this dissertation briefly. This thesis includes five chapters in total.

Chapter 1 presents a concise overview of the current global energy landscape, followed by an exploration of the driving factors behind research on CZTS thin film solar cells. The study identifies existing research gaps and formulates hypotheses to address them, conclusively detailing the study's intended outcomes.

Chapter 2 gives a brief introduction to the underlying physics of solar cells, with an emphasis on CTZS cells in particular. An in-depth analysis of CZTS solar cells made of thin films follows a discussion of the structure and operating principles of CTZS solar cells. The present chapter examines the extrinsic doping methods used in the production of CZTS solar cell thin films. This chapter also looks at the use of CdS (or ZnS) in CZTS hetero junctions and the possibility of GZO as the window layer.

Chapter 3 presents study encompasses the research methodology and expounds upon the experimental setup employed to conduct the research, which includes simulation analysis and modeling approach. The various techniques used for characterization are presented in the form of overviews.

Chapter 4 delves into the obtained outcomes and systematically presents them in alignment with the research objectives. The outcomes and results of the simulation are depicted, elucidated, and contrasted.

Chapter 5 culminates by providing a summary of the principle results for each of the research objectives that were delineated. Potential theoretical and experimental avenues for further advancing CZTS thin film solar cell technology are proposed.

Chapter 2: LITERATURE REVIEW

This chapter provides a contextual framework to improve understanding of the thesis, which presents a comprehensive overview of photovoltaic technology. It also involves a comprehensive analysis of the structural development and photovoltaic performance of CZTS kesterite thin film devices, accompanied by a critical evaluation to improve the understanding of CZTS thin film solar cells. The subsequent sections present a comprehensive analysis of the study undertaken using an objective-driven methodology.

2.1. Introduction to photovoltaic

2.1.1. Energy band and Band gap in solids

An individual atom is composed of a central nucleus and electrons occupying distinct energy levels. Bohr's atomic model postulates the existence of orbits that circle the nucleus in a circular pattern. Electrons are capable of undergoing a transition from one orbit to another through the absorption or emission of energy. The 3D orbitals contain the electron, and its position within these orbitals is determined by Schrödinger's wave function, as demonstrated in Eq. 2.1. This function explains the electron's wave motion within the structure of crystals and is a combination of a periodic function, which reflects the crystal lattice's periodicity, and the plane-wave envelope function, which depicts the electron's localization.

$$\psi_{n\mathbf{k}}(\mathbf{r}) = e^{i\mathbf{k}.\mathbf{r}} U_{n\mathbf{k}}(\mathbf{r}) \tag{2.1}$$

Each orbit has a number of electron states. It is impossible for two electrons to be in the same quantum state since electrons are fermions. Electrons fill up the orbits closest to the nucleus first. The outermost electrons in an atom are known as the valence electrons. Valence electrons are responsible for chemical bonding and electrical conductivity in a crystal. As the probability functions of two electrons overlap one another, the electrons interact. The two electrons are not allowed to occupy the same electronic state, so the states split into two. If a large number of isolated atoms come together, the discrete electronic states split-up into (quasi-) continuous energy states, known as *energy bands*.

It is possible to excite the valence electrons from their valence band location into the conduction band. The term *band gap* is used to describe the space between bands, which indicates a range of energy in which no permissible electronic states exist. Simply put, the energy required to excite a semiconductor electron from a highly localized state to a detached excited state is the bandgap energy. In Figure 2.1, a schematic depiction of the creation of an energy band is shown. Energy-momentum, or E-k, diagrams are useful for grasping the idea of band gap because they illustrate how the law of conservation of momentum applies during the transfer of electrons from the valence band to the conduction band. According to the nature of the transitions they undergo, semiconductors may be further categorized as direct or indirect. Since the transition of electrons from valence band to conduction band must satisfy the conservation of momentum, the concept of band gap can clearly be understood by so called energy-momentum or E-k diagram. The type of semiconductor is thus also classified as direct and indirect depending on transition types.

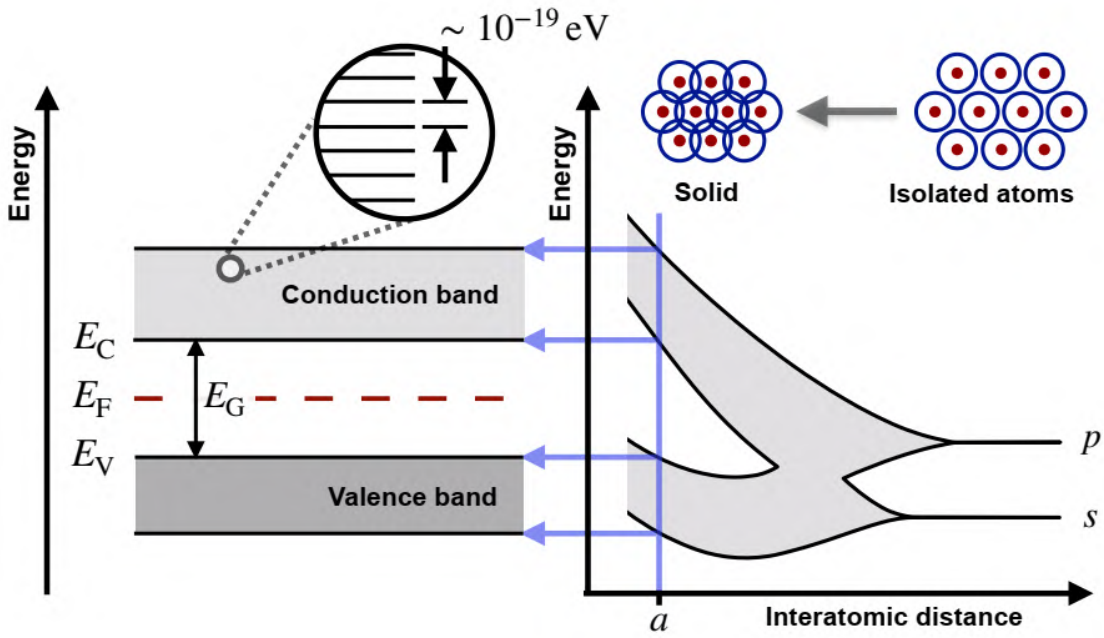

Figure 2.1: The formation of electronic bands in solid

- **Semiconductor with a direct band gap**
  In k-space, the valence band top coincides with the conduction band bottom. If the photon's energy is greater than the bandgap, the material will absorb it. Mathematically, $E_c{}^{electron} = E_v{}^{electron} + \hbar\omega, \hbar\omega \geq E_g$
- **Semiconductor with an indirect band gap**
  The top of the valence band is shifted from the bottom of the conduction band in k-space. In these materials photons with energies between the bandgap and the vertical gap can

only be absorbed in the presence of a lattice vibration (a phonon), which can donate its momentum towards the optical transition. Mathematically, $E_c{}^{electron} = E_v{}^{electron} + \hbar\omega + E_{phonon}, E_g \leq \hbar\omega \leq E_{vertical}$

Figure 2.2 shows the E-k diagrams of GaAs and Si as to show an example of direct and indirect band gap semiconductor materials.

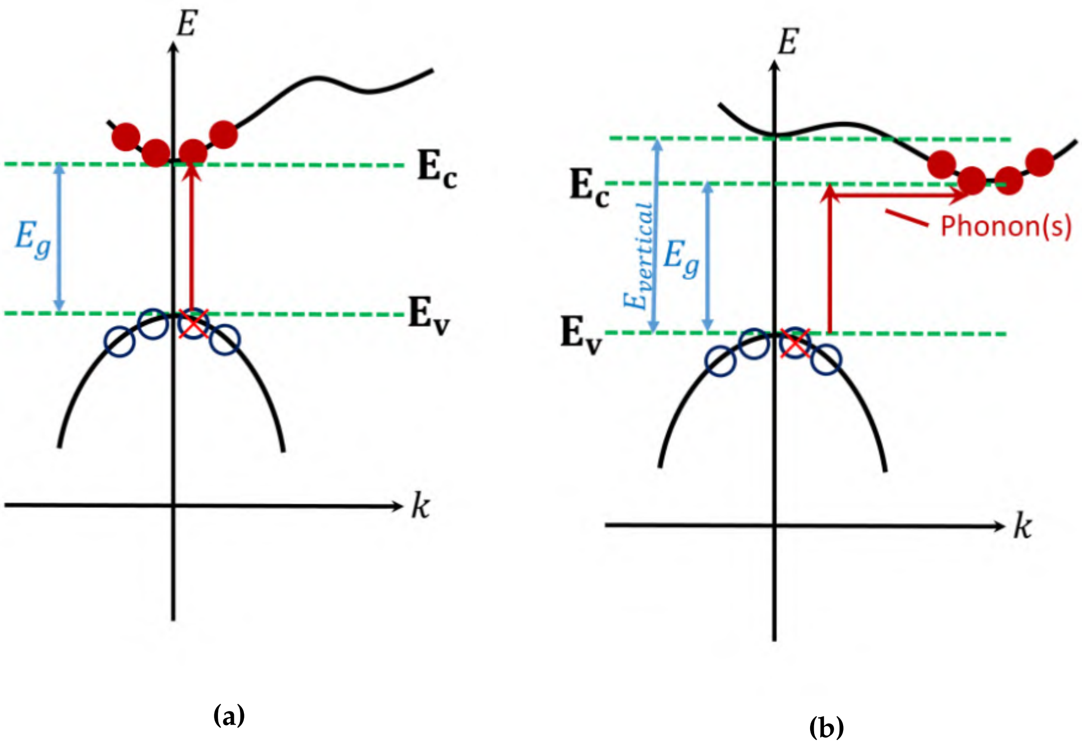

Figure 2.2: (a) GaAs semiconductor (direct band gap), and (b) Si semiconductor (indirect band gap)

2.1.2. Classes of materials

In solid state physics, the band gap (E_g) value of a material is used to classify it as a conductor, semiconductor, or insulator (Figure 2.3). Obviously, their conductivity relies on availability of conduction electrons in conduction band. We are mainly concerned about semiconductor materials. In semiconductor material, conduction electron can spontaneously available upon thermal radiation. Doping and illumination may also contribute to conduction electrons as well. Semiconductors are of intrinsic and extrinsic types. The predominant charge carriers in extrinsic semiconductors further define them as either n-type or p-type. Knowing the location of the Fermi energy level, E_F, may be used to distinguish between intrinsic and extrinsic semiconductors. For intrinsic semiconductor, the position of the E_F is midway between CBM and VBM. For n and p type extrinsic semiconductor materials, the position of E_F is just below the CBM and above the VBM respectively.

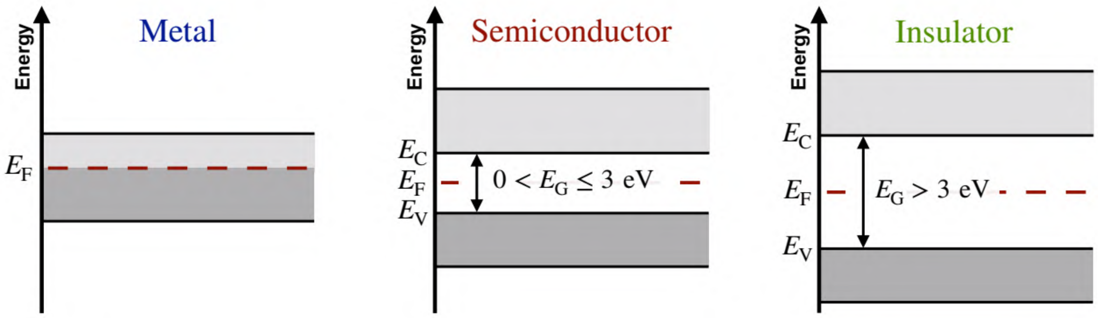

Figure 2.3: Classifications of materials

2.1.3. PV: The history of innovations

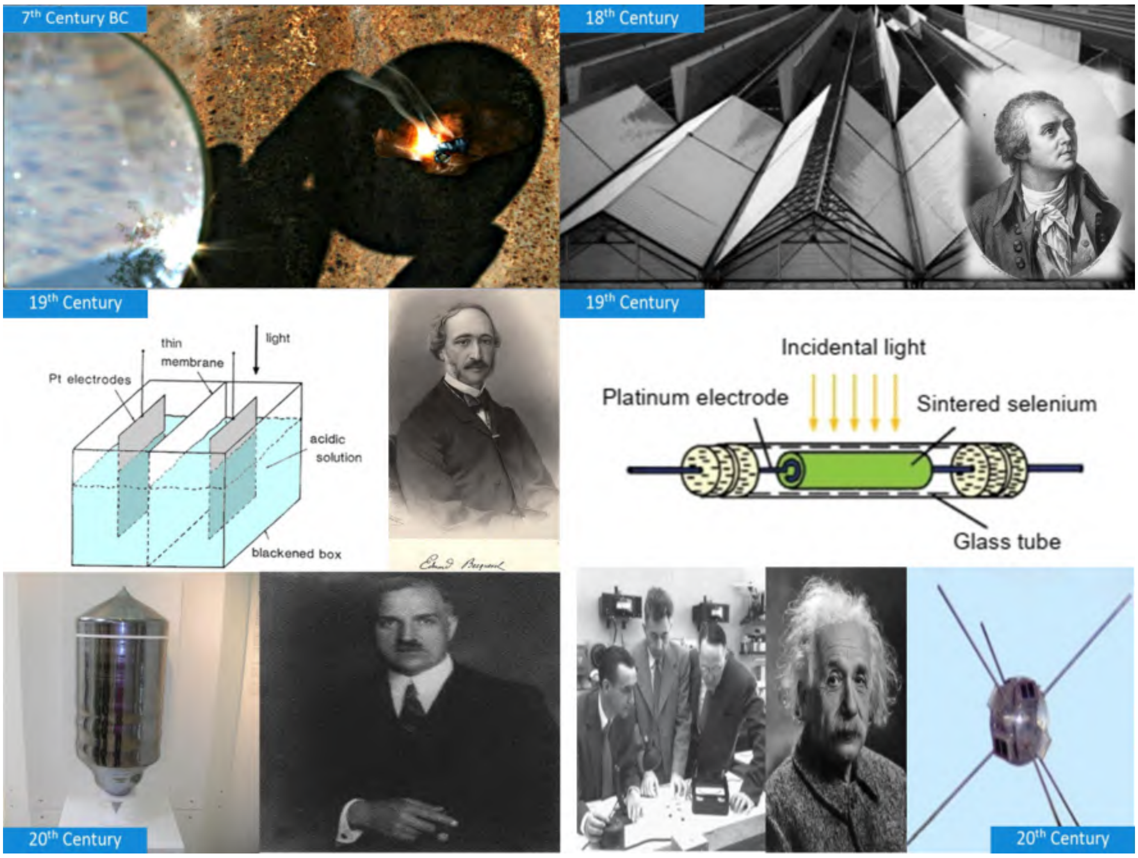

Figure 2.4: The history of photovoltaics by centuries

Since the 7th century BCE, the utilization of solar technology has been documented in human history. Magnifying glasses were utilized to initiate combustion. Subsequently, the utilization of concentrating mirrors for the aforementioned objective was also observed among the Romans and Greeks.

During the 18th century, Horace de Saussure constructed heat traps, which can be classified as miniature greenhouses. The individual fabricated hot enclosures by assembling a glass container within a larger glass container, with the potential for up to five nested boxes. Upon exposure to direct solar irradiation, the temperature within the inner bottom box increased to a level of 108°C, which is sufficiently warm to facilitate the boiling of water and cooking of food. These containers may be regarded as the initial solar collectors globally.

The photovoltaic effect was discovered by Edmond Becquerel, a French physicist, at the youthful age of 19 in the year 1839. The photovoltaic effect refers to the phenomenon of producing voltage or current in a substance upon exposure to light. The effect was observed in an electrolytic cell. The experimental setup consisted of a cell comprising of two platinum electrodes immersed in an acidic solution of silver chloride serving as the electrolyte. Through the application of light, the observer noted an augmentation in the electrical current within the cell.

The inaugural solid-state solar cell was constructed by William Adams and Richard Day in 1877. The experimental setup involved the placement of two platinum electrodes on a rod of solidified selenium that was exposed to illumination. This pioneering experiment provided evidence that a solid material has the ability to convert light energy into electrical energy without the need for an intermediary mechanism. After a span of seven years, Charles Fritts successfully developed a photovoltaic device utilizing a gold-selenium junction, which exhibited a conversion efficiency of 1% from light to electricity.

In 1905, Albert Einstein authored a scholarly article in which he explicated the photoelectric effect by postulating the existence of discrete units of energy, referred to as photons, that transport light energy. In 1921, Einstein was awarded the Nobel Prize for his work related to this paper.

In 1918, Polish scientist Jan Czochralski developed a technique for growing single crystal silicon. This technique has significant implications for solar cell technology that relies on c-Si wafers and has been refined during the latter half of the 20th century.

In 1950, William B. Shockley, one of the co-inventors of the transistor, provided a theoretical account of the operational mechanism of a pn-junction.

In 1954, Daryl Chapin, Calvin Fuller, and Gerald Pearson of Bell Labs created the first silicon solar cell. The device exhibited a surface area of 2 cm^2 and a conversion efficiency of 6%. The device integrated the principle of the pn-junction as proposed by Shockley, utilizing silicon material grown through the Czochralski method, with the theoretical framework of the photovoltaic effect.

Solar cells were first deployed in space in 1958. The initial satellite to be outfitted with solar cells was Vanguard-1. The device functioned for a duration of six years by utilizing six silicon solar cells affixed to its exterior.

The impetus behind the advancement of solar cell technology during the 1960s was primarily attributed to the demands of space exploration. The oil crisis of 1973 stimulated a surge of interest in exploring novel alternative sources of energy. The installed capacity of photovoltaic systems on a global scale has experienced a significant increase in recent times.

2.1.4. The pn junction solar cell

Several devices can be built using pn junctions:

- pn junction under applied voltage:
  diode, transistors, Light Emitting Diode (LED), Light Amplification by Stimulated Emission of Radiation (LASER)
- pn junction under illumination:
  solar cells, photodetectors

There are essentially three necessary processes in order for a pn junction in a solar cell to function properly:

- Production of electron-hole pairs within the cell.
- At the interface, electrons and holes are kept apart.
- Terminal charge collection of electrons and holes.

Every photovoltaic device must obey:
Power Conversion Efficiency (PCE) , $\eta = \frac{\text{Output energy}}{\text{Input energy}}$
This is broken down as follows in Figure 2.5 for the vast majority of solar cells:

1. Spectra of the sun
2. Light scavenging
3. Excitation of charges
4. Diffusion and drift of charges
5. Distinction of charges
6. Accumulating charges

Figure 2.5: Conversion of solar energy to electricity

Spectra of the sun

When examining the solar spectrum, as illustrated in Figure 2.6, the majority of power is concentrated within the visible region. Ideally, the absorber layer should possess a high degree of spectral absorption. However, the occurrence of transmission losses arises when the band gap of the absorber material exceeds a certain threshold. Hence, it is advantageous for absorbers to possess a band gap ranging from 1.1 to 1.6 eV in order to effectively utilize the visible region of the electromagnetic spectrum [23].

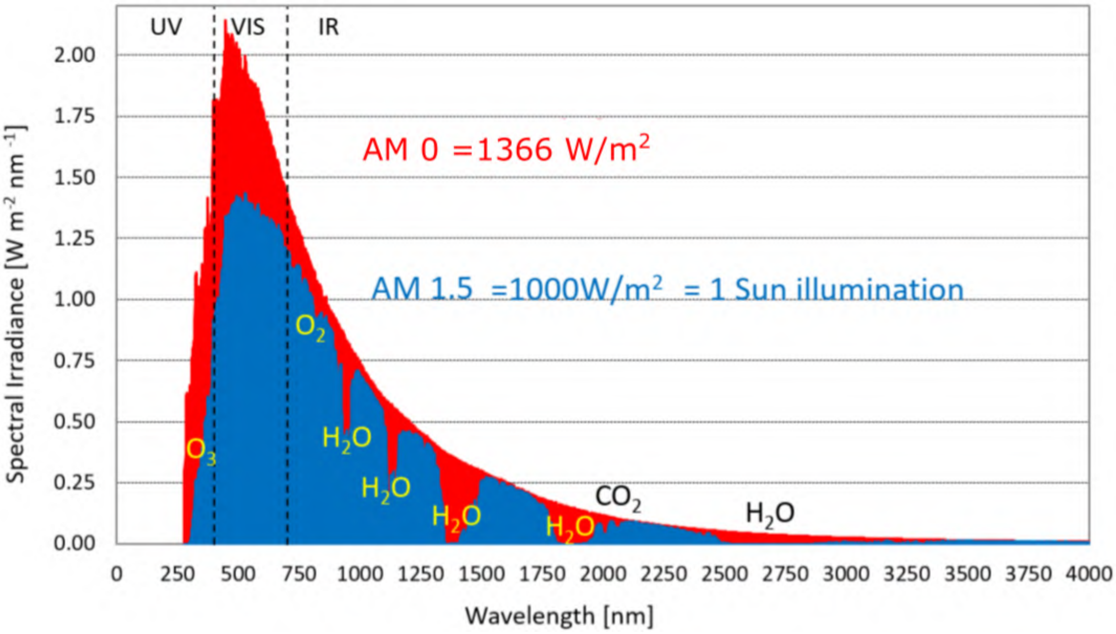

Figure 2.6: Solar irradiance spectra according to ASTM G173-03 standard

Excitation of charges

Photovoltaic cells are responsible for the creation of carriers. Most carriers in semiconductors are created by thermal generation or photogeneration (Figure 2.7). The transition of electrons from the band known as valence to the band of conduction often occurs through thermal generation. This occurs because the width of the Fermi distribution increases with temperature. Thermogenesis may be broken down into two subcategories: direct and indirect. Electrons, for instance, go from the valence band to the conduction band through the intermediate band (IB) in the case of indirect heat generation. An intriguing strategy, photogeneration involves a photon interacting with an electron to boost an electron to the band of conduction and create a hole. To put it another way, when a material absorbs a photon, an electron-hole pair is created. The kind of semiconductor makes a big difference in the photogeneration. The rate of photogeneration is directly proportional to the photon flux, which is the standard unit of measurement for incoming light. It may be written as Eq. 2.2 in its simplest form.

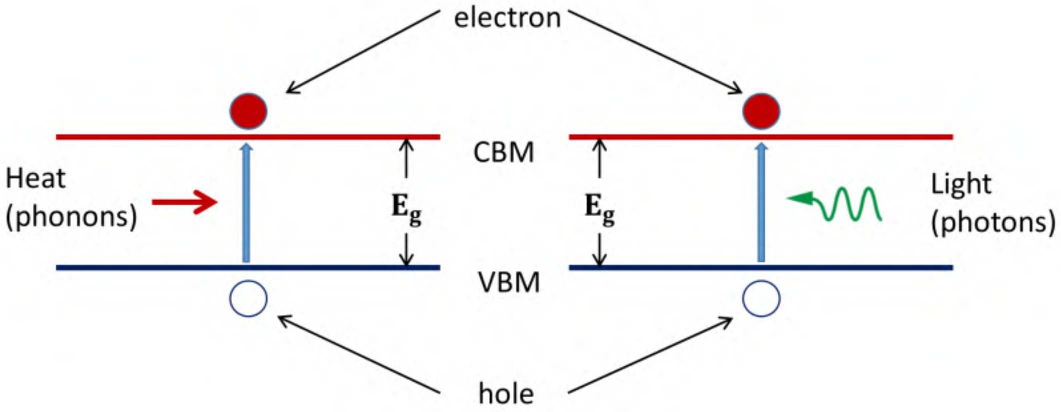

Figure 2.7: Thermal and photogeneration processes

$$G \propto \frac{\text{absorbed photons}}{\text{sec}} = \alpha.\phi \tag{2.2}$$

where, G= photogeneration rate, electrons/sec

α= absorption coefficient

ϕ= photon flux, photons/sec

If photo-generated electrons are not diffused into the depletion area, they are likely to return to the valence band or *recombine* with their holes. The photo-created holes and electrons would be swiftly swept in opposing directions by the electric field present inside the depletion area. This implies that the field will drive the holes and electrons (in that order) that are created and/or diffuse into the depletion zone deeper into the majority of the material. The junction's intrinsic field pulls apart electron-hole pairs as they approach the interface. The n-side is pushed with electrons, whereas the p-side is pushed with holes. There are several recombination processes, which are shown in the Figure 2.8. These recombination processes are responsible to limit the PCE. The processes are as follows:

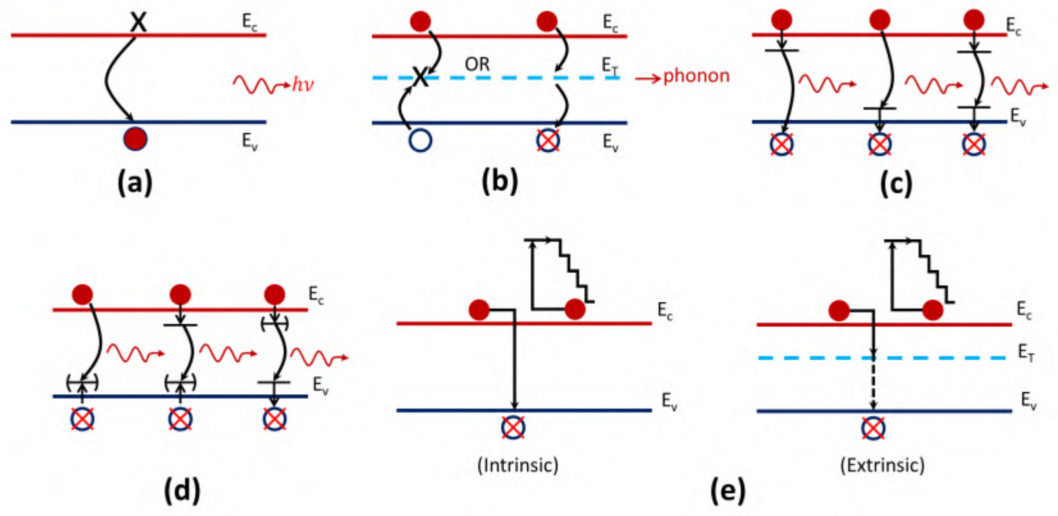

Figure 2.8: Mechanisms of recombination: (a) Recombination from band to band, (b) Recombination at the R-G center, (c) Recombination through shallow depths, (d) Excitons are involved in recombination, and (e) Recombination by Auger

- <u>Recombination from band to band:</u>

  The photon is released upon direct recombination of the electron and hole pair created during the absorption process. A re-entry of the electron into the valence band "fills" the vacancy.

- <u>Recombination at the R-G center:</u>

  If the bandgap contains energy levels (states). These points may serve as trap states or sites of recombination production. The phonons that cause the lattice to vibrate may cause electrons to leap into lower energy states, where the excess energy is dissipated as heat.

- <u>Recombination through shallow depths:</u>

  If there are energy levels in the bandgap near to the conduction or valence band, it is possible for electrons or holes to go to those levels, where they may undergo recombination and release photon energy. This phenomenon lies between "recombination from band to band" and "recombination at the R-G center".

- Excitons are involved in recombination:
  This recombination process is similar to "recombination from band to band" with the exception that in this case, an electron and a hole first form a bonded pair - exciton - with an energy just below the bandgap. Excitons operate like hydrogen atoms, with the hole playing the role of the nucleus and the electron being attached to the hole.
- Recombination by Auger:
  There's an extra electron involved in this process. In this case, the energy that is lost through electron-hole recombination is utilized to boost the other electron to a higher energy level, where it then promptly drops, releasing energy as heat in the process.

The photon-generated holes and electrons, however, would be swiftly swept in opposing directions by the electric field present inside the depletion area. This implies that the field will drive the holes and electrons (respectively) that are created and/or diffuse into the depletion zone deeper into the majority of the material.

Diffusion and drift of charges

The drift current, in its most basic form, is the current that occurs from the application of an externally provided voltage. As a result, the Ohm's law may be used to describe this current. Diffusion of charge carriers, on the other hand, is a process first described by Fick's law in which charge carriers travel from higher concentration regions to lower concentration regions, eventually initiating diffusion current. Electrons and holes are responsible for both drift and diffusion currents in a pn-junction semiconductor. Initially, current flow is primarily governed by diffusion; however, drift current eventually becomes a significant contributor to the process. The equations for the drift of the minority carrier and the diffusion current are as in Eqs. 2.3.

$$\begin{aligned} J_n &= q\mu_n n\varepsilon - qD_n\frac{dn}{dx} \\ J_p &= q\mu_p p\varepsilon - qD_p\frac{dp}{dx} \end{aligned} \tag{2.3}$$

where, D_n and D_p are diffusion constants for minority carriers of electrons and holes.

The overall bias voltage dependency of junction current can be calculated as shown in Eq. 2.4.

$$J = q\left(\frac{D_n}{L_n}\frac{{n_i}^2}{N_A} + \frac{D_p}{L_p}\frac{{n_i}^2}{N_D}\right)\left(e^{\frac{qV_a}{k_BT}} - 1\right) = J_s\left(e^{\frac{qV_a}{k_BT}} - 1\right) \tag{2.4}$$

where, $L_{n,p} = \sqrt{D_{n,p}\tau_{n,p}}$ are lengths of minority carrier diffusion.

Distinction of charges

The pn-junction diode aids in the process of charge segregation. In a p-type semiconductor, the Fermi level is close to the VBM, whereas in an n-type semiconductor, it is close to the CBM. Carriers move under the force of diffusion when materials come into contact, and after the chemical potentials on both sides have equalized, the level of Fermi must be in the same place on both the p and n sides. As a result, there is band bending. These behaviors are shown in Figure 2.9. P-type materials absorb holes when electrons diffuse into them and recombine with them. Hole diffusion and recombination with electrons occurs in n-type materials. This means that ultimately all free carrier will be depleted in the vicinity of the junction, leaving only stripped ions, which would produce an electric field, $\varepsilon = \frac{1}{q}\frac{dE_c}{dx}$ across the junction. The presence of a non-zero charge density close to the junction creates an electric field. Figure 2.10 shows the energy difference across the junction, denoted by the symbol dE_c.

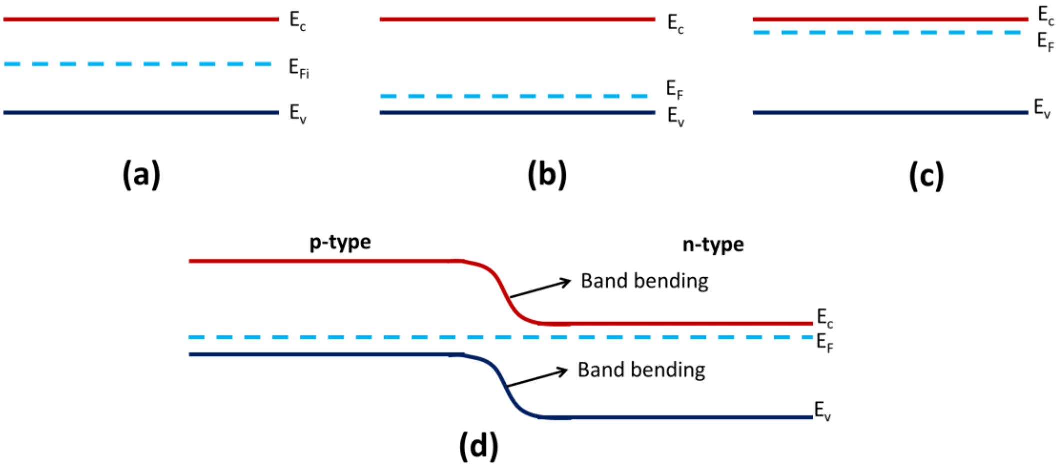

Figure 2.9: The position of E_F in E_g: (a) Intrinsic semiconductor, (b) p-type semiconductor , (c) n-type semiconductor, and (d) pn-juction at thermal equilibrium

When the drift flux is equal to the diffusive flux of the carriers, a steady-state equilibrium of carriers is attained at the junction. Built-in voltage, or V_{bi}, is another way of expressing the loss of neutrality of charges at the junction. The junction's V_{bi} and electric field may be determined from the ionized donor density (also called space charge, $\rho(x)$).

$$\varepsilon = \int \frac{\rho(x)}{\varepsilon_r \varepsilon_0} dx \tag{2.5}$$

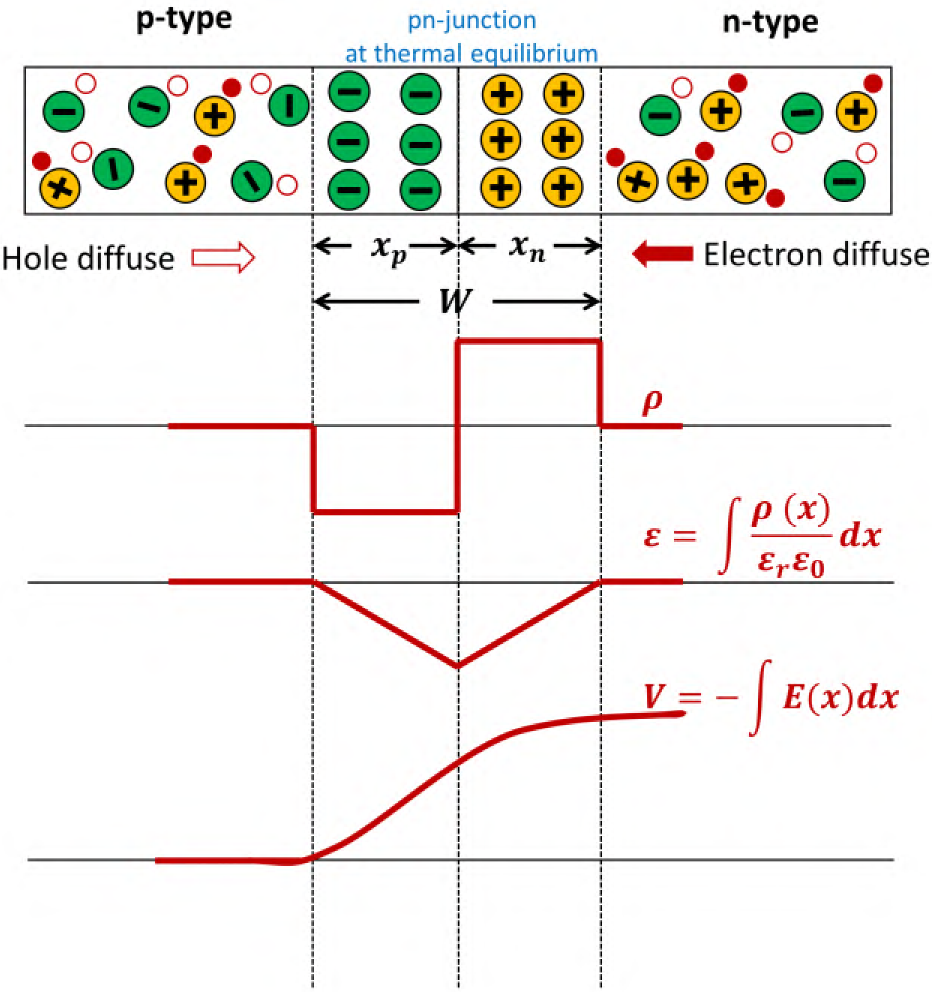

Figure 2.10: The pn-juction at thermal equilibrium. (Only the dopant atoms with their corresponding ionization states are depicted in the schematic)

where, ε_r, ε_0 are the relative and absolute dielectric permittivities respectively.

$$V_{bi} = -\int \varepsilon(x)dx \tag{2.6}$$

The *depletion region* refers to the area close to the junction where free charge carriers have been exhausted. The depletion area has a width of,

$$W = \sqrt{\frac{2\varepsilon_r \varepsilon_0 V_{bi}}{q} \frac{(N_A + N_D)}{N_A N_D}} \tag{2.7}$$

The size of the positively charged zone remaining after the n-type region has been depleted:

$$x_n = \sqrt{\frac{2\varepsilon_r \varepsilon_0 V_{bi}}{q} \frac{N_A}{N_D(N_A + N_D)}} \tag{2.8}$$

The size of the negatively charged zone left behind after the p-type region has been depleted:

$$x_p = \sqrt{\frac{2\varepsilon_r \varepsilon_0 V_{bi}}{q} \frac{N_D}{N_A(N_A + N_D)}} \tag{2.9}$$

Consequently,

$$N_A x_p = N_D x_n \tag{2.10}$$

Therefore, the depletion zone of highly doped material will be more small and the depletion region of low doped material would be more broad at the junction. The difference between the Fermi levels of p- and n-type semiconductors before they were linked is the built-in voltage.

$$qV_{bi} = E_{Fn} - E_{Fp} E_{Fp} = E_{Fi} - k_B T \ln\left(\frac{N_A}{n_i}\right) E_{Fn} = E_{Fi} + k_B T \ln\left(\frac{N_D}{n_i}\right) \tag{2.11}$$

Once the doping concentrations are known, the inherent voltage may be calculated as:

$$V_{bi} = \frac{k_B T}{q} \ln\left(\frac{N_A N_D}{{n_i}^2}\right) \tag{2.12}$$

Minority carriers are defined as either electrons traveling from p-type to n-type or holes travelling from n-type to p-type. The foregoing equations demonstrate that the obstacle to minority carriers injection is qV_{bi}:

$$p_n = p_p e^{\frac{-qV_{bi}}{k_B T}} n_p = n_n e^{\frac{-qV_{bi}}{k_B T}} \tag{2.13}$$

Accumulating charges

Solar cell contacts extract carriers from device and prevent back-diffusion of carriers into device. Contacts are influenced heavily by surface states. Materials commonly used for contacts are metals and Transparent Conducting Oxides (TCO). Contacts are often made of metals or TCO. In contrast to metals, which are both opaque and electrically insulating, TCOs are transparent but conduct electricity. When separation of charges is not a concern, ohmic contacts, which exhibit a straight I-V curve, are utilized. On the otherhand, Schottky contacts show exponential

I-V curve and used when charge separation is desired. Figure 2.11 shows the evaluation of metals for contacts in Schottky model.

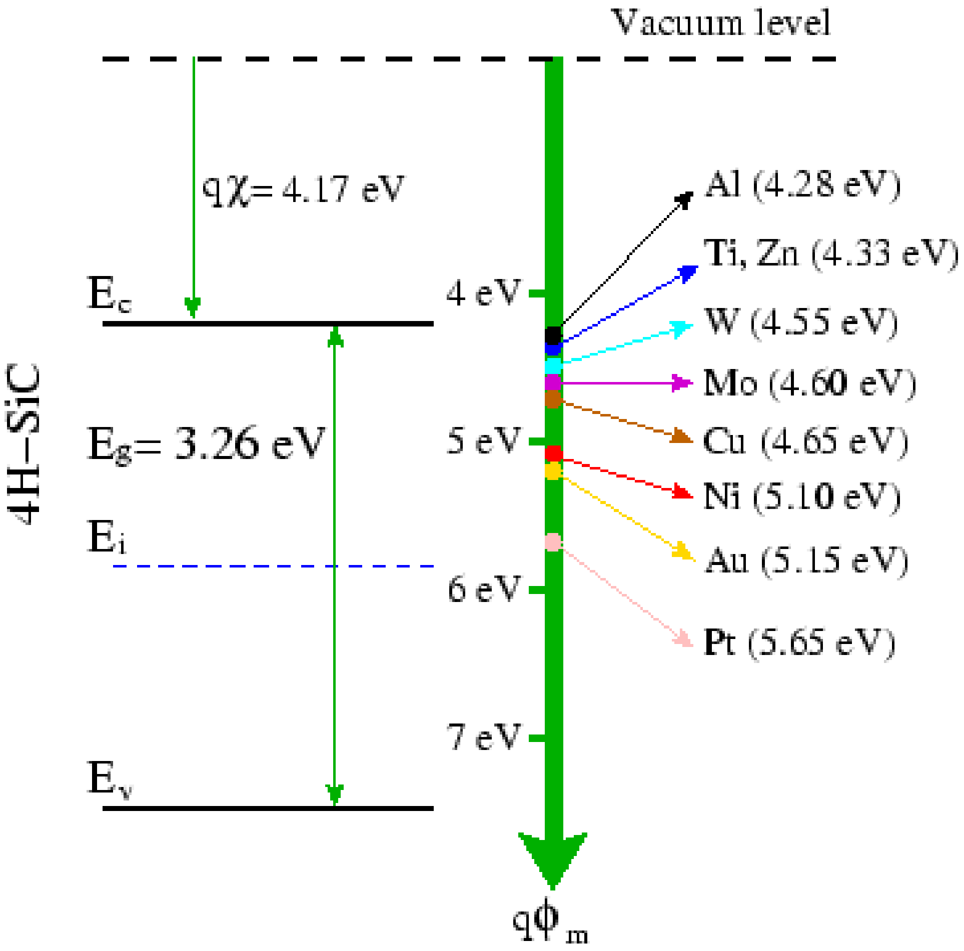

Figure 2.11: The evaluation of metals for contacts in Schottky model [**Source**: http://www.iue.tuwien.ac.at/phd/ayalew/node56.html]

The formation of a homo-type junction is not a ubiquitous phenomenon, indicating that the coexistence of n-type and p-type impurities within a semiconductor material such as silicon is not always feasible. Finding the optimal contact material may not always be a practical endeavor. Consequently, it is imperative to initiate communication with an alternative semiconducting material, commonly referred to as a heterojunction.

The three broad categories of heterojunctions are shown in Figure 2.12. The material has a large band of energy gaps on the left and a small one on the right. The detected band alignment may be traced back to the arrangement of vacuum levels. Type-I has poor photovoltaic efficiency. An electron-hole pair may be stimulated in a type-II device, making it similar to a PN junction. Because of the field, the electron may go through, but the hole is repelled. From a photovoltaic point of view, the Type-II connection is strongly suggested.

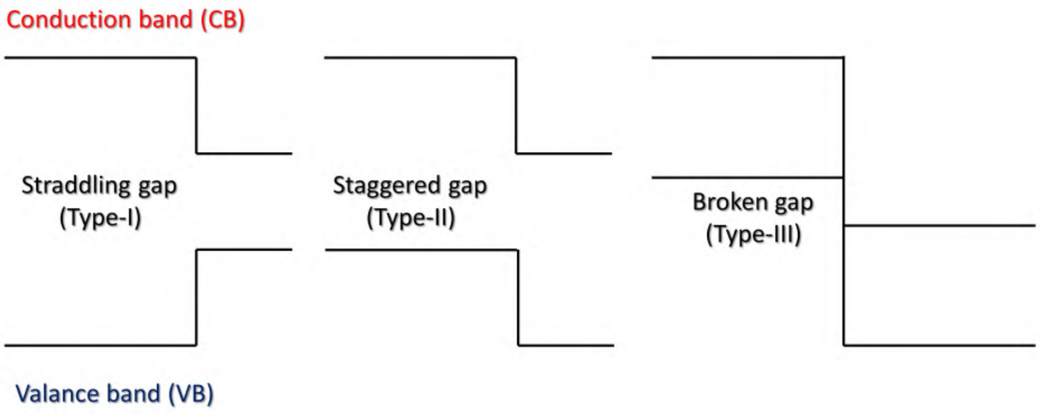

Figure 2.12: Three types of heterojunctions

Charge segregation may be maintained at a Type-III junction. The electron is predicted to go across the cell, from left to right. In the field of photovoltaics, Type-III is typically considered undesirable.

2.1.5. Characteristics of solar cells

One input parameter, the incoming photon flux, ϕ and three output parameters, open-circuit voltage, V_{oc} short-circuit current density, J_{sc} and fill factor, FF describe solar Power Conversion Efficiency (PCE) as summarized in Figure 2.13. Figure 2.14 provides much more specific information on how to extract those factors in order to compute a solar cell's efficiency.

2.1.5.1. Open-circuit voltage

The greatest voltage produced by a solar cell, known as the open-circuit voltage, V_{oc}, exists when no current flows through the cell. The quantity of forward bias on the solar cell is proportional to the open-circuit voltage because of the offset of the photovoltaic cells junctions resulting from light-generated current.

2.1.5.2. Short-circuit current density

Once the solar cell is short-circuited, its current is the short-circuit current. Short-circuit current density, J_{sc} in mA/cm^2 is usually stated instead of short-circuit current to eliminate solar cell area dependency.

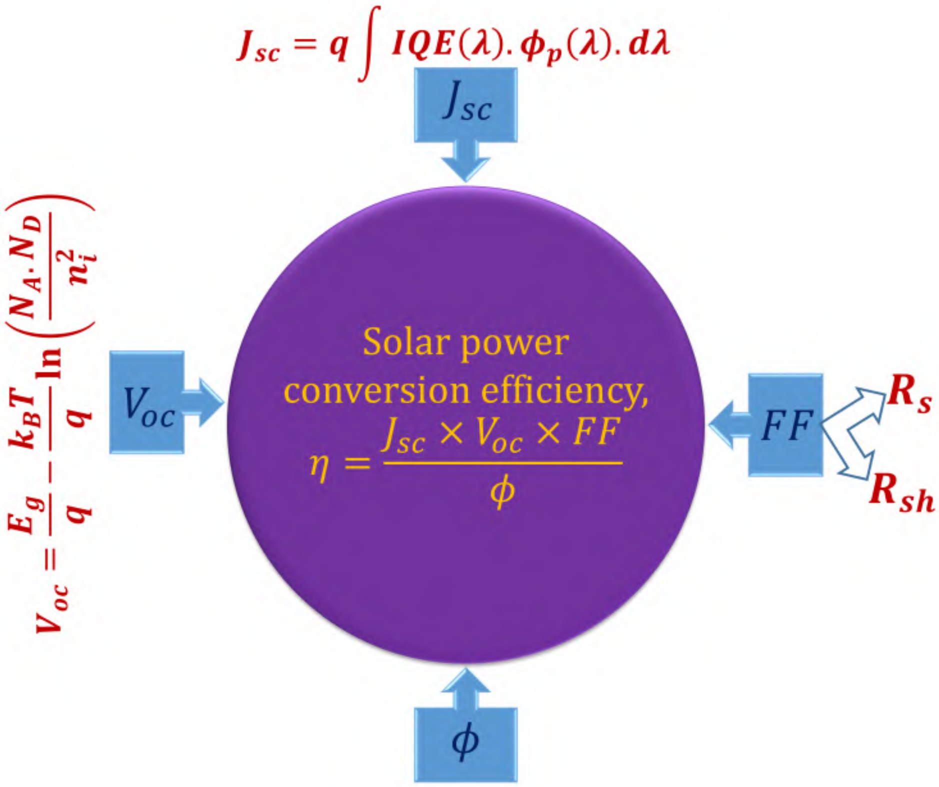

Figure 2.13: Factors involved in PCE

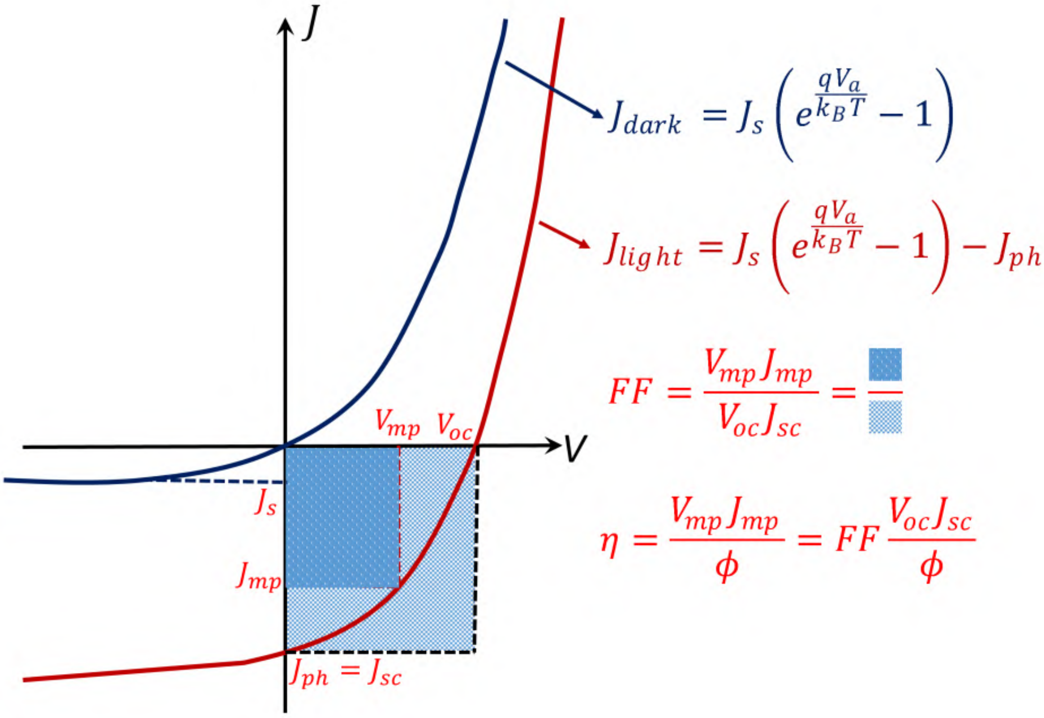

Figure 2.14: Simple I-V plot showing its essential parameters which are the functions of PCE

2.1.5.3. *Fill factor*

Simply by connecting a load to a solar cell, energy may be drawn from it. It has been discovered that the load resistance plays a significant role in determining how much energy can be harvested from a photovoltaic cell. Only a rectangle between V_{oc} and J_{sc}, with $P_{max} = J_{mp}V_{mp}$ in its inside, may be used to retrieve useful information from a J-V plot. Consequently, the optimal load has a resistance of R_{mp}.

$$R_{mp} = \frac{V_{mp}}{I_{mp}} \tag{2.14}$$

Solar cell power maximization is beneficial, and it can be achieved by minimizing the gap between the V_{oc} and the J_{sc}, and approaching the rectangle formed by the V_{mp} and I_{mp}. The defining parameter is commonly referred to as the fill factor (FF).

$$FF = \frac{V_{mp}J_{mp}}{V_{oc}J_{sc}} \tag{2.15}$$

2.1.5.4. *Power conversion efficiency*

The efficiency of power conversion is defined as the ratio of the amount of energy retrieved to the amount of energy in the incident light.

2.1.5.5. *Solar cell equivalent circuit: simple case*

The current-voltage characteristics (sometimes referred to as "dark characteristics") of a pn-junction diode is given by Eq. 2.16.

$$J_{dark} = J_s\left(e^{\frac{qV_a}{k_BT}} - 1\right) \tag{2.16}$$

Diode’s illumination current-voltage characteristic is given by Eq. 2.17.

$$J_{light} = J_{dark} - J_{ph} = J_s\left(e^{\frac{qV_a}{k_BT}} - 1\right) - J_{ph} \tag{2.17}$$

In the open-circuit regime, when we solve for voltage, we get V_{oc}:

$$V_{oc} = \frac{k_BT}{q}\ln\left(\frac{J_{sc}}{J_s} + 1\right) \tag{2.18}$$

A simple solar cell equivalent circuit is shown below (Figure 2.15).

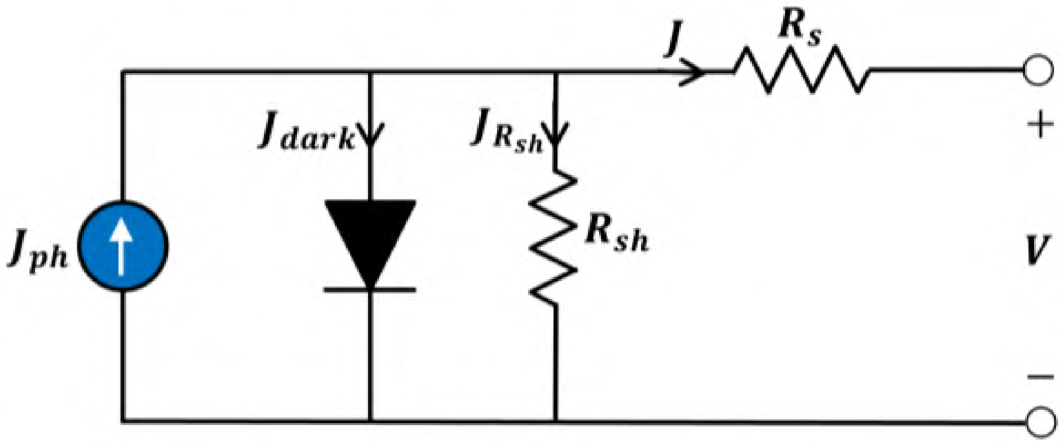

Figure 2.15: An elementary equivalent circuit for solar cells

2.1.5.6. Resistances in series and shunt and their effects

A perfect p-n junction solar cell's J-V curve has been taken into account. With the increase of series resistance the slope around the open circuit voltage point starts to become less steep. The larger the series resistance, the less steep the slope will be. Furthermore, the maximum power point is affected as well by increasing the series resistance as depicted in Figure 2.16a.

The larger the series resistance, the smaller the maximum power point will be. This also implies that the larger the series resistance will be, the smaller the FF. So, the series resistance has to be as small as possible for high FF's. There is no change in open-circuit voltage as a result of the series resistance. Since there is no current flow at the open-circuit voltage, there is no voltage drop across the series resistance.

If the shunt resistance is decreased (Figure 2.16b), the slope at the short-circuit current density point starts to become more positive. The maximum power point and FF is affected as well. The smaller the shunt resistance, the smaller the FF will be. Current density divided by voltage equals one over the resistance, hence the slope is the current divided by the voltage.

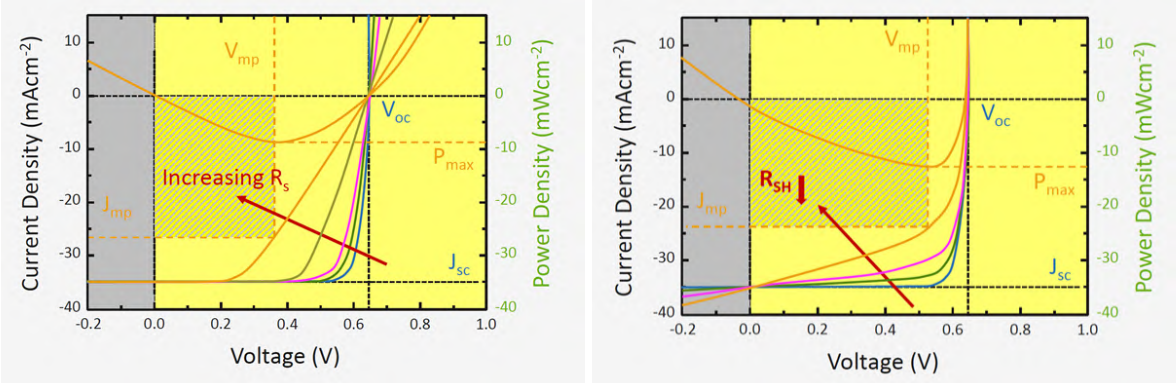

(a) **(b)**

Figure 2.16: Solar cell performance with series/shunt resistances

2.2. PV technologies

The two most common techniques for harnessing solar energy are photovoltaic (PV) and concentrated solar power (CSP). Solar photovoltaics (PV) are now the most common method of producing energy from the sun. Solar cells utilize sunlight as fuel, allowing them to produce electricity at ambient temperature with no moving parts. It is common practice to refer to solar cell technologies by the name of the primary light-absorbing material they use. One kind of PV cell is made on a silicon wafer, while another is made from a thin sheet. Wafer-based cells are manufactured on semi-conducting wafers and can be treated without a substrate, in contrast to modules, which often include a transparent coating for rigidity and protection. Thin-film cells are made by layering a semiconducting material, such as glass or flexible plastic, over an insulating substrate. In the field of thin-film PV, there are two distinct groups: commercial enterprises and academic laboratories. Three generations [24] are used in the current standard for classification, which are:

- Monocrystalline and polycrystalline c-Si and GaAs wafer-based cells make up first-generation technology.
- Thin-film cells, such as a-Si:H, CdTe, and CIGS, make up the second generation of technology.
- Third-generation technologies use a wide range of "exotic" ideas and methods, such as spectral-splitting devices (like MJ cells), hot-carrier collection, carrier multiplication, and thermo-photovoltaics, as well as new thin-film devices like dye-sensitized, organic, and Quantum Dot (QD) solar cells.

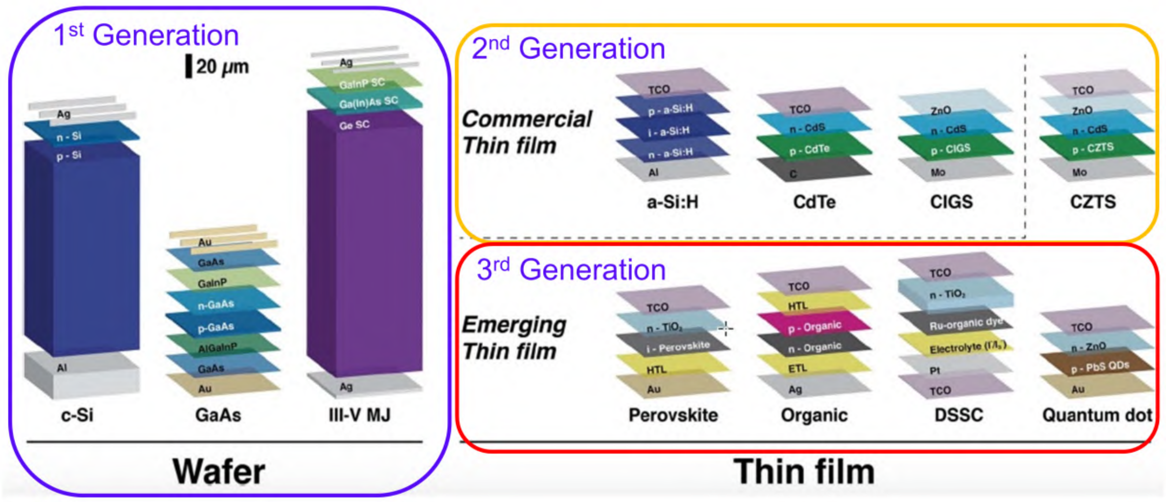

Figure 2.17: Solar PV technologies by generation

2.2.1. Summary of the reported efficiencies

Table 2.1 summarizes the measured efficiencies with cell characteristics and a complete best research cell efficiency chart provided by NREL [25] is shown in Figure 2.18.

Table 2.1: Summary of the reported efficiencies with cell parameters

Technology/Material		**V_{oc} (volt)**	**Fill factor**	**Efficiency,η**	**Area (cm^2)**	**Affiliation**
Crystalline Si Cells	Multicrystalline	0.713	82.5%	**24.4%**	267.5	Jinko Solar
	Si heterostructures (HIT)	0.738	84.9%	**26.7%**	79.0	Kaneka
Thin-Film Technologies	CIGS	0.734	80.4%	**23.4%**	1.043	Solar Frontier
	CdTe	0.887	78.5%	**22.1%**	0.4798	First Solar
Emerging PV	Perovskite	1.179	84.6%	**25.7%**	0.096	UNIST
	CZTSSe	0.529	72.9%	**13.0%**	0.107	NJUPT

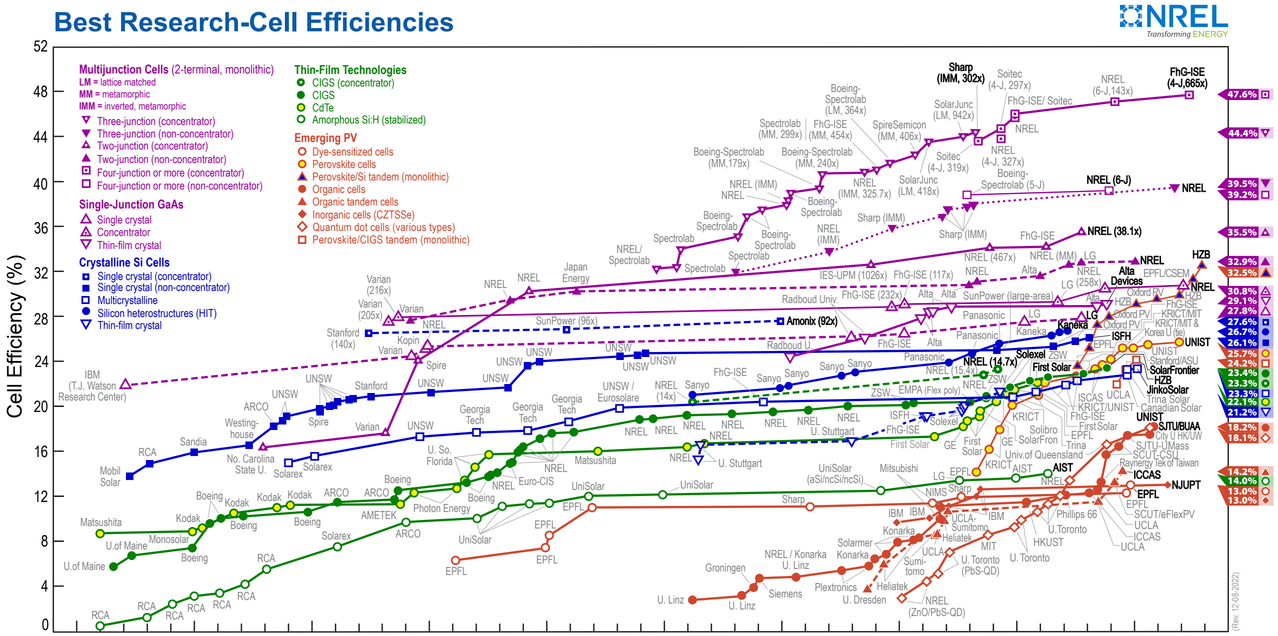

Figure 2.18: Best Research-Cell Efficiency Chart
[**Source:** NREL]

2.3. CZTS

The kesterite $Cu_2ZnSnS_{4-x}Se_x$ family comprises various compound semiconductors, including pure sulfide Cu_2ZnSnS_4 (CZTS), pure selenide $Cu_2ZnSnSe_4$ (CZTSe), and selenosulfide $Cu_2ZnSn(S,Se)_4$ (CZTSSe). The abbreviation CZTS is frequently utilized to refer to the family of compounds denoted as $Cu_2ZnSnS_{4-x}Se_x$. The CZTS compound is produced through the process of cation mutations, specifically cross-substitutions, in $CuInS_2$. Two In atoms are swapped out for single Zn and a single Sn atom, as has been shown in prior research [26, 27].

The absorption coefficient of CZTSSe is reported to be more than 10^4 cm^{-1}, its band gap is adjustable between 1.0 eV and 1.5 eV, it exhibits inherent p-type conductivity, and its three-dimensional carrier transport is symmetrical [28]. The great interest in CZTS's exceptional photovoltaic capabilities has led to rapid expansion in the field in recent decades. Most efficient are Cu_2ZnSnS_4 (11% PCE), $Cu_2ZnSnSe_4$ (12.5% PCE), and $Cu_2ZnSn(S,Se)_4$ (13% PCE) [25, 29, 30]. These materials are highly appreciated for their use in inorganic thin-film photovoltaic (PV) systems since they are both RoHS-compliant and CRM-free.

2.3.1. CZTS timeline

1966: Nitsche, Sargent, and Wild created the CZTS single crystal, while attempting to build a sequence of $A^{I}_{2}B^{II}C^{IV}X_4$-type quaternary chalcogenides through iodine vapor transfer [31].

1988: Ito and Nakazawa showed for the first time that CZTS has a photovoltaic effect on a hetero junction diode made of a clear conducting layer of cadmium-tin oxide and a thin film of CZTS on a stainless steel base. The open-circuit voltage was found to be 165 mV [32] under AM1.5 light. After heating the cell up in the atmosphere, the open-circuit voltage went up to 250 mV and the short-circuit current went down to 0.1 mA/cm^2.

1996: Using a device configuration of ZnO:Al/CdS/CZTS/Mo/SLG , Katagiri et al. [1] presented the first CZTS solar cell with PCE of 0.66% at PVSEC-9 in 1996. Thin films of CZTS were fabricated by sulfurizing their E-B-evaporated predecessors in the vapor phase.

1997: In 1997, Friedlmeier et al. [33] presented a CZTS solar cell that used thermal evaporation to achieve a PCE of 2.3% and an open-circuit voltage of 570 mV.

1999: In 1999, the Katagiri team improved PCE to 2.63% [34]. Between then and 2007 [35], they toiled away at optimizing the CZTS thin film, eventually raising efficiency to 5.74%.

2008: Katagiri et al. [36] report an improvement in performance to 6.7%. Significant progress has been achieved in the last decade thanks to the efforts of several research institutions and solar cell companies including Toyota, IBM, NREL, Solar Frontier, EMPA, HZB, ZSW, UNSW, and others. The incorporation of Se has been more popular, which has helped to hasten the progress of PCE [37, 38]. Vacuum depositing, solution approach, electrochemical deposition, and other techniques have been used to produce CZTS thin films, as mentioned in [19, 38, 39].

2011: In 2011, IBM's Thomas J. Watson Research Institute achieved a benchmark efficiency of 10% for CZTS solar cells [37], marking a major advancement in the field and pointing to commercial potential for the CZTS-based category of thin film PV elements. Several new world records for efficiency were set as a result of this breakthrough [19, 39], further establishing IBM as the leader in the study of CZTS PV technology.

2014: Due to a lack of progress since 2014, when IBM last revised its efficacy breakthrough [39], the highest PCE for CZTS solar cells has remained at 12.6%. Due to increased knowledge of the CZTS substance and the device's loss mechanism, many groups have recently developed CZTS PCE with efficiencies close to the benchmark 12.6% [30, 40–44].

2021: In 2021, Xin et al. [25] from Nanjing University of Posts and Telecommunications (NJUPT) achieved a new world record for CZTS efficiency with an efficiency of 13%. This efficiency was recently upgraded and is now included in the NREL Best Research-Cell Efficiency Chart. A lot of work has gone into this one modest advancement, and its proponents are hoping it will attract the interest and support of the CZTS R&D community. The study, reported in the International Journal of Energy & Environmental Science, determined that the deficiency of V_{oc} kesterite solar cells was caused by the two grain development methods of Sn^{2+} and Sn^{4+} precursors in Dimethyl sulfoxide (DMSO) solution.

2.3.2. Chemical and physical characteristics of a CZTS film

It is crucial for the development of this area of technology to analyze and comprehend the properties of CZTS thin films. Extensive research was conducted during the rapid development phase, resulting in a comprehensive understanding of the physical and chemical properties of CZTS.

2.3.2.1. Structure of CZTS crystals

The CZTS compound is a result of cation mutations of the $CuInS_2$ (CIS) compound. CZTS and CIS have a common ancestor in binary II-VI semiconductors that have either a cubic zinc-blende (or hexagonal wurtzite) structure, as seen in Figure 2.19 [27]. The quaternary compound CZTS has two well-known crystal structures: kesterite (with space group ***I*4**) and stannite-type (with space group ***I*42m**). Both of these formations are an offshoot of chalcopyrite as depicted in Figure 2.20 [45].

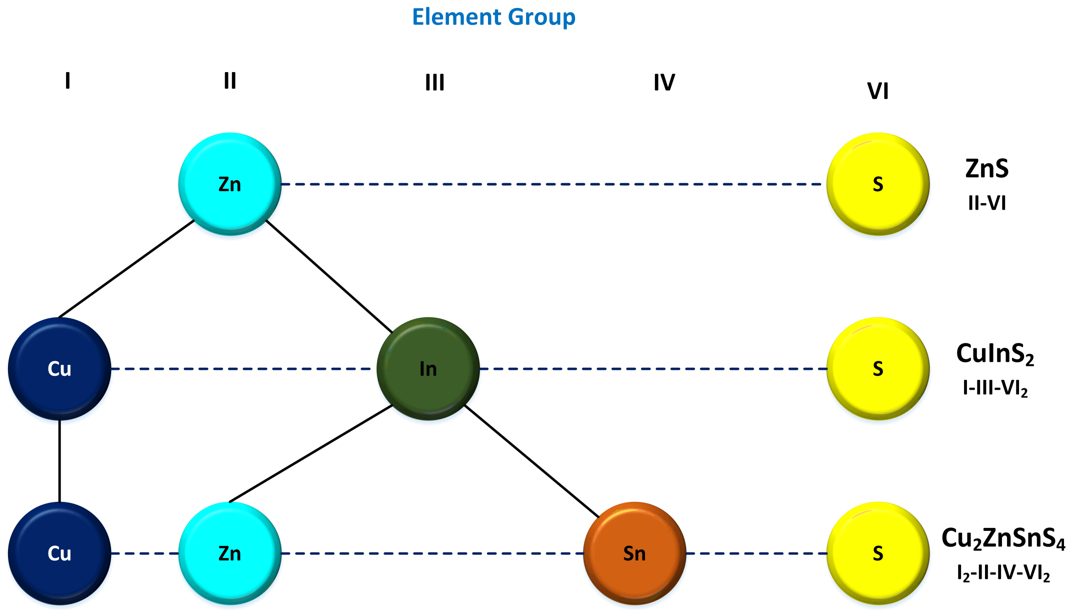

Figure 2.19: Hypothetical beginning of CZTS structure

The structure of kesterite is the most commonly described in this thesis. The primary distinguishing factor between the two structures pertains to the disposition of cations. In either configuration, the S anions form a cubic close-packed lattice, wherein cations occupy fifty percent of the tetrahedral interstices. In both arrangements, the Sn atoms are situated in identical, predetermined positions.The positions of Cu and Zn atoms are opposite to each other, as reported in [46].

The arrangement of cation layers in the CuZn, CuSn, CuZn, and CuZnSn compounds occurred in an alternating manner at specific positions along the z-axis, namely z = 0, ¼, ½, and ¾, respectively. Meanwhile, the ZnSn and Cu_2 layers were arranged in an alternating pattern within the stannite structure. The identification of kesterite and stannite through conventional X-ray diffraction and Raman spectroscopy methods poses a challenge due to their structural similarities, as noted in previous studies [47]. According to sources cited as Susan Schorr [46, 48], solely contemporary techniques like neutron powder diffraction analysis have the capability to differentiate them.

It has been observed that the kesterite structure exhibits greater thermodynamic stability as compared to the stannite structure. The aforementioned experimental results have been taken into account [6, 46]. Multiple theoretical studies [26, 49, 50] have provided evidence that the kesterite is the most stable CZTS structure.

The nomenclature of CZTS is attributed to its crystallization pattern resembling that of kesterite structure. The disparity in energy between kesterite and stannite-type structures

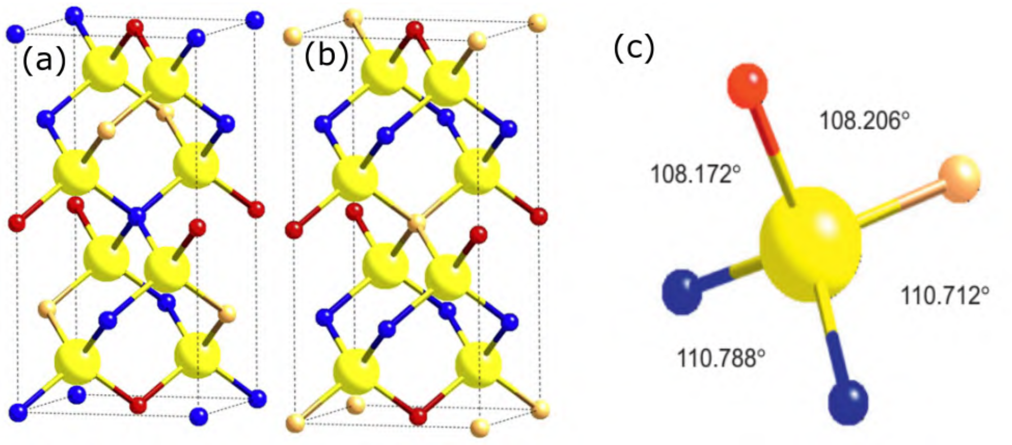

Figure 2.20: Two common CZTS crystal structure and associated bond angles in tetrahedral coordination. (blue-Cu^+, red-Sn^{4+}, orange-Zn^{2+}, and yellow-S)

is relatively insignificant, as reported in various studies [26, 49–52]. The aforementioned statement suggests that the kesterite structure is expected to manifest under conditions of growth equilibrium. However, it is possible for both phases to coexist, particularly when the growth methodology and parameters are altered. Consequently, the production of materials featuring a blend of phases should be relatively straightforward. The findings of Schorr [53] suggest that a greater degree of randomness in the cation site distribution for copper and zinc may account for the presence of disordered structure.

2.3.2.2. *Electronic band structure*

The tetrahedral bonds present in kesterite CZTS exhibit a similar shape to those found in conventional semiconductors belonging to groups I-V, III-V, and II-VI. The octet rule proposed by Lewis is clearly followed as each anionic atom, namely S or Se, exhibits a stable electron configuration with eight electrons in its valence shell. According to Gong [49], the anion's four bonds combine to create a tightly packed valence shell. The Cu-based quaternary compound is quite different from the binary semiconductors that fall into groups I-V, III-V, and II-VI. CZTS bonds are formed using Cu-d-anion-p conjugated anti-bonding states. It is noteworthy that the element Copper (Cu) present in Copper Zinc Tin Sulfide (CZTS) possesses a solitary valence s-type electron.

Diverse first-principle studies [49, 51, 52, 54] have shown how the electronic bands of CZTS are put together. All of the CZTS and kesterite materials are direct-gap semiconductors. Different ways of doing the math led to slightly different results. Overall, the results show that E_g is about 1.5 eV in CZTS and about 1.0 eV in CZTSe [55–57], and the amount of Se present causes a linear increase or decrease in E_g.

Density Function Theory (DFT) study has also been used to figure out the Density of States (DOS) of kesterite Cu_2ZnSnS_4 and $Cu_2ZnSnSe_4$. Cu_2ZnSnS_4 and $Cu_2ZnSnSe_4$ have similar DOS because their tetrahedral bond geometries are the same. Cu_2ZnSnS_4 has a larger energy gap than $Cu_2ZnSnSe_4$, hence its conduction bands have a higher DOS by around 0.5 eV. The VBM in Cu-based chalcogenides is like CIS and CZTS comes from anion p forms and Cu d forms hybridizing. Cu has more d orbital energy than Zn, Ga, In, and Sn [52, 58]. CZTS has a lower-energy S valence p level than Se. This explains sulfides' lesser VBM than selenides. Anion p-Cu d overlaps (p-d hybridized), which is more prevalent in the shorter Cu-S bond and lowers the anti-bonding VBM level of the sulfide compared to the selenide, reduces this disparity. Thus, Cu_2ZnSnS_4 and $Cu_2ZnSnSe_4$ have valence band gaps below 0.2 eV. Sn-s and anion p-like forms limit what is known as the DOS of the CZTS CBM as Sn has a lower s energy orbital than other cations [52, 58].

CZTS also localizes energy by separating the smallest conduction band from the greater energy bands. Sn-site alloyed with additional group-IV elements like Ge will affect CZTS's CBM due to its confined conduction band. Cation alloying may improve optical efficacy by changing band gap energy.

2.3.2.3. *Phase transitions and variations in composition*

CZTS is a quaternary semiconductor with up to two chalcogens and three metals. This permits several composition modifications and subsequent phase synthesis. Nevertheless, in order to achieve high efficiency, TFSC made of CZTS require a kesterite absorber composed of a single phase. The presence of secondary phases in the absorber material can potentially diminish the performance of the solar cell.

For the creation of high-quality, single-phase CZTS absorbers, the regulation of compositional and chemical potential are crucial. Because stable area is substantially narrower, zinc concentration is especially critical. Furthermore, it is well established experimentally and theoretically that CZTS absorbers with solar cells with a high efficiency need compositions that are rich in zinc and low in copper [29, 55, 56, 59–63]. This makes controlling the creation of secondary phases more challenging. Most often reported additional phases in the Cu, Zn, Sn, and S/Se system shown in Table 2.2 [64].

Both the secondary phases' position in the film and their physical properties dictate how much of an effect they have on solar cell efficiency. For instance, $Cu_2S(Se)$ phases in the ultimate film, which have high conductance and interact with the front and back surfaces, may function as a shunting channel. However, $Cu_2S(Se)$ is a powerful fluxing agent that facilitates sideways

Table 2.2: The probable secondary phases with their band gap values in the CZTS system

Phases	E_g, eV	Source	Phases	E_g, eV	Source
Cu_2ZnSnS_4	1.5	[11]	$Cu_2ZnSnSe_4$	1.0	[11]
Cu_2SnS_3	1.0	[65]	Cu_2SnSe_3	0.8	[66]
ZnS	3.7	[67]	ZnSe	2.7	[67]
SnS_2	2.5	[68]	$SnSe_2$	1.0-1.6	[69]
SnS	1.0 indirect, 1.3 direct	[70, 71]	SnSe	1.3	[72]
Cu_2S	1.2	[73]	Cu_2Se	1.2	[74]

grain expansions during film formation [55]. In general, the open-circuit voltage of a solar cell will be limited by the secondary phase if its band gap is less than that of the CZTS absorber. Secondary phases with larger band gaps than CZTS are generally less damaging, although they may nevertheless hinder transport [75] or at the very least increase series resistance [76] if they are present in large enough quantities.

Taking into consideration the Zn-rich and Cu-poor circumstances, ZnS(Se) emerges as the most probable secondary phase. ZnS(Se) has a large energy gap, hence it is unlikely to do any damage at low concentrations. It has even been observed that ZnS with crystalline structures similar to CZTS may passivate grain boundaries or heterojunction interfaces by lowering recombination velocities and decreasing strain [63, 77]. Since tin compounds are very volatile and would evaporate under normal preparation conditions, they are extremely uncommon. Table 2.2 shows that the ternary $Cu_2SnS(Se)_3$ is a low-band-gap secondary phase in the Cu_2ZnSnS_4 and $Cu_2ZnSnSe_4$ systems, which may be one reason why the composition range of Zn-rich and Cu-poor solar cells is optimal. However, under normal preparation conditions, such detrimental secondary phases might occur because of the CZTS film's non-homogeneous composition [78]. As a consequence, research into methods for controlling the presence and distribution of secondary phases inside the CZTS absorber is essential.

2.3.2.4. Lattice defects

Lattice defects directly affect electron–hole pair generation, separation, and recombination, making them vital to solar cell performance. The increasing number of component elements, comparable cation size, and slight chemical mismatch of Cu^+ and Zn^{2+} make kesterite CZTS system lattice defects (vacancies, interstitials, antisites) problematic. The p-type conductivity mechanisms, the effect of Zn-rich and Cu-poor conditions on growth, and the constraints on device performance resulting from lattice defects are all crucial areas of study for kesterite

CZTS solar cells.

Formation energy determines lattice defect concentration. Figure 2.21 [4, 6] plots the predicted production energies of several defects as functions of the Fermi energy (0 implies VBM, 1.5 or 1.0 eV means CBM). In both Cu_2ZnSnS_4 and $Cu_2ZnSnSe_4$, the Cu_{Zn} is the defect with lowest energy, unlike their host structure in CIGS ($CuInSe_2$ or $CuGaSe_2$), where the dominating defect is the Cu vacancy, V_{Cu} [4, 6, 79]. Most acceptor defects have lower formation energies than defects created by donars, elucidating the literature-observed p-type conductivity [49, 67, 80–84].

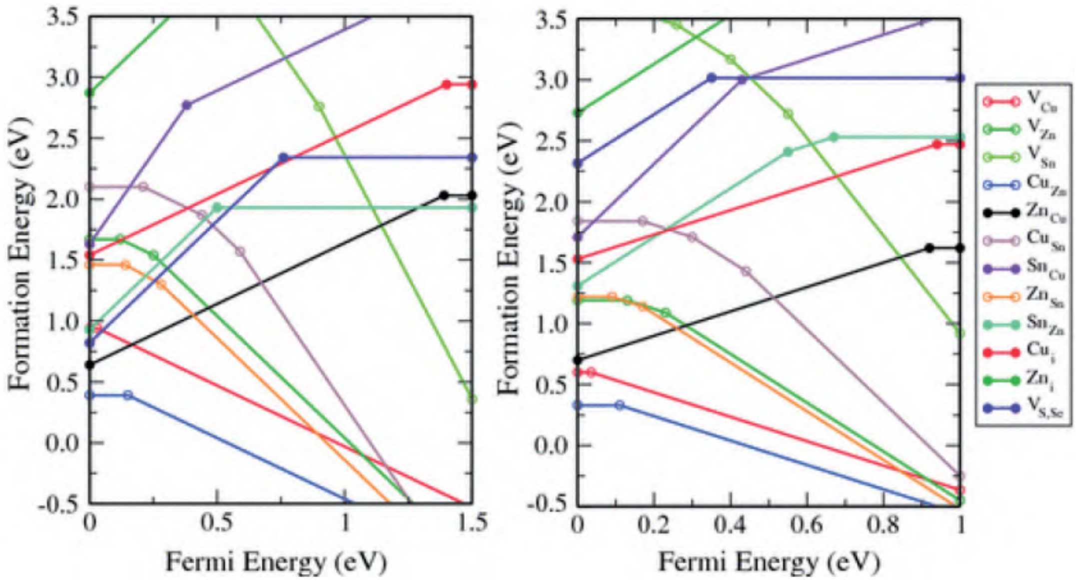

Figure 2.21: Fermi energy-dependent defect formation energy

Ionization (transition) levels affect whether lattice defects may create free carriers and increase electrical conductivity. Figure 2.22 shows the inherent defect band gap ionization levels of Cu_2ZnSnS_4 and $Cu_2ZnSnSe_4$. First, the main defect Cu_{Zn} has an acceptor level deeper than V_{Cu} ($Cu_2ZnSnSe_4$ is 0.11 eV above VBM, whereas Cu_2ZnSnS_4 is 0.15 eV above VBM). CZTS's deep dominant antisite defect limits open-circuit voltage and device performance. Because it reduces formation energy and increases shallow V_{Cu} population, Zn-rich and Cu-poor situations are usually favorable to solar cell efficiency. Cu_{Sn}, Zn_{Sn}, V_{Zn}, and V_{Sn} acceptor defects have higher formation energy and contribute less to p-type. For very profound transition levels, they might serve as nexuses for recombination like (4-/ 3-) and (3-/ 2-) in band-gap Figure 2.22 [4].

Due of its many low-energy intrinsic defects, CZTS can create self-compensated defect clusters in addition to point defects. Defect complexes like $[2V_{Cu}{}^{-} + In_{Cu}{}^{-}]$ self-passivate

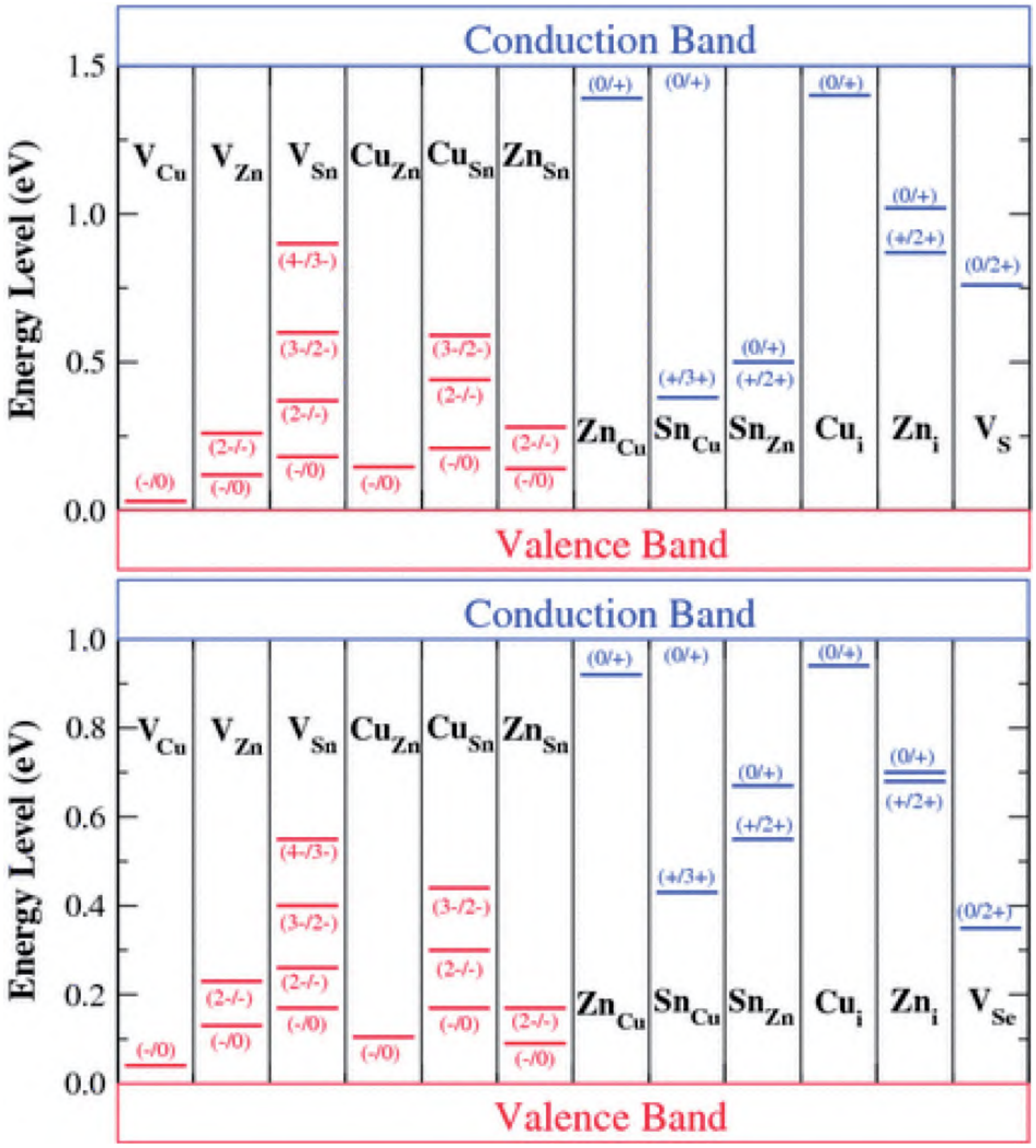

Figure 2.22: Band gap intrinsic defect ionization levels of CZTS (top) and CZTSe (bottom)

inherent defects in ternary CIS, making defect compensation electrically benign. Thus, it is intriguing to explore if quaternary kesterites behave similarly. Cu_{Zn} and Zn_{Cu} are the acceptor with low-energy and donor type defects, respectively, hence antisite pair $[Cu_{Zn}^{-} + Zn_{Cu}^{+}]$ requires few energy to form. Luckily, its effect on optical and electrical characteristics is modest. Sn_{Zn}, Sn_{Cu}, Cu_{Sn}, and Zn_i deep-level defect clusters are harmful. Clusters containing Sn_{Zn} produce a significant downshift in the conduction band edge, which might limit solar cell performance if photo-generated electrons are trapped in the deep induced states. $[2Cu_{Zn} + Sn_{Zn}]$ clusters may be present in considerable numbers in mono-phase CZTS, which degrade solar cell efficiency. Since its creation energy is dependent on the chemical potential of zinc, Zn-rich and

Cu-poor conditions may hinder $[2Cu_{Zn} + Sn_{Zn}]$ cluster formation. From a defect standpoint, Zn-rich and Cu-poor solar cells are more efficient.

2.3.3. Device structure

Due to their comparable optical and electrical characteristics, the conventional device design (Figure 2.23) of kesterite CZTS, takes after its ancestor chalcopyrite $CuInSe_2$ solar cells.

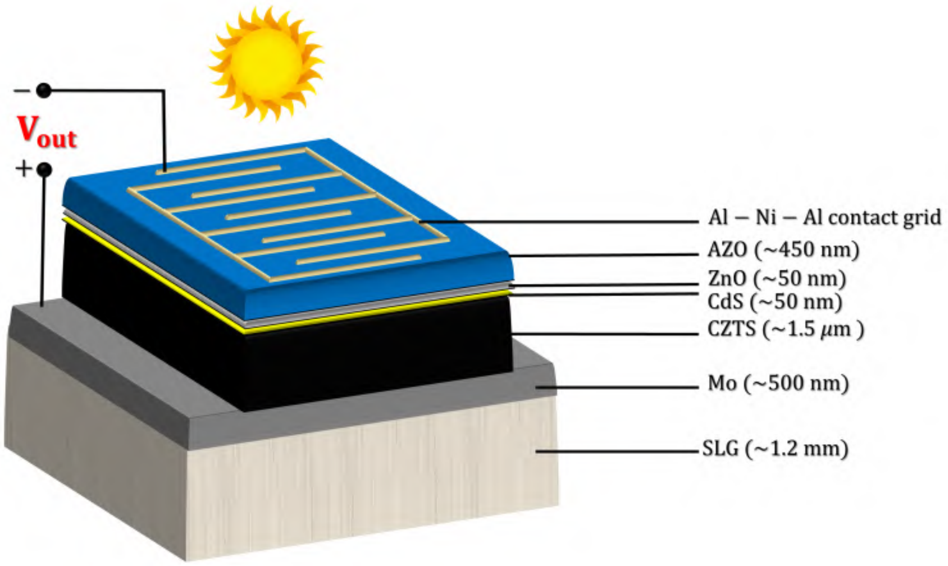

Figure 2.23: Substrate structured Cu_2ZnSnS_4 thin film solar cell (not drawn in scale)

This architecture is referred to as *substrate structure*. Sputtering is commonly used to deposit Mo back contact electrode on SLG or other substrates. A p-type CZTS and an n-type CdS buffer layer are deposited afterwards. ZnSnO, Zn(O, S), ZnCdS, and other buffer materials have all been studied to see whether they can correct the band alignment issues seen at the p-n junction, particularly in pure sulfide Cu_2ZnSnS_4. Following that, a high-resistive intrinsic ZnO (i-ZnO) layer is deposited. Al-doped Zinc Oxide (AZO) or Indium Tin Oxide (ITO) window layer is deposited then. For enhanced current collection, Ni/Al metal contacts are placed on the window layer. Sometimes MgF_2 is used as an anti-reflecting coating.

During the development of this technology, many deposition processes for manufacturing high-quality CZTS layers were examined. These deposition processes are roughly characterized as vacuum and non-vacuum. Because of the fine process control, vacuum-based technologies are typically thought to be straightforward to scale up to commercial size. This category includes all physical vapor deposition methods such as thermal evaporation, E-beam evaporation [1], sputtering [29, 62, 63, 85], and pulsed laser deposition [86]. Non-vacuum-based processes are always thought to be low-cost, high-throughput approaches that can be used in roll-to-roll manufacturing. Electrochemical deposition [87], nanoparticle-based synthesis [88], sol-gel spin coating [42], Chemical Bath Deposition (CBD) [89], Successive Ionic Layer Adsorption and Reaction (SILAR) [90], screen printing [91], and other techniques are often used.

2.3.4. Loss mechanisms

2.3.4.1. Open-circuit voltage, V_{oc}

Most people agree that the efficiency difference between the best-performing device and the theoretical limit [2] in kesterite CZTS solar cells is mostly attributable to the V_{oc} loss [92]. The recombination mechanism of a device is what determines how much V_{oc} loss it experiences. The absorber's quasi-neutral zone, where band-to-band recombination might occur due to flaws, or the space charge area, may be the site of principal recombination. There may also be recombination sites at the edges of heterojunctions.

As a result, it is thought that absorber difficulties like excessive point defects, defect clusters (i.e., cation disordering), and composition disparity lead to recombination. Cu and Zn substitution with low energy results in a massive population of Cu_{Zn} and Zn_{Cu}, and related defect complexes. As a result, substantial electrostatic potential fluctuation and band tailing may be seen [10]. Furthermore, micro-inhomogeneities in composition, nonuniform strain, and secondary phase formation cause band gap oscillations, which are equally harmful to V_{oc}. Furthermore, acceptor-like Cu_{Zn} will cause Fermi level pinning to a squat energy level [93], lowering band bending and diminishing the electric field in the absorber.

Reducing recombination in the layer of absorber has been a major focus of research and development in recent years. Since the introduction of larger size cations could result in superior cationic ordering, hence reducing the defects generated by the Cu and Zn substitution, cation substitutions have been the subject of substantial research. Previous research [16, 94–96] has indicated that Ag, Cd, and Ge are widely employed as replacements for Cu, Zn, and Sn, respectively, since they all belong to the identical cation group. Many outstanding efficiencies and mechanisms of the defect forming with cation substitution have been shown, showing that significant progress has been made both experimentally and theoretically in this area. Deliberately controlling the synthesis circumstances is another way to deal with the cationic disorder and associated band tailing and activate the shallower defect. For instance, the CZTS lattice ordering and band gap may be improved by post-annealing the absorber within the crucial range of temperatures of 200-250°C for a tolerable time range of 1 to 4 hours [97]. It has been demonstrated that manipulating the fabrication process of the precursors—including the metal stack order and the valence states of the Sn source—can result in a less defective absorber and a corresponding high-efficiency devices [98, 99]. The generation of a favorable local chemical environment [30] by sulfurization or selenization conditions adjustment may aid in preventing the formation of detrimental intrinsic defects and defect clusters.

Interface recombination route is mostly caused by unpassivated charge imperfections at the heterojunction and/or poor band alignment between the CZTS absorber and traditional CdS buffer layer. In CZTS, the band alignment issue is more acute due to the higher conduction band position. It has been demonstrated that using ZnCdS [62], Zn(O,S) [100], or ZnSnO [101] as a large band gap buffer layer material may help alleviate band alignment issues. Charge defects at the interface may be reduced by alloying Ag with intrinsic or weak n-type $(Cu,Ag)_2ZnSn(S,Se)_4$ [94, 102] or by introducing an extremely thin layer with a better lattice fit with CZTS [29, 63]. Passivation of interface defects by dielectric layers has been investigated with the goal of reducing interface recombination [85, 103].

2.3.4.2. *Short-circuit current density, J_{sc}*

In CZTS, J_{sc} is a primary factor preventing efficiency gains on par with those attributable to V_{oc} loss. There are two main causes for the decrease in J_{sc}.

The first is photons that are either absorbed or reflected by non-electronegative layer above the CZTS (such buffer or window layers). When the diffusion length or depletion width is small, carrier collection efficiency is also poor. First, the amount of incoming light reaching CZTS may be improved by antireflection coating and by tweaking the optical geometries of the layers above CZTS. The suggested method has been shown to be effective via the use of a substantial band gap buffer layer [85, 101] and the reduction of the thickness and irregularities of the top layers [92]. CZTS typically has a short wavelength response in its EQE curve [60], which may be due to the material's low carrier lifetime. A high level of defects in the absorber layer or a significant recombination losses at the back contact or front surface might both contribute to the short lifespan. Therefore, methods for avoiding the formation of harmful faults like V_{oc} loss, J_{sc} improvement is beneficial. Band gap grading, developed by CZTS, modifies the proportion of $[S]/[S + Se]$ on the front and rear surfaces to improve EQE [104].

2.3.4.3. *Fill factor (FF)*

The nonohmic back contact might be produced via the Schottky barrier or by the creation of a secondary phase [105]. Because of the decrease in concentration, the effect is magnified in CZTS with a wide band gap. Furthermore, secondary phases with a smaller band gap in CZTS may act as a shunting route, reducing the FF and making the device less appealing. This restricts the FF's potential. Research and control of chemical reactions at the back interface have been proposed as a means to modify the interface's microstructure and boost the device's performance [106]. To enhance the quality of the back interface, a barrier layer was placed at the CZTS/Mo interface [107]. Both of these problems were addressed by doing this.

2.4. RF magnetron sputtered CZTS thin films: Effect of deposition temperatures

Till date, efficient CZTS based TFSC consists of mainly two stage process to synthesize CZTS absorber. Traditionally, in the first stage, precursors with proper composition control (preferably off-stoichiometric cu-poor zn-rich condition) are deposited. The next stage is the high temperature (at ~ 580°C) crystallization phase along with elemental sulfur or hydrozen-sulphide gas (H_2S) flow under N_2 gas flux. Due to volatile nature of Sn element, sometimes additional Sn is incorporated with elemental sulfur during this high temperature sulfurization process. RF magnetron sputtering is one of the popular methods to deposit this CZTS absorber layer followed by high temperature sulfurization.

CBD is often used for the production of a thin n-type layer with a p-type absorber to generate a heterojunction [5]. Layers of intrinsic zinc oxide and zinc oxide with metal dopants form a transparent "window" layer, mostly deposited by RF magnetron sputtering. Antireflection coating (optional) and collection grids are also deposited using RF magnetron sputtering as well.

Due to deposition process variability and interdependence, little is known about how absorber, buffer, and window layers affect CZTS-TFSC production. RF magnetron sputtering could assist to deposit all layers.The main idea is to fabricate CZTS-TFSC in-situ by RF magnetron sputtering process, bypassing high temperature annealing stage. It is hypothesized to use substrate heating during deposition.

2.5. Ge-alloyed CZTS thin films employing RF magnetron co-sputtering

Advances in Cu_2ZnSnS_4 (CZTS) thin film research have been a topic of tremendous interest since its commencement in 1988 [1]. Depending on the S/Se ratio, three compounds are possible: CZTS, CZTSe, and CZTS (Se), having band gaps of 1.5, 1.0, and 1.0~1.5 eV, respectively. CZT(S,Se) has a reported maximum power conversion efficiency of 13.0% [25].

CZTS thin film solar cells can't even keep up with CIGS(Se) and CdTe despite research and improvements [108]. The open-circuit voltage, V_{oc} deficit (greater than 0.7V) in CZTS-based thin films is thought to be the primary cause of low power conversion efficiency [29, 109, 110]. Multiple oxidation states of Sn cause deep recombination centers in CZTS and CZTSe PV cells and, thus, it contributes to V_{oc} [109]. Recently, Ge is a potential option that has been suggested for replacing the Sn-site in CZTS or CZT(S,Se) kesterite in order to improve optoelectronic properties such as open-circuit voltage [5]. Ge is more likely to have +4 oxidation states than Sn, which can avoid potentially harmful +2 oxidation states [111] . This helps create band alignment with the n-type heterojunction partner, commonly the CdS buffer layer. All these can reduce non-radiative recombination, improving minority charge carrier lifetime and reducing the V_{oc} deficit [109, 112].

Substituting Sn for Ge in CZTS(Se) solar cells has improved performance in a few studies [109, 113, 114]. For solar cell purposes, Dhruba et al. looked into engineering the band gap of Ge-alloyed CZTS and CZTSe films [115]. Using spectroscopic ellipsometry, E. Garcia-Llamas et al.[116] examined the optical, electrical, and vibrational properties of CZTGS single crystals with wide range of composition ratio in the ultra-violet and near infra-red region. The bandgap range of these CZTGS alloys has been reported to be 1.5 to 2.25 eV [115–118]. This feature is helpful for creating band gap grading in monojunction and multijunction devices [119, 120]. Li et al. produced CZTGS nanocrystals with various Ge source materials and investigated the fluctuation of optical band-gap depending on the Ge/Sn proportion [121]. However, in all of the above studies, the CZTGS thin films were fabricated using non-vacuum or non-sputtering techniques. J. Chen et al. claimed to be the first to report on the physical synthesis of CZTGS utilizing magnetron sputtering [122]. Nevertheless, the elemental components of thin films were arranged layer-wise. They examined how Ge layer order affects CZTGS thin films' properties.

To date, there has been no documentation of the utilization of RF magnetron co-sputtering in the production of pure sulfide CZTS thin films that have been alloyed with germanium. The utilization of co-sputtering techniques in the production of CZTGS thin films presents a number of notable benefits, including expedited fabrication processes, concurrent crystal growth, and streamlined optimization of sulfurization temperatures. The present investigation delineates the utilization of RF magnetron co-sputtering method for making thin films out of Ge-alloyed CZTS. The impact of Ge-alloying on microstructural, morphological, and optoelectronic characteristics was explicated and substantiated.

2.6. Superstrate structured CZTS thin film solar cell: A co-doping approach

While CZTS thin film solar cell has been successfully fabricated, it is still outclassed by other in the thin film market, such as CIGS(Se) and CdTe [108]. Passivating crystal defects inside the CZTS absorber is necessary for optimizing the optical band gap and morphological characteristics in order to design an effective solar cell [4]. The manufacturing method, dopants at the film level, and interface layers drastically change the functional link between the structure, morphology, and optoelectronic characteristics of CZTS when they are applied to devices [104].

The fabrication processes can play crucial and essential functions in producing highly competent properties in thin films [123]. The production of CZTS and its derivative can be separated into two types: vacuum and non-vacuum. Vacuum-based processes include sputtering, thermal evaporation, and atomic layer deposition (ALD) [124]. Sol-gel spin coating, doctor blading, sequential ionic layer adsorption and reaction (SILAR), spray pyrolysis, the hot injection method, and chemical bath deposition (CBD) are non-vacuum manufacturing methods that primarily depend on chemical synthesis [125–127].

Sol-gel offers several benefits over other processes, including greater homogeneity, adjustable stoichiometry, high purity, the capacity to make phase-solid powders at a comparatively lower temperature, and the versatility to produce thick monoliths, thin films, or nanoparticles [128–131]. In addition to these possible advantages, the fabrication of thin films may be accomplished in a rapid, simple, and efficient manner. The control of chemical risks during synthesis and disposal is a serious challenge, despite the fact that non-vacuum techniques are easier and less expensive. For example, there is a study on a CZT(S,Se)-based device with a 12.6% PCE that uses hydrazine, an extremely toxic chemical [39]. So, adopting a chemical synthesis pathway and utilizing eco-friendly, non-hazardous chemicals may be a wise choice during the manufacturing process.

Copper, zinc, and tin can be mixed with thiourea in a dimethyl sulfoxide (DMSO) solvent to produce a solution of precursor molecular complexes [38]. A DMSO molecular ink technique has several benefits over conventional solution-phase manufacturing methods. It is significantly safer than hydrazine ink and quicker to produce than nanocrystal ink. It also provides a novel method for adding dopants and accurately controlling the absorber's stoichiometry [132]. According to [38], adding the precursors progressively into the solvent DMSO, a precursor solution that has been redox-balanced results in a higher-quality and more efficient CZTS. The processing of DMSO solutions, on the other hand, has several difficulties, such as a rough surface and a lack of crystallinity, which hinder the device's performance [133].

Thin film solar cells may be broken down into two groups: those with the absorber layer on the substrate, and those with the absorber layer on a separate layer, called a superstrate. Substrate-structured solar cells have a substrate as a supporting material for the absorber layer, and the electrical contacts are usually placed on the backside of the substrate. On the other hand, superstratrate-structured solar cells have a transparent conducting oxide (TCO) layer as a supporting material for the absorber layer, and the electrical contacts are placed first of the TCO layer. The main advantage of *substrate-structured solar cells* is their high stability and robustness, as the substrate provides mechanical support and protection for the absorber layer. Furthermore, substrate-structured solar cells are more suitable for high-temperature processing techniques, which may be implemented to enhance crystallinity of the absorber layer and enhance the conversion efficiency [134]. However, the substrate material may absorb some of the light, which reduces the light penetration and decreases the efficiency of the solar cell. *Superstratrate-structured solar cells* have a higher light absorption efficiency because the TCO layer is transparent and allows more light to reach the absorber. In addition, superstratrate-structured cells may be fabricated on flexible substrates, which enables making solar cells that are both lightweight and bendable for a range of applications [135]. However, superstratrate-structured solar cells are more vulnerable to mechanical stress and environmental degradation because the absorber layer is not protected by a substrate [136]. In brief, substrate-structured solar cells have higher stability and are more suitable for high-temperature processing, while superstratrate-structured solar cells have higher light absorption efficiency and can be fabricated on flexible substrates. The choice of substrate or superstratrate structure depends on the specific application and processing requirements. Superstrate structured thin film solar cells using CdS as the window layer have been investigated due to its ease of manufacture.

Off-stoichiometric CZTS beat stoichiometric in photovoltaic performance [3]. Multinary compounds Cu_2ZnSnS_4, CZTSe, and CZTSSe may be generated in non-stoichiometric compositions, especially in the Cu-poor-Zn-rich domain. An off-stoichiometric composition can create harmful binary and ternary secondary phases. After Katagiri's 2005 combinatorial study, many have been done [34]. Nevertheless, changing the absorber stoichiometry alone does not improve device performance to that of other thin film solar cells [5]. Consequently, extrinsic atoms are being added to the kesterite-type crystal matrix to enhance absorbers [5].

There is a possibility that the CZTS compound will produce a wide range of intrinsic defects and defect clusters [4], such as vacancies, antisites, and interstrials. When it comes to ternary compounds like CIS, the most common p-type acceptor is the Cu vacancy, often known as V_{Cu}. Because CZTS is fabricated as an off-stoichiometric Cu-poor Zn-rich material, it was previously assumed that V_{Cu} is the major p-type acceptor defect in CZTS like CIGS [137]. This belief was based on the fact that CZTS is synthesized in this manner. Nonetheless, the difference in valence between Cu(I) and Zn(II) in the copper-zinc antisite (Cu_{Zn}) in the quaternary complex CZTS is just one, which means that it is the same as V_{Cu} [6]. As a result, Cu_{Zn} may be a good candidate for the position of dominant p-type acceptor. Cu_{Zn} has a lower formation energy than V_{Cu}, which allows it to form more easily, and it is also more abundant than V_{Cu}. Because of this antisite, carrier recombination centers may arise that are predominated by defect states. This brings about a reduction in the open-circuit voltage, which in turn brings about an efficiency reduction in the device's power conversion (V_{oc}).

Thus, one method for lowering the V_{oc} deficiency is to make CZTS thin films with an extrinsically doped other element that partially replaces Zn atoms. This may be done during the manufacturing process. The density of defects associated with the Cu_{Zn} antisite will decrease as a result of this. It is also possible to swap the Cu-cationic site with the goal of decreasing defects caused by the Cu_{Zn} antisite; nevertheless, the focus of this thesis was on the Zn-cationic site. When it comes to choosing the dopant atoms for Zn-cationic sites, the size of the atom as well as its position in the periodic table are both very essential factors. When heavier atoms from same subset of the periodic table are substituted in compound semiconductors, the band gaps in these materials have been shown to decrease [16]. During the dopant selection process, the atoms that have the same isoelectronic configuration as zinc, the same number of valence electrons as zinc, and a bigger atomic size than zinc are taken into consideration [17].

Doping the CZTS crystal with Cd (which is in the same ionic group II-B as Zn) is thought to result in a partial Zn-cation substitution. Cd and Zn atoms are isoelectronic because they share the same number and kind of electrons. According to J.C. Slater [18], the atomic radii of zinc (Zn) and cadmium (Cd) are 1.35Å and 1.54Å respectively. The Cd atom is thus larger than the Zn atom. Furthermore, the ionic radii of Zn^{2+} and Cd^{2+} ions in tetrahedral coordination are 0.6Å and 0.78Å, respectively. It has been shown that the V_{oc} deficiency may be mitigated by doping with Cd for partial Zn cation replacement, which in turn mitigates defects caused by Cu_{Zn}.

$Cu_2Zn_xCd_{1-x}SnS_4$ (CZCTS) compound is presented by several researchers in the running for a role in popularizing existing kesterite solar cell technology. CZCTS with Cd incorporation has been studied less for its physical qualities than CZTSSe complex. In particular, there is a paucity of knowledge on the impact of the Cd element on the electrical characteristics of CZCTS. As a result, research into the mechanics underlying Cd alloying processes has been conducted to aid in the advancement of CZCTS solar cell efficiency.

For the most part, chemical methods have been used in the published work on CZCTS processing. Sol-gel preparation of the CZCTS compound has been reported in just a small number of these experiments [16, 138–140], spin-coating [141–143], electrospinning [144].

Initial research made by Maeda et al. [145], where authors presented a DFT study on the effects of adding Cd in CZTS and CZTSe materials, which are promising candidates for thin-film solar cells. The authors used DFT computations to investigate the electronic and optical characteristics of the Cd-doped materials. Their findings suggest that Cd atoms preferentially substitute Zn or Cu atoms in CZTS and CZTSe structures, depending on the Cd concentration and the formation energy of different doping configurations. The authors found that Cd doping can effectively reduce the bandgap of CZTS and CZTSe, leading to enhanced light absorption and thus higher solar cell efficiency. Furthermore, the authors investigated the impact of Cd doping upon the defect characteristics of CZTS and CZTSe. They discovered that Cd doping can introduce shallow acceptor states near the valence band edge, ruling to improved p-type conductivity. However, excessive Cd doping can also introduce deep defect states that may serve as hotspots for recombination, reducing the device's efficiency. Therefore, the optimal Cd doping concentration needs to be carefully controlled to balance the reduction of the bandgap and the introduction of defects. The authors also compared the Cd-doping effects in CZTS and CZTSe. They found that Cd doping is more effective in reducing the bandgap in CZTSe than in CZTS, which is attributed to the larger ionic radius of Cd compared to S. They also observed that Cd doping can enhance the p-type conductivity more effectively in CZTS than in CZTSe, which is attributed to the stronger Cd-S bonding and the smaller electron affinity of S compared to Se.The results suggest that Cd doping can effectively reduce the bandgap and improve the p-type conductivity, but the doping concentration needs to be carefully optimized to avoid the introduction of deep defect states. The study also highlights the differences in the Cd-doping effects between CZTS and CZTSe, which is important for designing efficient PV devices. From the theoritical studies, Cd-doping was found to be a propitious approach to escalate the electronic and optical characteristics of CZTS based thin film absorber, which can lead to increased efficiency. Of course, these improvements in carrier concentration, electrical conductivity, band gap, absorption coefficient, and efficiency varied depending on the specific material, doping concentration, and synthesis procedures as well.

Rondiya et al. [146] studied the impacts of replacing Cd^{2+} in Zn^{2+} locations on a lattice in CZTS nanocrystals by a liquid-based technique and observed smaller values for the optical band gap from 1.51eV to 1.1eV. In a different investigation, novel cadmium surface diffusion doping in CZTSSe [147] improved crystal quality, reduced charge density in depletion layers, inhibited the growth of surface secondary phases, and increased power conversion efficiency. The Cd/(Zn+Cd) proportion of 0.4, found to be excellent, reported in [16] with more than 11% competent Cd-doped CZTS thin film PV cell adopted in [95]. This optimal value was adopted as a reference during experiment and reported in this thesis.

Toxic Cd doping in non-toxic CZTS, might, however, cause additional issues that can exceed the advantages. Taking this into account, the aim behind this objective was to reduce the Cd content by introducing another dopant atom at the same Zn-cationic site in such a way to get same benefit as Cd-dopant alone. In order to fulfill this aim, the effects of dopants were studied individually first, then co-doping were done in a separate set of experiments. There are several reports on co-doping in different cationic sites of CZTS crystal matrix. Co-doping has not been reported to be used for partial cation substitution at the same cationic location. Therefore, it is proposed in this investigation to introduce Cd and Mg atoms together to replace Zn atoms.

As a possible second dopant, we selected Mg as a non-toxic counterpart of Cd, which is a group II-A element having 1.50Å atomic radius [18], 0.57Å ionic radius, and same valence electrons as Zn atoms. In a work, Y. Wang et al. [148] doped magnesium atoms into CZTS using a DMF-based solution technique, resulting in better electronic, microstructural, and power conversion efficiency. At 20% Mg doping, low-cost sol-gel spin coating was used to get the best electrical and morphological performances in CZTS films [149].

Many heterojunction solar cells' band alignment is determined by chemical interdiffusion across the heterointerface [150]. Cd and S can permeate into CdS in CZTSe/CdS solar cells [151]. Interdiffusion between CZTS and CdS may potentially help the situation by boosting the CBO to a positive spike. More Cd diffusion into CZTS means higher Cd_{Zn} substitution. This increases the CBO and decreases the hole population, which reduces interface recombination [152]. Thus interdiffusion may enhance an initially cliff-like CBO to a spikelike CBO within the ideal range for photovoltaics in CZTS solar cells. Interdiffusion increases lattice matching at the CZTS/CdS interface, which may lower interface defect density and recombination velocities as well. This may explain the success of solar cells based on the CZTS/$ZnCd_{1-x}S_x$ heterojunction [62], where Zn was alloyed with Cd to boost CBO. CZTS/CdS solar cells should promote Cd and Zn interdiffusion assuming no adverse consequences occur. Thus, co-doping in the CZTS absorber must be examined for its implications on heterojunction interface band alignments.

2.7. Band alignment study of CZTS/CdS and CZTS/ZnS heterojunction interface

Band offsets affect the electrical transport properties of heterojunction solar cell devices mostly by blocking charge carriers at the interface, which lowers the power conversion efiiciency [153]. This makes band discontinuity studies an important part of device design because the offsets between the valence band and conduction band determine how electricity moves at the interface. Understanding or controlling band edge discontinuities helps align the valence and conduction bands of both semiconductors for solar cell fabrication.

For heterojunction solar cells, the best CBO is between +0 eV and +0.4 eV and looks like a spike [152, 154]. If the spike is too big (> + 0.4 eV), because to the high heterointerface electron barrier the electrons stops from moving from the CZTS to the top contact. For a heterointerface VBO to be irrelevant, the buffer's band gap must be much wider than the absorber.

The *standard* buffer used in CZTS solar cells, which were decided to make from chalcopyrite CIGS, is CdS. The huge V_{oc} deficit (0.6 eV), which is likely caused by a less-than-ideal alignment of the conduction bands between the p-CZTS absorber and the n-buffer layer, has harmed CZTS solar cells' efficiency.

The "spike-like" alignment of CdS/CIGS conduction bands with a desirable band offset of 0.2–0.3 eV makes CIGS solar cells efficient, especially at high V_{oc} [152]. CBO problem with CdS/CZTS cells not yet solved.

Theoretically, the CBO of CdS/CZTS is negative (like a cliff), but experimental values are different because of both experimental and measurement artifacts. Also, Fermi level pinning, the function of interface orientation, surface changes, interdiffusion, and band gap shifts may all contribute to these unfavorable band offsets. The role of the band gap changes because of cation disorder, problems with band tailing, phase mix, quantum confinement, and epitaxial growth. "Cliff-like" or "negative" CBO means that at the heterointerface, the maximum of the CdS conduction band is below that of the CZTS band. CZTS and its usual heterojunction partner CdS have been compared to a cliff in terms of its CBO, because a large number of known CBO measurements [57, 151, 155–169] and calculations [4, 12, 154, 164, 170–173] support it.

From first principles computations, Chen et al. [170] anticipated that at the CdS/CZTS the CBO would be like a little cliff and the VBO would be 1.01 eV. Richard et al. report a CBO of +0.41 eV [57], but others have found CBO values of 0.06, 0.33, and 0.34 eV [155, 158, 159] that are more like cliffs. Bär et al. [155] found that the valence band (VB) and the conduction band (CB) coincide at the CdS/CZTS interface, as determined by Ultraviolet Photoelectron Spectroscopy (UPS) and Inverse Photoelectron Spectroscopy (IPES). For an absorber that hasn't been etched, they found a 0.33 eV CBO that appears as cliff and a 1.19 eV VBO. Haight et al. [57] used a femtosecond laser and a pump-probe UPS to measure a 0.54 eV VBO, which led to a CBO that looked like a spike.

Still, if the CBO of CdS/CZTS is like a cliff, other buffer materials must be found to align the bands of CZTS best (small spike-like CBO of 0.1–0.2 eV). Finding a different buffer layer is important not only for the problem of material toxicity, but also for matching the lattice of the absorber/buffer interface. A slight lattice mismatch exists between CdS and some absorber materials, such as $Cu(In,Ga)Se_2$ (1.5%) and $Cu_2ZnSnSe_4$ (2.4%), but the mismatch is much bigger with CZTS (7%) [174]. So, it's likely that there will be a lot of intrinsic states at the CZTS/CdS interface. ZnS is one of the materials that has been chosen as Cd-free buffer layer in CZTS (pure sulfide). In the zinc blende crystal structure, the lattice of ZnS is almost the same as that of CZTS. CZTS lattice constant : 5.43Å; lattice constant of ZnS: 5.42Å [175]; therefore, a lattice misfit of less than 0.18% only! This makes it possible to make a good epitaxial interface, which could solve the problem of interface recombination.

The authors [176] stress the importance of X-Ray Photoelectron Spectroscopy (XPS) with adjustable synchrotron radiation and/or fixed photon energy as a direct tool for measuring valence band discontinuities in hetero-junctions. So, XPS measurements are used to look at how offsets at energy bands change at the different interfaces.

2.8. Fabrication and characterization of ZnO:Ga (GZO) thin film by RF magnetron sputtering

Thin film solar cells need a clear conducting electrode to allow sunlight to reach the light-absorbing layer. For transparent electrode layers, metal oxide layers with high conductivity and transmittance have been studied. TCOs with low optical resistivity and high optical transmittance for a solar cell's light-absorbing layer, inexpensive material prices, and good processing temperature stability are desired.

In addition to its use in solar cell technology, TCOs have attracted a great deal of interest for utilities such as transparent transistor film [177], LEDs [178], heat mirrors [179], and electronic equipment [177] that requires excellent electrical conductivity.

Indium Tin Oxide (ITO) has been the prototypical TCO material [180], because of the excellent transmittance and squat resistance, the RF magnetron sputtering process is a reliable method for producing ITO thin films with desirable electro-optical properties across a wide surface area [181]. However, because to the increasing demand for ITO brought on by the booming flat panel display market, the price of indium is on the rise [182]. Also, alternatives to indium as a TCO material are essential in light of the European Union's adoption of the RoHS [183] and CRM [184].

ZnO is a feasible substitute for ITO in thin-film transparent electrode operations because of its low material cost and excellent chemical stability [185]. Because of its extensive spectral separation (3.37 eV), high binding energy of exciton, electron mobility, and inherent electrical conductivity ($\sim 10\times10^{-7}$ S/cm), ZnO film is commonly accepted for TCO applications [186]. Doping is one of the most successful methods for improving material structure and characteristics [187]. Several research communities have used elements of group-III like Al, In, Ga, Ce [188–193], B [194], and F [195] as impurities to enhance the aforementioned aspects of films in terms of the production of electronic defects as well as impurities.

Al is a common dopant. Al has a high reactive potential. Oxidation happens during film growth, decreasing its potential and electrical properties [196].

Ga is less reactive and has excellent resistance to oxidation than Al [197], according to the list of doping group-III elements. Moreover, by doping ZnO with Ga, defects such as lattice distortion may be reduced, hence enhancing its electrical conductivity [198]. In addition, the lengths of the covalent bonds between Zn–O is 1.97Å and Ga-O is 1.92Å. The fact that the bond length of Ga–O is somewhat shorter than that of Zn–O implies that ZnO lattice will have the minimal deformation even in the presence of a large Ga concentration [199].

GZO films can be deposited using a variety of processes, including magnetron sputtering [200], spray pyrolysis [201], CVD [202], Sol-gel [203], Pulsed laser deposition [204], and Molecular beam epitaxy [205].

Several research have examined how sputtering working pressures affect doped ZnO-based TCOs. A throttle valve may regulate pumping speed to maintain sputtering working pressure for a particular Ar flow after base pressure. This study's sputtering machine uses a mass flow controller to regulate Ar flow rates up to 9×10^{-3}. It presents RF magnetron sputtering in depositing GZO thin films at room temperature with different Ar flow rates. Ar flow rates determine sputtering working pressure. GZO films, a developing TCO substitute for ITO or AZO in PV applications, were studied for structural, optoelectronic, and electrical properties.

Chapter 3: EXPERIMENTAL METHODS

The present chapter delineates the methodology employed by the study to accomplish its intended goals and objectives. The following sections outline the methodology employed in the study and the sequential phases through which the methodology was executed. Furthermore, this chapter enumerates all the tools utilized in the research and provides a rationale for their selection. The chapter also provides an account of the data analysis methodology employed, as well as the potential issues and constraints that may have arisen during the process.

3.1. Substrate preparation

The first and most important task in the fabrication of TFSC is substrate preparation. For the most part, SLG was used as the substrate. They were of various sizes and thicknesses according on the process needs. Some film characterizations were performed on bare glass substrates, whereas device fabrication was performed on coated glass substrates. For device fabrication, two types of coated glass substrates were used: Mo coated glass and Fluorine doped Tin Oxide (FTO).

Cleaning glass substrates is required prior to depositing thin films on them. The procedures taken to clean the substrate are detailed below.

- Mechanically scribing of glass using Micro90 solution.
- 10 minutes of methanol-based ultrasonic glass cleaning.
- 10 minutes of acetone-based ultrasonic glass cleaning.
- 10 more minutes of ultrasonic glass cleaning with methanol.
- 15 minutes of ultrasonic glass washing in De-ionized Water (DIW).
- Removing the water bubbles from the surface of the glass using N_2 gas jet blowing.
- Drying on a hotplate at 120°C for 10 minutes.

Cleaned substrate were then kept inside vacuum desiccator to use in thin film preparation.

The research methodology, as depicted in Figure 3.1, is designed to accomplish the objectives related to the absorber, buffer, and window layers.

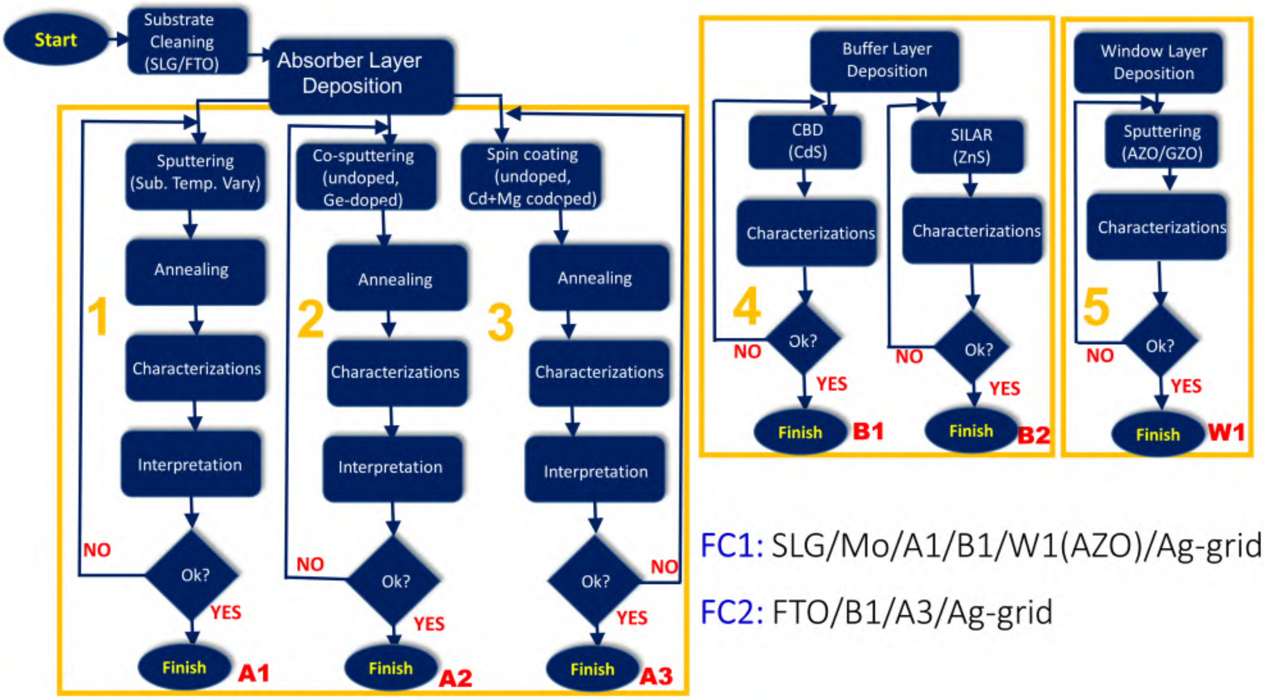

Figure 3.1: The research methodology at a glance

3.2. Methods of thin film preparation

3.2.1. RF magnetron sputtering

The US-made Nanomaster Inc. NSC 3500 Radio Frequency (RF) magnetron sputtering apparatus was used for thin film deposition. It has two 13.56 MHz RF guns. Figure 3.2a shows the sputtering machine schematic. Thin film deposition equipment is vacuum-based. Plasma from a ceramic target coats a substrate in sputter deposition. A plasma sputtering system requires a vacuum chamber with a negative cathode and a positive anode. Argon (Ar) must be introduced into the chamber to create and sustain a glow discharge or plasma. Reactive gases may change the film's chemical composition without reacting with the deposited components. Atoms are ejected from plasma positive ions to the cathode. Evaporated particles form a thin layer on the substrate.

Chamber gas pressure is important. Low pressures—around 3 mTorr can cause sputtering. Pressure reduces ion arrival to the substrate, slowing deposition. Reduced diffusion and thermalization of sprayed atoms slows the process . Thus, pumping systems should be used to drop base pressures to 1×10^{-5} Torr before purging the system with argon (Ar). Low base pressure is essential for high-quality thin film deposition with substrate adherence. In this work, the system was pumped down to 2×10^{-6} Torr. The machine utilized turbo molecular and roughing pumps.

The cylindrical chamber has a 5-inch window for sample and target exchange. It also has two cathode guns with 2-inch cylinders positioned evenly from the chamber center. Planar magnetrons have target cathodes near permanent magnets. The cathode's planar magnetic and electric fields are orthogonal. Science and engineering use magnets to focus plasma on the target.

A matching circuit that was hooked up to a 13.56 MHz RF generator powered the cathode. In the NSC 3500 sputtering machine, the material can be heated to as high as 500°C. Ar was used as the process gas. Mass Flow Converter (MFC) with a flow rate of 100 Standard Cubic Centimeters per Minute (SCCM) was used. To make reactive sputtering easier, a MFC that supplies oxygen at a rate of 10 SCCM was put in place. A LabView program was also used to control the pressure in the box. The pressure before deposition is kept below 10^{-5} Torr.

3.2.2. Sol-gel spin coating

The utilization of this technique is widespread in the fabrication of thin films, enabling accurate regulation of their thickness and morphology. During the sol-gel process, nanoparticles are

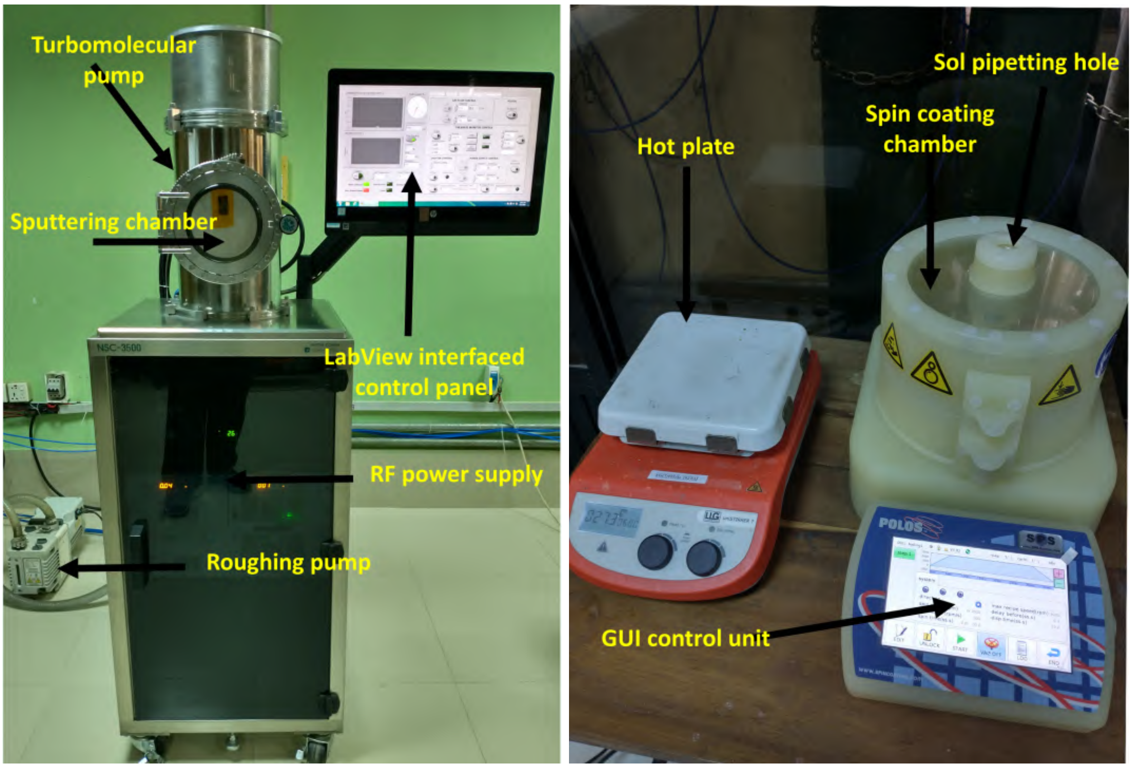

(a) RF magnetron sputtering machine **(b)** Spin coating machine

Figure 3.2: Vacuum and non-vacuum based deposition systems

initially transformed into a colloidal suspension, commonly referred to as a sol, within a liquid medium. Subsequently, gelation occurs, resulting in the formation of a solid matrix. During the spin coating process, a small amount of sol is applied onto a rotating substrate, commonly composed of glass or silicon. The sol is then uniformly distributed across the substrate's surface through the high-speed rotation of the substrate. The rotational speed, sol viscosity, and solvent surface tension are a few variables that have an impact on the intricate physics of the sol-gel spin coating process.

The sol-gel spin coating process has utilized various solvents, such as Dimethyl sulfoxide (DMSO), ethanol, methanol, and isopropyl alcohol. The selection of a solvent is of utmost importance due to its potential to exert a substantial influence on the characteristics of the resultant thin film. Dimethyl sulfoxide (DMSO) is often used as a solvent in sol-gel spin coating applications because it has a high boiling point and can dissolve many metal alkoxides that are important for sol-gel chemistry. DMSO exhibits minimal toxicity and possesses the ability to facilitate the development of a compact and homogeneous coating. Ethanol is often used as a solvent in the sol-gel process. It is often used as a co-solvent to make metal alkoxides more soluble and make it easier to make a thin film. Methanol and isopropyl alcohol are frequently employed as solvents in the sol-gel spin coating technique. These solvents possess distinct characteristics and can be employed to regulate the surface tension, evaporation, and viscosity of the solute's fluid rate.

During the spin coating process, the solute is applied to a substrate that is subjected to rotational motion. The resultant centrifugal forces arising from this spinning motion facilitate the uniform distribution of the solute across the substrate's surface. The thickness of the resultant film is determined by the balance between centrifugal forces, which are influenced by the density of the sol, and capillary forces, which are regulated by the surface tensions and viscosity of the sol.

The viscosity of the sol is a critical parameter in the spin coating process, as it governs the level of resistance to flow and the extent of spreading over the substrate. When the viscosity of the sol is high, it can result in uneven spreading, thereby causing the formation of non-uniform films. Conversely, sols with low viscosity can lead to the formation of extremely thin films or inadequate surface coverage. So, it is important to control the viscosity of the sol by changing things like the concentration of the precursor, the solvent, or the addition of a surfactant to improve the way the substrate sticks to itself.The role of the solvent's surface tension in the spin coating process is crucial, as it governs the solvent's capacity to wet the substrate and achieve uniform spreading over the surface. Solvents exhibiting elevated surface tension have a tendency to form droplets on the substrate, resulting in inadequate coverage and the formation of non-uniform films. Hence, solvents possessing a low surface tension are favored for the process of spin coating due to their ability to facilitate the dispersion of the solute across the substrate, leading to the formation of a film that is both homogeneous and compact.

Furthermore, it should be noted that the spin coating process has the potential to generate shear stresses within the sol, thereby exerting an influence on the characteristics of the resultant film. The crystalline structure and optical properties of ZnO thin films can be influenced by the shear stress generated during spin coating. Shear forces can exert an influence on the orientation of nanoparticles within a sol, resulting in the creation of thin films that exhibit anisotropic properties.

The drying process is a crucial factor in the development of thin films in sol-gel spin coating. The concentration of nanoparticles in the solution increases as the solvent undergoes evaporation, resulting in the formation of a gel-like structure. The morphology and properties of the resulting thin film can be influenced by the rate at which the solvent evaporates. The occurrence of cracks and defects in the film can be attributed to the rapid evaporation of the solvent, whereas an uneven film can be formed as a result of slow evaporation. Gaining a comprehensive comprehension of the physics underlying sol-gel spin coating holds the potential to enable researchers to enhance the optimization of the synthesis process for the production of thin films possessing tailored properties. Gaining comprehension of the underlying principles of sol-gel spin coating is crucial for researchers to effectively enhance the synthesis of thin films, enabling them to achieve desired properties.

3.2.3. Chemical bath deposition (CBD)

Chemical Bath Deposition (CBD) is a simple and low-cost method for depositing thin films of various materials, including semiconductors, metal oxides, and chalcogenides. CBD is based on the chemical reaction between metal ions and a reducing agent in an aqueous solution at a low temperature, typically around 60-90 °C. The deposition process can occur either on a substrate surface or in a bulk solution, depending on the specific parameters of the experiment.

CBD has been widely used in the production of thin film materials for electronic, optoelectronic, and photovoltaic devices. The method is attractive because it can produce high-quality films with excellent adhesion, uniformity, and thickness control. Moreover, the process is scalable, making it a good candidate for large-scale production. The physics of CBD involves several interrelated processes, including mass transport, nucleation, growth, and surface reaction. These processes are influenced by various factors such as solution composition, temperature, pH, and substrate properties.

The mass transport of reactants and products is one of the key factors determining the deposition rate and the film quality in CBD. The transport of metal ions and reducing agents occurs through diffusion, which is governed by Fick’s laws. The diffusion coefficient of the reactants in the solution depends on the solvent viscosity, temperature, and the size of the reactant molecules. The substrate can also affect the mass transport process by changing the solution hydrodynamics and the reaction rate at the substrate surface.

Nucleation and growth are the fundamental processes of thin film deposition. Nucleation occurs when metal ions in the solution interact with the substrate surface and form a stable nucleus. The critical nucleus size is determined by the interfacial energy between the metal and the substrate, the surface tension, and the supersaturation of the solution. Once the nucleus forms, the growth process begins, which can occur by several mechanisms, including ion-by-ion deposition, island growth, and layer-by-layer growth.

The surface reaction between metal ions and the reducing agent is also critical for the

CBD process. The reduction of metal ions can occur through various mechanisms, such as complexation, ligand exchange, or direct electron transfer. The reaction rate is affected by several factors such as the concentration of reducing agent, pH, and temperature. The surface energy is a measure of the energy required to create a new surface on the substrate. The deposition of a thin film on the substrate involves the nucleation and growth of metal atoms on the surface, and the surface energy of the substrate determines the ease with which these processes occur. A substrate with a higher surface energy will tend to promote the nucleation of metal atoms, leading to the formation of a more uniform and compact film.

Another essential aspect in the CBD process is the pH of the solution. The pH of a solution can influence the concentration of metal ions and reducing agents, as well as the formation of metal complexes. The temperature of the bath also has an impact on the deposition process. Temperature can affect the solubility of metal ions and reducing agents in solution, as well as the pace of their chemical reaction. CBD has been used to deposit thin-film materials such as CdS, ZnO, $CuInS_2$, and PbS. CdS thin films, for example, have been deposited using a solution of cadmium nitrate, thiourea, and ammonium hydroxide.

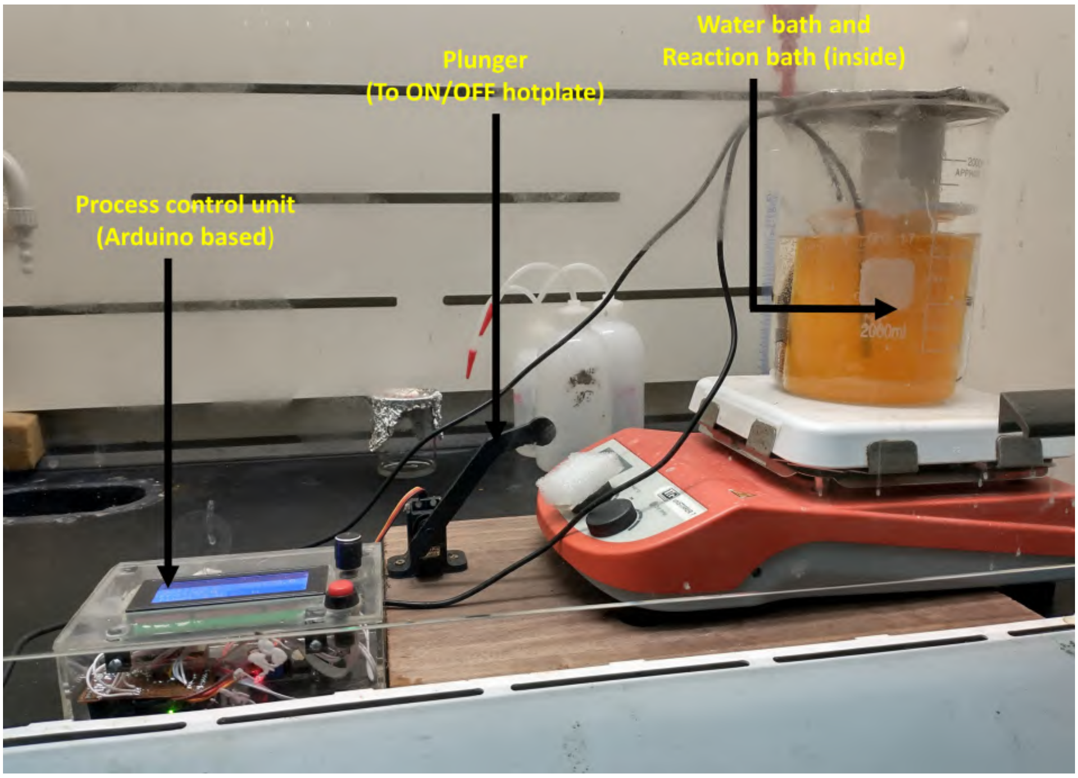

Figure 3.3: Chemical bath deposition system

3.2.4. Successive ionic layer adsorption and reaction (SILAR)

Successive Ionic Layer Adsorption and Reaction (SILAR) is a thin film deposition technique widely employed in the fabrication of diverse material structures, including semiconductors, metals, and oxides, due to its capacity for precise control over film thickness and composition.

The SILAR deposition system is typically composed of a reaction chamber, precursor solutions, substrates, and gas handling apparatus. The reaction chamber is designed to maintain controlled environmental conditions, such as vacuum or inert gas atmosphere, to minimize contamination and undesirable side reactions.

Two or more precursor solutions are used in the SILAR process, wherein inorganic salts or complexes are dissolved in suitable solvents. Each precursor solution contains the constituent elements essential for thin film formation. These precursor solutions are meticulously prepared to ensure stability and compatibility with the deposition process.

The substrates selected for deposition undergo thorough cleaning procedures to eliminate impurities and contaminants, ensuring a pristine surface for thin film growth. The choice of substrate material is dictated by the specific application and desired properties of the thin film.

The SILAR deposition process involves sequential and repetitive cycles of precursor adsorption and reaction on the substrate surface. Initially, the substrate is immersed in the first precursor solution, leading to wetting of the substrate surface by the solution. After a defined immersion time, the substrate is transferred to the second precursor solution, where it reacts with the adsorbed layer from the first solution. This reaction generates a thin solid layer on the substrate surface. Subsequently, the substrate is rinsed to remove residual solution, and the process is iteratively repeated to incrementally build up the desired film thickness. The number of SILAR cycles is a decisive factor in determining the final thickness of the deposited film.

Parametric control, such as immersion time, precursor concentration, temperature, and cycle count, enables precise regulation of the thin film's thickness and composition. Proper optimization of these parameters is crucial to achieve homogenous and desired material properties.

Post-deposition treatment, such as annealing, may be employed to further modify the thin film's characteristics. Annealing involves subjecting the film to controlled heating at specific temperatures for predetermined durations, inducing structural alterations or enhancements in electrical and optical properties.

In summary, the SILAR-based deposition system provides a versatile and powerful methodology for fabricating thin films with high controllability over thickness and composition. Its widespread applications span multiple fields, including electronics, optoelectronics, solar cells, sensors, and catalysis.

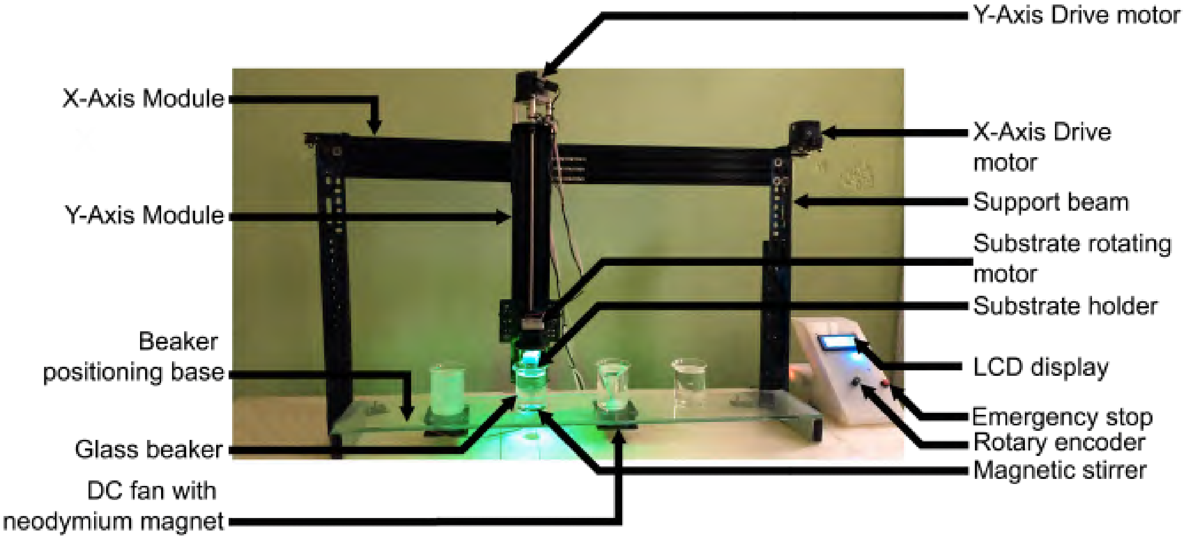

Figure 3.4: SILAR based thin film deposition machine

3.3. Thermal annealing

The thermal annealing machine is shown in Figure 3.5. The steps were as follows:

- Films were annealed with 100 mg sulfur pallets inside a graphite box in a tube furnace (GSL-1100X, MTI corporation, USA).
- The tube furnace was evacuated with a base pressure of 300 mTorr.
- Temperature ramp 20°C per min to reach a peak of 550°C , set to remained for 30 min and then allowed to cool naturally.
- After removing from furnace, soaked in DI water for 20 min followed by drying with N_2 jet.

3.4. Methods of thin film characterization

The following characterizations were employed in this study:

- Film thickness measurements by Dektak profilometer or by FESEM X-sectional images.
- The morphology and surface roughness of the films were investigated using FESEM and 3D profilometer (Filmetrics, San Diego, CA, USA) respectively.

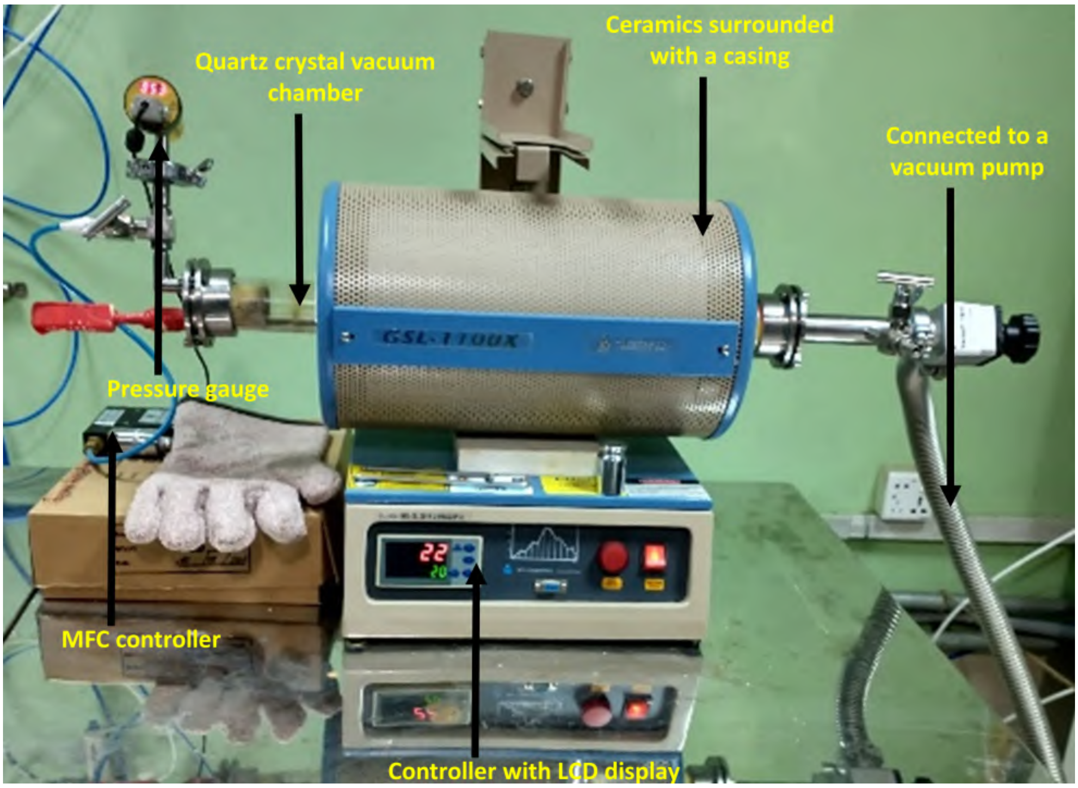

Figure 3.5: Thermal annealing machine

- Using a Bruker D8 advanced (Bruker Corporation, Billerica, MA, USA) X-ray diffractometer equipped with Cu Kα radiation, XRD measurements were taken in the range of 10°-90° over the 2θ angle range. Rietveld refinement was performed on the XRD data obtained from the samples.
- The Renishaw spectrometer (in Via Raman Microscope, UK) fitted with a Charge Coupled Device (CCD) detector was used to carry out the Raman measurements. For excitation, a diode-pumped solid-state laser with a wavelength of 785 nm was utilized.
- Morphology and chemical composition analysis (Energy dispersive X-ray spectroscopy, EDS) was carried out using FESEM and Thermofisher Quattro S ESEM (Thermo Fisher Scientific Inc., Waltham, MA, USA).
- EDS was carried out with a total acquisition time of approximately 29 s. The average count rate and acceleration voltage were16011 cps and 15 kV, respectively.
- The SHIMADZU UV-2600, UV-Vis NIR spectrophotometer (Country of origin: Japan) was used to explore the optical properties over an optical wavelength range of 200 nm to 1400 nm.
- For pH measurements, pH-indicator strips (nonbleeding, 0-14) MColorpHast^{TM} (Merck

KGaA, Dramstadt,Germany) were used. Dynamic viscosity of the prepared solutions was measured by Fungilab RT500 (Bercelona, Spain).

- Electrical characteristics including carrier concentration, resistivity, and mobility were determined for all samples using a Hall effect measuring system (HMS ECOPIA 3000) applying a magnetic field of 0.57 T and a probe current of 1 mA.
- In order to quantify the binding energies and oxidation states of the CZTS thin films, XPS experiments were carried out with a conventional Mg Kα X-ray source (exciting photon energy 1253.6 eV). Following the execution of a Shirley-type background subtraction, the XPS spectra were fitted using Gaussian peak forms.
- Solar Cell Capacitance Simulator (SCAPS) is a comprehensive simulation software tool developed by a team of researchers at the University of Ghent in Belgium, led by Prof. Jef Poortmans and Dr. Michiel Burgelman [206]. For numerical simulation study the SCAPS 1-D was used in this study.
- Device I-V characteristics were measured by 1-sun simulator with AM1.5 standard.

3.5. Material and methods

3.5.1. RF magnetron sputtered CZTS thin films: Effect of deposition temperatures

Corning® soda lime glasses (75 mm × 50 mm × 1.2 mm) were used as substrate. At first, glasses were cleaned ultrasonically. As-deposited thin-films of absorbers were prepared as per sputtering recipe (Table 3.1), followed by DI water soaking and drying. Full-cell was fabricated with SLG/Mo/CZTS/CdS/i-ZnO/ZnO:Al/Ag stacks. Mo, i-ZnO, and ZnO:Al layers were deposited by sputtering. Ag grids were given by screen printing using Ag gels. CdS layer was deposited by homemade CBD system using the recipe as outlined in [207]. The working flowchart is shown in Figure 3.6.

3.5.2. Ge-alloyed CZTS thin films employing RF magnetron co-sputtering

All thin film depositions were carried out on 75×50×1.2 mm^3 Corning® soda lime glasses (SLGs). As-deposited thin-films of absorbers were prepared as per sputtering recipe (Table 3.2), followed by DI water soaking and drying. Finally, a diamond cutter chops samples to various sizes for characterizations. The working flowchart is shown in Figure 3.7.

Table 3.1: Sputtering process parameters to synthesize CZTS thin films

Parameters	**Conditions**
Target	CZTS (off-stoichiometric, purity 99.99%, 2-inch diameter)
Base pressure	5×10^{-6} Torr
Ar flow rate	10 sccm
Working pressure	2.5 mTorr
Pre-sputtering time	20 minutes
Substrate rotation	10 rpm
Substrate to target distance	10 cm
RF power(s)	Gun-1: CZTS (50W for all depositions)
Deposition temperature	RT,150°C,250°C,350°C,450°C, and 500°C
Film thickness(s)	~1.8 μm (by setting 'thickness control' feature)

Table 3.2: Co-sputtering process parameters to synthesize CZTS:Ge (CZTGS) thin films

Parameters	**Conditions**
Target	CZTS (off-stoichiometric, purity 99.99%, 2-inch diameter) Ge (purity 99.99%, 2-inch diameter)
Base pressure	1×10^{-6} Torr
Ar flow rate	20 sccm
Working pressure	5 mTorr
Pre-sputtering time	20 minutes
Substrate rotation	10 rpm
Substrate to target distance	10 cm
RF power(s)	Gun-1: CZTS (53W for all depositions) Gun-2: Ge (0W, 10W, and 15W)
Deposition temperature	350°C
Film thickness(s)	~1 μm (by setting 'thickness control' feature)
Sample identification	Ge00, Ge10, Ge15 (after sulfurization)

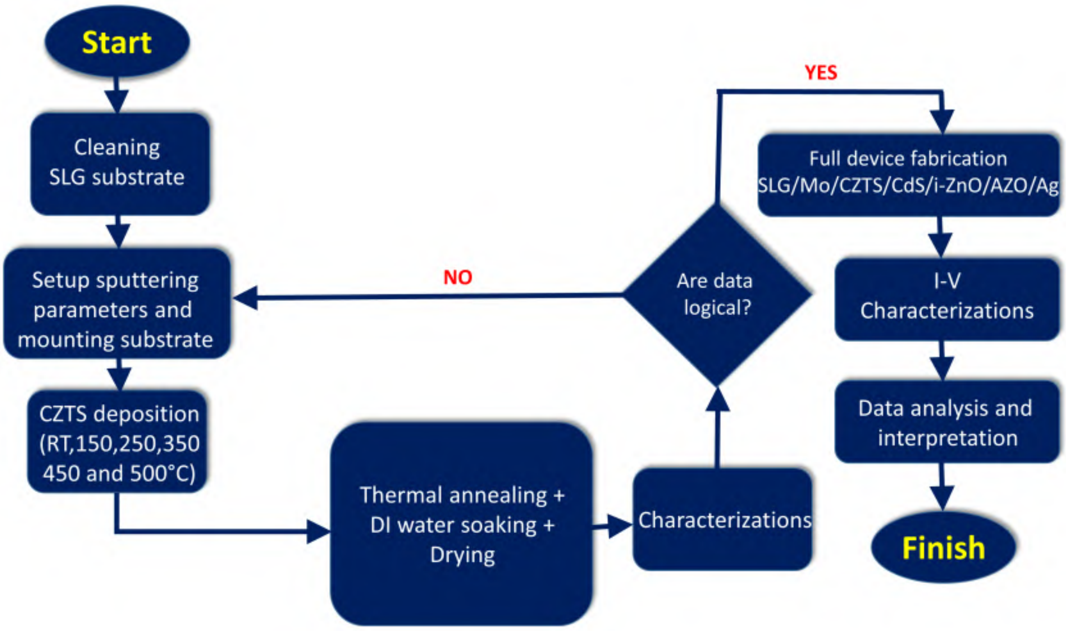

Figure 3.6: The working flowchart of Objective-1

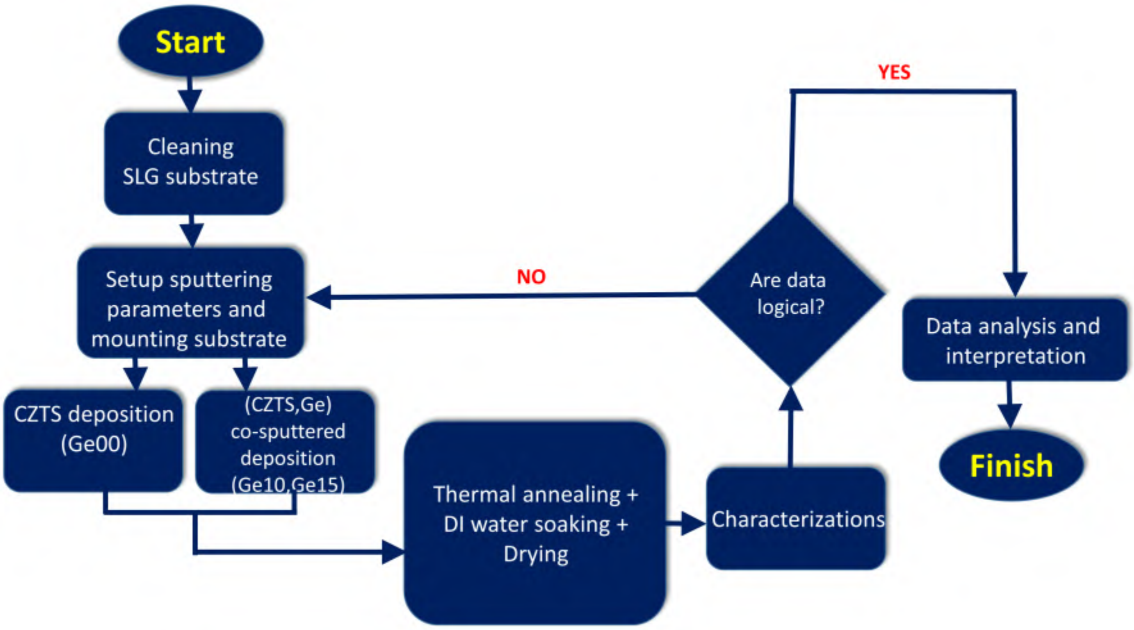

Figure 3.7: The working flowchart of Objective-2

3.5.3. Superstrate structured CZTS thin film solar cell: A co-doping approach

Corning® Soda Lime Glass with the dimensions 50×50×1.2 mm^3 were used as a substrate for all thin film depositions. SLGs were ultrasonically cleaned with sequential immersion into methanol, acetone, methanol again, and deionized water (DI water). The working flowchart is shown in Figure 3.8. All reagents and chemicals were purchased from Alfa Aesar, USA of analytical grade and used without further purification. The CZTS sols were made by adding 1.14M copper acetate monohydrate ($Cu(CH_3COO)_2.H_2O$, 99%), 0.79M stannous chloride dihydrate ($SnCl_2.2H_2O$, 98%), 0.82M anhydrous zinc chloride ($ZnCl_2$, 98%), and 4.1M thiourea (CH_4N_2S, 99%) into 50ml Dimethyl sulfoxide (DMSO) at room temperature as described in [132]. For doped CZTS samples, the precursors cadmium chloride monohydrate ($CdCl_2.H_2O$) and magnesium chloride hexahydrate ($MgCl_2.6H_2O$) were used in preparing cadmium and magnesium doped sols, respectively.

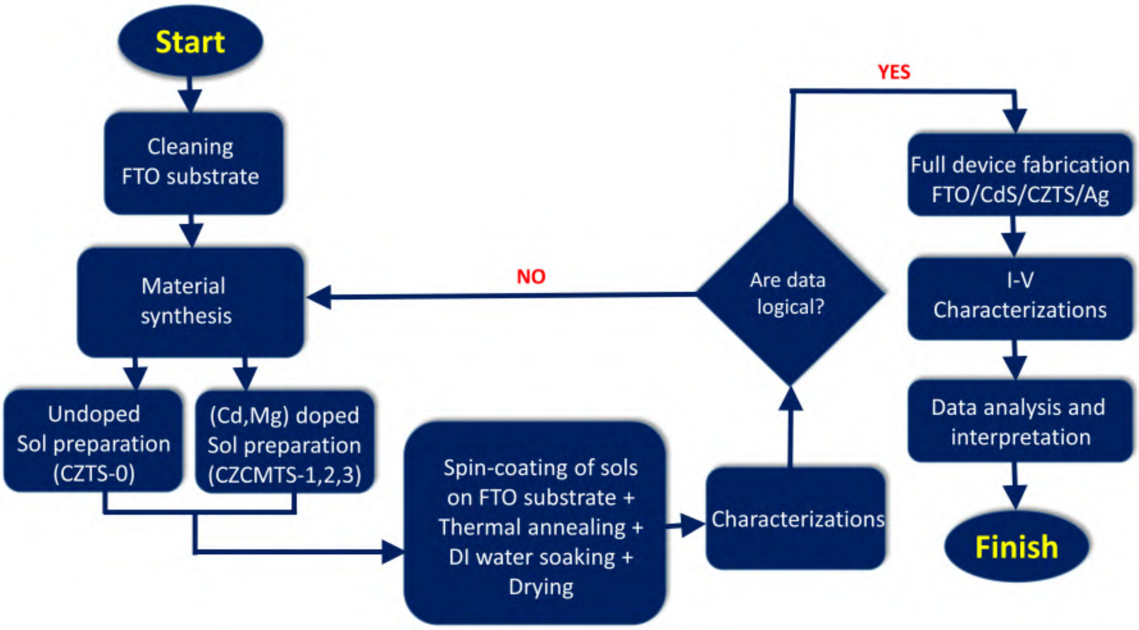

Figure 3.8: The working flowchart of Objective-3

The sols were aged for 72 hours and kept in a dark place before the spin coating process started. Before coating, the aged sols were passed through a 0.22 micron Polytetrafluoroethylene (PTFE) syringe filter manufactured by Corning® in the USA. For the fabrication of thin films on SLG substrates, we utilized use of a spin coater called a POLOS SPIN 150i from SPS Europe B.V. in the Netherlands. In the beginning, the SLG substrate is put on the chuck of the spin coater, and then the vacuum switch is turned "ON" so that the substrate may be bonded securely. In the second step, 750 μl of sols were carefully pipetted and deposited in the middle of the substrate . This was done to ensure that the sols were distributed evenly. Thirdly, the process of spin coating was initiated at a spin speed of 1500 rpm for a period of 60 seconds. The coating was then annealed on a hotplate at a temperature of 320°C for 1 minute, after which it was allowed to cool naturally for an additional 2 minutes. This procedure was carried out a total of 5 times. The fabrication process was carried out in the same manner for each and every sample. The as-deposited samples were then subjected to thermal annealing followed by DI water soaking and drying.

Recipe to study the effect of Cd and Mg doping separately:

Both the dopants were at 50 mol% relative to $ZnCl_2$ precursor in the sols. The undoped, Cd-doped, and Mg-doped samples are identified as C-00, C-Cd, and C-Mg, respectively. The prepared sols are shown in Figure 3.9.

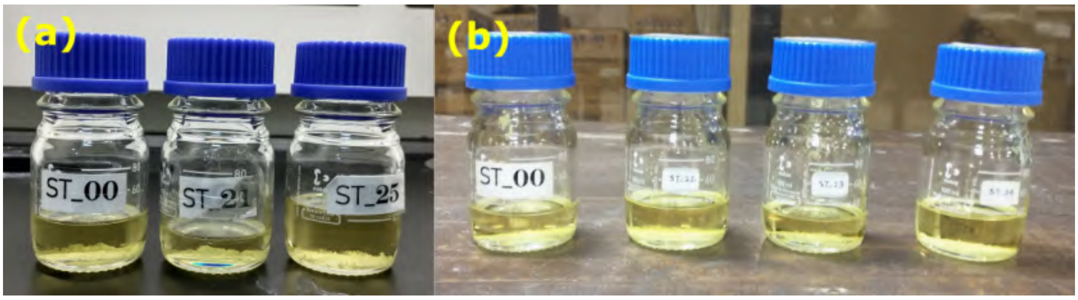

Figure 3.9: Prepared sols: (a) individual dopant, (b) co-dopants

Recipe to study the effect of Cd and Mg co-doping:

The doping in the precursor solutions (in mol%) with corresponding sample codes are shown in Table 3.3 and prepared sols are shown in Figure 3.9.

Table 3.3: Recipe of co-doping investigations

Sample code	**Doping in precursor solutions** **Target compound: $Cu_2Zn_{(1-x-y)}Cd_xMg_ySnS_4$** x = **Cd/(Cd+Zn)**	 y = **Mg/(Mg+Zn)**
CZTS-0	0.00	0.00
CZCMTS-1	0.375	0.125
CZCMTS-2	0.25	0.25
CZCMTS-3	0.125	0.375

Device fabrication: In the co-doping studies, thin film solar cells were fabricated in superstrate structured as shown in Figure 3.10. A typical superstrate structured thin film solar cell is shown in inset.

The CdS buffer layer was deposited by Chemical Bath Deposition (CBD) in a home made setup as shown in Figure 3.3, using deposition recipe as mentioned in Objective-1. Ag contacts were printed upon CZTS absorber layer using masks by screen printing.

It was looked at how the bands lined up in both undoped and co-doped CZTS absorbers

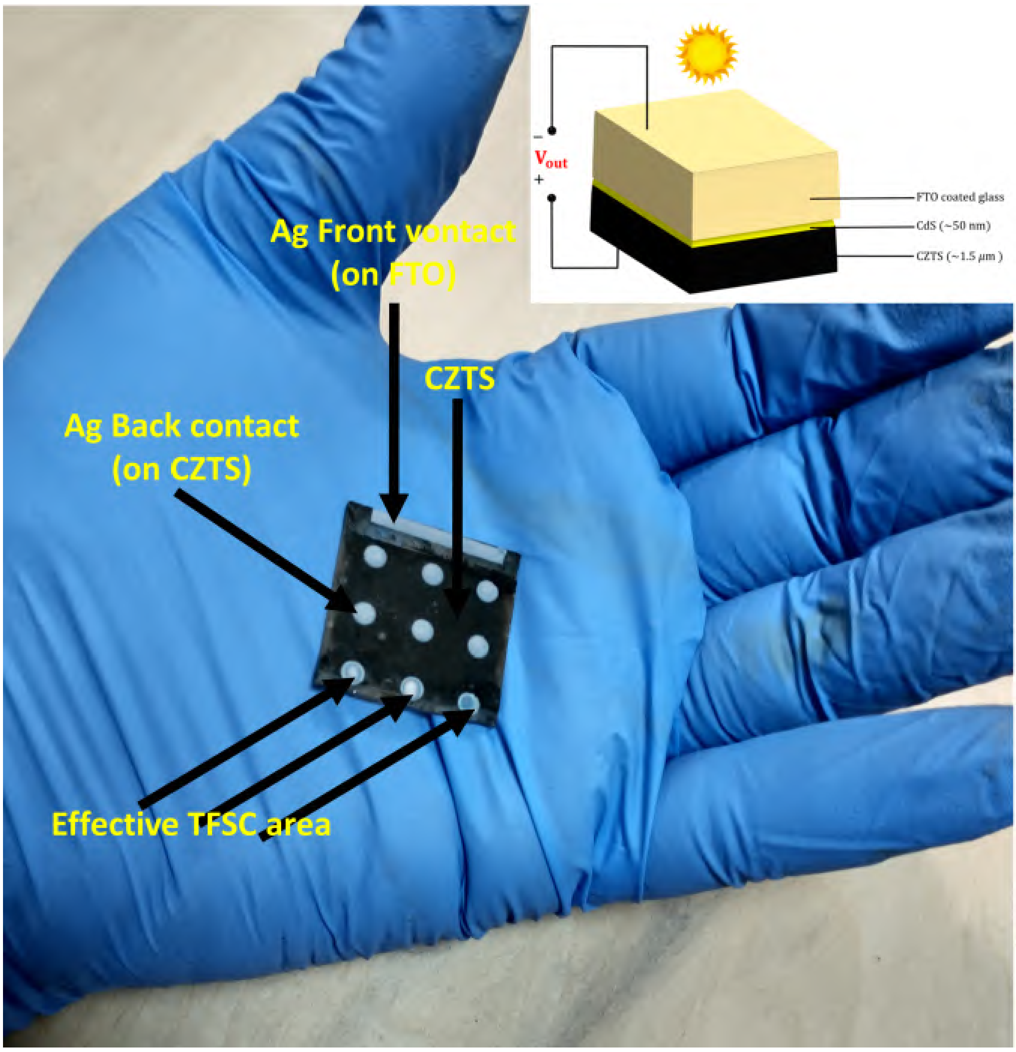

Figure 3.10: Superstrate structured CZTS thin film solar cell (dimensions are not in scale)

and in CdS, which was used as a buffer. For this VBMs of the absorbers are determined as can be found in Figure 4.28 at Chapter 4. CdS's optoelectronic properties may be found in the literature because it is one of the most researched materials used as a buffer layer. Thus, the 1.9 eV VBM value of CdS was adopted from [159]. After that, using the formulas for VBO and CBO, the offsets were calculated. In the following section, a comprehensive procedure for the band alignment determination process has been provided.

3.5.4. Band alignment study of CZTS/CdS and CZTS/ZnS heterojunction interface

The CZTS-0 sample and CdS sample were taken from the previous study. ZnS thin film was deposited by homemade SILAR setup using the recipe outlined in [208]. Deposited CZTS, CdS, and ZnS thin films are shown in Figure 3.10, Figure 3.12a, and Figure 3.12b respectively. The working flowchart is shown in Figure 3.11.

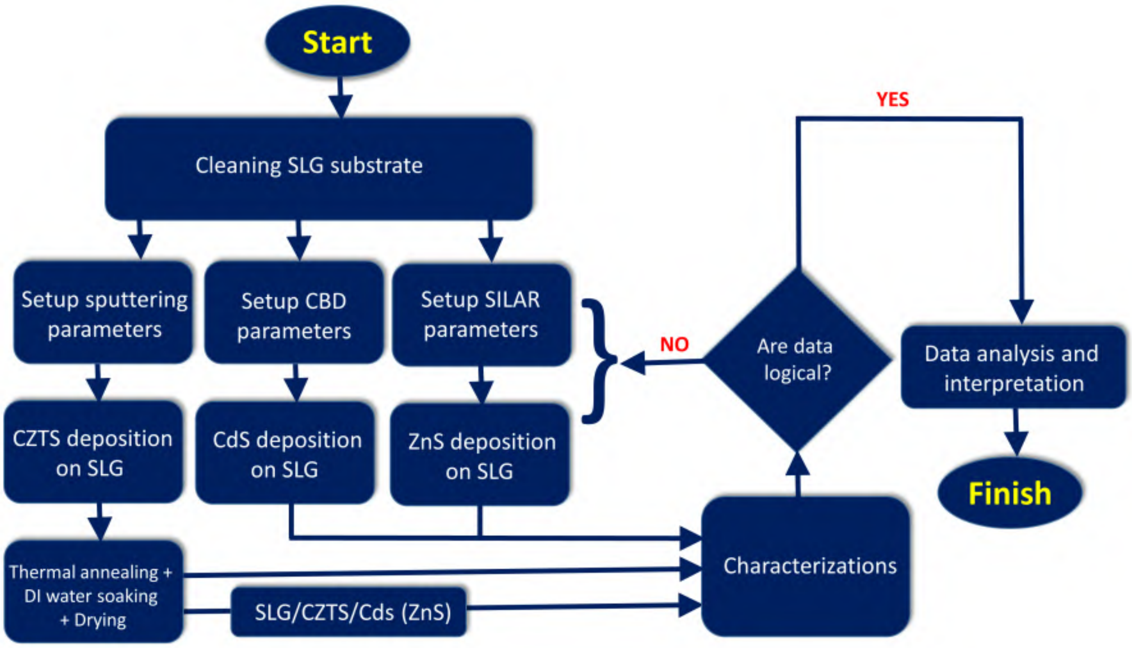

Figure 3.11: The working flowchart of Objective-4

Along with these three separate films, thin layers of CdS on CZTS and ZnS on CZTS were also made so that XPS could be used to study the interface.

The XPS analysis was carried out at lower binding energies in order to determine the VBM of CZTS absorber. The VBM values of CdS (1.9 eV) and ZnS (2.0 eV) were adopted from [159] and [209] respectively.

The Valance Band Maximum (VBM) relative to the Fermi level (E_F) at an energy of 0 eV, was determined by proceeding with the three following steps:

1. First, performing a Shirley baseline subtraction.
2. Fitting the lower binding energy side of the VB with a linear curve.
3. Extending the linear fitting line and intersecting it with the baseline.

Next, the linear part of the lower energy side of the VB is extrapolated to the spectral baseline to determine the VBM value. It is important to note that this method of locating the VBM is frequently utilized in literature [157, 159, 210]. The VBM of CZTS is determined and shown in Figure 4.28a at Chapter 4. The VBO can be determined by the Eq. 3.1 [158].

$$\triangle E_V^{a/b} = \left(E_{Sn\ 3d}^{a} - E_{VBM}^{a}\right) - \left(E_{Cd\ 3d}^{b} - E_{VBM}^{b}\right) - \triangle E_{CL}^{a/b} \tag{3.1}$$

where, $\triangle E_V^{a/b}$ = Valance Band Offset (VBO) ; a = CZTS ; b = CdS or ZnS

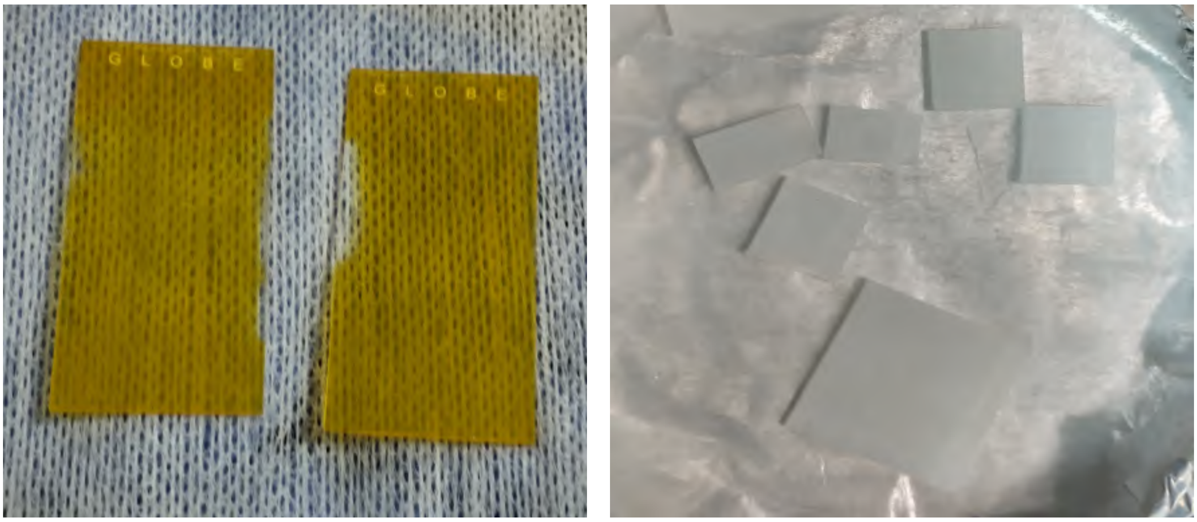

(a) CdS thin film deposited by CBD **(b)** ZnS thin film deposited by SILAR

Figure 3.12: Deposited thin films for band alignment study

$\triangle E_{CL}^{a/b}$ = The energy difference across the interface between the Sn 3d core level in the CZTS side and Cd 3d or Zn 2p core level in the CdS side or ZnS side of the junction. The CBO can be calculated from Eq. 3.2.

$$\text{Conduction band offset, (CBO)} = \triangle E_{C}^{a/b} = \triangle E_{g}^{a/b} - \triangle E_{V}^{a/b} \tag{3.2}$$

3.5.5. Fabrication and characterization of ZnO:Ga (GZO) thin film by RF magnetron sputtering

All thin film depositions were carried out on 75×50×1.2 mm^3 Corning® soda lime glasses (SLGs). As-deposited thin-films of absorbers were prepared as per sputtering recipe (Table 3.4), followed by DI water soaking and drying. The working flowchart is shown in Figure 3.13.

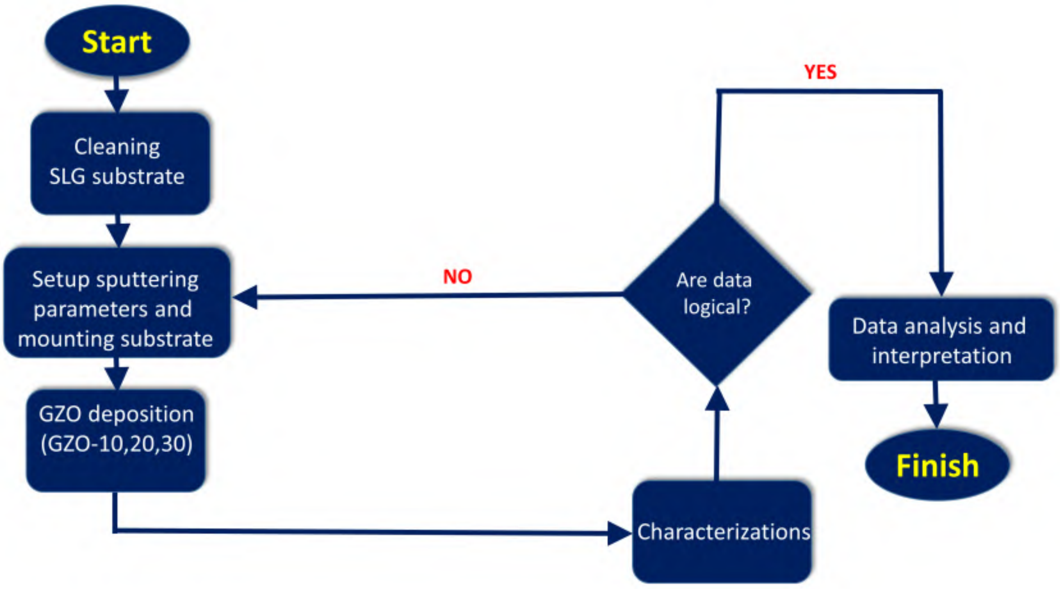

Figure 3.13: The working flowchart of Objective-5

Table 3.4: Sputtering process parameters to fabricate as-deposited GZO thin films

Parameters	Conditions
Target	GZO (ZnO 97.5 wt% + Ga_2O_3 2.5 wt%) purity 99.95%, 5 cm diameter
Base pressure	1×10^{-6} Torr
Ar flow rate	10 sccm, 20 sccm and 30 sccm
Working pressure	2.5 mTorr, 5 mTorr and 7.4 mTorr
Pre-sputtering time	20 minutes
Substrate rotation	15 rpm
Substrate to target distance	10 cm
RF power density (Gun-1)	2.5 W/cm^2
Deposition temperature	RT
Deposition time	60 minutes
Sample identification	GZO-10, GZO-20 and GZO-30

Chapter 4: RESULTS AND DISCUSSION

This chapter describes the outcomes of the characterization analysis conducted on the absorber layer of Cu_2ZnSnS_4 *(CZTS) thin film, as well as the CZTS thin film solar cell. Initially, an alternative approach to the two-step fabrication process of CZTS thin film absorbers is presented. Subsequently, the findings of two investigations pertaining to extrinsic doping in CZTS absorbers through RF magnetron sputtering and spin coating techniques are delineated. Subsequently, findings pertaining to the band alignment of heterojunctions between CZTS/CdS and CZTS/ZnS are presented. The band alignment investigation involved the utilization of distinct fabrication techniques for the CZTS, CdS, and ZnS materials. Specifically, spin coating was employed for the CZTS fabrication, while the CBD and SILAR methods were utilized for the CdS and ZnS fabrication, respectively. Finally, findings from research on the potential of the Ga: ZnO (GZO) window layer are being presented.*

4.1. RF magnetron sputtered CZTS thin films: Effect of deposition temperatures

Substrate structured a pure sulphide CZTS Thin Film Solar Cell (TFSC) consists of several layers. This chapter describes the fabrication of CZTS-TFSC, using RF magnetron sputtering. In particular, it describes deposition and characterization of CZTS thin-film to be used as an absorber layer in a full cell using RF magnetron sputtering with substrate temperature varied from Room Temperature (RT) to 500°C (i.e. RT, 150°C, 250°C, 350°C, 450°C and 500°C).

4.1.1. Composition of elements

The elemental composition ratio, as probed by EDS and summarized in Table 4.1 makes it abundantly evident that the composition that was achieved at a deposition temperature of 500°C is appropriate for improved photovoltaic performance. As a result, the additional parameters of the sample that was deposited at 500°C were computed.

4.1.2. Structural properties

X-ray Diffractometry (XRD) was carried out to evaluate the effect of deposition temperatures on the structural properties of fabricated CZTS thin films.

Although high-temperature films frequently exhibit a dominant diffraction peak at the (112) plane, another kesterite characteristic peak at the (220/204) plane was observed, confirming its

Table 4.1: Elemental composition ratio of CZTS thin-films for various deposition temperatures

Deposition temperature	**Cu/(Zn+Sn)**	**Zn/Sn**	**Cu/Sn**	**S/Metal**
RT	0.57	0.98	1.13	0.98
150°C	0.57	0.76	1.00	0.90
250°C	0.48	0.68	0.60	1.02
350°C	0.56	0.73	0.97	0.89
450°C	0.60	0.99	1.19	0.93
500°C	0.65	0.85	1.20	0.97

polycrystalline nature. According to [115, 211, 212], all of these properties fit within the kesterite structure (JCPDS# 26-0575). Except for low temperature deposition, a preferential orientation along the (112) plane was found, with intensity rising with increasing substrate temperatures (Figure 4.1). Secondary phases did not show any further notable peaks. The crystallographic data for the sample deposited at a substrate temperature of 500°C are reported in Table 4.2. Crystallographic data was determined for three samples, deposited at temperatures of 305°C, 450°C, and 500°C. Because of their poor crystallization, samples deposited at lower temperatures were deemed unusable for calculations.

The average crystallite size (D) using the Scherrer formula [213], the microstrain (ε) [214], and the dislocation density (δ) [215] of the deposited films of the principal diffraction peak at the (112) plane were determined as given by Eqs. [4.1]-[4.3] respectively.

$$D = \frac{0.94\lambda}{\beta \cos \theta} \tag{4.1}$$

$$\varepsilon = \frac{\beta}{4 \tan \theta} \tag{4.2}$$

$$\delta = \frac{n}{D^2} \tag{4.3}$$

where,

λ = X-ray wavelength, 1.540056Å and β = Full-width at half-maximum

θ = Half of the Bragg's diffraction angle and n=1

The film deposited at highest temperature, i.e. at 500°C, is subjected to compressive stress, due to the lowest value of inter planar spacing, d. So deposited film is less likely to be peeled off. The values of the lattice constants match the structures of kesterite.

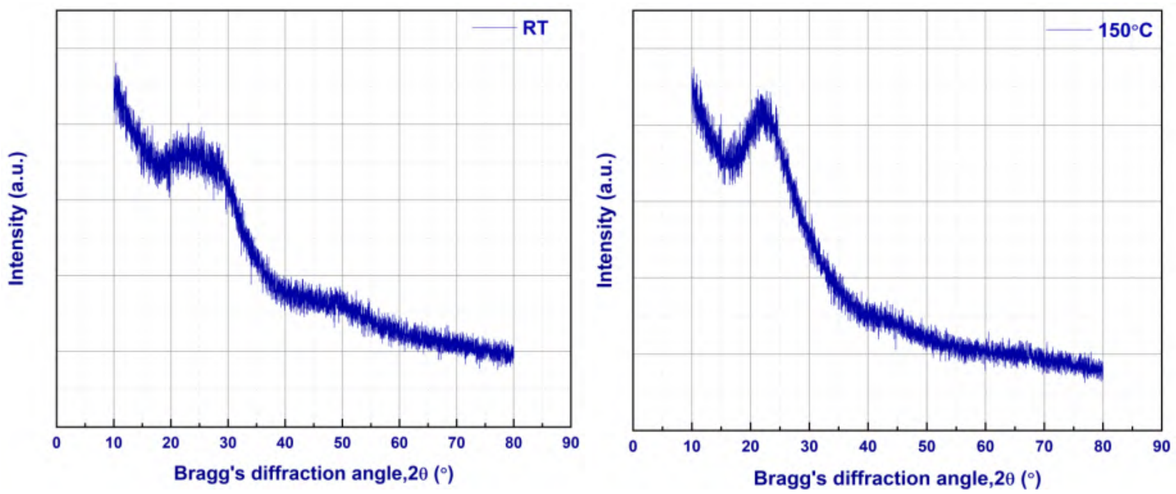

(a) Room temperature (RT)

(b) 150°C

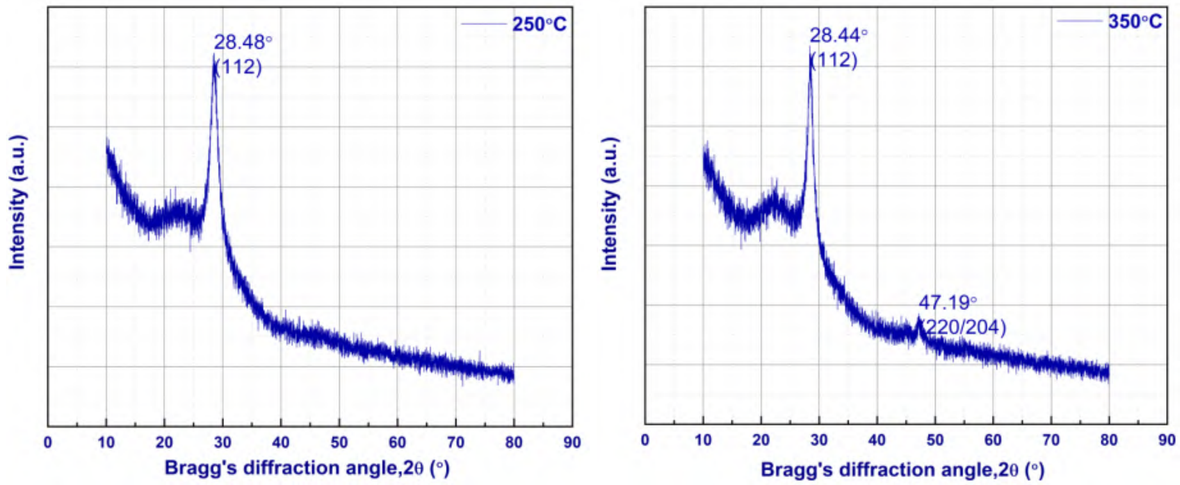

(c) 250°C

(d) 350°C

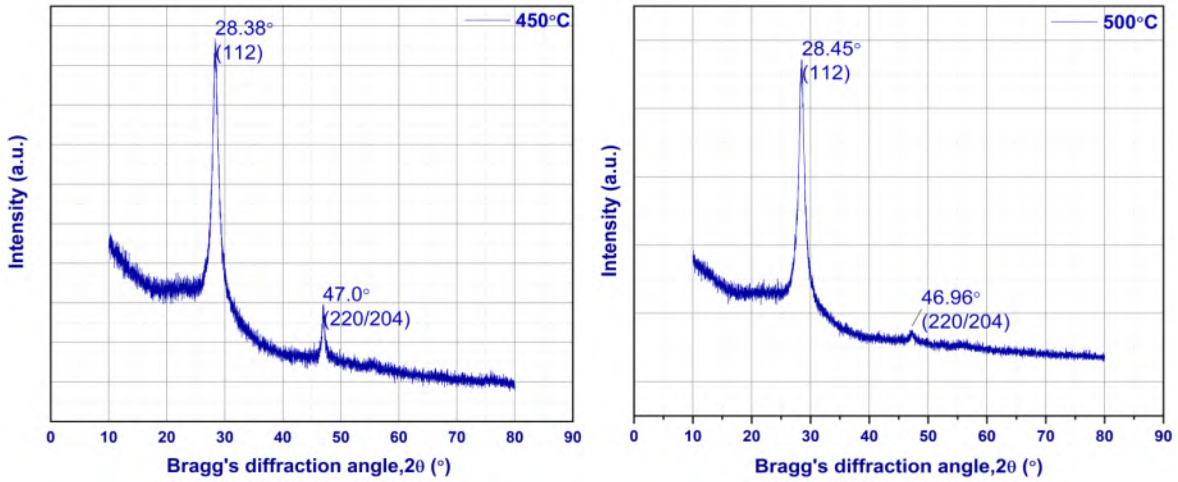

(e) 450°C

(f) 500°C

Figure 4.1: XRD pattern of CZTS thin-films at various substrate temperatures

Table 4.2: Crystallographic data of CZTS thin-films at substrate temperatures of: (a) 350°C, (b) 450°C, and (c) 500°C

Substrate temperatures	**2θ (°)**	**d (Å)**	**D (nm)**	**a (Å)**	**c (Å)**	**c/2a**	**(Å^3)**	**ε ($\times 10^{-3}$)**	**δ ($\times 10^{11}$)**
350°C	28.44	3.135	7.887	5.44	10.815	0.994	320.37	17.89	16.07
450°C	28.38	3.142	6.421	5.46	10.801	0.988	322.39	22.02	24.25
500°C	28.45	3.134	3.968	5.47	10.708	0.979	320.13	35.55	63.51

4.1.3. Morphological properties

The grains and grain boundaries are clearly visible for the films deposited at high substrate temperatures as evident form the Figure 4.2.

4.1.4. Optical properties

Optical properties of selected sample showed in Figure 4.3 and optical band gap as obtained from Tauc's plot is 1.57 eV which is close to the optimum band gap value of CZTS (1.5 eV).

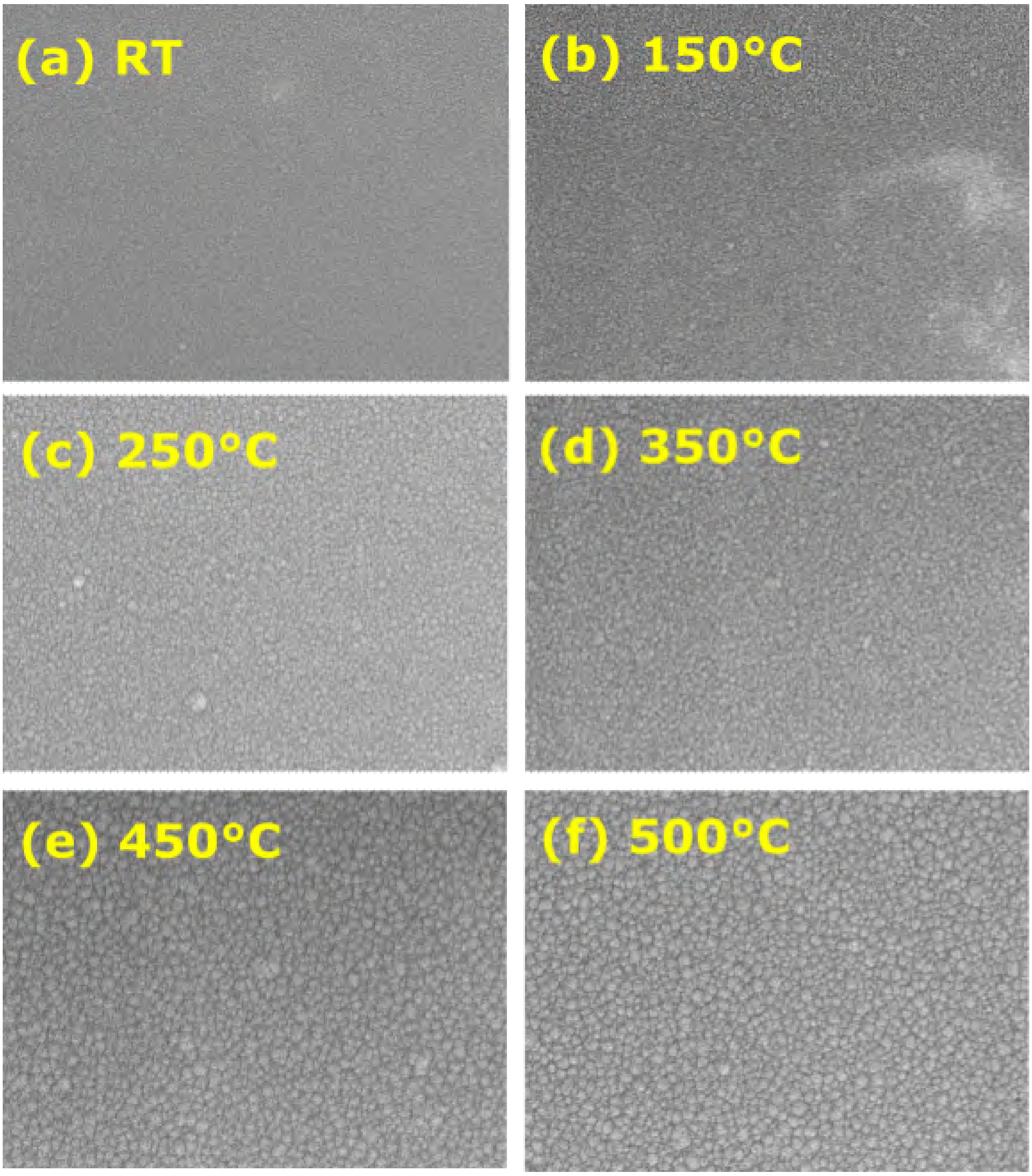

Figure 4.2: FESEM micrographs of CZTS thin-films at various substrate temperatures

4.1.5. Electrical properties

Electrical properties were performed for the sample deposited at 500°C using Hall measurements. The selected sample showed p-type conductivity with fair carrier concentrations and mobility suitable to use as an absorber layer, and tabulated in Table 4.3.

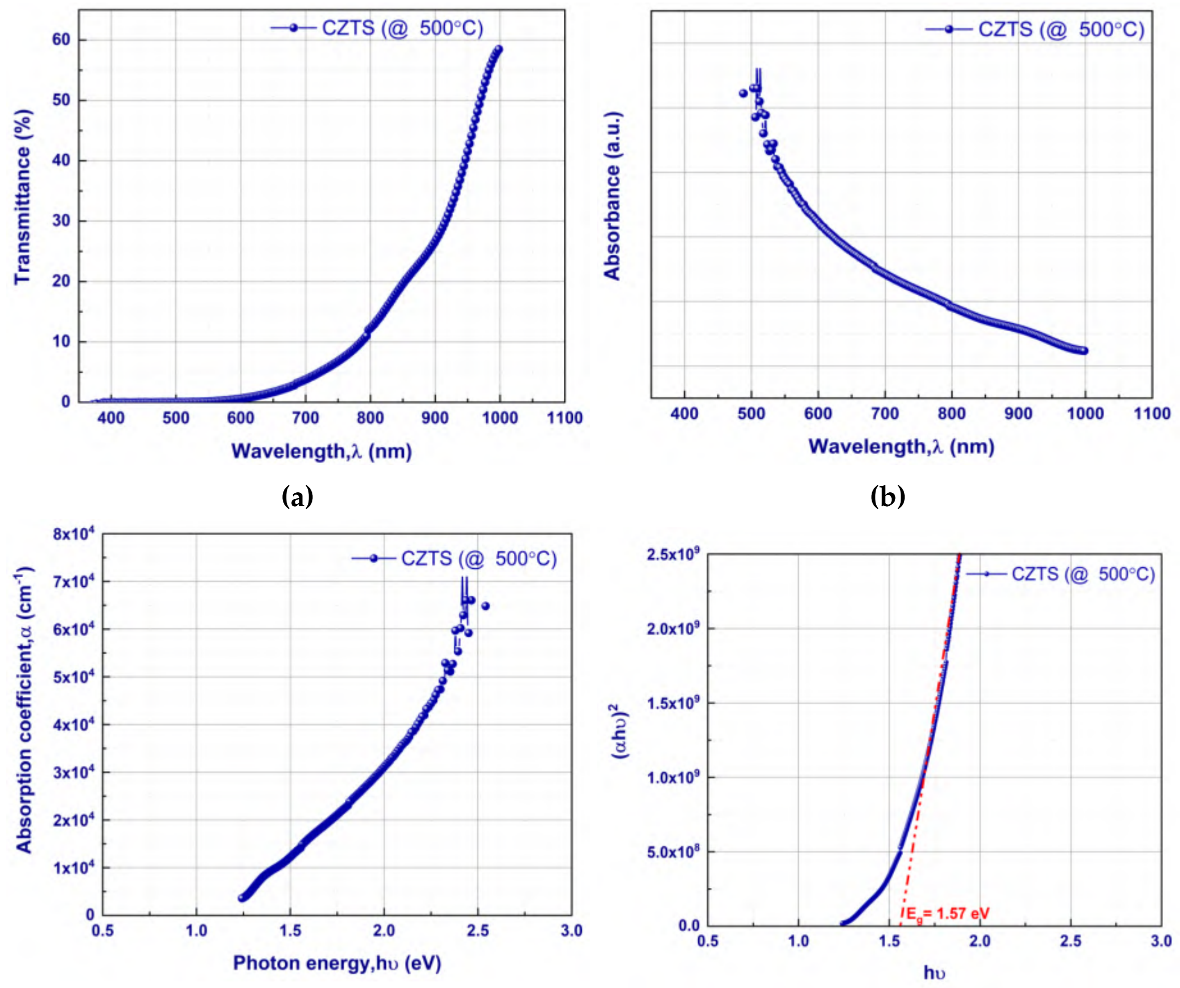

(a) (b) (c) (d)

Figure 4.3: Optical properties of CZTS thin-films at substrate temperature of 500°C: (a) transmittance, (b) absorbance, (c) absorption coefficient, and (d) Tauc's plot

Table 4.3: Electrical properties of CZTS thin-film deposited by RF magnetron sputtering

Properties	**Values at 500°C**
Carrier concentration (cm^{-3})	6.558×10^{19}
Carrier mobility (cm^{2}V^{-1}s^{-1})	6.210×10^{-2}
Resistivity (Ω.cm)	1.533
Average Hall coefficient (cm^3/C)	9.519×10^{-2}
Conductivity type	p

4.1.6. Photovoltaic properties

Two CZTS-TFSCs were fabricated with buffer layer (CdS) synthesize using two processes, sputtering and CBD. The open-circuit voltage (V_{oc}) value remains greater when the device is built using a cadmium sulfide (CdS) buffer layer formed through CBD compared to CdS deposited via sputtering, as seen in Table 4.4. This was the first CZTS-TFSC (substrate structured) fabricated in renewable energy laboratory, EEE, CUET as shown in Figure 4.4.

Table 4.4: Complete CZTS-TFSC with CdS buffer layer

CZTS-TFSC	V_{oc} (mV)
CdS buffer layer (sputtering)	272
CdS buffer layer (CBD)	350

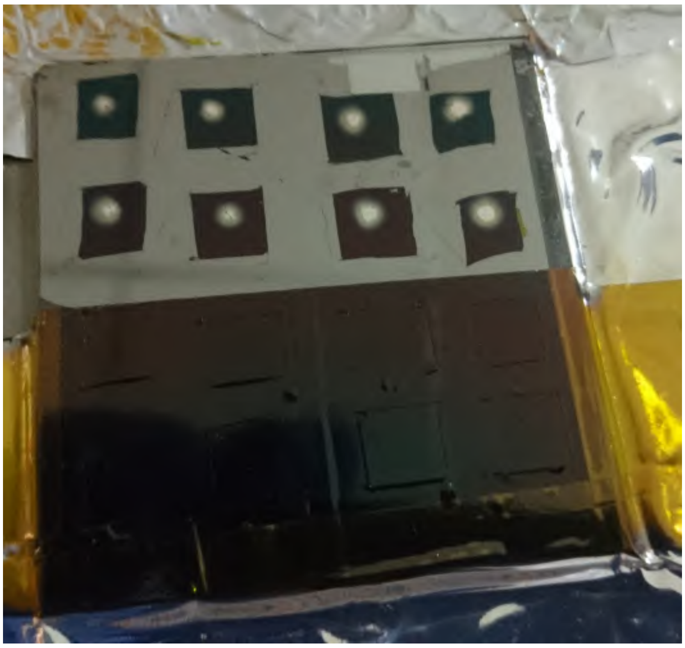

Figure 4.4: First CZTS-TFSC fabricated in renewable energy laboratory, EEE, CUET

4.2. Ge-alloyed CZTS thin films employing RF magnetron co-sputtering

4.2.1. Elemental composition ratio

The atomic percentages and elemental composition ratio of the constituents in the deposited thin films was calculated using EDS results, as shown in Table 4.5 and Table 4.6 respectively. All of the thin films fabricated had an off-stoichiometric Cu-poor, Zn-rich ratio, which is required for high efficiency CZTS thin film solar cells [3]. Ge ratio values (x=Ge/(Ge+Sn)) for Ge10 and Ge15 samples were found 0.38 and 0.51, respectively. Elemental Zn loss is noticeable in alloyed samples, as seen by diminishing Zn/(Ge+Sn) ratios as x increases. The atomic ratios of Cu/(Sn+Ge) are virtually the same in all sulfurized samples.

Table 4.5: Elemental atomic percentages of sulfurized CZTGS thin films

Sample	Cu (at%)	Zn (at%)	Sn (at%)	Ge (at%)	S (at%)
Ge00	22.00	15.94	21.63	0.00	50.94
Ge10	22.95	11.99	15.35	9.50	40.20
Ge15	27.13	11.53	13.64	14.26	36.90

Table 4.6: Elemental composition ratio of sulfurized CZTGS thin films

Sample	x=Ge/(Ge+Sn)	Cu/(Zn+Ge+Sn)	Zn/(Ge+Sn)	Cu/(Ge+Sn)	S/metal
Ge00	0.00	0.59	0.74	1.02	0.86
Ge10	0.38	0.62	0.48	0.92	0.67
Ge15	0.51	0.69	0.41	0.97	0.55

4.2.2. Structural properties

To assess the influence of Ge-alloying on the structural properties of CZTGS absorber, XRD and Raman characterization were performed.

The XRD pattern for the sulfurized CZTGS films (x=0, 0.38, 0.51) is given in Figure 4.5a. The major diffraction peak at the (112) plane is common in all sulfurized samples accompanied with weak peaks from the (220) and (312) planes . All of these observations are compatible with the kesterite structure indicated by JCPDS# 26 0575 [28, 216] . An expanded view of the peak shift around the principal diffraction plane (112) following Gauss fitting of the samples

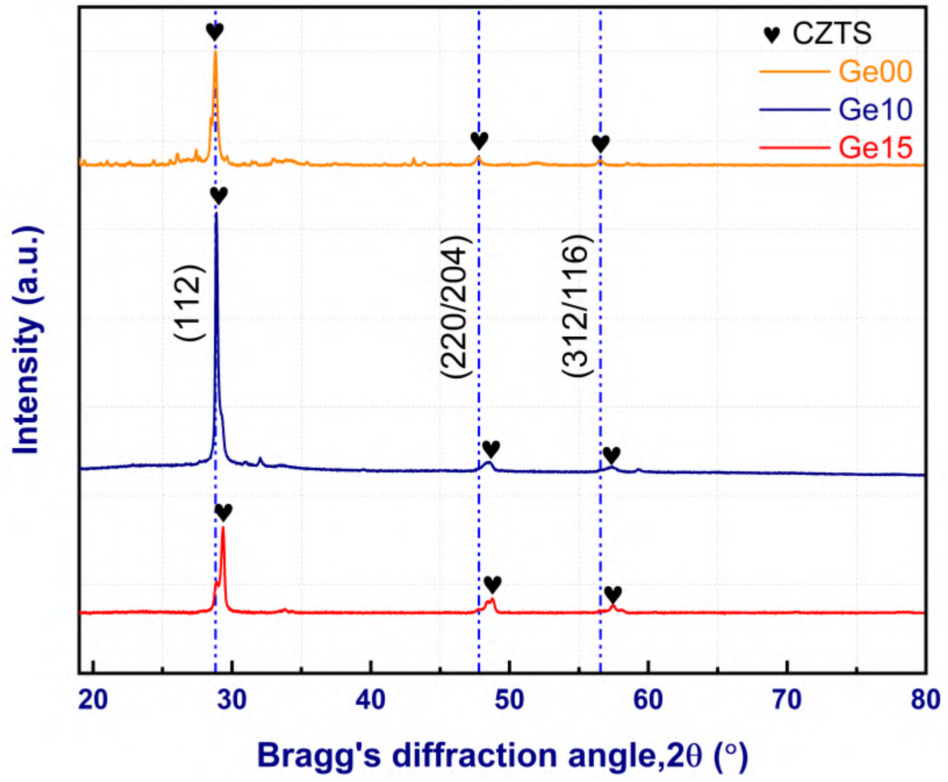
♥ CZTS
Ge00
Ge10
Ge15
(112)
(220/204)
(312/116)
Intensity (a.u.)
20
30
40
50
60
70
80
Bragg's diffraction angle,2θ (°)

(a)

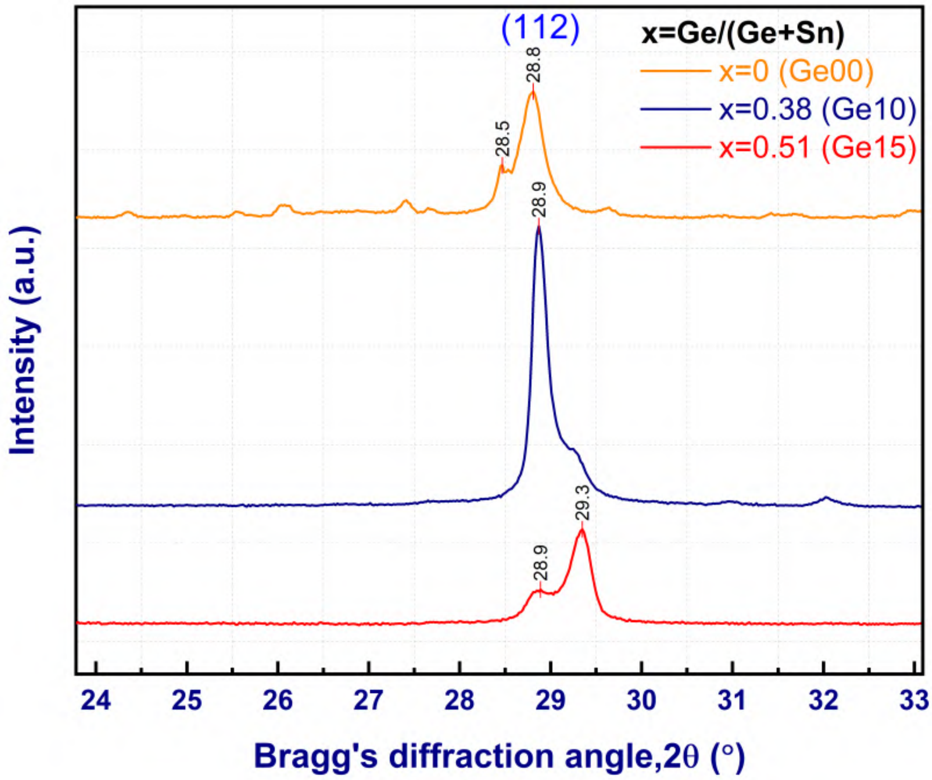
(112)
x=Ge/(Ge+Sn)
x=0 (Ge00)
x=0.38 (Ge10)
x=0.51 (Ge15)
28.8
28.5
28.9
29.3
28.9
Intensity (a.u.)
24
25
26
27
28
29
30
31
32
33
Bragg's diffraction angle,2θ (°)

(b)

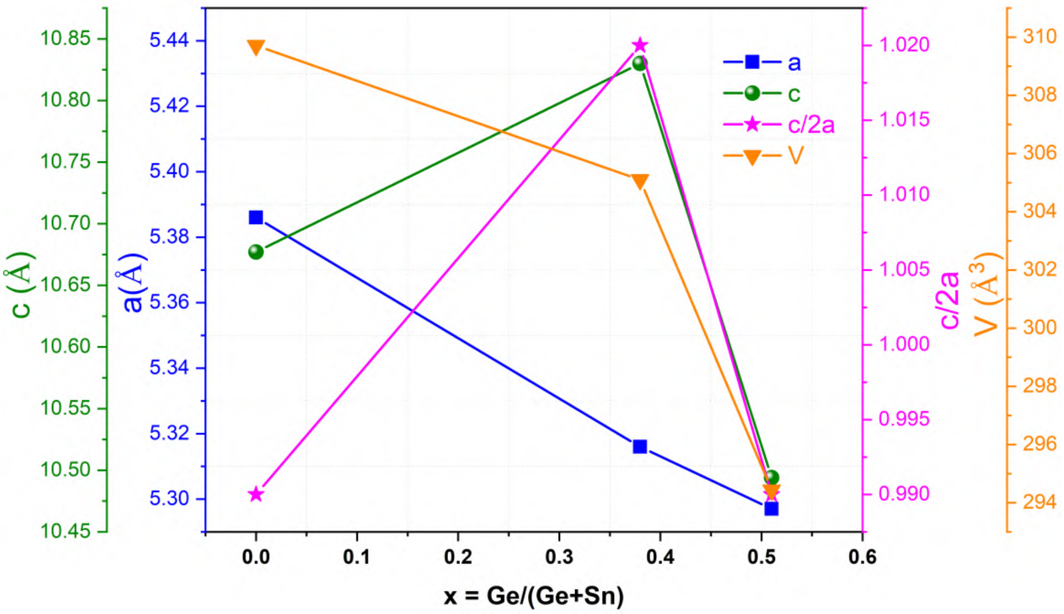

(c)

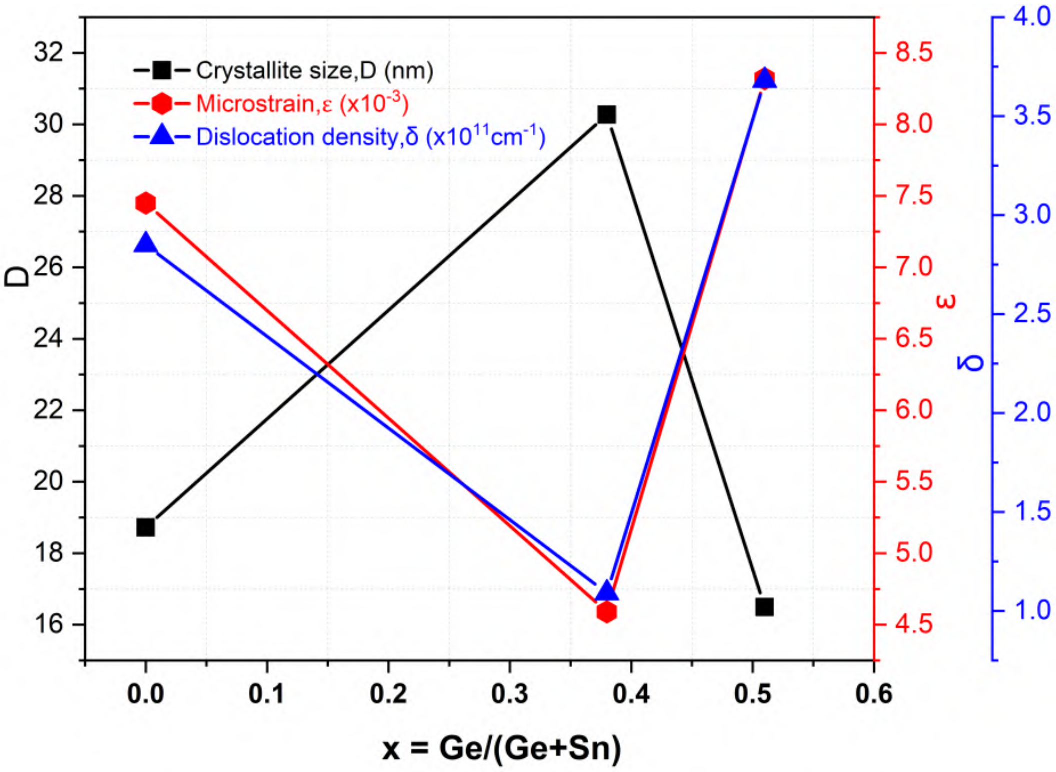

(d)

Figure 4.5: (a) XRD patterns, (b) Enlarged view of XRD patterns along the peak at (112) plane, (c) Variation of lattice constants with x, and (d) Variation of lattice parameters with x

under investigation is shown in Figure 4.5b. Small Ge atoms (ionic radius of 0.53 Å) replace large Sn atoms (ionic radius of 0.71 Å), leading XRD peaks to move to higher diffraction angles.

Moreover, the right shift of diffraction peaks is associated with decrease in interplanar distance, d indicates that the alloyed samples are subjected to compressive stress. As demonstrated in Table 4.8, the shrinkage of lattice constants (a,c) with a commensurate drop in unit cell volume supports this. Similar findings were reported in [115, 122]. The observed decrease in lattice constants with added Ge implies that the partial substitution of Ge ions for Sn ions without affecting the kesterite crystal structure. CZTGS alloys can have tetragonal kesterite or stannite crystal structures, as indicated by the c/2a ratio [119]. The ratio c/2a is less than one, indicating a kesterite type crystal structure. As c/2a is somewhat more than 1, we may predict the creation of stannite type crystal structure in Ge10 sample (Table 4.8). According to [47], a shoulder-like peak traced to the left hand side of the peak along (112) plane in Ge00 and Ge15 films (Figure 4.5b) might be attributable to a Cu_2S secondary phase connected to cation disordering. Figure 4.5c depicts the change of lattice constants with the inclusion of Ge in the films. It can be seen that XRD peak intensities change a lot depending on the active composition ratio of the Cu/(Zn+Ge+Sn) stoichiometry (Table 4.6). When this ratio is 0.62 for a Ge10 sample, the XRD peak intensity is the highest. It is a medicore value, XRD peak intensity decreases when this ratio is 0.59 for a Ge00 sample and 0.69 for a Ge15 sample. Using

Table 4.7: Crystallite sizes of post sulfurized CZTGS thin films at (112) plane

Sample	**x = Ge/(Ge+Sn)**	**$2\theta_{112}$ (°)**	**d_{112} (Å)**	**Crystallite size,D (nm)**
Ge00	0	28.77	3.10	18.72
Ge10	0.38	28.89	3.09	30.27
Ge15	0.51	29.27	3.05	16.49

Table 4.8: Lattice constants of post sulfurized CZTGS thin films at (112) plane

Sample	**Lattice constants (Å)**		**c/2a**	**V ($Å^3$)**	**ε ($\times 10^{-3}$)**	**δ ($\times 10^{11}$)**
	a	**c**				
Ge00	5.386	10.677	0.99	309.71	7.45	2.85
Ge10	5.316	10.830	1.02	305.10	4.59	1.09
Ge15	5.297	10.494	0.99	294.43	8.32	3.68

Scherrer's formula, the mean size of crystal (D), the microstrain (ε), and the dislocation density (δ) of the deposited films of the principal diffraction peak at (112) plane were determined as given by Eq. [4.1], Eq. [4.2], and Eq. [4.3] respectively.

The microstrain and dislocation density confirm the considerable deviation in the structural imperfections [215]. The variation of crystallite size, microstrain, and dislocation density with x is shown in Figure 4.5d. The Ge10 sample with low Ge concentrations shows the highest crystallite size and minimum values of microstrain and dislocation density of the other samples under investigation. The lower value of average crystallite size for Ge15 sample may be attributed to disturbance in the host crystal lattice, which suppresses the crystal growth, as supported by the work reported at [217]. On the other hand, the associated increase in crystallite size for Ge10 sample may be attributed to the lattice expansion, c caused by distortions around the dopant atoms as a result of the mismatch between ionic radii [217].

4.2.3. Raman analysis

There is a possibility that some secondary phases may occur in the same diffraction angle, resulting in an overlapped peak at the (112) plane [218]. However, XRD studies alone cannot confirm the presence of a secondary phase along with kesterite CZTS. Therefore, Raman spectroscopy with an excitation wavelength of 785 nm was utilized to identify possible secondary phases on the pristine and Ge-alloyed thin films, as shown in Figure 4.6.

The main Raman peak, which corresponds to the primary vibrational A1 symmetry mode of single-phase CZTS with a kesterite structure, occurs at 338 cm^{-1} [219] as shown in Figure 4.6a. This particular A1 phonon mode is connected to the vibration of sulfur atoms that are surrounded by atoms from other molecules. The Ge00 sample exhibits this primary CZTS peak, which is a sign that the film is crystalline in kesterite structure. A shoulder peaks at 369 cm^{-1}, 293 cm^{-1} correspond to the characteristic of kesterite structure at mode E/B-TO LO [220] are also detected in the Ge00 sample. This shoulder peak is detected at 376 cm^{-1} in the Ge10 sample (4.6b) and at 382 cm^{-1} in the Ge15 sample (4.6c), respectively.

The CZGS compound's A1 mode location at 357 cm^{-1} has been reported [221]. Thus, depending on Ge concentrations in the film, the Ge-alloyed sample's A1 mode has peak locations between 338 cm^{-1} and 357 cm^{-1}. A "blue shift" occurred when Germanium alloyed Ge10 and Ge15 samples' A1 mode primary Raman peak migrated to 341 cm^{-1} and 346 cm^{-1}, respectively. 38% Sn^{4+} ion replacement finds Ge10's A1 mode primary Raman peak at 341 cm^{-1}, while Ge15's peak is at 346 cm^{-1}. The A1 mode's frequency was unaffected by Ge.

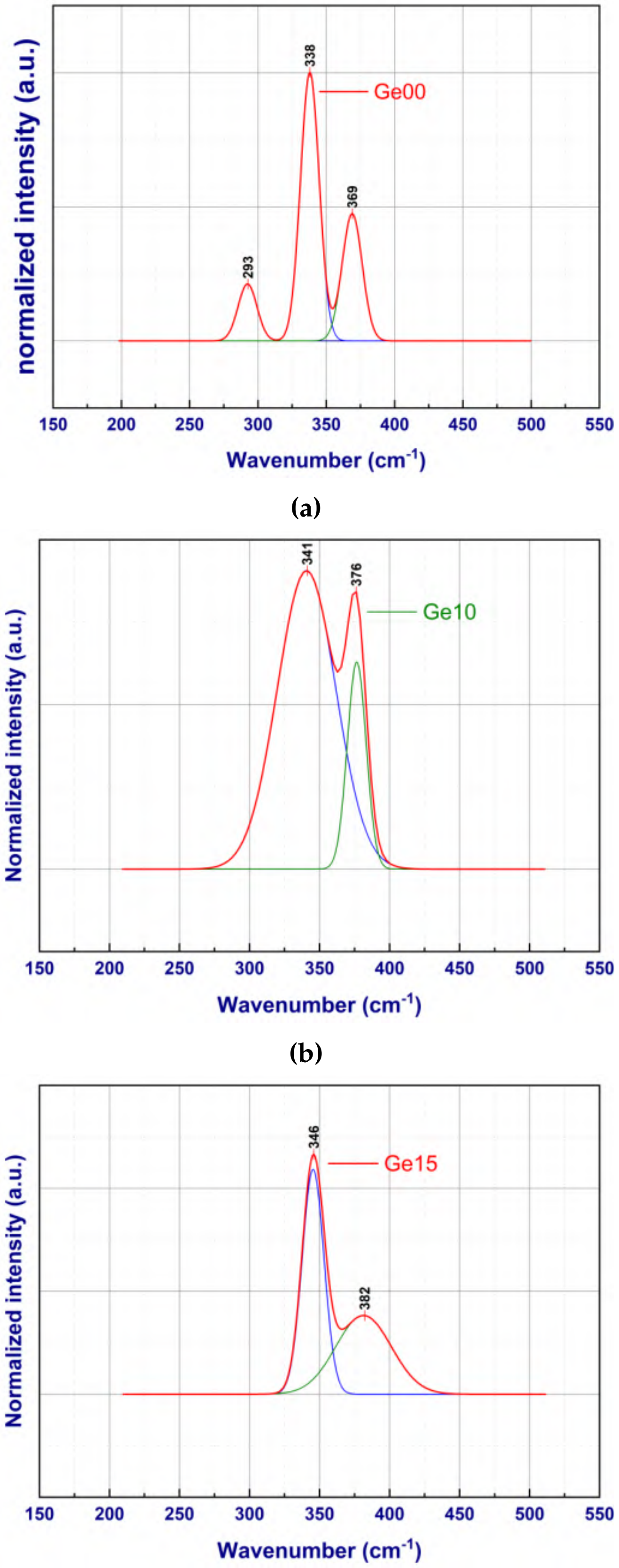

(a)

(b)

(c)

Figure 4.6: Raman spectra of CZTS and CZTGS thin films [λ_{ext} = 785 nm]

4.2.4. Morphological properties

The impact of alloying on the morphology and surface roughness of the films were investigated using FESEM and a 3D profilometer, respectively. SEM micrographs, and surface roughness of the deposited thin films are shown in Figure 4.7. For sulfurized CZTGS films, the grain size is the primary factor in establishing the level of surface roughness, which changes and improves as Ge concentration increases. Images of the surface roughness of CZTGS films are displayed on the right-hand side of Figure 4.7 for Ge10 and Ge15 samples, respectively. The surface textures of the Ge15 sample are among the roughest of the bunch. Grains with closely packed together were observed for Ge10 sample, which were not observed in the Ge15 or Ge00 samples. The reported variations in crystallite size are consistent with SEM findings.

According to the three-dimensional profilometry results (Table 4.9), both alloyed samples had lower Root Mean Square (RMS) heights, with the Ge10 sample having the lowest value,

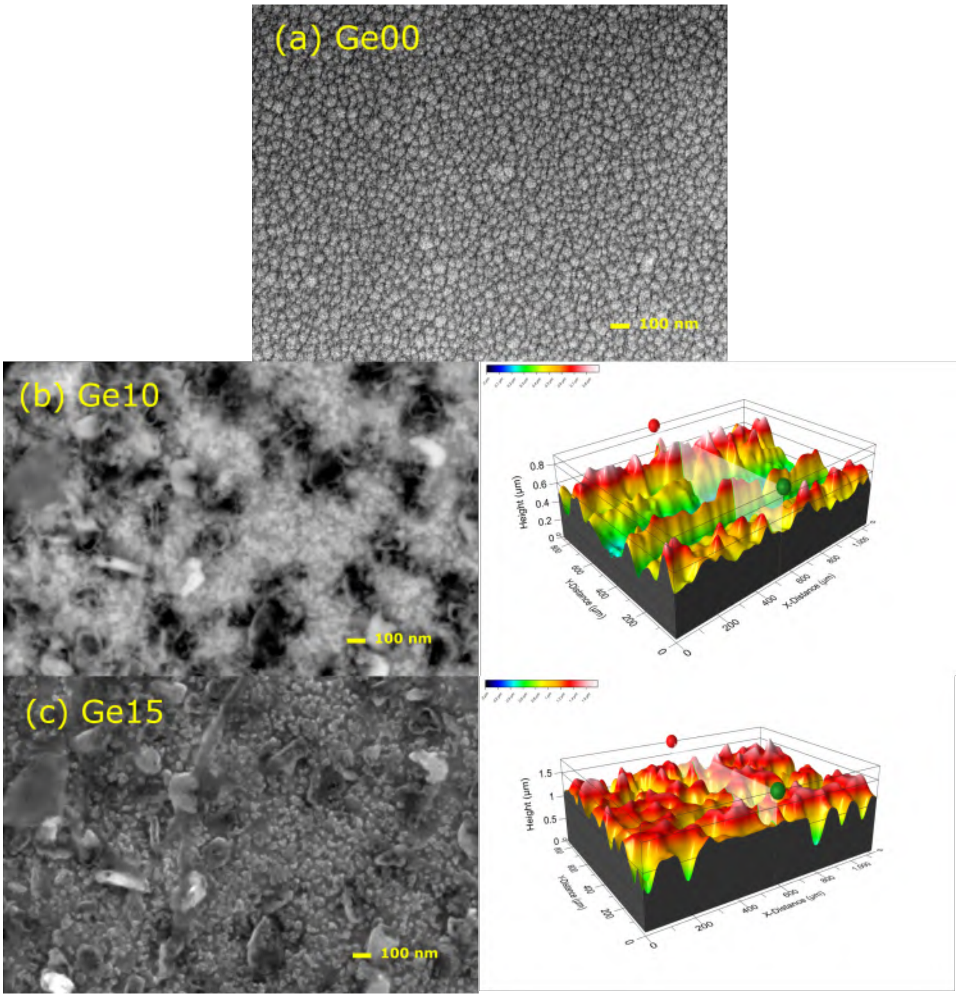

Figure 4.7: FESEM images with surface roughness: (a) Ge00 sample, (b) Ge10 sample, and (c) Ge15 sample

around 178 nm.

Table 4.9: Surface roughness data from 3D profilometry

Parameters[1]	**Ge10**	**Ge15**
S_p (Peak height, μm)	0.573	0.612
S_v (Valley height, μm)	0.323	1.005
S_t (Maximum peak to valley height, μm)	0.896	1.618
S_a (Arithmatic mean height, μm)	0.153	0.244
S_q (Root mean square height, μm)	0.178	0.298
S_{sk} (Skewness)	0.439	-0.822
S_{ku} (Kurtosis)	2.208	2.959

4.2.5. Optical properties

Figure 4.8 reveals the optical properties of CZTS and CZTGS thin films. Figure 4.8a shows the absorption coefficient as a function of wavelength of incident photon. The absorption coefficients are found to be on the order of 10^4 cm^{-1} for all of the samples. This supports the fact that the material experienced direct transitions from one state to another. From the visible spectrum range, it is clearly seen that the band edge shifts towards lower wavelengths or "blue shift" with the increase of Ge concentrations in the thin films. The results are in good agreement with the previously described Raman analysis. The optical absorption coefficient, α of a direct band gap semiconductor near the band edge, for photon energy, hν greater than the band gap energy, E_g of the semiconductor, is given by Tauc's relation [222], as in Eq. [4.4].

$$(\alpha h\nu)^{\gamma} = A\left(h\nu - E_g\right) \tag{4.4}$$

where, A is a constant, h is Planck's constant, and ν is the frequency of the incident photon, $\gamma = 2$ for direct allowed transitions. The Tauc's plots of $(\alpha h\nu)^2$ versus incident photon energy, $h\nu$ for the undoped and doped samples are plotted. Extrapolating the linear part of the Tauc's plot curves to intercept the energy axis at $(\alpha h\nu)^2 = 0$ yielded the band gap energy.

There was a report of a $Cu_2ZnSn_{1-x}Ge_xS_4$ compound with an optical band gap of 2.25 eV for x = 1 in [223]. So, it was expected that the optical band gap, E_g of the Ge-alloyed sample would be less than that of that value. In our study, the band gaps we calculated using Tauc's plot (Figure 4.8b) are 1.64 eV (x=0), 1.97 eV (x=0.38), and 2.12 eV (x=0.51). The high value of

---

[1] Area (Width= 564.4 μm; Height= 421.6 μm) roughness

the optical band gap for an unalloyed CZTS sample may be due to the presence of defect or trap states within the forbidden energy gap [224].

It is observed that the optical band gap values of alloyed samples Ge10 and Ge15 increased monotonically (Figure 4.8c) as a clear consequence of “blue shift ” of absorbance spectra as shown earlier. Another possible band edge shift towards lower wavelengths and hence higher band gaps may be attributed by corresponding change in crystallite sizes and associated FWHW and change in defect states [225]. Ge-alloy related secondary phases may also contribute to the “blue shift” of the optical absorption edge, resulting in a higher band gap [226].

Urbach energy, E_u plays a vital part in the process of discovering solutions to band tailing problems associated with structural disorder, phonons, excitons, and contaminants. Urbach’s tail refers to the absorption edge that is below the energy gap, which rises exponentially [227]. The E_u of deposited thin films was determined for each sample as illustrated in Figure 4.8d. E_u is explained within the context of Einstein’s model, and it is possible to condense it into an empirical formula presented by [228] and shown in Eq. [4.5].

$$\alpha = \alpha_0 \exp\left(\frac{h\nu}{E_u}\right) \tag{4.5}$$

The methods of determining the numerical values of E_u are also well detailed in the literature [229]. The Urbach energy of 124 meV was shown to be the lowest for x=0.38. Band tailing problems were observed to be significant for x=0.51 with high Ge concentrations in the films, which corresponds to E_u = 609 meV. Finally, it can be summarized as, using RF magnetron co-sputtering and subsequent sulfurization, polycrystalline CZTGS thin films were fabricated. The structural, morphological, and optical properties of the un-alloyed and Ge-alloyed CZTS thin films were evaluated, analyzed, and compared. XRD investigation revealed a linear reduction in lattice constants with increasing Ge concentration in alloyed thin films. This tendency was further corroborated by the blue-shifting of the A1 mode Raman peak when Ge was substituted in all alloyed films. A ratio of c/2a equal to 1.02 suggested the creation of a tetragonal stannite-type crystal structure at x = 0.38 in a film. EDS analysis showed that the off-stoichiometric "active composition ratio" soared in the doped samples, which is suitable for photovoltaic applications. The alloyed film with x = 0.38 exhibited better morphology, crystallite size, microstrain, and dislocation density. The band gaps of CZTGS films rose monotonically and virtually linearly with increasing Ge concentrations. The optical band gaps of 1.97 eV and 2.12 eV were found for Ge10 and Ge15 samples for x = 0.38 and x = 0.51 respectively. For the alloyed thin film with x = 0.51 and Urbach’s energy of 609 meV, a greater tail state absorption was found. So, in order to achieve perfect cation ordering in Ge-alloyed films, the Ge concentration needs to be optimized. This study contributes to better understanding the impact of Ge-alloying in CZTS crystal matrix on the different properties of CZTS thin films. Incorporated Ge thus modifies the optoelectronic band structure with a partial substitution of Sn-atom in the CZTS crystal matrix.

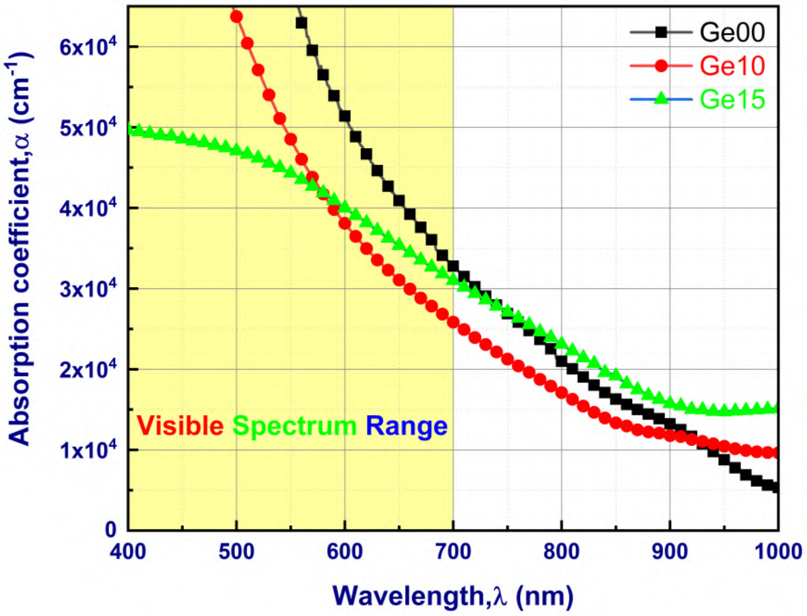

(a)

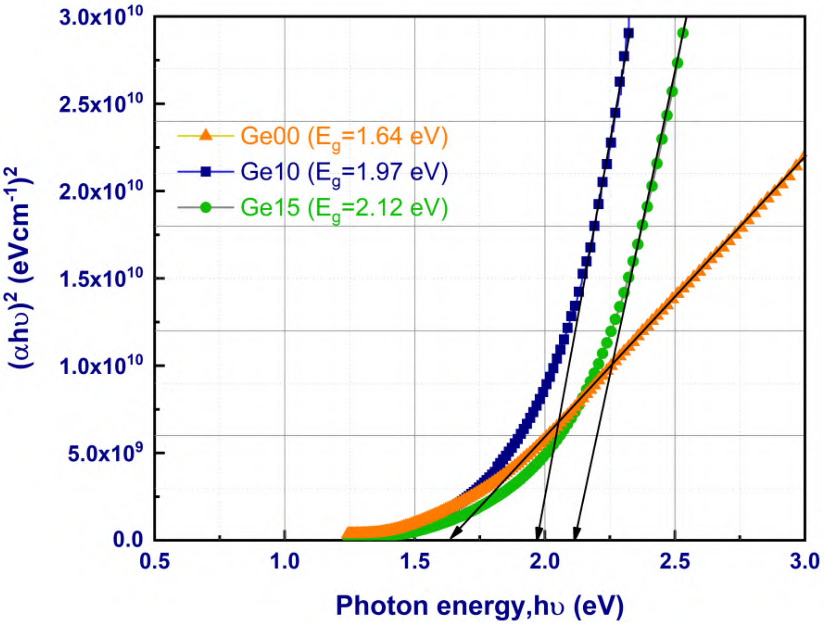

(b)

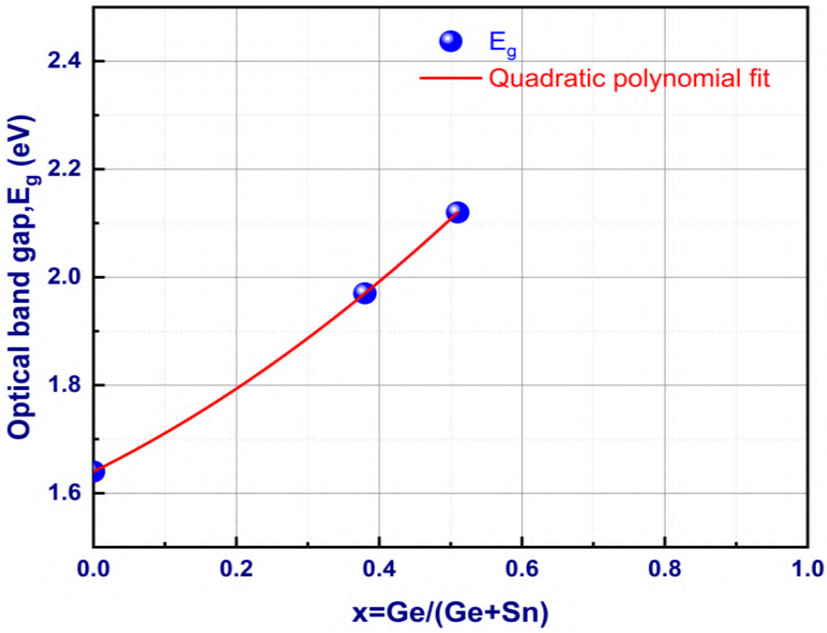

(c)

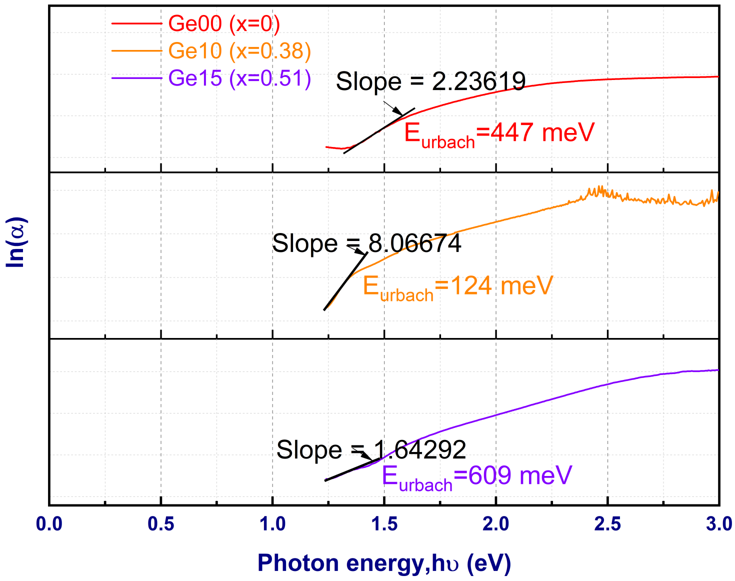

(d)

Figure 4.8: Optical properties CZTS and CZTGS thin films (a) Absorption coefficient, (b) Tauc's plot, (c) Variations of E_g with x=Ge/(Ge+Sn), and (d) Estimation of Urbach energy, E_u

4.3. Superstrate structured CZTS thin film solar cell: A co-doping approach

4.3.1. Effect of Cd and Mg doping separately

4.3.1.1. Structural properties

X-ray Diffractometry (XRD) and Raman characterization were carried out to evaluate the effect of dopants on the structural properties of CZTS absorbers.

The XRD patterns of sulfurized CZTS thin films that were produced from precursor solutions with undoped and doped contents are shown in Figure 4.9a. Although a dominant diffraction peak at the (112) plane is common in all the sulfurized samples, the C-Cd sample exhibits three crisp narrow and strong diffraction peaks from the (112), (220), and (312) planes. All are consistent with the kesterite structure (JCPDS# 26-0575) as reported in [211, 212]. At a Bragg's diffraction angle of 21.18°, orthorhombic SnS phase is detected in a C-Mg sample (JCPDS# 39 0354). Other polycrystalline CZTS phase characteristic peaks that correspond to JCPDS# 26-0575 are also indexed. Figure 4.9b shows an enlarged view of the peak shift around the main diffraction plane (112) after Gauss fitting of the samples under investigation.

The average crystallite size (D) using the Scherrer formula, the microstrain (ε), and the dislocation density (δ) of the deposited films of the principal diffraction peak at the (112) plane were determined as given by Eq. [4.1], Eq. [4.2], and Eq. [4.3] and shown in Table 4.11.

The Rietveld refinement method is a useful process for extracting crystal structure information from XRD data. Hence, Rietveld refinement was conducted on the XRD data for all of the samples (C-00, C-Cd, and C-Mg) that fell within the 2θ range. The refinement process

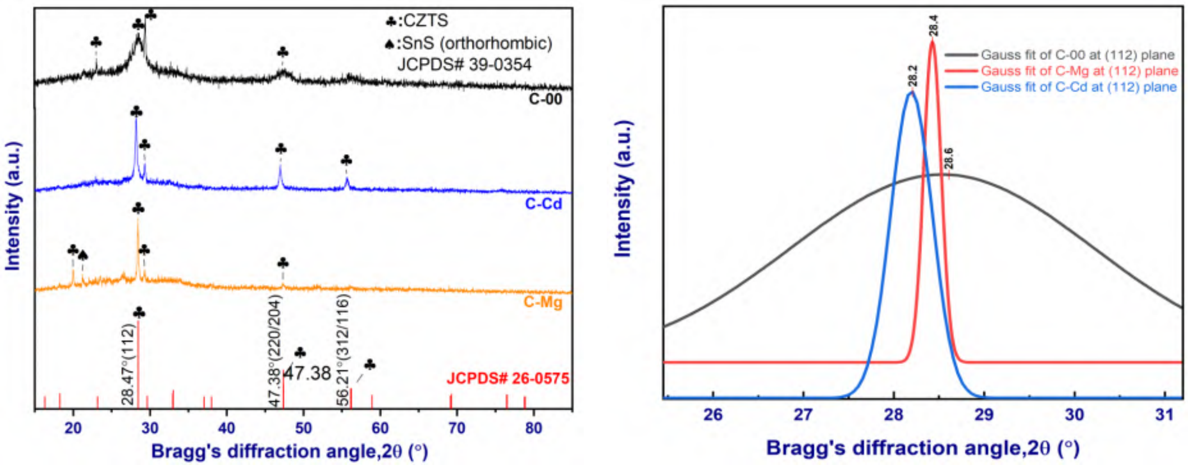

(a) **(b)**

Figure 4.9: (a) XRD patterns for undoped (C-00), Cd-doped (C-Cd), and Mg-doped (C-Mg) samples; (b) Enlarged view of XRD patterns along the main peak at (112) plane

was carried on until the optimal value for the goodness of fit (χ^2) could be determined. In this particular instance, the space group was determined to be I42m, and the peak shape function was decided upon as being pseudo voigt. The refined parameters can be found in Table 4.10.

Table 4.10: Rietveld refinement parameters with lattice constants

Sample code	χ^2	R_F (%)	a = b (Å)	c (Å)	c/2a	Volume (Å^3)
C-00	1.94	10.9	5.424	10.712	0.99	315.16
C-Cd	1.92	10.7	5.467	10.990	1.00	328.45
C-Mg	1.94	9.39	5.426	10.925	1.00	321.70

The refined data was used further to draw Maximum Entropy Method (MEM) map which is used in many analysis to get bonding nature and charge density [230, 231]. Obtained 3D MEM images are represented in Figure 4.10. Electron density has been reduced by the doping of Cd and Mg in the parent CZTS compound. All maps show clear the electrostatic attraction, repulsion by the convex, concave nature in the contours of electron density. Moreover, ionic nature of the constituent atomic bonding is also visible in the maps. The absence of residual charges represents the low level of noise for the data [232]. Furthermore, MEM explores the charge density aspects by investigating materials in multiple dimensions [233]. The crystal structures for all investigated samples are also formed and represented in Figure 4.11. In all cases, expected alternate layers of Sn-Zn-Sn and Zn-Sn-Zn are found. Ionic radius and bonding between different atoms can be seen clearly from these crystal structures. Hence, all structural information of the compound can be obtained through the analysis.

Improved crystallite sizes followed by corresponding improvements in microstrain and dislocation densities are found in doped cases, as shown in Table 4.11.

Table 4.11: Estimation of crystallite size (D), micro strain (ε) and, dislocation density (δ) from XRD data at preferred orientation plane at (112)

Sample code	**$2\theta_{112}$ (°)**	**d_{112} (Å)**	**FWHM (°)**	**D (nm)**	**ε ($\times 10^{-3}$)**	**δ ($\times 10^{11}$ cm^{-2})**
C-00	28.6	3.12	2.376	3.45	40.67	83.99
C-Cd	28.2	3.16	0.328	24.94	5.70	1.61
C-Mg	28.4	3.14	0.217	37.69	3.75	0.70

The main diffraction peak along the (112) plane occurs at $2\theta_{112}$=28.6° in the C-00 sample. The left shift of main diffraction peak at $2\theta_{112}$ = 28.2° for C-Cd sample and $2\theta_{112}$ = 28.4° for C-Mg sample with corresponding increase in interplanar spacing "d", indicates that both samples are subjected to tensile stress. Accordingly, cell volume also increased. This peak shift is due to the variation in the effective ionic radii of Cd^{2+}, Mg^{2+}, and Zn^{2+} ions [234]. When Cd

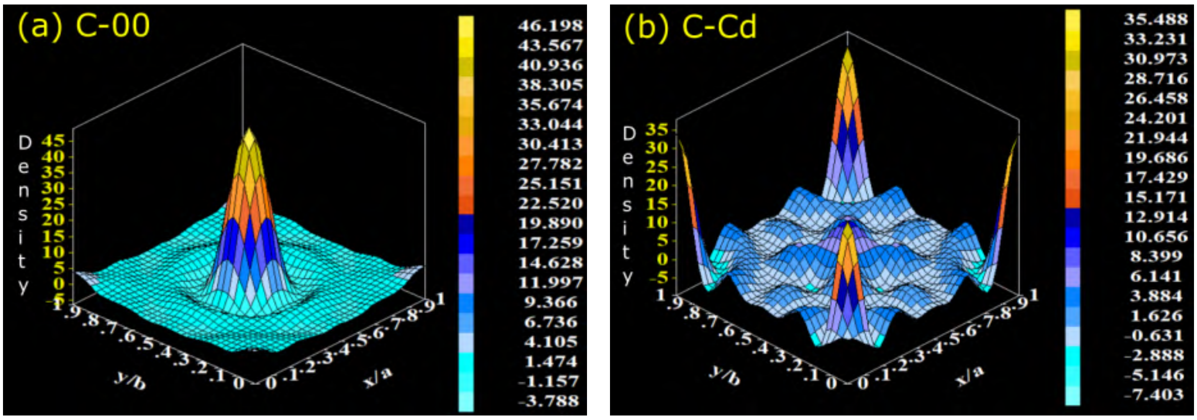

(a) C-00 **(b)** C-Cd

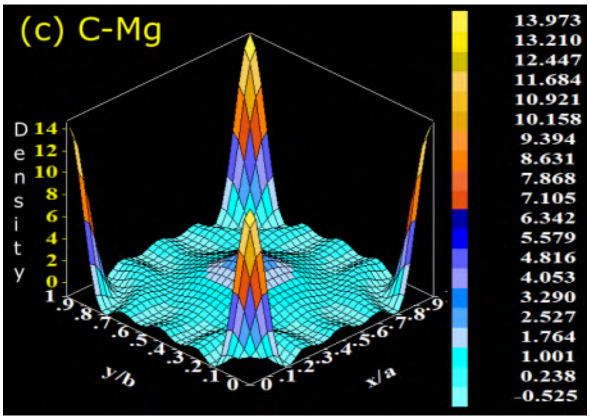

(c) C-Mg

Figure 4.10: MEM maps: (a) C-00, (b) C-Cd, and (c) C-Mg

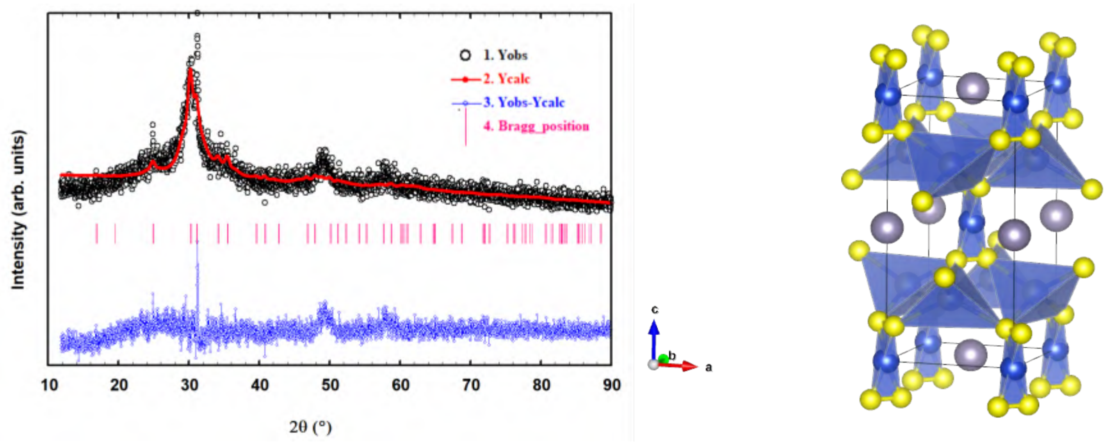

(a) C-00

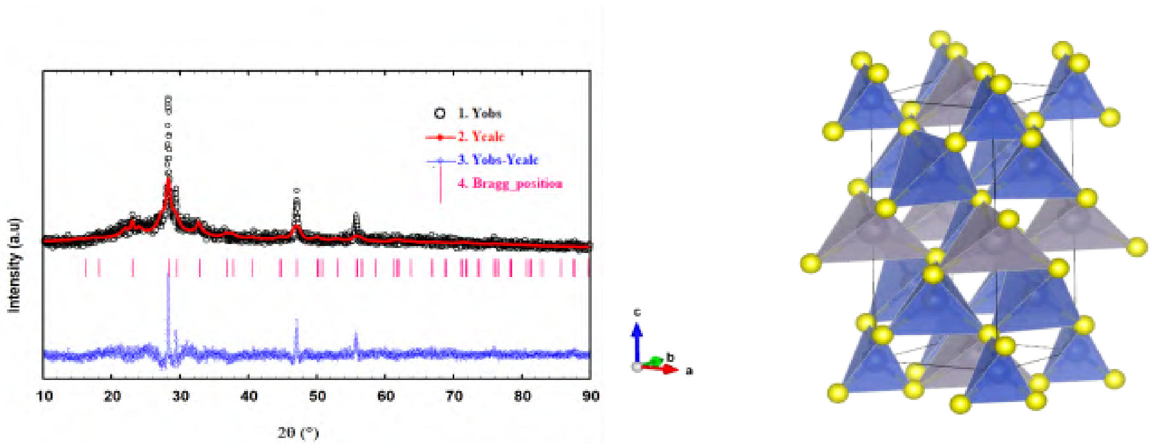

(b) C-Cd

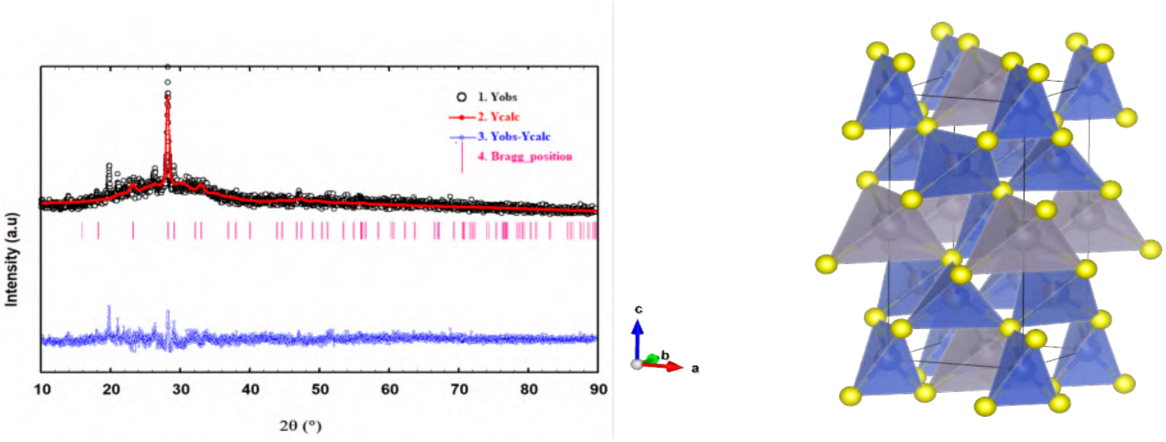

(c) C-Mg

Figure 4.11: Reitveld refinement with corresponding tetrahedral coordination of atoms: (a) C-00, (b) C-Cd, and (c) C-Mg

and Mg doped samples are compared to undoped samples, the lattice constants "a" and "c" clearly increase. The observed increase in lattice constant with dopants implies the substitution of Cd and Mg ions for Zn ions without affecting the kesterite structure. As $c/2a \leq 1$ for the doped samples, it confirms the persistence of kesterite crystal structure after doping [17]. The crystallite sizes behaved similarly. The hydrolysis reaction of the metal ions [211] could be one of the reasons for this increase in crystallite size of the doped CZTS, and the samples could have minor structural imperfections [235]. The associated increase in crystallite size may also be attributed to the lattice expansion caused by distortions around the dopant atoms as a result of the mismatch between ionic radii [217]. When comparing the average crystallite size of the C-Cd and C-Mg samples, the lower value for the C-Cd sample may be attributed to disturbance in the host crystal lattice, which suppresses crystal growth, as supported by the work reported at [217].

The microstrain and dislocation density confirm the considerable deviation in the structural imperfections [215]. In our study, the behavior of the dislocation density and the microstrain is not identical; rather, their behavior varies depending on the dopants and is minimally suffered by the Mg-doped sample. Deterioration of crystalline quality suggests the highest lattice dislocation levels in the undoped C-00 sample.

4.3.1.2. Raman analysis

There is a possibility that some secondary phases, such as tetragonal Cu_2SnS_3, will occur in the same diffraction angle, resulting in an overlapped peak at the (112) plane [218]. However, XRD studies alone cannot confirm the presence of a secondary phase along with kesterite CZTS. Therefore, Raman spectroscopy with an excitation wavelength of 785 nm was utilized to identify possible secondary phases on the undoped and doped CZTS thin films, as shown in Figure 4.12.

The main Raman peak, which corresponds to the primary vibrational A1 symmetry mode of single-phase CZTS with a kesterite structure, occurs at 338 cm^{-1} [219]. This particular A1 phonon mode is connected to the vibration of sulfur atoms that are surrounded by atoms from other molecules. However, the undoped C-00 sample does not exhibit this primary CZTS peak, which is a sign that the film is weakly crystalline. A shoulder peak at 376 cm^{-1} corresponds to the characteristic of kesterite structure at mode E/B-TO LO [236, 237] is also detected in the C-00 sample. This peak is detected at 368 cm^{-1} in the C-Cd sample and at 369 cm^{-1} in the C-Mg sample, respectively.

The Cu_2CdSnS_4 compound's A1 mode position at 326 cm^{-1} has previously been reported

[17]. In this sense, the A1 mode of the Cd-doped sample has peak positions between 338 cm^{-1} and 326 cm^{-1} depending on the Cd concentrations in the film. When doping a C-Cd sample, some of the Zn^{2+} ions are replaced by the larger Cd^{2+} ions. In our study, the A1 mode main Raman peak moved to a lower wavenumber at 334 cm^{-1} upon cadmium doping, which is called a "redshift," while subsequent increases in Cd concentration did not affect the frequency of the main A1 mode.

When 60% of the Zn^{2+} ions were replaced with Mg^{2+} ions, the redshift of the A1 mode peak was discovered to be at 333 cm^{-1} [149]. This shifting was discovered at 335 cm^{-1} for 5% Zn^{2+} ion replacement in another study [148]. In our investigation, magnesium doping with 45% Zn^{2+} ion replacement results in the detection of the A1 mode primary Raman signal at 339 cm^{-1}. It could be a possibility for lattice flaws to cause dislocations that alter the distribution of lattice constants [224]. According to Figure 4.9a, one of the distinctive kesterite peaks for the C-Mg sample is not present along the (312) plane, and a new characteristic peak is identified at 23.18°. Additionally, while lattice constant 'a' remains almost constant, the change in lattice constant 'c' impacts the rise in cell volume (Table 4.10).

In three samples, three Cu-Sn-S (CTS) related secondary phases with different crystal structures have been identified. Cubic Cu_2SnS_3 phase at 305 cm^{-1} [238] in C-00, tetragonal Cu_2SnS_3 phase at 296 cm^{-1} [239] in C-Cd, and orthorhombic Cu_3SnS_4 at 291 cm^{-1} [238, 240] in the C-Mg sample.

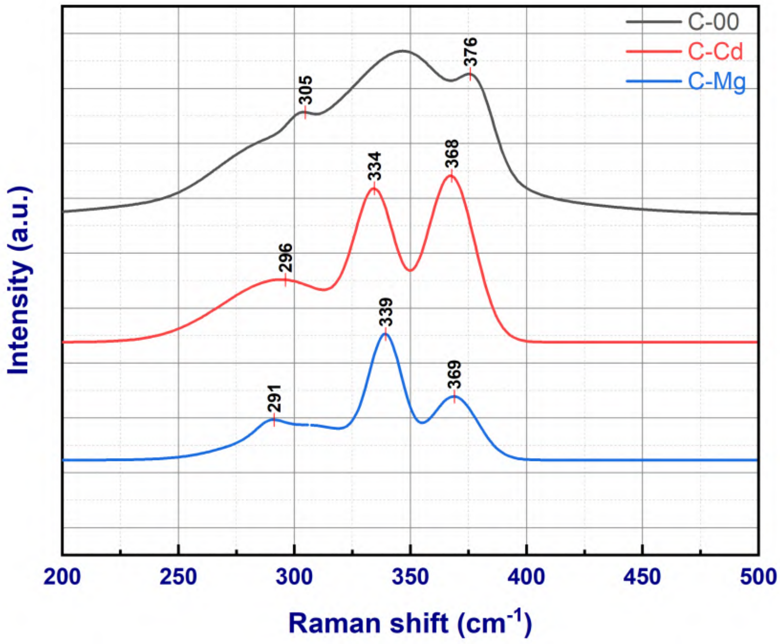

Figure 4.12: Raman spectra of sulfurized C-00, C-Cd, and C-Mg samples

4.3.1.3. *Morphological properties*

The impact of doping on the morphology and surface roughness of the films were investigated and probed by FESEM and 3D profilometry, respectively. SEM micrographs along with surface roughness of the deposited thin films are shown in Figure 4.13.

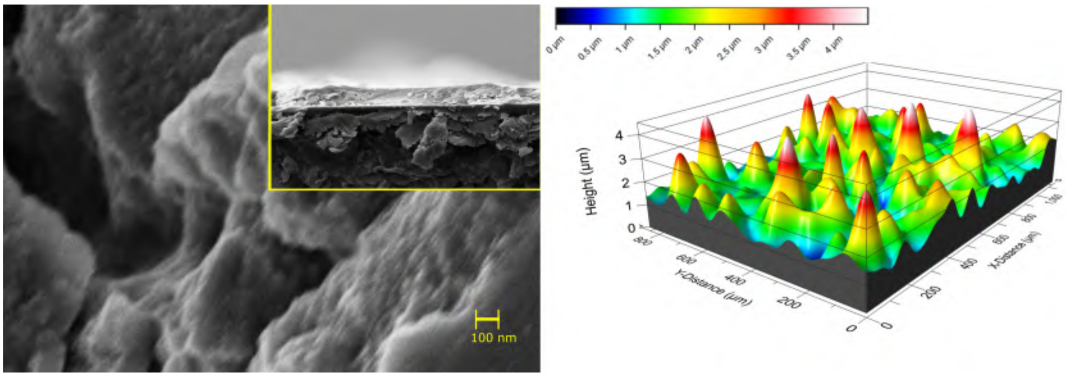

(a) C-00

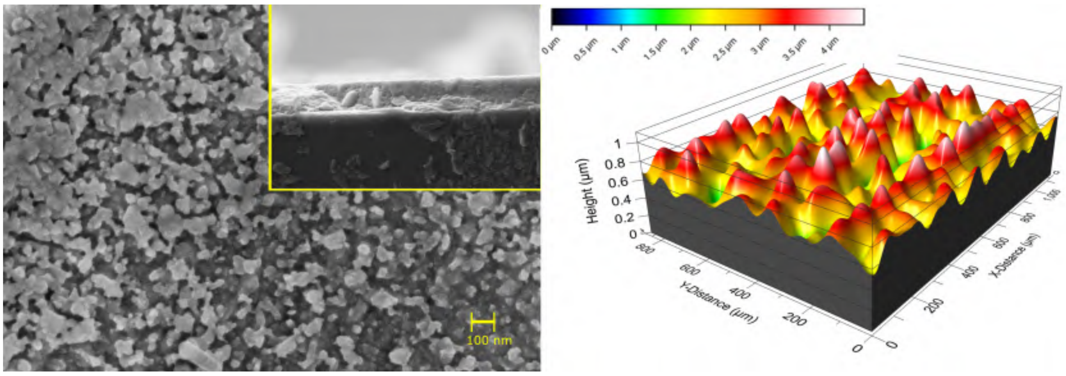

(b) C-Cd

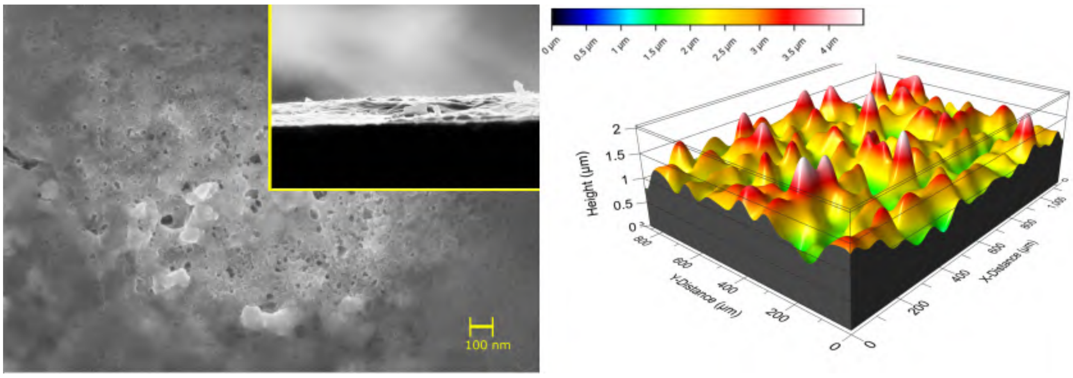

(c) C-Mg

Figure 4.13: Top-view of FESEM images (inset: cross-sectional) and 3D profilometric surface roughness of CZTS thin films: (a) C-00, (b) C-Cd, and (c) C-Mg

The scanning electron microscopy images showed that the Cd-doped sample had grains that were closely packed together, which were not observed in the Mg-doped or undoped samples. The reported variations in crystallite size are consistent with SEM findings.

Thin films with high crystalline quality are made by choosing the right chemical precursors, type of solvent, and other factors that control solution parameters like pH and viscosity [224]. The pH of all precursor solutions prepared for thin film fabrication using the sol-gel spin coating technique was about 5.5. The centipoise (cp) is a measurement unit for dynamic viscosity. For the sample C-00, C-Cd, and C-Mg solutions, the observed values for dynamic viscosity (room temperature= 28°C) were 22.6 cp, 22.0 cp, and 23.8 cp, respectively. As a result, the C-Mg sample was found to be more adherent to the SLG glass substrate, which was attributed to better crystallinity.

According to the three-dimensional profilometry results (Table 4.12), both doped samples had lower RMS heights than the undoped sample, with the Cd-doped sample having the lowest value, around 147 nm.

EDS was also utilized in conjunction with SEM analyses to estimate the elemental composition ratio of the elements in the deposited thin films. Figure 4.14 depicts the at% of the elements as determined by EDS measurements. The doping and elemental composition ratios of sulfurized samples as obtained by EDS are shown in Table 4.13. The off-stoichiometric Cu-poor, Zn-rich ratio was seen in all of the fabricated thin films. A similar observation was also reported in [3]. It appears that 45% of the zinc atoms in both the C-Cd ($CZn_{0.55}Cd_{0.45}TS$) and C-Mg ($CZn_{0.55}Cd_{0.45}TS$) samples are partially substituted by cadmium and magnesium atoms, respectively. Some of the Mg in sample C-00, which has not been doped, could come from the soda lime glass substrate.

It can be seen that XRD peak intensities change a lot depending on the active composition ratio of the Cu/(Zn+Cd+Mg+Sn) stoichiometry (Table 4.13). When this ratio is 0.89 for a C-Cd sample, the XRD peak intensity is the highest. It gradually decreases when this ratio is 0.78 for a C-Mg sample and 0.64 for a C-00 sample.

Taking into account the foregoing, we might conjecture as to what prompted the doped thin films' morphological change. Films created on a glass substrate were neither tightly packed nor homogeneous, despite the fact that Mg-doped samples were formed in a more crystalline manner than Cd-doped samples, resulting in marginally higher crystallite sizes. Mg-doped sample also had the highest RMS surface roughness as a result. In SEM images of the Mg-doped sample, the grain boundaries are challenging to figure out. Sn amounts on the surface, may influence the morphology changes when Cd and Mg dopants are introduced. When comparing the C-Cd and C-Mg samples, EDS and XPS reveal that the C-Cd sample has a more Sn-rich surface.

Table 4.12: Surface roughness data from 3D profilometry [Area (W = 564.4 μm; H = 421.6 μm)]

Parameters	**C-00 (μm)**	**C-Cd (μm)**	**C-Mg (μm)**
S_p (Peak height, μm)	2.885	0.392	0.939
S_v (Valley height, μm)	1.178	0.531	1.020
S_t (Maximum peak to valley height, μm)	4.063	0.923	1.960
S_a (Arithmatic mean height, μm)	0.455	0.116	0.215
S_q (Root mean square height, μm)	0.615	0.147	0.280

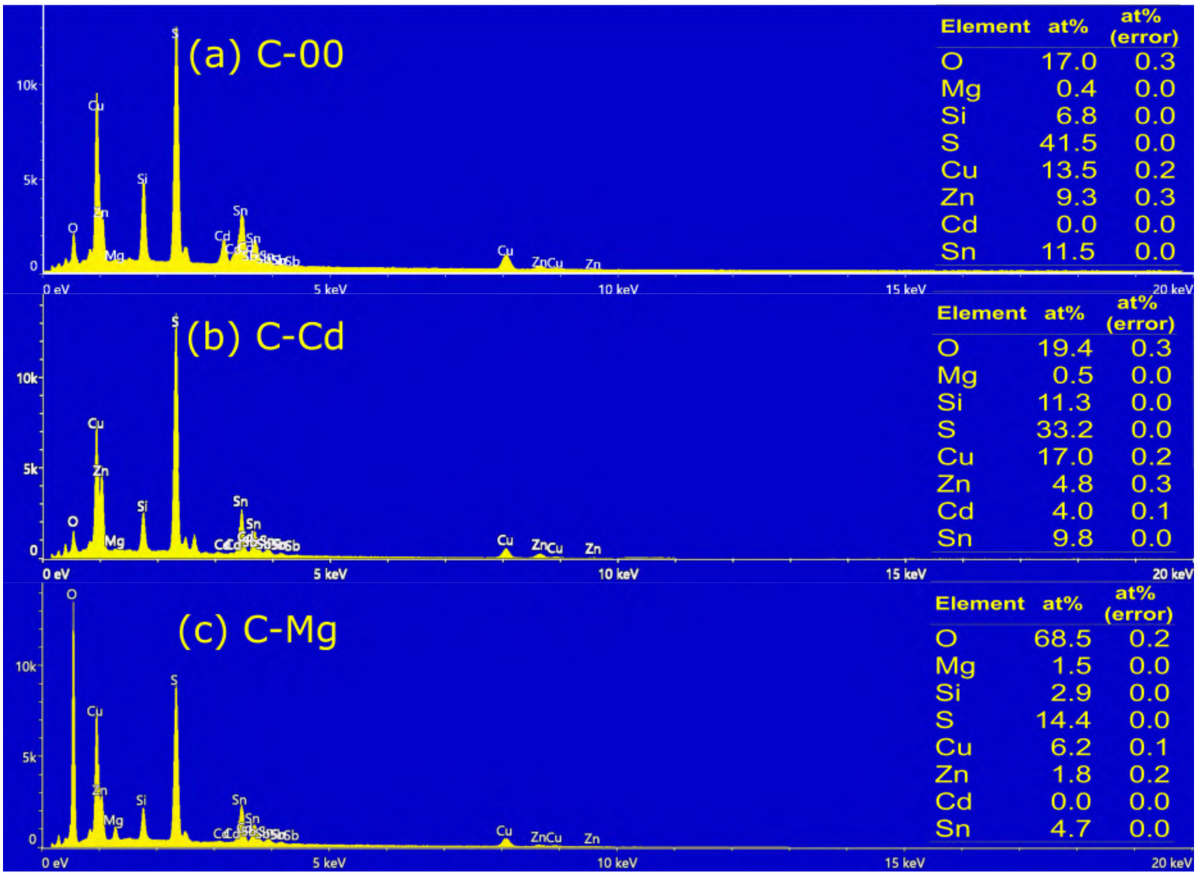

(a) C-00

Element	at%	at% (error)
O	17.0	0.3
Mg	0.4	0.0
Si	6.8	0.0
S	41.5	0.0
Cu	13.5	0.2
Zn	9.3	0.3
Cd	0.0	0.0
Sn	11.5	0.0

(b) C-Cd

Element	at%	at% (error)
O	19.4	0.3
Mg	0.5	0.0
Si	11.3	0.0
S	33.2	0.0
Cu	17.0	0.2
Zn	4.8	0.3
Cd	4.0	0.1
Sn	9.8	0.0

(c) C-Mg

Element	at%	at% (error)
O	68.5	0.2
Mg	1.5	0.0
Si	2.9	0.0
S	14.4	0.0
Cu	6.2	0.1
Zn	1.8	0.2
Cd	0.0	0.0
Sn	4.7	0.0

Figure 4.14: EDS spectrum of CZTS samples: (a) C-00, (b) C-Cd, and (c) C-Mg

Table 4.13: Doping and the elemental composition ratio of sulfurized samples probed by EDS

Sample code	Doping ratio		Active composition ratio		
	$Cu_2Zn_{1-x}Cd_xSnS_4$	$Cu_2Zn_{1-y}Mg_ySnS_4$			
	x = Cd/(Cd+Zn)	y = Mg/(Mg+Zn)	A	B	S/Metal
C-00	0.00	0.04	0.64	0.84	1.19
C-Cd	0.45	0.09	0.89	0.95	0.92
C-Mg	0.00	0.45	0.78	0.70	1.01

A = Cu/(Zn+Cd+Mg+Sn)
B = (Zn+Cd+Mg)/Sn

4.3.1.4. Optical properties

Before investigating the optical properties of fabricated thin films, the thickness of the samples was measured using cross-sectional FESEM images. The samples C-00, C-Cd, and C-Mg each had an average thickness of 2.075 μm, 0.724 μm, and 0.527 μm, respectively. The cross-sectional images are shown at Figure A.1 in Appendix A.

The absorbance spectra of the CZTS thin films were found and are shown in Figure 4.15a. Figure 4.15b and Figure 4.15c show the corresponding absorption coefficients and Tauc's plots.

The optical absorption coefficient, α of a direct band gap semiconductor near the band edge, for photon energy, $h\nu$ greater than the band gap energy, E_g of the semiconductor, is given by Tauc's relation [222], as in Eq. [4.4].

The absorption coefficients are found to be on the order of 10^4 cm^{-1} for all of the samples. This supports the fact that the material experienced direct transitions from one state to another.

There was a report of a Cu_2CdSnS_4 compound with an optical band gap of 1.38 eV in [223]. So, it was expected that the optical band gap, E$_g$ of the Cd-doped sample would be less than that of the undoped sample. The E$_g$ is estimated to be approximately 1.61 eV in the undoped sample, C-00. This higher value of the optical band gap for an undoped CZTS sample may be due to the presence of defect or trap states within the forbidden energy gap [224]. The band gap was found to fall to 1.56 eV after doping with cadmium.

On the other hand, the optical band gap value decreased even further to 1.01 eV for magnesium doping. Similar results were also reported in the previous studies [241, 242]. The following arguments can be used to explain why band gaps decreased after doping. Firstly, as shown in Figure 4.15a, the location of the absorption edge shifts toward higher wavelengths (redshift). As a result of this 'redshift', the band values of the doped thin films decreased from higher to lower energy values. This is most likely due to the increase in crystallite size [243] with a corresponding decrease in FWHW and decrease in the defect states [211, 225, 244, 245] of the C-Cd and C-Mg thin films. Secondly, the band gap energy may also alter owing to p-d hybridization between Cu d-levels and S p-levels along with the impurity phases present in the samples [6, 246]. Thirdly, the formation of donor levels below the conduction band [247], as well as the possibility of dopant-related secondary phases [226], may both contribute to the redshift of the optical absorption edge, resulting in a smaller band gap.

In addition, the segregation of the host (undoped) atoms besides the grain boundaries can reduce the E_g of doped thin films [248] which is supported by SEM micrographs (Figure 4.13). Figure 4.15a shows that the absorbance of the C-Cd sample is higher than that of the C-Mg sample. We have already seen that the crystallite size of a C-Cd film is smaller than that of a C-Mg film. Doping increased the optical absorbance because decreasing the size of crystallites can lead to an increase in their specific surface area [243].

Urbach energy, E_u plays a vital part in the process of discovering solutions to band tailing problems associated with structural disorder, phonons, excitons, and contaminants [249]. Urbach's tail refers to the absorption edge that is below the energy gap, which rises exponentially [227]. The E_u of deposited thin films was determined for each sample as illustrated in Figure 4.16. The Urbach energy is explained within the context of Einstein's model, and it is possible to condense it into an empirical formula presented by [228] and shown in Eq. [4.5].

The Urbach energies of undoped, cadmium doped, and magnesium doped samples were determined from Figure 4.16a-Figure 4.16c. In this study, significant band tailing problems were observed for the Mg-doped sample (E_u= 1072 meV). Cd-doped sample suffers less band tailing issues with a minimum E_u , 284 meV. These values are consistent with the other characterization results acquired in our experiments. A plot of the variation of optical band gaps as obtained for sulfurized samples (C-00, C-Cd, and C-Mg) with respect to their Urbach energies is shown in Figure 4.15d.

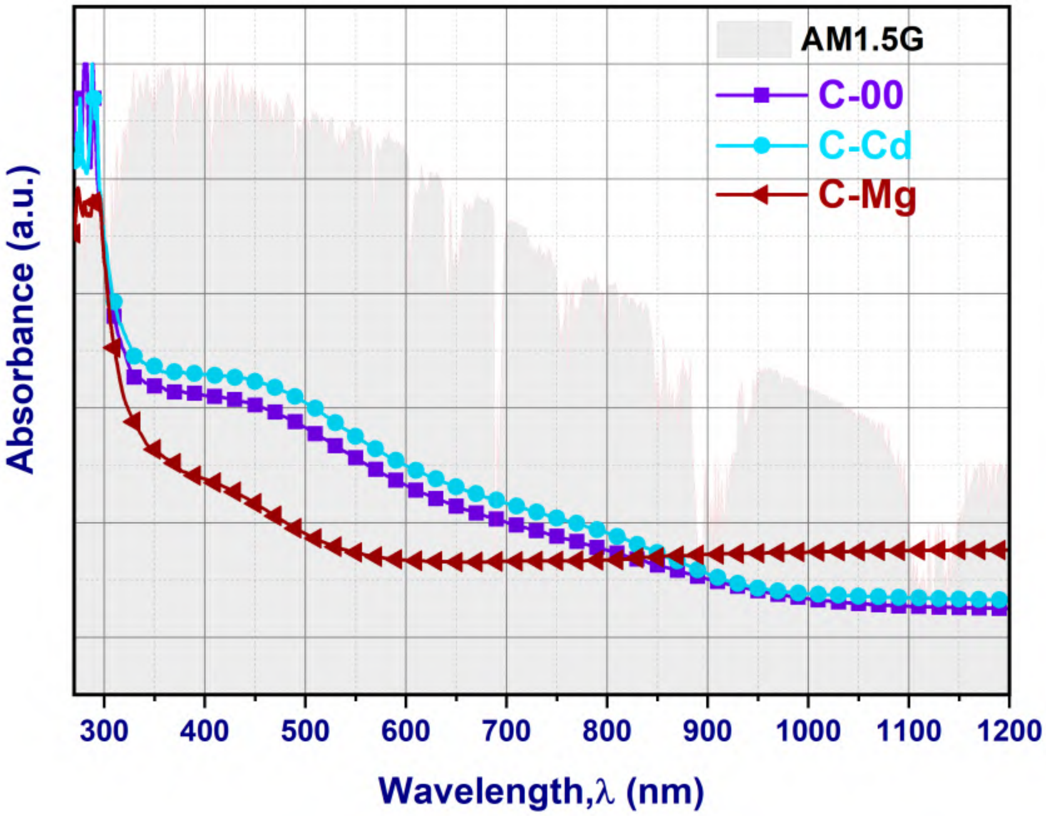
AM1.5G
C-00
C-Cd
C-Mg
Absorbance (a.u.)
300
400
500
600
700
800
900
1000
1100
1200
Wavelength,λ (nm)

(a)

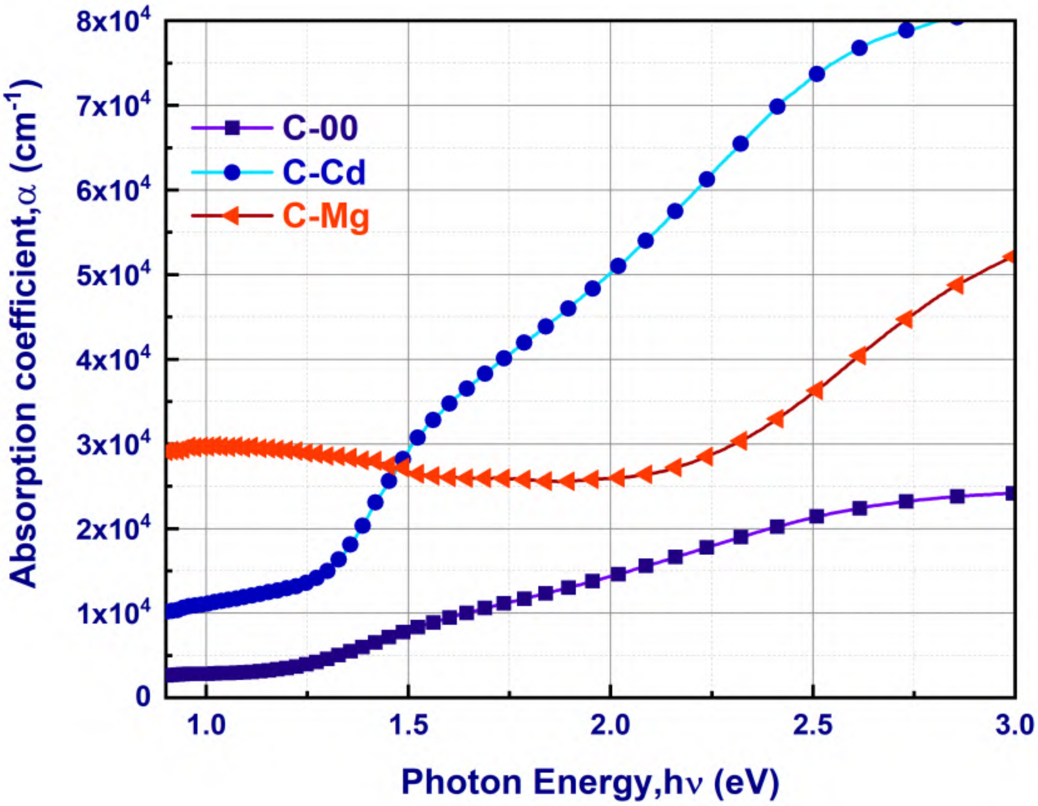
C-00
C-Cd
C-Mg
Absorption coefficient,α (cm-1)
8x10⁴
7x10⁴
6x10⁴
5x10⁴
4x10⁴
3x10⁴
2x10⁴
1x10⁴
0
1.0
1.5
2.0
2.5
3.0
Photon Energy,hν (eV)

(b)

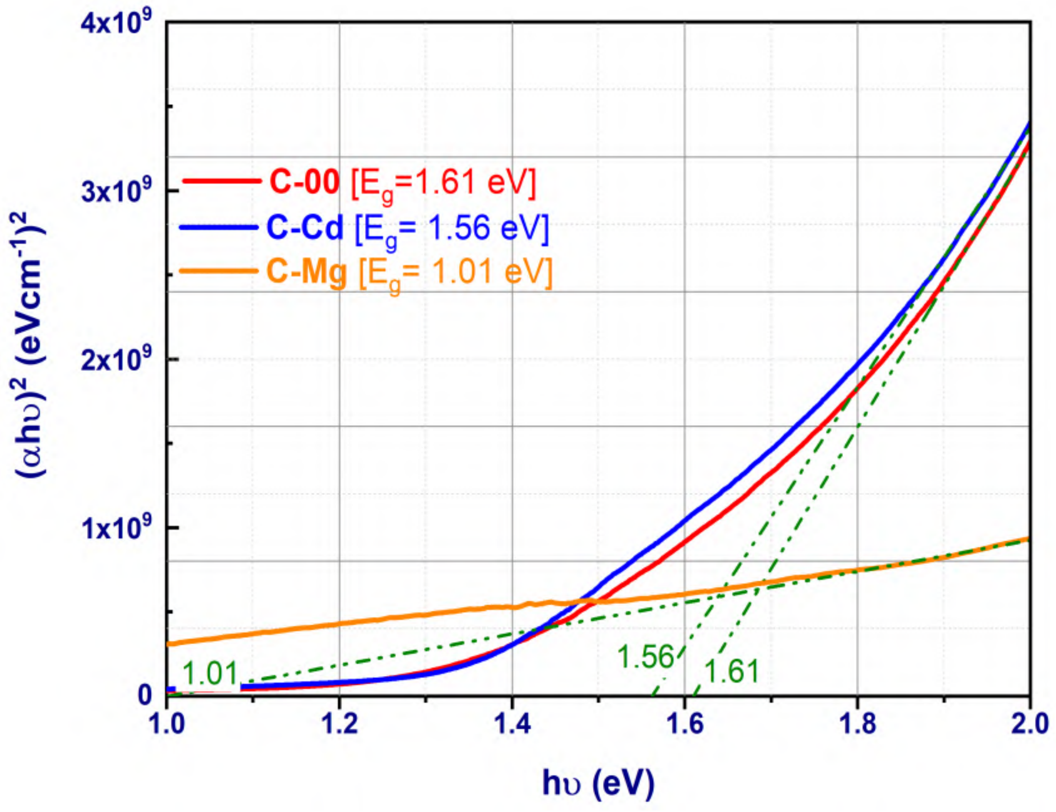

(c)

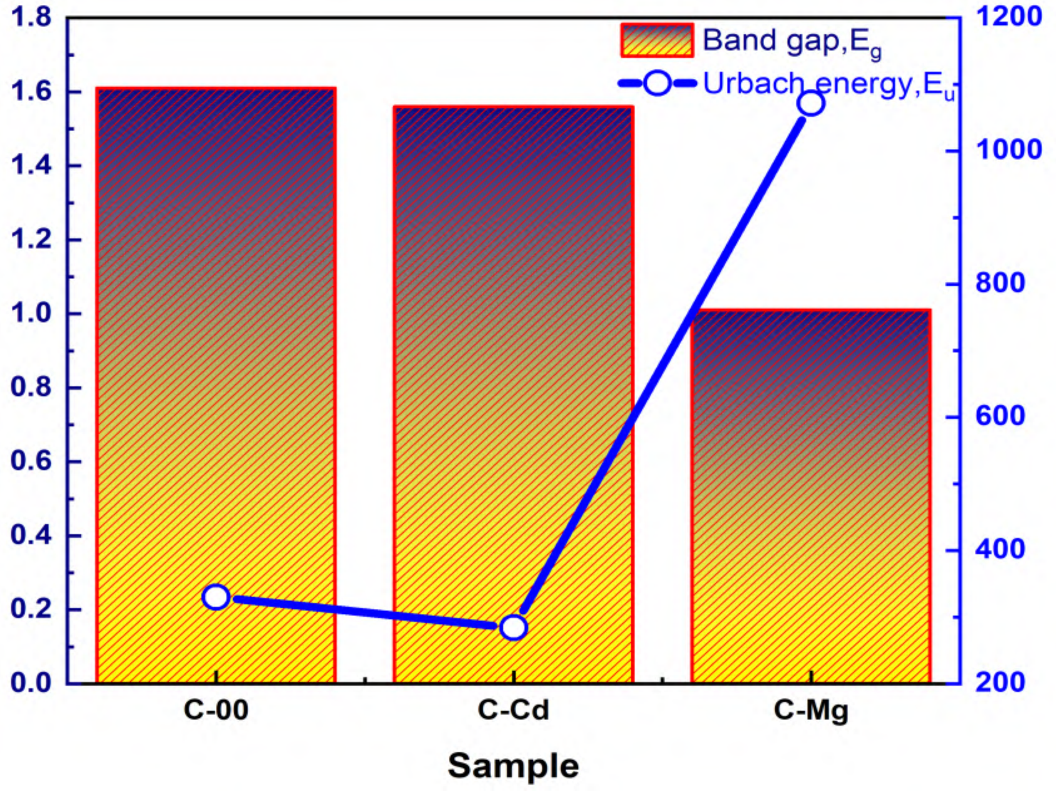

(d)

Figure 4.15: Optical properties CZTS thin films for undoped and doped samples: (a) absorbance spectra, (b) α vs hν, (c) Tauc's plots, and (d) variations of E_g with E_u

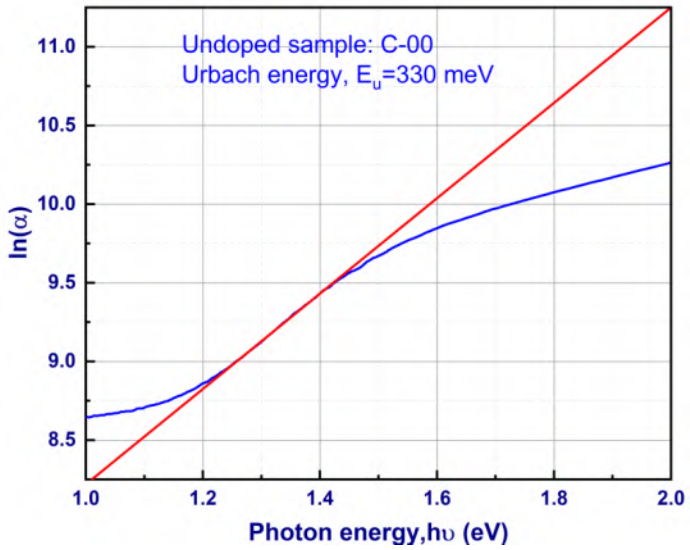

(a) C-00

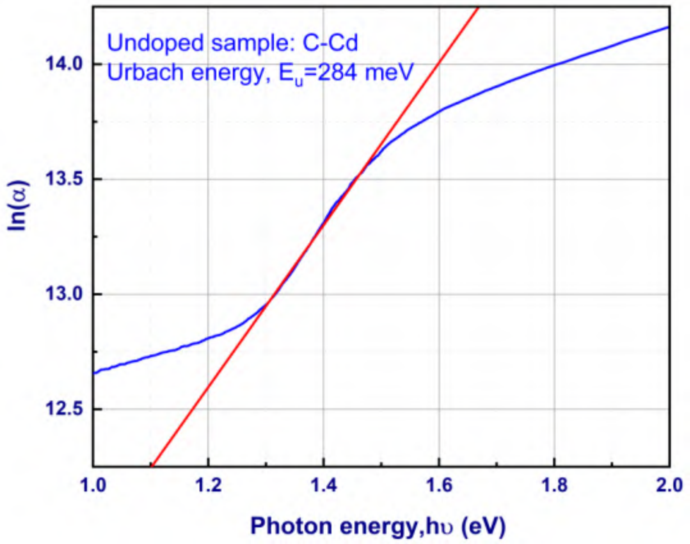

(b) C-Cd

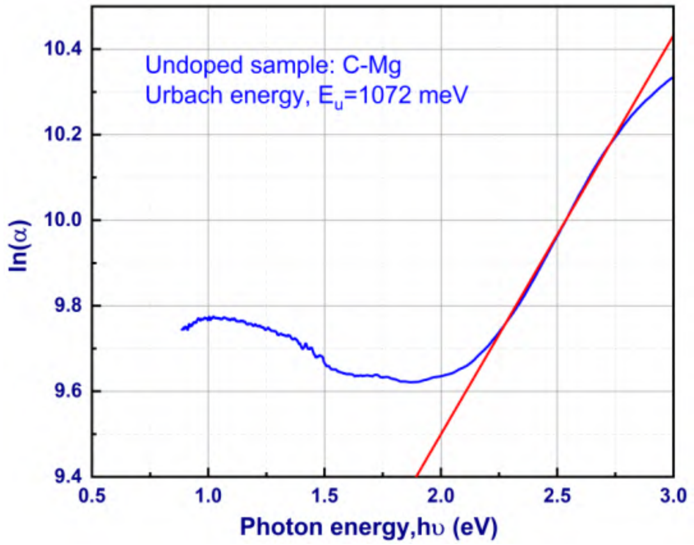

(c) C-Mg

Figure 4.16: Determination of Urbach energy for undoped, Cd-doped, and Mg-doped samples

4.3.1.5. XPS analysis: Chemical bonding and oxidation states

The XPS analysis was performed to find the chemical bonding states in the doped thin film samples. Typical XPS wide-scan survey spectra of C-Cd and C-Mg samples are shown in Figure 4.17a and Figure 4.17b, respectively. The primary peaks of Cu, Zn, Sn, S, Cd, Mg, and O, as well as the secondary photoelectron emission (Augur lines) lines of these elements, were all found to be present and identified. The oxidation states of the component elements were determined by measuring spectra with a high resolution of the elements Cu 2p, Zn 2p, Sn 3d, and S 2p, as well as O 1s (Figure 4.17c-Figure 4.17f, Figure 4.17i). In the Cu 2p spectrum, there were two peaks that appeared at the binding energies of 930.82 eV and 949.51 eV for the C-Cd sample, with a peak splitting energy of 18.69 eV. Furthermore, some satellite peaks were discovered at the higher binding energy position. This indicates that the sample contains more than just Cu(I). On the other hand, the Cu 2p spectrum can be seen for the C-Mg sample when the binding energy is between 931.7 eV and 951.5 eV, and the peak splitting energy is 19.8 eV. In addition, there were several satellite peaks. When compared to C-Cd, the intensity of Cu 2p in C-Mg is much greater. This observation suggests that the surface contains a comparatively larger concentration of Cu. Zn 2p is responsible for the peaks that appear at binding energies of around 1020.10 eV and 1043.31 eV in each of the samples, with a peak separation of 23.20 eV that corresponds to Zn (II). Both samples show Sn(IV) 3D peaks with nearly identical peak splitting energies of 8.4 eV [143]. For the C-Cd sample, which has a more Sn-rich surface than the C-Mg sample, the Sn (IV) 3d peaks are located at 486.25 eV and 494.65 eV. The shifting of Sn(IV) 3d peaks was found at lower binding energy for the CZTSSe sample [250]. However, in this study, the peaks of the Sn 3d core levels shifted towards a higher energy when some satellite peaks appeared in the C-Mg sample. This is in contrast to the shifting that occurred at a higher energy for the C-Mg sample. The peaks of S 2p that arise at binding energies of 161.36 eV and 163.55 eV for the C-Cd sample have matching peak separations of 2.19 eV. This observation indicates that sulfur is present in the sulfide (-II) form. In the case of the C-Mg sample, there is an indication of the existence of the sulfur as sulphate (-II) state in the form of a single peak of S 2p at 168.9 eV. The fact that the intensity of O 1s in C-Mg is higher than that of C-Cd, as shown in Figure 4.17i, implies that there is oxygen contamination on the surface. The presence of cadmium is demonstrated by the appearance of two peaks in the Cd 3d spectra (Figure 4.17g), which are located at the binding energies of 405.51 eV and 412.41 eV for the C-Cd sample. The peak splitting energy is 6.9 eV. A peak in the Mg 2p spectra (shown in Figure 4.17h) that appears at a binding energy of 49.39 eV confirms Mg in C-Mg sample.

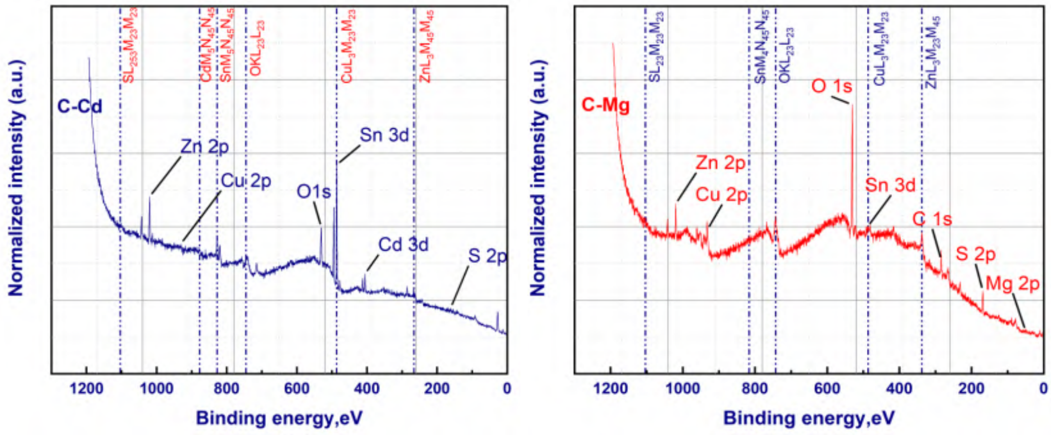

(a) Survey spectra: C-Cd **(b)** Survey spectra: C-Mg

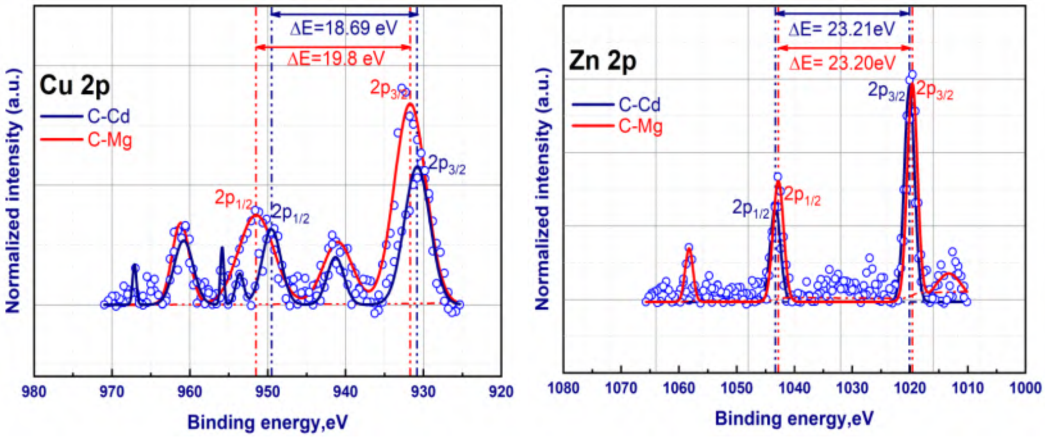

(c) Cu 2p core level spectra **(d)** Zn 2p core level spectra

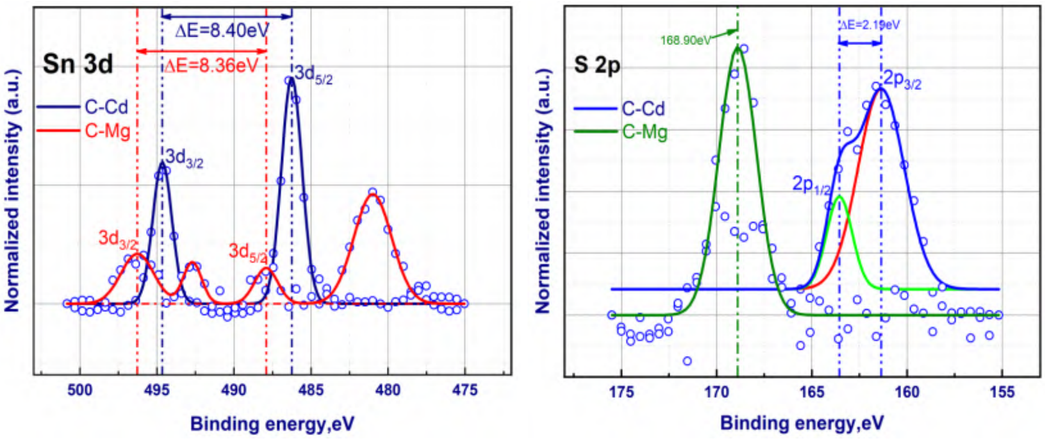

(e) Sn 3d core level spectra **(f)** S 2p core level spectra

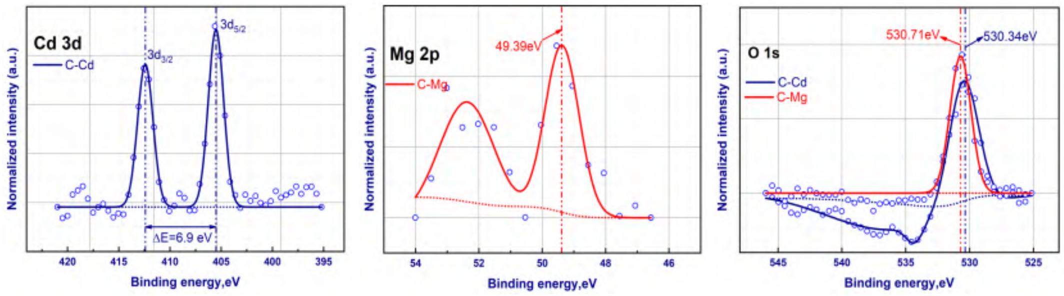

(g) Cd 3d core level spectra **(h)** Mg 2p core level spectra **(i)** O 1s core level spectra

Figure 4.17: XPS survey and high resolution core level spectra of the CZTS thin films with Cd and Mg doping

4.3.2. Effect of Cd and Mg co-doping

4.3.2.1. EDS analysis

EDS was utilized to estimate the elemental composition ratio of fabricated co-doped thin films. Table 4.15 tabulated the results of the at% of the elements as determined by EDS measurements. The corresponding EDS spectrums are shown in Figure 4.18. The off-stoichiometric Cu-poor, Zn-rich ratio was seen in all of the fabricated thin films. 40% of the Zn atoms are partially replaced by Cd (29%) and Mg (11%) jointly clearly seen form the results for CZCMTS-1 sample.A similar observation was also reported in [16], where 40% of Zn atoms were replaced by Cd atoms only, and this was claimed as optimum for better performance of solar cells.

The studies published in [251–254] demonstrated the capacity of kesterite-type compounds to tolerate deviations from stoichiometric composition while retaining the kesterite-type structure but exhibiting cation ratios Cu/(Zn+Sn) and Zn/Sn less than or greater than 1. The structural flexibility stems from the kesterite-type structure's proclivity to stabilize copper vacancies, anti-sites, and interstitials. Charge balance is maintained in these compounds by suitable replacements on the cationic sites. Only specific substitutions may be envisioned to account for the charge balance in off-stoichiometric kesterites if the oxidation states of cations and anions are kept. As a result, some point defects correlate to the off-stoichiometric composition. This association serves as the foundation for the 'off-stoichiometry concept,' which was initially postulated by Lafond et al [255]. Susan et.al. [45] also includes an overview of the off-stoichiometry categories, referred to as A-L [254]. Accordingly, "cation ratio plot" (Figure 4.19) is also used here to illustrate the off-stoichiometry in kesterite-type materials. It is evident that the samples CZTS-0 (undoped) and CZCMTS-1 are within the desired region Type-A (Cu-poor Zn-rich); whereas other two samples namely CZCMTS-2, CZCMTS-3 belongs to Type-L and Tye-J regions respectively.

Table 4.14: Atomic percentages of elements in the deposited films

Sample code	**at% of the elements**					
	Cu	**Zn**	**Sn**	**S**	**Cd**	**Mg**
CZTS-0	23.32%	17.25%	13.05%	46.39%	0.00%	0.00%
CZCMTS-1	28.52%	11.55%	12.38%	41.42%	4.67%	1.46%
CZCMTS-2	25.78%	10.86%	16.57%	40.45%	3.85%	2.51%
CZCMTS-3	22.76%	9.18%	14.14%	50.97%	1.13%	1.82%

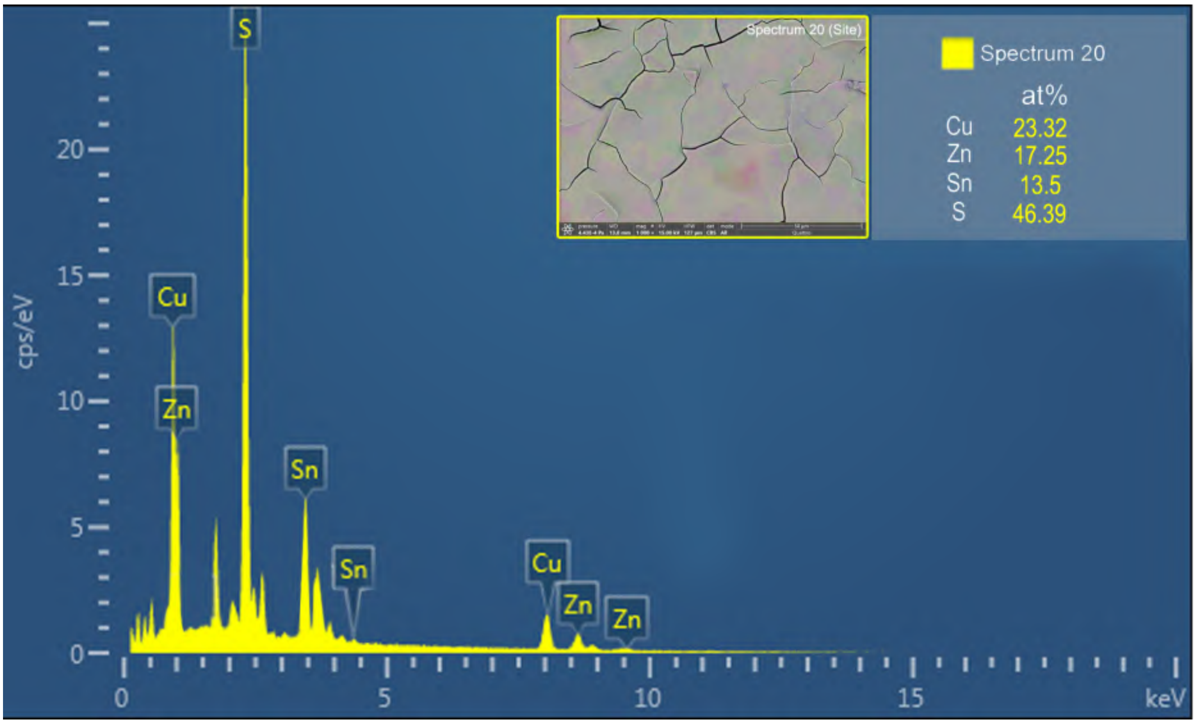

(a) CZTS-0

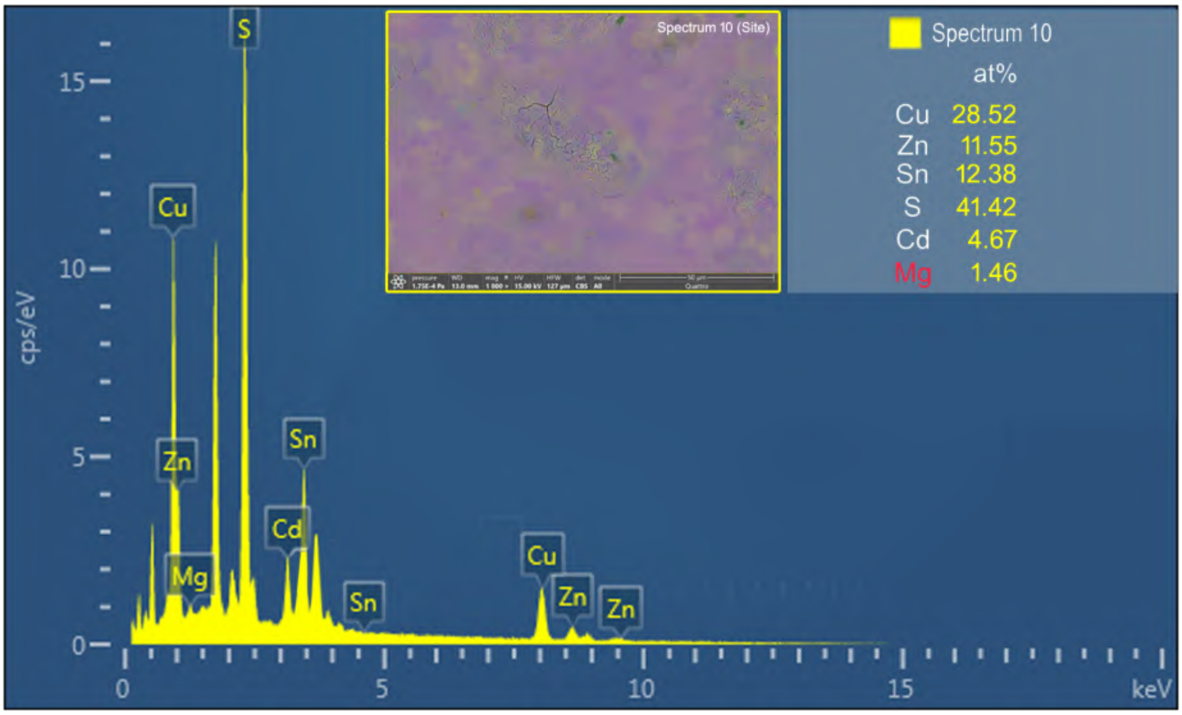

(b) CZCMTS-1

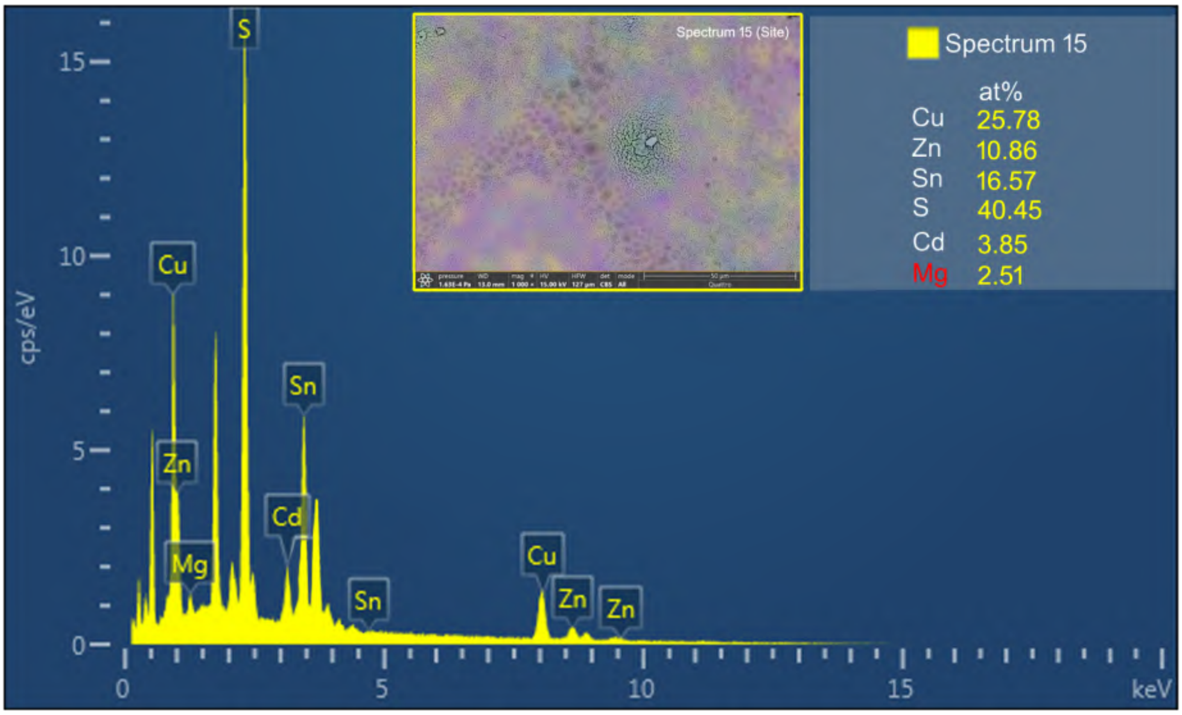

Spectrum 15

	at%
Cu	25.78
Zn	10.86
Sn	16.57
S	40.45
Cd	3.85
Mg	2.51

(c) CZCMTS-2

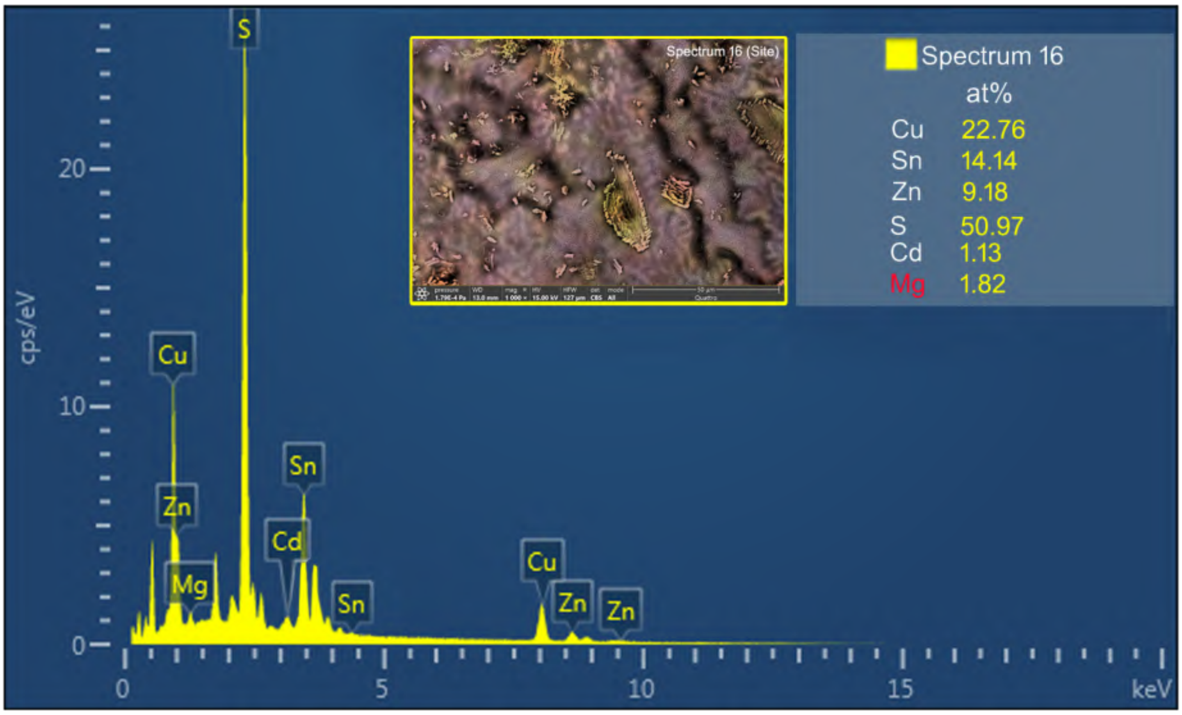

Spectrum 16

	at%
Cu	22.76
Sn	14.14
Zn	9.18
S	50.97
Cd	1.13
Mg	1.82

(d) CZCMTS-3

Figure 4.18: The EDS spectrum of pristine (a) and (Cd,Mg) co-doped CZTS samples (b,c,d)

Table 4.15: Cd and Mg contents and active composition ratio of fabricated samples

Sample	**Cd and Mg contents**				**Active composition ratio**			
	Precursor		**Film**		**A**	**B**	**C**	**D**
	x	y	x	y				
CZTS-0	0.00	0.00	0.00	0.00	0.64	1.32	1.79	0.87
CZCMTS-1	0.375	0.125	0.29	0.11	0.61	1.43	2.30	0.71
CZCMTS-2	0.25	0.25	0.26	0.19	0.53	1.04	1.56	0.68
CZCMTS-3	0.125	0.375	0.11	0.17	0.57	0.85	1.61	1.04

Target compound: $\mathbf{Cu_2Zn_{(1-x-y)}Cd_xMg_ySnS_4}$
$x = \mathrm{Cd/(Cd+Zn)}$ and $y = \mathrm{Mg/(Mg+Zn)}$
A = Cu/(Zn+Cd+Mg+Sn) and B = (Zn+Cd+Mg)/Sn
C = Cu/Sn and D = S/all metals

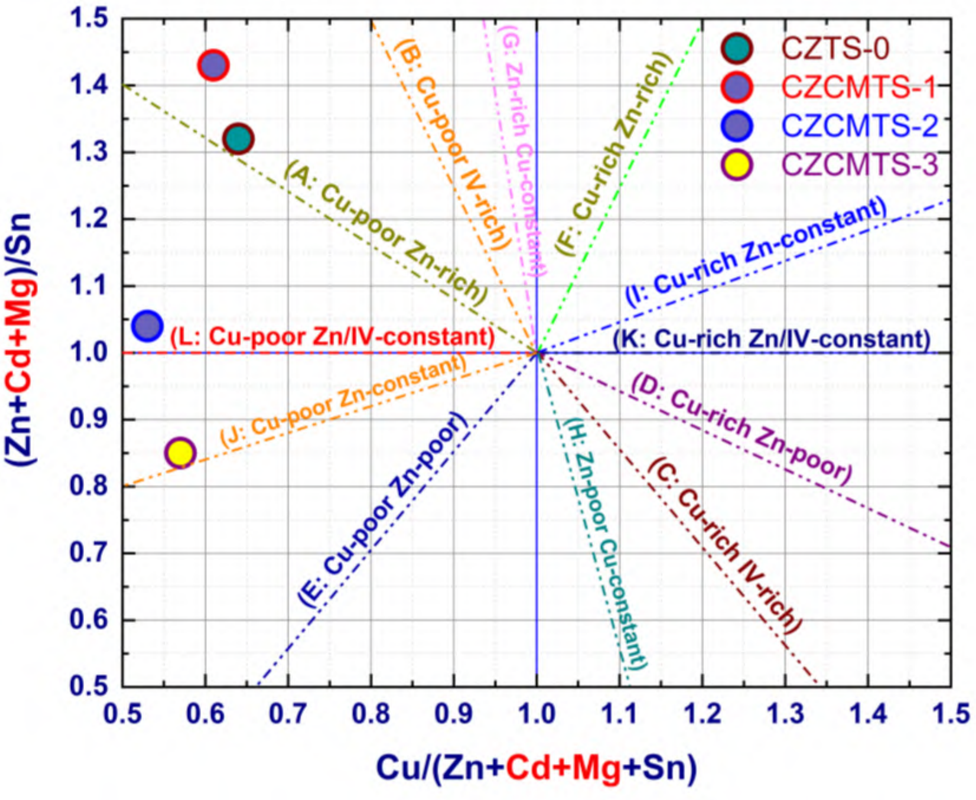

Figure 4.19: Cation ratio plot showing off-stoichiometry types of deposited CZTS samples

4.3.2.2. *Microstructural properties*

X-ray diffraction and Raman characterization were carried out to evaluate the effect of co-dopants Cd and Mg on the microstructural properties of fabricarted CZTS absorber thin films with respect to undoped absorber sample.

XRD analysis

Figure 4.20(a) depicts the XRD patterns of sulfurized CZTS thin films produced from precursor solutions with undoped and co-doped contents. Although all sulfurized samples have a dominating diffraction peak at the (112) plane, the CZCMTS-1 and CZCMTS-2 samples have three narrow and strong diffraction peaks from the (112), (220), and (312) planes. All of them agree with the kesterite structure (JCPDS# 26-0575) described in [216]. In a CZCMTS-3 sample , orthorhombic SnS phase is identified at a Bragg's diffraction angle of 21.18° (JCPDS# 39 0354). Additional JCPDS# 26-0575 polycrystalline CZTS phase characteristic peaks are also indexed.

Figure 4.20(b) shows an enlarged view of the peak shift around the main diffraction plane (112) after Gauss fitting of the samples under investigation. The average crystallite size (D) using the Scherrer formula, the microstrain (ε), and the dislocation density (δ) of the deposited films along the principal diffraction peak at the (112) plane were determined as given by Eq. [4.1], Eq. [4.2], and Eq. [4.3] respectively and shown in Table 4.16.

Improved crystallite sizes are found in doped cases, as shown in Table 4.16. The main diffraction peak along the (112) plane occurs at $2\theta_{112}$=28.58° in the CZTS-0 sample. The left shift of main diffraction peak at $2\theta_{112}$=28.24° (CZCMTS-1), $2\theta_{112}$=28.23° (CZCMTS-2), and $2\theta_{112}$=28.34° (CZCMTS-3) samples with corresponding increase in interplanar spacing "d", indicates that co-doped samples are subjected to tensile stress. Accordingly, cell volume also increased with respect to undoped sample. This peak shift is due to the variation in the effective ionic radii of Cd^{2+}, Mg^{2+}, and Zn^{2+} ions [234]. The lattice constants "a" and "c" are also clearly increased. The observed increase in lattice constant with dopants implies the substitution of Cd and Mg ions for Zn ions without affecting the kesterite structure. As $c/2a \leq 1$ for the co-doped samples, it confirms the persistence of kesterite crystal structure after doping [17]. The crystallite sizes behaved similarly. The hydrolysis reaction of the metal ions could be one of the reasons for this increase in crystallite size of the doped CZTS, and the samples could have minor structural imperfections [235]. The associated increase in crystallite size may also be attributed to the lattice expansion caused by distortions around the dopant atoms as a result of the mismatch between ionic radii [217].

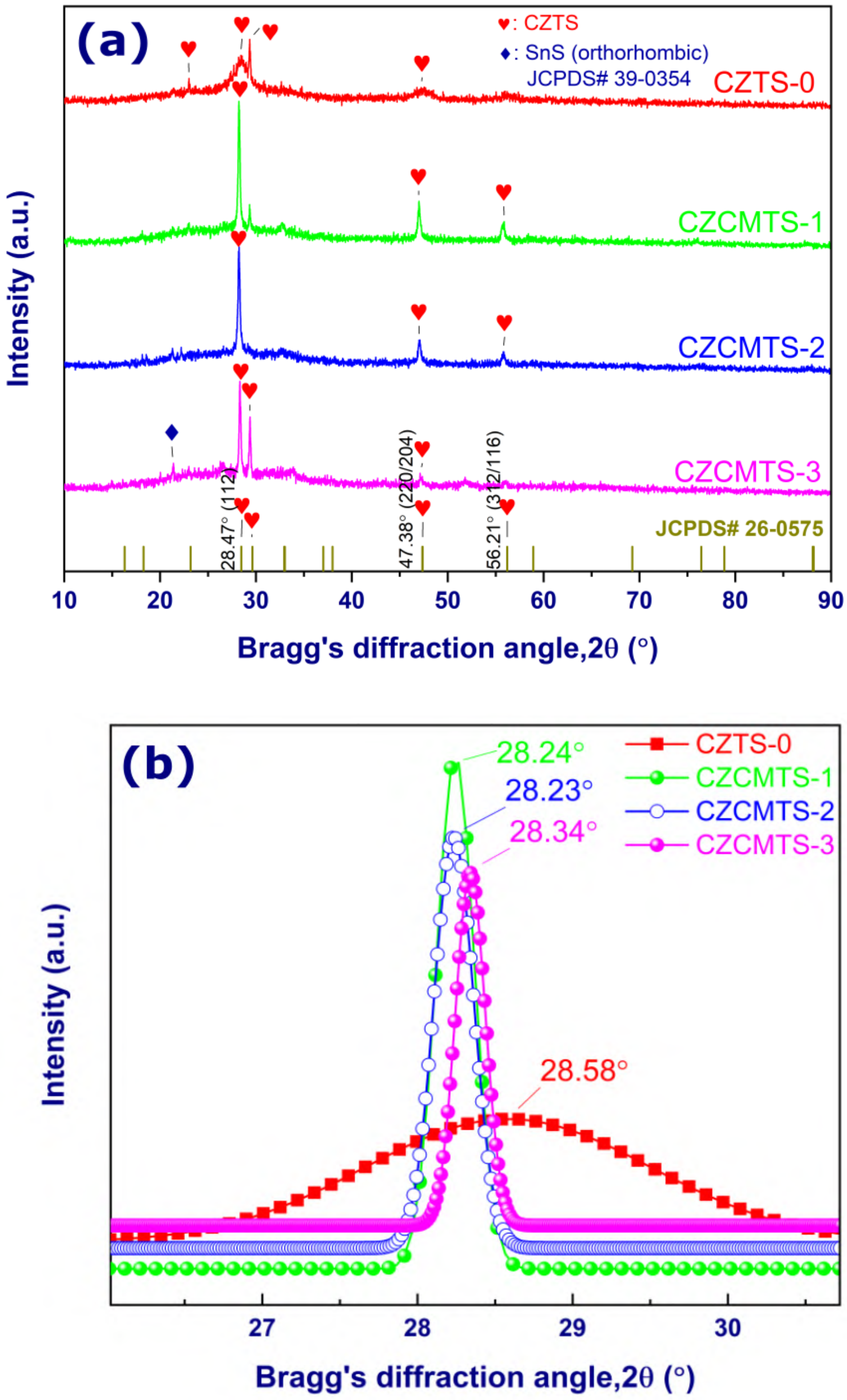

Figure 4.20: (a) XRD patterns of undoped and co-doped CZTS samples (b) an enlarged view of the peak shift of co-doped samples around the main diffraction plane (112) after Gauss fitting

Table 4.16: The crystallographic data for co-doped samples

Sample code	2θ (°)	d(Å)	FWHM (°)	D (nm)	a (Å)	c (Å)	c/2a	Volume (Å^3)
CZTS-0	28.58	3.120489	2.17679	3.77	5.42319	10.73742	0.989954	315.7981
CZCMTS-1	28.24	3.157281	0.28621	28.62	5.46234	10.96221	1.003435	327.0809
CZCMTS-2	28.23	3.158377	0.34572	23.69	5.45796	10.99151	1.006925	327.4293
CZCMTS-3	28.34	3.146368	0.22626	36.21	5.42535	10.99861	1.013631	323.7376

Raman analysis

Some tetragonal phases like Cu_2SnS_3 may exist in the same diffraction angle, causing an overlapping peak at the (112) plane [218]. XRD cannot alone demonstrate that kesterite CZTS has a secondary phase. As shown in Figure 4.21, Raman spectroscopy at 785 nm was used to identify probable secondary phases on undoped and co-doped CZTS thin film samples.

Single-phase CZTS with a kesterite structure shows a prominent Raman peak at 338 cm^{-1} [219], which is associated with the major vibrationa A1 symmetry mode. The vibration of sulfur atoms surrounded by atoms from other compounds is related to this specific A1 phonon mode. The CZTS-0 sample exhibits two shoulder peaks at 348 cm^{-1} and 371 cm^{-1}, which is indicative of the kesterite structure in mode E/B-TO LO [236, 237]. These shoulder peaks are observed at a frequency of 351 cm^{-1} and 369 cm^{-1} in the CZCMTS-1 sample (Figure 4.21a); 351 cm^{-1} and 371 cm^{-1} in the CZCMTS-2 sample (Figure 4.21b); and 354 cm^{-1} and 372 cm^{-1} in the CZCMTS-3 sample (Figure 4.21c).

The A1 mode location of Cu_2CdSnS_4 has been reported before to be at 326 cm^{-1} [17] and of Cu_2MgSnS_4 to be at 335 cm^{-1} [148, 256]. Co-doping with Cd,Mg, whose atomic radii are less than those of Zn atoms, can cause a shift in the raman main peak toward lower wavenumbers within anywhere within these ranges. Results (Figure 4.21) show that Cd,Mg co-doping "redshifts" the major Raman peak of the A1 mode to a lower wavenumber at 333 cm^{-1} (CZCMTS-1), 328 cm^{-1} (CZCMTS-2), and 330 cm^{-1} (CZCMTS-3). Among the redshifted peaks CZCMTS-2 sample shows the low peak intensity, which may be attributed to the increase in Mg contents in the samples with respect to others.

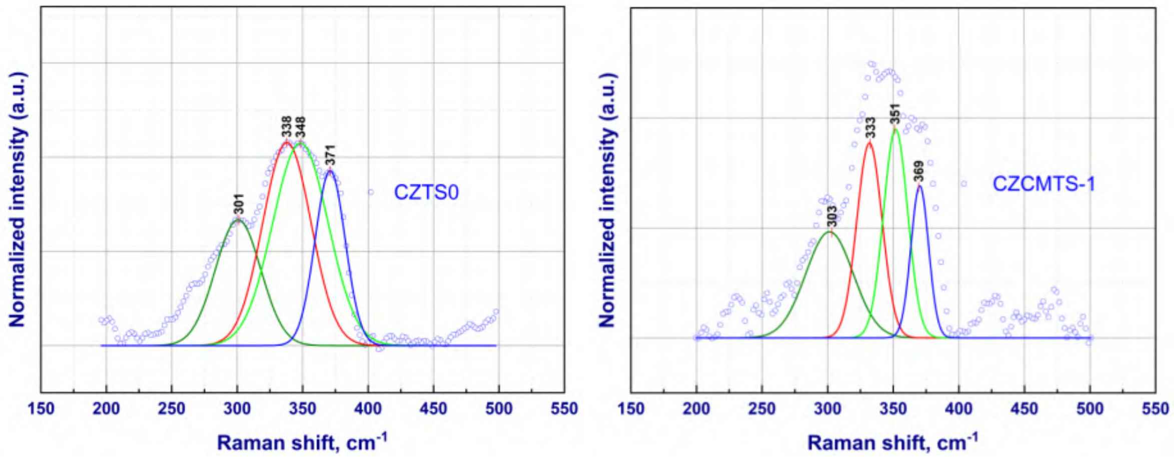

(a) CZTS-0 **(b)** CZCMTS-1

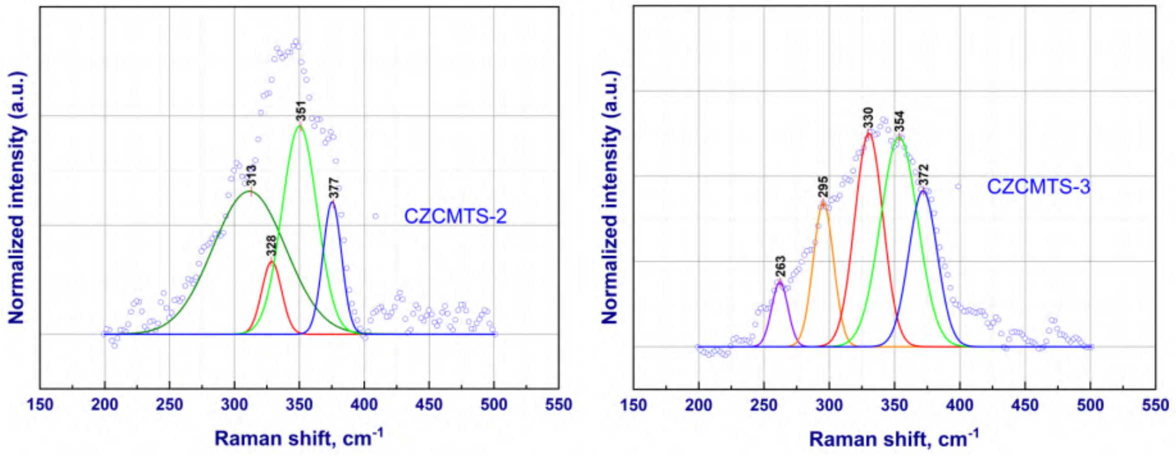

(c) CZCMTS-2 **(d)** CZCMTS-3

Figure 4.21: The Raman spectra of co-doped thin films

4.3.2.3. Morphological properties

The SEM micrographs along with surface roughness of undoped and co-doped CZTS films are shown in Figure 4.22. The scanning electron microscopy images showed that the CZCMTS-1 sample (where Cd and Mg are jointly contributed to 40% of Zn replacements) had grains that were closely packed together, which were not observed in the other Cd,Mg-doped or undoped samples. The reported variations in crystallite size are consistent with SEM findings.

Thin films with high crystalline quality are made by choosing the right chemical precursors, type of solvent, and other factors that control solution parameters like pH and viscosity [224]. The pH of all precursor solutions prepared for thin film fabrication using the sol-gel spin coating technique was about 5.5. The centipoise (cp) is a measurement unit for dynamic viscosity. For the sample C-00, C-Cd, and C-Mg solutions, the observed values for dynamic viscosity (room temperature= 28°C) were 22.6 cp for CZTS-0 sample, whereas Cd,Mg co-doped samples are found within the range of 22.0 cp to 23.8 cp. So, when the Mg concentration in the films was raised, they adhered better to the SLG glass substrate.

According to the three-dimensional profilometry results (Table 4.17), RMS height is found to be lowest for CZCMTS-1 sample, 119 nm. In terms of surface roughness, CZCMTS-2 sample is found to be roughest (561 nm), even than the undoped sample.

It can be seen that XRD peak intensities change a lot (Figure 4.20) depending on the active composition ratio of x and y stoichiometry (Table 4.15). The XRD peak intensity is found to be highest for CZCMTS-1 sample when $x = 0.29$ and $y = 0.11$. Considering the above, we might speculate as to what caused the co-doped thin films' morphological alteration.

Table 4.17: Surface roughness data from 3D profilometry [Area (W= 564.4 μm; H= 421.6 μm)]

Parameters	**CZTS-0 (μm)**	**CZCMTS-1 (μm)**	**CZCMTS-2 (μm)**	**CZCMTS-3 (μm)**
S_p	2.411	0.259	5.423	0.484
S_v	0.799	0.467	0.8968	0.731
S_t	3.211	0.727	6.320	1.216
S_a	0.360	0.092	0.305	0.168
S_q	0.492	0.119	0.561	0.214
S_{sk}	1.760	-1.04	4.977	-0.762
S_{ku}	6.775	3.851	37.870	3.477

S_p = Peak height (μm)
S_v = Valley height (μm)
S_t = Arithmatic mean height (μm)
S_a = Peak height (μm)
S_q = Root mean square height (μm)
S_{sk} = Skewness
S_{ku} = Kurtosis

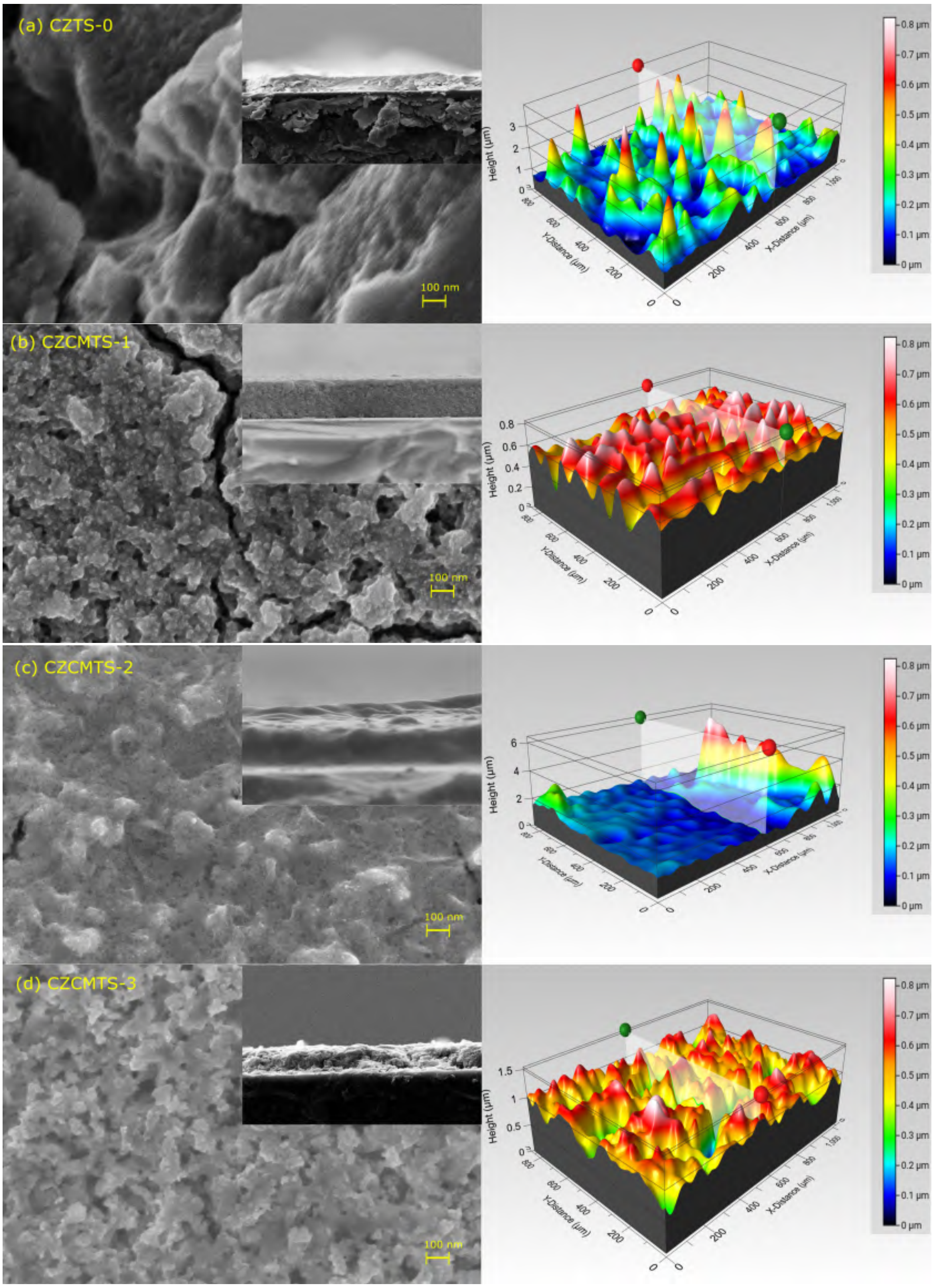

Figure 4.22: SEM micrographs with surface roughness of undoped and co-doped thin films

4.3.2.4. *Optoelectronic properties*

Before investigating the optical properties of fabricated thin films, the thickness of the samples was measured using cross-sectional SEM observations. The samples of CZTS-0, CZCMTS-1, CZCMTS-2, and CZCMTS-3 had a thickness of 2.11 μm, 783.4 nm, 1.129 μm and 668 nm, respectively as shown in Appendix A [Figure A.2].

The absorbance spectra of the CZTS thin films are shown in Figure 4.23a. Figures 4.23b and 4.23c show the corresponding absorption coefficients and Tauc's plots.

The optical absorption coefficient, α of a direct band gap semiconductor near the band edge, for photon energy, $h\nu$ greater than the band gap energy, E_g of the semiconductor, is given by Tauc's relation [222], as in Eq. 4.4. The absorption coefficients are found to be on the order

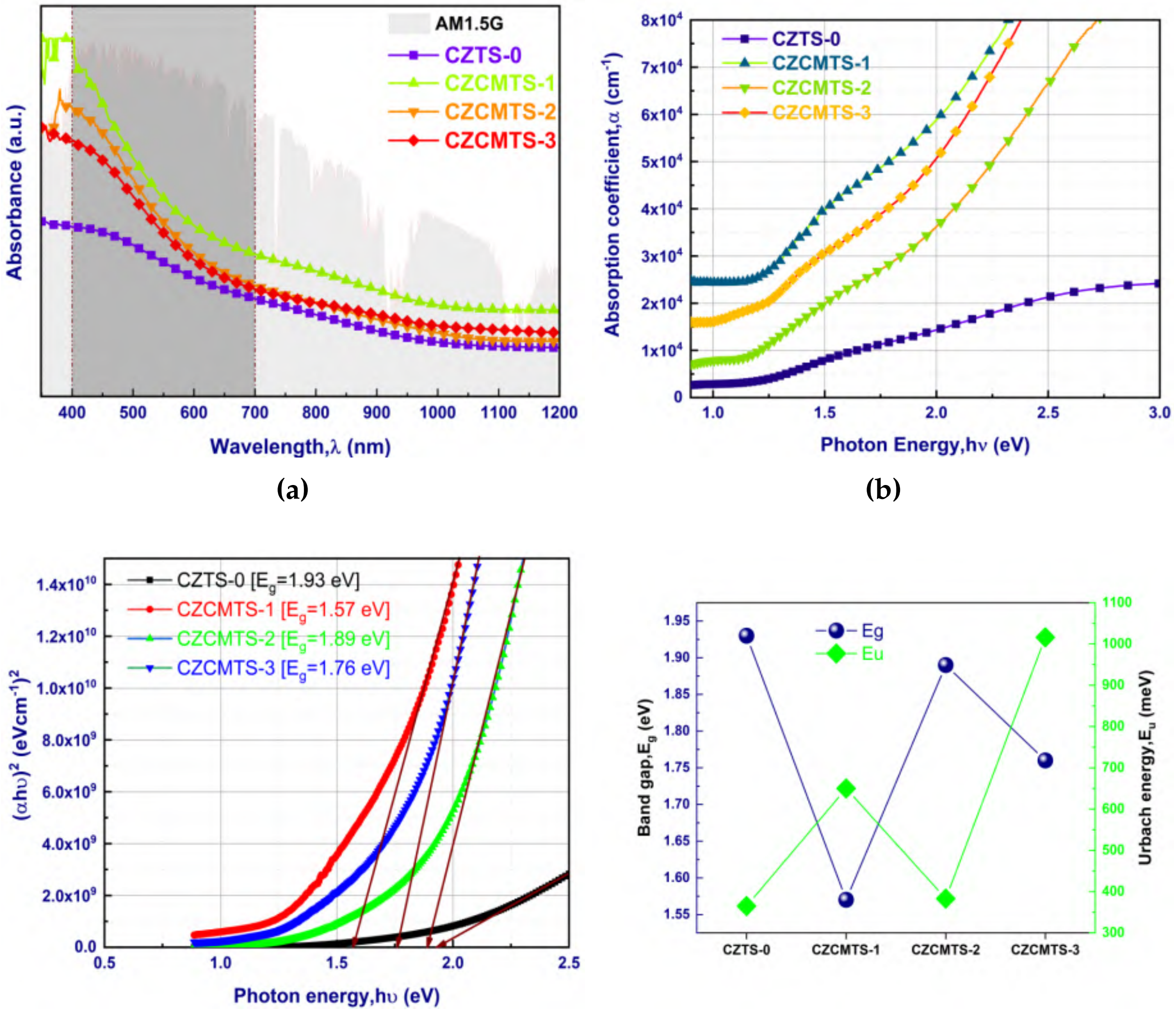

(a) **(b)**

(c) **(d)**

Figure 4.23: Optoelectronic properties of undoped and co-doped thin films

of 10^4 cm^{-1} for all of the samples. This supports the fact that the material experienced direct transitions from one state to another.

The E_g is estimated to be approximately 1.93 eV in the undoped sample, CZTS-0. This higher value of the optical band gap for an undoped CZTS sample may be due to the presence of defect or trap states within the forbidden energy gap [224]. The band gap was found to fall after co-doping with Cd and Mg. The corresponding band gap values are 1.57 eV (CZCMTS-1), 1.89 eV (CZCMTS-2), and 1.76 eV (CZCMTS-3).

The position of the absorption edge moves toward higher wavelengths, as seen in Figure 4.23a (redshift). The band gap values of the co-doped thin films fell from higher to lower as a result of this redshift. The co-doped thin films' increased crystallite size [243] and accompanying decreases in FWHM and defect states [211] are most likely to be responsible for this. In addition, the presence of impurity phases in the samples as well as p-d hybridization between Cu d-levels and S p-levels may cause the band gap energy to change [246]. The likelihood of dopant-related secondary phases [226] as well as the creation of donor levels below the conduction band [247] may both play a role in the optical absorption edge's redshift, resulting in a narrower band gap.

The segregation of the host (undoped) atoms besides the grain boundaries can reduce the E_g of co-doped thin films which is supported by SEM micrographs (Figure 4.22). Doping increased the optical absorbance because decreasing the size of crystallites can lead to an increase in their specific surface area [243].

Urbach energy, E_u plays a vital part in the process of discovering solutions to band tailing problems associated with structural disorder, phonons, excitons, and contaminants. Urbach's tail refers to the absorption edge that is below the energy gap, which rises exponentially [227]. The E_u of deposited thin films was determined for each sample as illustrated in Figure 4.24 and the associated equation shown in Eq. 4.5.

A plot of the variation of optical band gaps as obtained for sulfurized samples (CZTS-0, CZCMTS-1, CZCMTS-2, and CZCMTS-3) with respect to their urbach energies is shown in Figure 4.23d. In this study, significant band tailing problems were observed for the CZCMTS-3 sample (E_u = 1016 meV). CZCMTS-2 sample suffers less band tailing issues with a minimum E_u , 383 meV. These values are consistent with the other characterization results acquired in other experiments.

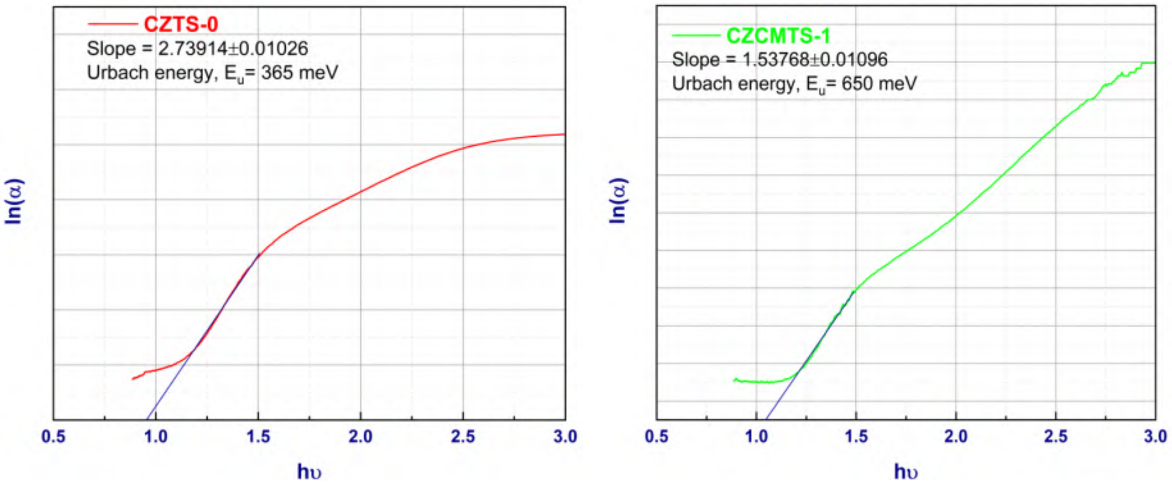

(a) CZTS-0 **(b)** CZCMTS-1

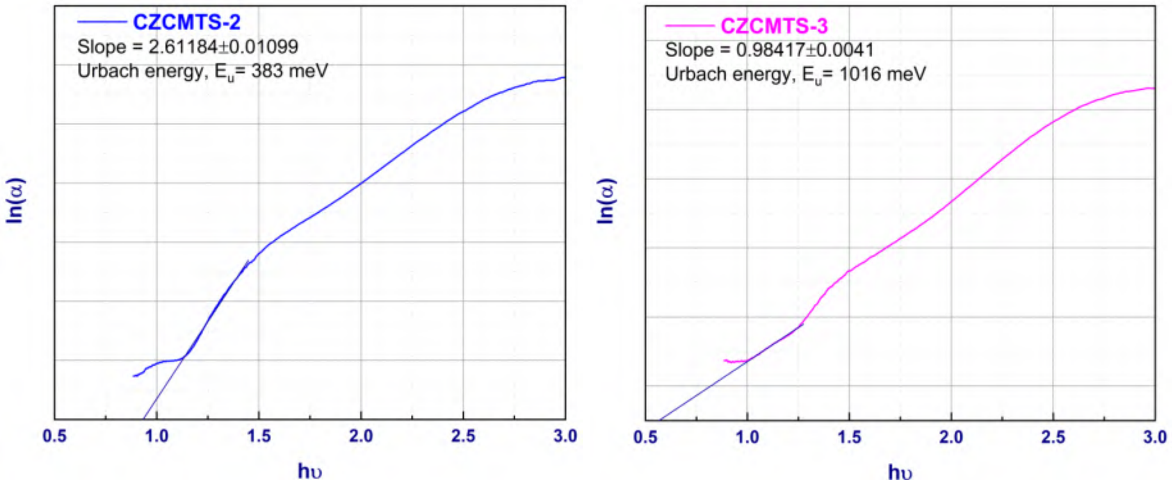

(c) CZCMTS-2 **(d)** CZCMTS-3

Figure 4.24: Urbach energy estimation of undoped and co-doped thin films

4.3.2.5. XPS analysis

Cu 2p, Zn 2p, Sn 3d, and S 2p XPS spectra with high resolution were used to identify the oxidation states of the constituent elements for fabricated undoped and co-doped thin films, as shown in Figure 4.25. Table 4.18 and Table 4.19 lists the matching atomic peak locations and peak splitting binding energies in comparison to reference data.

Two satellite peaks are seen in the Cu 2p spectra for co-doped samples. This shows that the sample has more than simply Copper in it (I). Yet, such satellite peaks aren't present in samples that weren't doped. Except for the CZCMTS-2 sample, the principal peaks' splitting energies range between 19.8 eV and 20.23 eV. This finding shows that there is a high concentration of Cu on the surface.

The peaks with binding energies of approximately 1021.80 eV and 1044.77 eV in the samples are attributed to Zn 2p, with a peak separation of 22.97 eV corresponding to Zn (II). The varying splitting energies of the investigated samples are close to the 22.97 eV reference value, confirming the oxidation states of Zn in the samples.

Peak splitting energy of 8.41 eV indicates Sn(IV) oxidation states. Except for the CZCMTS-3 sample, the splitting energies of the major peaks range between 8.41 eV and 8.51 eV. This finding shows that there is a high concentration of Sn on the surface.

Sulfur oxidation states are represented by the S 2p peaks that appear at binding energies of 164.0 eV and 165.18 eV with a peak spacing of 1.18 eV. The samples' splitting energies are close to 1.18 eV, supporting S oxidation states.

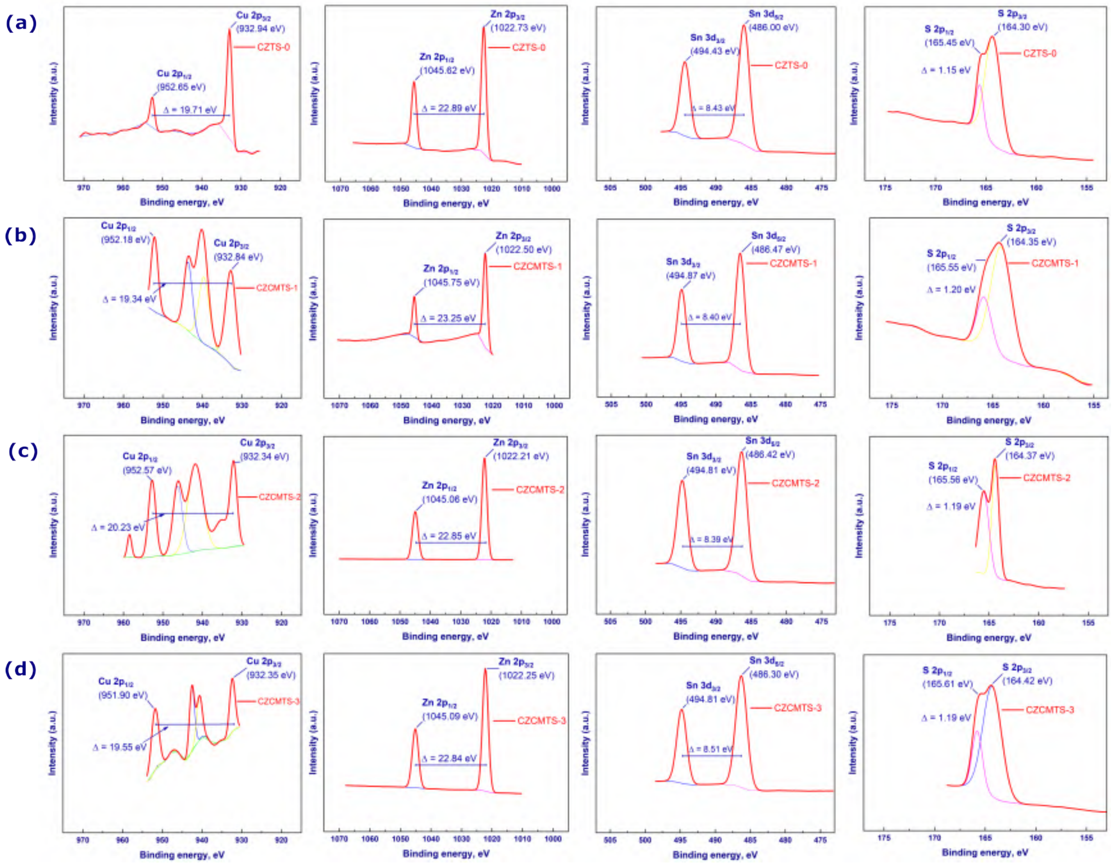

Figure 4.25: XPS analysis to reveal oxidation states of deposited samples: (a) CZTS-0, (b) CZCMTS-1, (c) CZCMTS-2, and (d) CZCMTS-3

Table 4.18: Atomic peak positions and peak splitting binding energies (Cu and Zn)

Sample code	**Cu (Binding energy, eV)**				**Zn (Binding energy, eV)**			
	Cu2p$_{3/2}$	**Cu2p$_{1/2}$**	**Peak splitting, △**	**△ (ref)**	**Zn2p$_{3/2}$**	**Zn2p$_{1/2}$**	**Peak splitting, △**	**△ (ref)**
CZTS-0	932.94	952.65	19.71	19.8	1022.73	1045.62	22.89	22.97
CZCMTS-1	932.84	952.18	19.38		1022.50	1045.75	23.25	
CZCMTS-2	932.34	952.57	20.23		1022.21	1045.06	22.85	
CZCMTS-3	932.35	951.90	19.55		1022.25	1045.09	22.84	

Table 4.19: Atomic peak positions and peak splitting binding energies (Sn and S)

Sample code	**Sn (Binding energy, eV)**				**S (Binding energy, eV)**			
	Sn3d$_{5/2}$	**Sn3d$_{3/2}$**	**Peak splitting, △**	**△ (ref)**	**S2p$_{3/2}$**	**S2p$_{1/2}$**	**Peak splitting, △**	**△ (ref)**
CZTS-0	486.00	494.43	8.43	8.41	164.30	165.45	1.15	1.18
CZCMTS-1	486.47	494.87	8.40		164.35	165.55	1.20	
CZCMTS-2	486.42	494.81	8.39		164.37	165.56	1.19	
CZCMTS-3	486.30	494.81	8.51		164.42	165.61	1.19	

4.3.2.6. Photovoltaic properties

Experimental

Plots in Figure 4.26 shows the current-voltage (I-V) characteristics (dark and illuminated) of undoped and Cd,Mg co-doped samples. The performance of the CZCMTS-1 sample in PCE is around ten times greater than that of the undoped sample. Cd and Mg jointly contributed to the partial cation substitution of Zn atoms in this sample to the tune of 40%, as was discovered by replacement by Cd atom exclusively [149]. According to CZCMTS-2 and CZCMTS-3, PCE performance varies with Mg concentrations in the fabricated samples. The adverse performance of J_{sc} might be attributed to trap states in the band gap that are responsible for carrier recombinations. Another explanation might be because of non-ohmic contacts with Ag. Fill factors were thus shown to be quite inadequate. Poor PCE among the examined

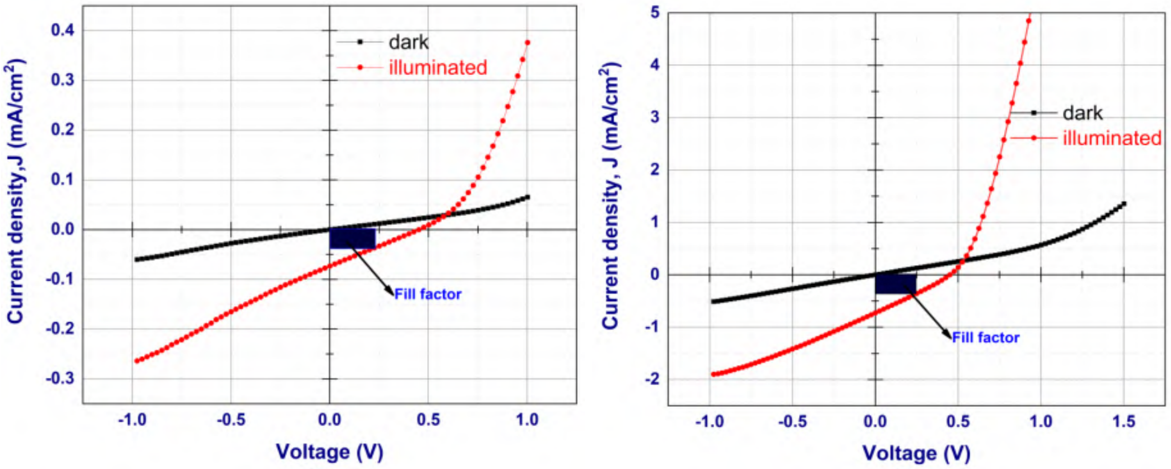

(a) CZTS-0 **(b)** CZCMTS-1

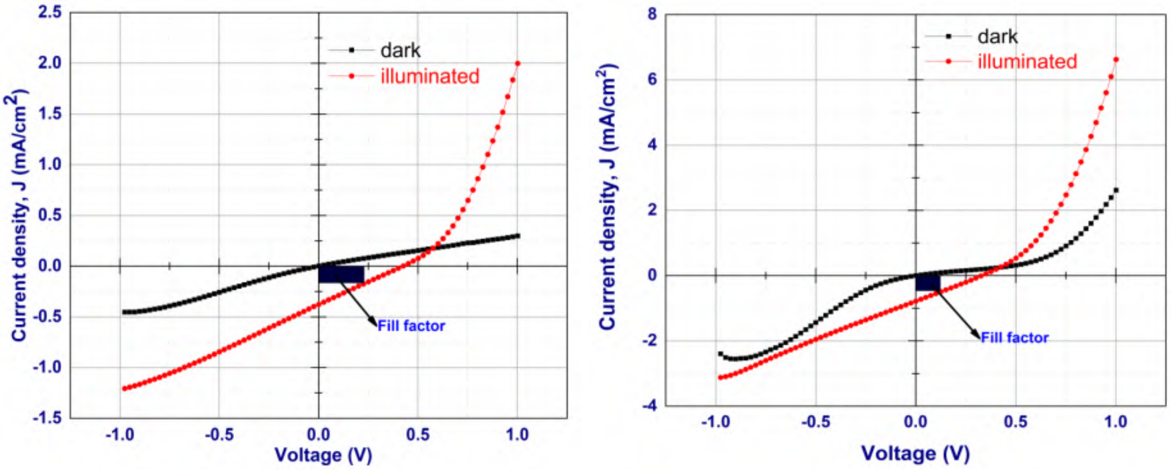

(c) CZCMTS-2 **(d)** CZCMTS-3

Figure 4.26: Photovoltaic properties of deposited co-doped thin films

substrate-structured thin film solar cells was caused by high series and shunt resistance values.

Numerical simulation

In order to validate experimental results, numerical simulation was done using SCAPS. First, a cell was simulated using SCAPS data, known as *Base Cell*. Then this base cell data was modified and simulated for "dark and illuminated" characteristics of five solar cells in accordance with thicknesses, optical band gaps, and absorption co-efficients as obtained during experimental study. Both experimentally and simulated obtained data are tabulated side by side in Table 4.20.

Our study's champion cell, CZCMTS-1, is something that both the experimental and simulation studies have in common. Some factors that affect PCE were evidently better determined by simulation research.

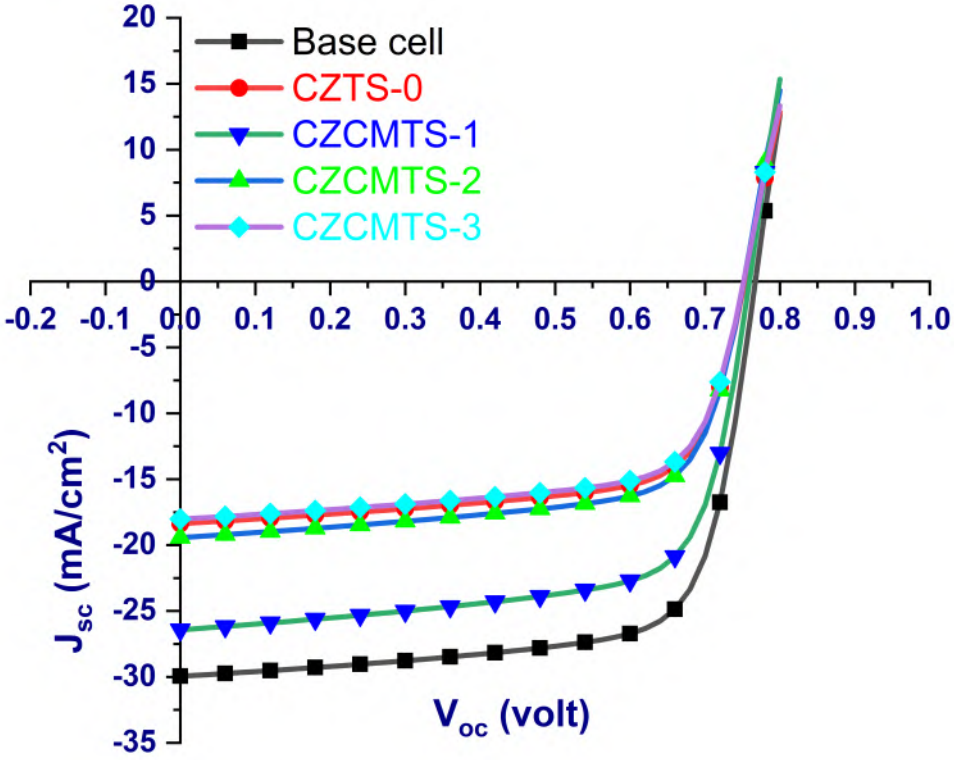

Figure 4.27: Photovoltaic properties of codoped thin films (Simulation)

---

[2] Data in "red" under simulation corresponds to Base cell

Table 4.20: Experimental and simulated photovoltaic performance data

Sample code	**Experimental**						**Simulation**			
	V_{oc} **(V)**	J_{sc} **(mA/cm^2)**	**FF (%)**	η **(%)**	R_s **(Ω.cm^2)**	R_{sh} **(Ω.cm^2)**	V_{oc} **(V)**	J_{sc} **(mA/cm^2)**	**FF (%)**	η **(%)**
							0.767[2]	**29.95**	**71.83**	**16.51**
CZTS-0	0.451	0.073	25	0.01	5490	6080	0.753	18.37	68.21	9.44
CZCMTS-1	0.426	0.73	29	0.09	303	689	0.759	26.42	69.43	13.93
CZCMTS-2	0.401	0.38	25	0.04	1090	1100	0.752	19.43	67.93	9.93
CZCMTS-3	0.401	0.78	24	0.06	393	436	0.752	18.03	67.97	9.22

4.3.2.7. *Band alignment at heterojunction*

Band alignments of Type-II (Figure 2.12 in Chapter 2) nature with a staggered-gap was observed in all cases. Figure 4.28 illustrates the VBM determination with respect to Fermi energy level of undoped and co-doped CZTS thin films. The measured and calculated CBOs and VBOs of the CZTS/CdS interface are shown in Figure 4.29 and Figure 4.30 respectively. Table 4.21 summarizes the measured and calculated results.

The interface exhibits CBOs that bear a negative resemblance to cliffs. The CBO value of CZCMTS-2 sample is found to be overestimated by 0.6 eV. The ideal Conduction Band Offset (CBO) for heterojunction solar cells is a moderately positive spike between +0 eV and +0.4 eV, as suggested by Palsgaard et al. [154]. However, a cliff-like CBO within this range is also desirable. This phenomenon can be attributed to the hindrance of light-generated carriers' movement and the presence of recombination traps.

Table 4.21: Band alignment study summary (experimental and simulation) of undoped and codoped CZTS thin films

Sample code	**Experimental**				**Simulation**			
	VBM (eV)	**CBM (eV)**	**VBO (eV)**	**CBO (eV)**	**VBM (eV)**	**CBM (eV)**	**VBO (eV)**	**CBO (eV)**
CZTS-0	1.05	0.88	0.85	-0.33	0.74	1.19	0.57	-0.10
CZCMTS-1	0.90	0.67	1.00	-0.12	0.37	1.20	0.93	-0.10
CZCMTS-2	0.74	1.15	1.16	-0.60	0.71	1.18	0.60	-0.10
CZCMTS-3	0.85	0.91	1.05	-0.36	0.57	1.19	0.74	-0.10

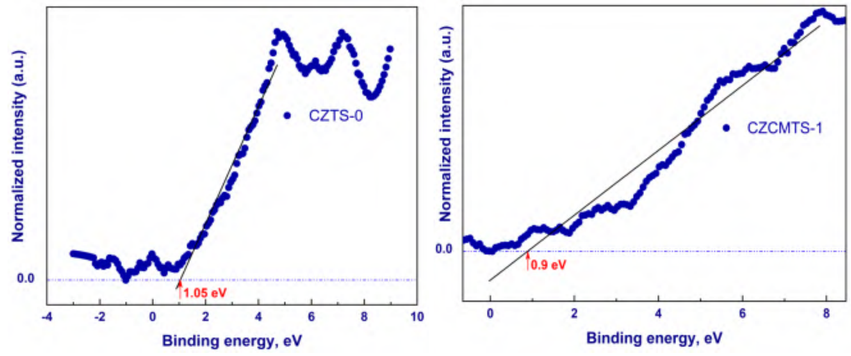

(a) CZTS-0 **(b)** CZCMTS-1

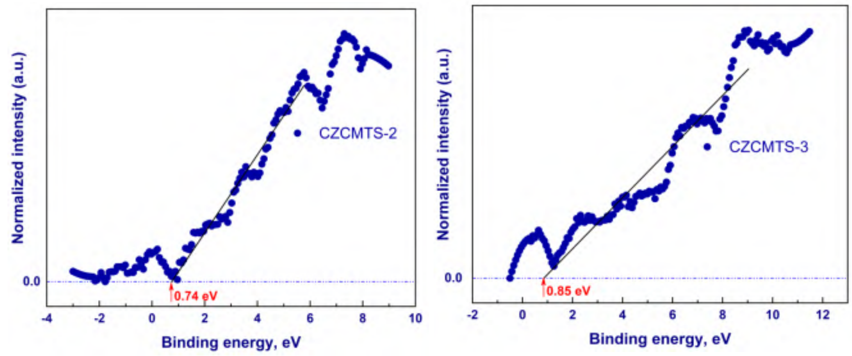

(c) CZCMTS-2 **(d)** CZCMTS-3

Figure 4.28: VBM determination of undoped and co-doped CZTS thin films probed by XPS at lower binding energy range

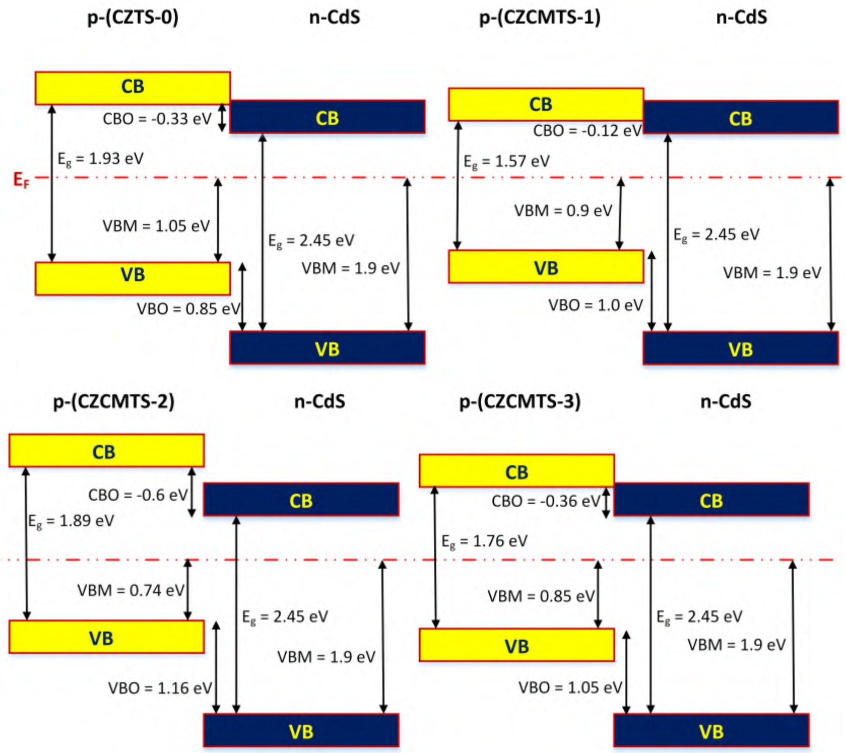

Figure 4.29: Band alignment of undoped and co-doped CZTS thin films at heterojunction with CdS buffer layer using experimental data

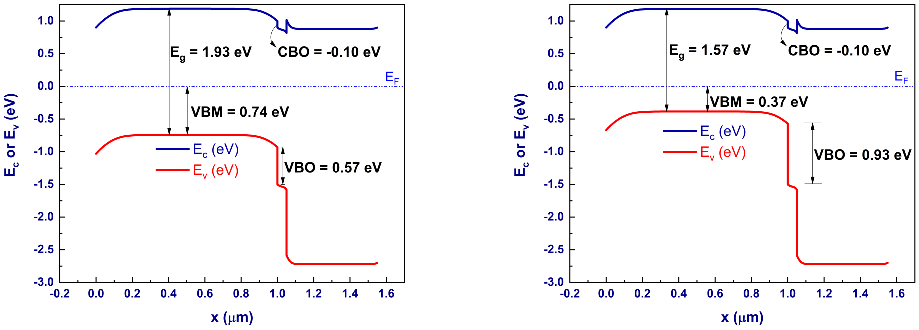

(a) CZTS-0 **(b)** CZCMTS-1

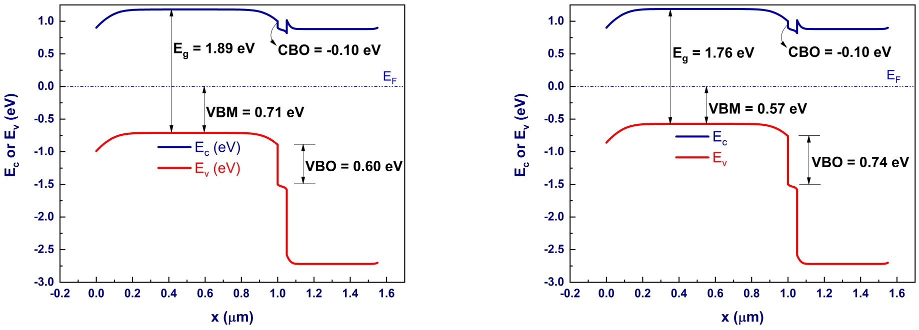

(c) CZCMTS-2 **(d)** CZCMTS-3

Figure 4.30: Band alignment of undoped and co-doped CZTS at heterojunction with CdS buffer using experimental data (Simulation)

4.4. Band alignment study of CZTS/CdS and CZTS/ZnS heterojunction interface

In light of the fact that the primary goal of this study was to investigate band alignment at CZTS/CdS and CZTS/CdS heterojunction interfaces, the first step is to investigate the microstructural, morphological, and optical features of each individual film.

4.4.1. Microstructural properties of the thin films

The XRD patterns of CZTS (sulfurized), CdS, and ZnS thin films that were fabricated from sol-gel spin coating, chemical bath deposition, and successive ionic layer adsorption and reaction are shown in Figure 4.31. Their characteristic peaks are associated with the relevant diffraction plane, confirming the formation of desirable films of interest. The crystallographic data of films are presented in Table 4.22.

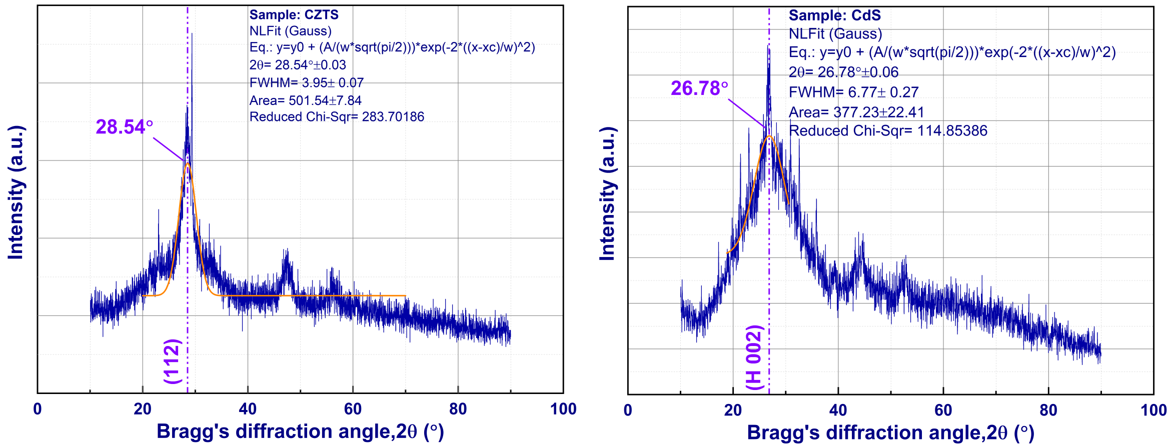

(a) CZTS **(b)** CdS

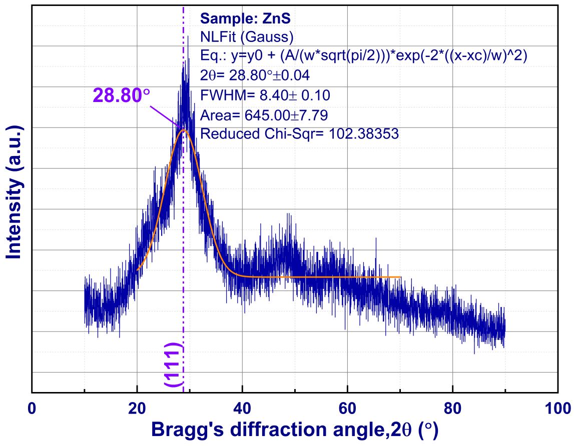

(c) ZnS

Figure 4.31: Microstructural properties of CZTS (sulfurized), CdS, and ZnS thin films

It is clear that the main diffraction peak of CZTS is along the 112 plane at Bragg's diffraction

Table 4.22: Crystallographic data of CZTS (sulfurized), CdS, and ZnS thin films

Film	**Method**	**Plane**	**2θ (°)**	**d (Å)**	**FWHM (°)**	**D (nm)**	**Lattice constants**
CZTS	Spin-coating	112	28.54	3.12	2.376	3.45	a=b=5.424;c=10.712
CdS	CBD	002 (H)	26.78	3.32	6.770	1.21	a=4.43;c=6.65
ZnS	SILAR	111	28.92	3.09	6.978	1.18	a=b=c=5.34

angle of 28.54°. The calculated lattice constants show that its crystal structure is tetragonal. For CdS crystal that is shaped like hexagonal wurtzite, diffraction occurs along the 002 plane at an angle of 26.78°. For cubic β-ZnS, phase diffraction takes place at 28.92° along Miller's plane 111. As far as crystallinity goes, CdS and ZnS films don't measure up. This is clear from their FWHM values.

4.4.2. Morphological properties and elemental composition ratio

SEM micrographs with corresponding EDS spectrum of prepared thin films are shown in Figure 4.32. The grain size is the most important component in determining the surface roughness. It is evident that fabricated CdS and ZnS films have a significantly rougher surface than CZTS film. The scanning electron microscopy pictures revealed that the grains in the manufactured samples are densely packed. The reported crystallite size corresponds to SEM results, and the elemental composition ratio as measured by EDS is also consistent with the formation of compounds.

4.4.3. Optical properties of the thin films

Before looking at their optical properties, samples of thin films were checked for thickness with a dektak profilometer.Thicknesses of 1.5 μm, 60 nm, and 100 nm were measured for the CZTS, CdS, and ZnS samples, respectively.Figure 4.33a shows the CZTS thin film's absorbance spectra. Within the visible spectrum, the absorption is barely detectable. As was previously described in detail in this thesis, the optical band gap values were calculated using Tauc's figure. E_g= 1.93 eV is determined for the CZTS thin film.

Buffer layers CdS and ZnS transmittance spectra are depicted in Figure 4.33c and Figure 4.33e. Nearly 90% transmittance is observed for both films, with wavelength invariance shown for the ZnS thin film. Tauc's figure investigates the optical band gaps, and finds them to be 2.45 eV and 3.63 eV for such transparent thin films.

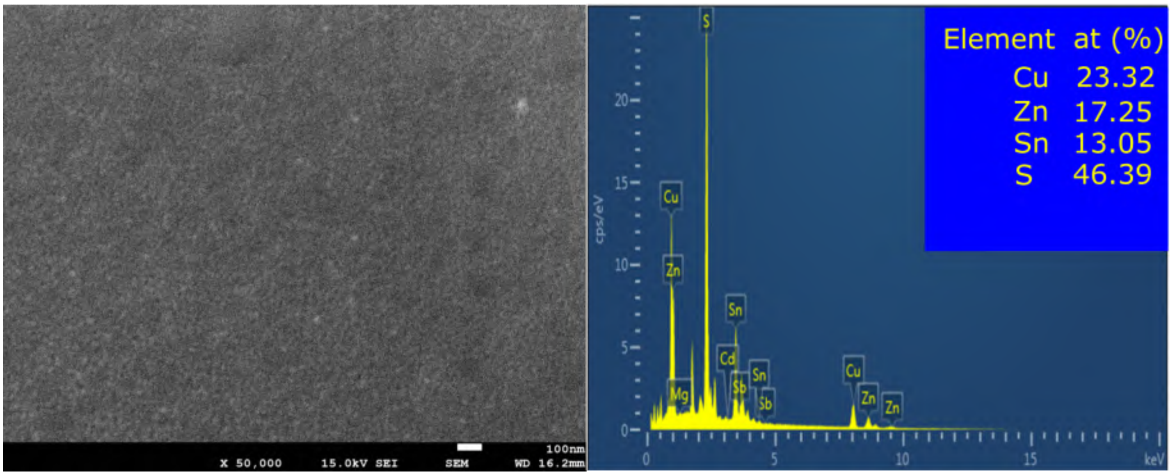

(a) SEM and EDS of CZTS thin film prepared by sol-gel spin coating method

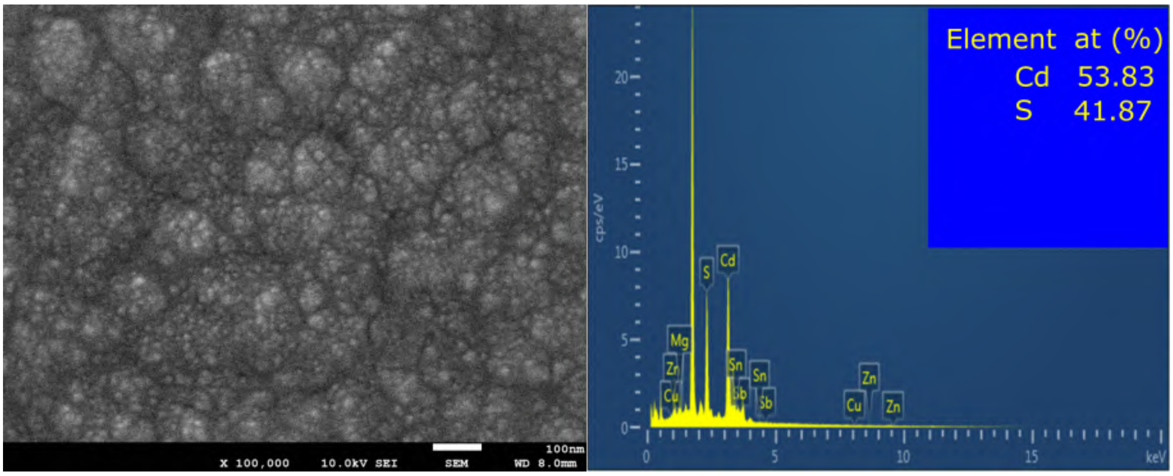

(b) SEM and EDS of CdS thin film prepared by chemical bath deposition method

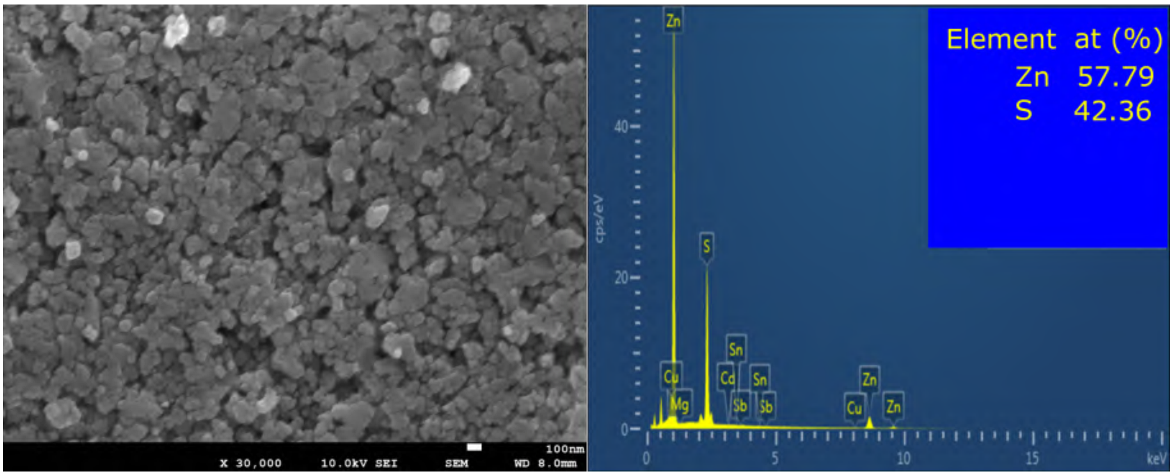

(c) SEM and EDS of ZnS thin film prepared by SILAR method

Figure 4.32: SEM micrographs with corresponding EDS spectrum of fabricated thin films

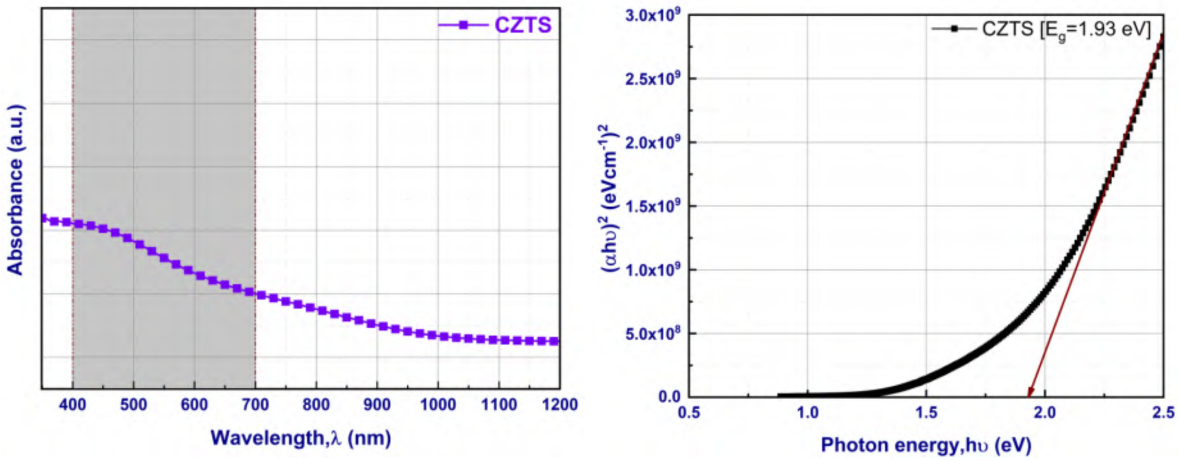

(a) Absorbance spectra: CZTS **(b)** Band gap estimation: CZTS

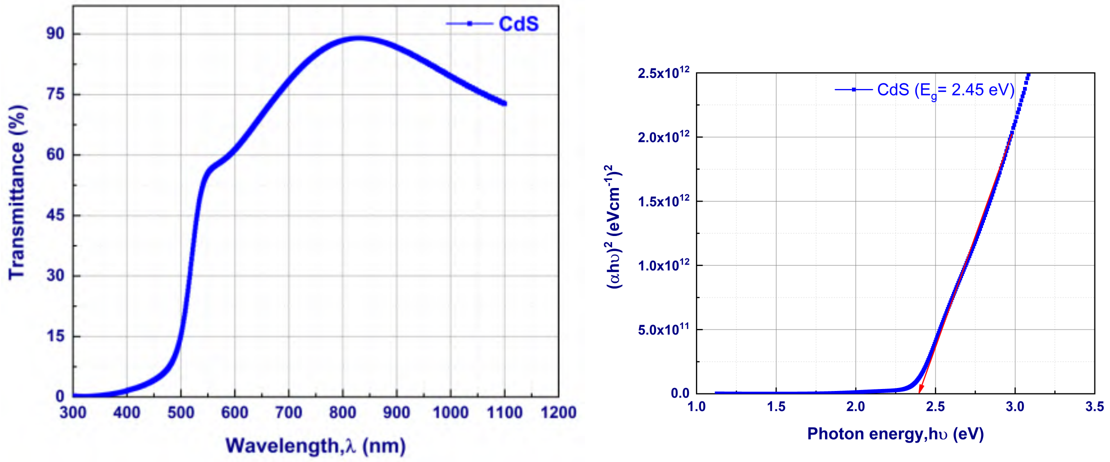

(c) Transmittance spectra: CdS **(d)** Band gap estimation: CdS

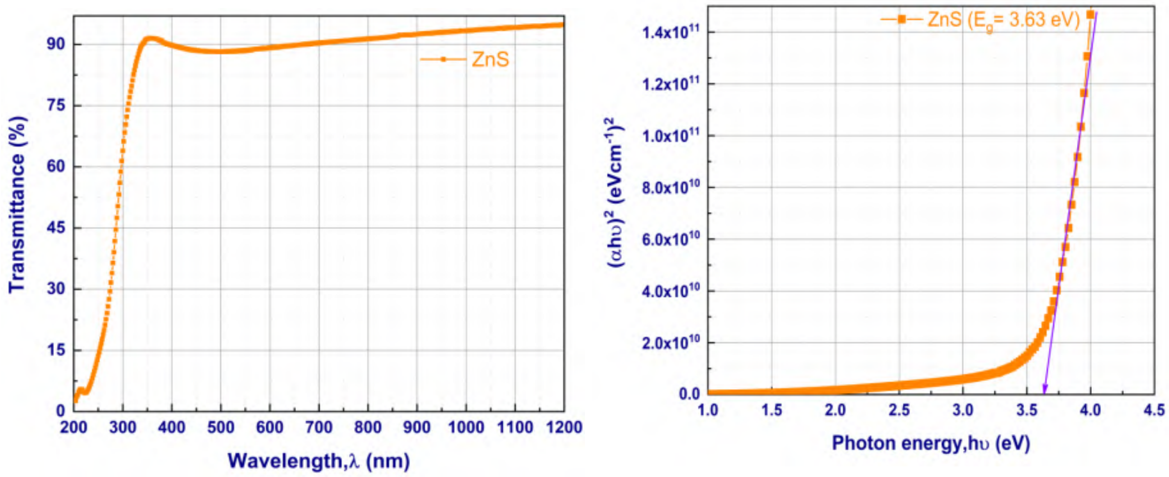

(e) Transmittance spectra: ZnS **(f)** Band gap estimation: ZnS

Figure 4.33: Optoelectronic properties of the fabricated thin films

4.4.4. Band alignment study at heterojunction interface

The band alignment at p-CZTS and n-CdS (or n-ZnS) was investigated using XPS and validated using SCAPS simulations.

Band alignments are Type-II (Figure 2.12 in Chapter 2) with a staggered-gap, as shown in Figure 4.34. CBO formed at the heterointerface of CZTS and CdS is conventionally "cliff-like" with -0.33 eV. In contrast, "spike-like" CBO at CZTS/ZnS is observed. As the observed value of CBO for this scenario is +0.75 eV, which is substantially higher than the permitted range [154], the barrier to the flow of light-generated carriers and recombination traps must be to blame.

SCAPS simulated observations are illustrated in Figure 4.35. When simulated using SCAPS data, very modest differences are seen in CBOs. Using experimental data in the SCAPS model reduces CBOs, though. In both instances, a 'cliff-like' CBO was obtained.

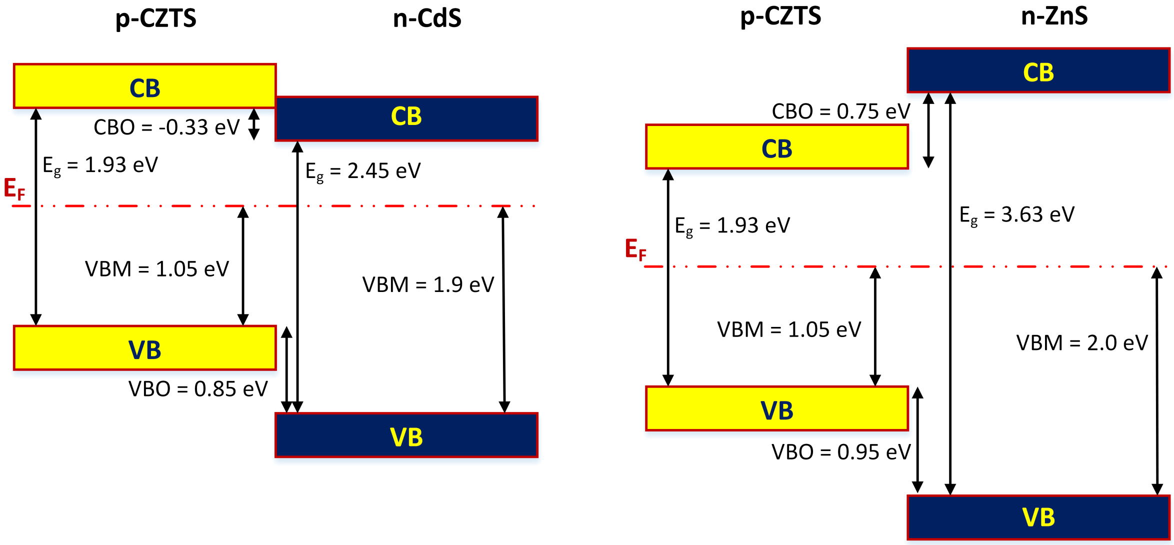

Figure 4.34: Band alignment at CZTS/CdS and CZTS/ZnS heterointerfaces using experimental data

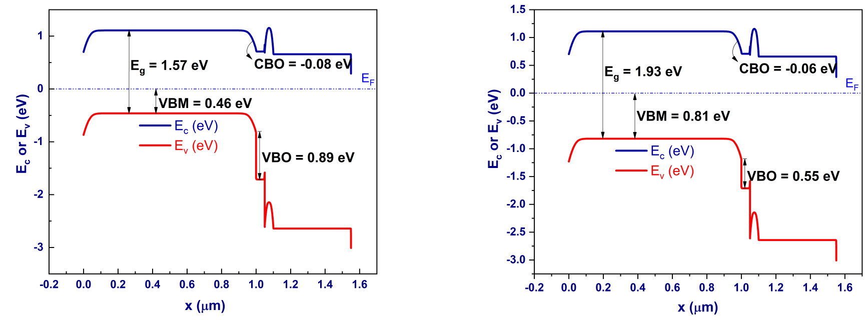

(a) Band alignment at CZTS/CdS (SCAPS) **(b)** Band alignment at CZTS/CdS (experimental)

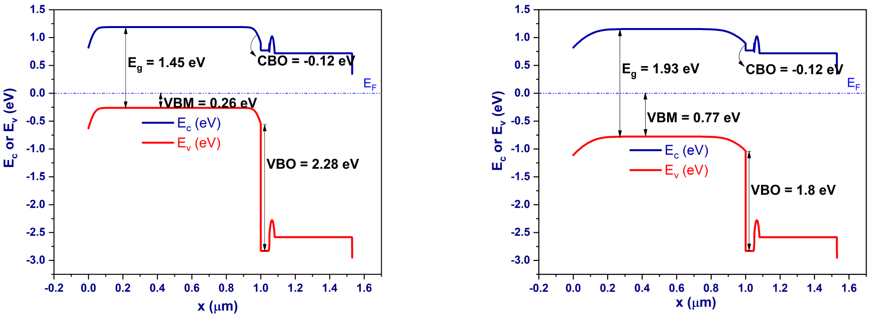

(c) Band alignment at CZTS/ZnS (SCAPS) **(d)** Band alignment at CZTS/ZnS (experimental)

Figure 4.35: Band alignment study at CZTS/CdS and CZTS/ZnS heterointerfaces using SCAPS and experimental data (Simulation)

4.5. Fabrication and characterization of ZnO:Ga (GZO) thin film by RF magnetron sputtering

4.5.1. Microstructural properties

Figure 4.36 displays the X-ray diffraction patterns of the Ga-doped Zinc Oxide (GZO) thin films grown at Ar flow rates of 10, 20, and 30 SCCM. The films that were deposited along the (002) plane are polycrystalline, as indicated by Bragg's diffraction peaks at 2θ = 33.98°, 33.91°, and 33.85°. These films have a hexagonal wurtzite crystal structure and an orientation along the c-axis that is perpendicular to the substrate. These findings are consistent with what we already know about the structural composition of ZnO:Al films [257]. The reason behind why GZO thin films have a tendency to be aligned along the c-axis is explained by the model that is described in [258]. This theory posits that during the first phases of deposition, nucleation can occur in a number of orientations. But, as the nuclei strive to develop, only the ones with the quickest growth rates will survive, and as a result, the c-axis orientation will be achieved. It became obvious that tensile tension was being created in the deposited thin films as the peaks migrated to lower diffraction angles as they progressed. The little shift in diffraction peaks may be caused by a low-level insertion of the Ga^{3+} cation into the ZnO crystal lattice, which occurs when the working sputtering pressure is changed [259]. We did not see any diffraction peaks resulting from the presence of any additional impurity phases. [260] research has shown that the ionic radius of Ga^{3+}, which is 0.62 Å, is smaller than that of Zn^{2+}, which is 0.74 Å. The predicted lattice constant, c, for all samples was found to be less than that of the ZnO thin films by themselves [261]. This was proven to be the case when the working pressures were increased. According to the findings of a study conducted by Li et al. [262], oxygen vacancies have the potential to lower this lattice constant. According to the findings of our most recent inquiry, the value of the lattice constant, c, although it did change slightly depending on the working pressures, stayed within the range of 5.27 to 5.29.

In order to determine the interplanar distance (d) and the lattice constant (c) [263], average crystallite size (D) using the Scherrer formula, the microstrain (ε), and the dislocation density (δ), and of the deposited films of the principal diffraction peak at the (002) plane, the equations given by Eq. [4.6], Eq. [4.1], Eq. [4.2], Eq. [4.3] were utilized and tabulated in Table 4.23.

$$\frac{1}{d_{hkl}^2} = \frac{4}{3}\left(\frac{h^2 + hk + k^2}{a^2}\right) + \frac{l^2}{c^2} \tag{4.6}$$

The crystallite size of the thin films remained practically unchanged at 19 nm even as the

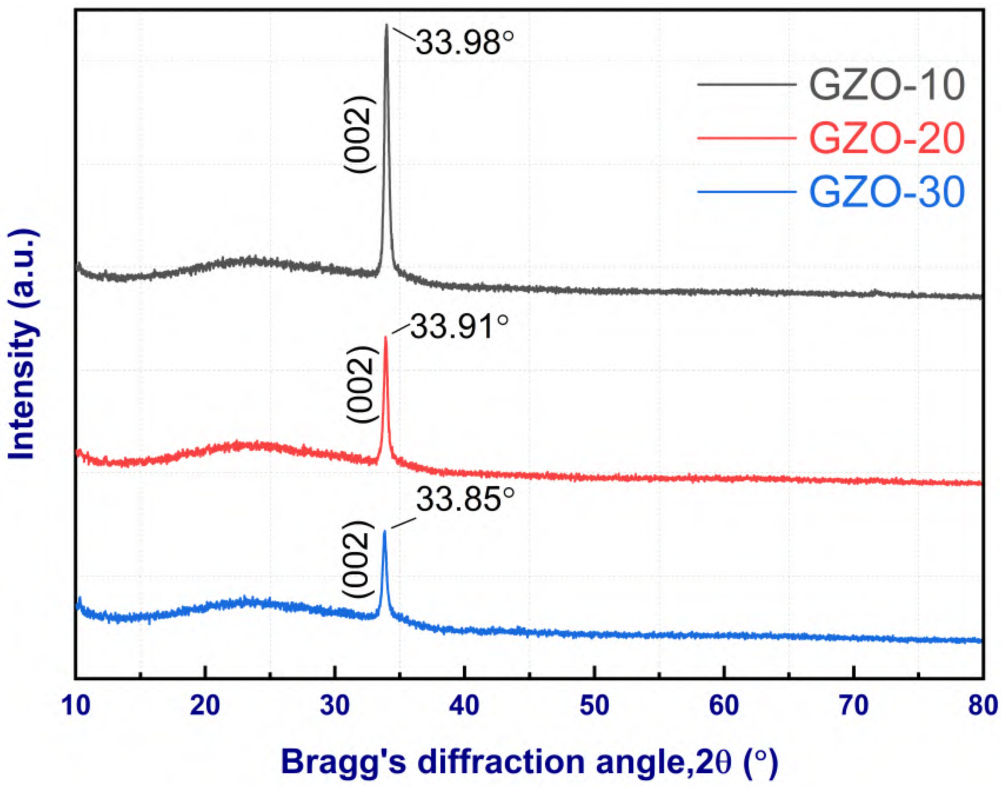

Figure 4.36: XRD patterns GZO thin films with different Ar flow rates

working sputtering pressure increased from 2.5 mTorr to 5.0 mTorr. (Table 4.23). When the working pressure was changed within these ranges, there was virtually very little difference in the microstrain and dislocation density. It is possible that the consequences of extrinsic point defects are to responsible for this. At high working pressures, more Ga^{3+} atoms enter the ZnO lattice, which results in the creation of extrinsic point defects such as Ga_{Zn} (Zn replacement by Ga) and Ga interstitial defects Ga_i. Increases in the working pressure of sputtering that were more than 3.8 mTorr led to a decrease in the intensity value of the diffraction peak [264]. This was because the value of the kinetic energy of the sputtered particles decreased as the working pressure was increased. As a direct consequence of this, the rate of deposition decreased even as the working pressure increased. In our analysis, a working pressure of 7.4 mTorr produced results that were comparable to those found in other studies. There is a possibility that contaminants in the sputtering chamber, such as N_2 and O_2, will prevent crystal formation [265]. As a consequence of this, it is possible to find that the generated thin films have improved crystallinity (as seen by the FWHW values) when the working pressure is kept low. This is because residual impurities are reduced to a less extent. In a similar vein, this is glaringly clear from our data. We are able to make the hypothesis that, at high working pressures, the

Table 4.23: The crystallographic data tabulated for the diffraction peak at (002) plane

Sample code	**2θ (°)**	θ^c	sinθ^c	cosθ^c	**d (Å)**	**FWHM (°)**	**D (nm)**	**c (Å)**	ε	δ
GZO-10	33.98	0.29653	0.29220	0.95635	2.64	0.430	19.3	5.27	6.14	2.68
GZO-20	33.91	0.29592	0.29162	0.95653	2.64	0.423	19.6	5.28	6.06	2.60
GZO-30	33.85	0.29540	0.29111	0.95668	2.65	0.502	16.5	5.29	7.20	3.66

majority of the Ga^{3+} atoms were located in the interstitial rather than in the crystal matrix.

4.5.2. Optoelectronic properties

4.5.2.1. Transmittance and optical band gap

Using Ultraviolet-Visible Near Infra Red (UV-Vis NIR) spectroscopy, an investigation into the optical properties of GZO thin films that were fabricated at varying Ar flow rates was carried out for the purpose of determining whether or not GZO could be useful as a TCO in PV applications. Figure 4.37a illustrates the average optical transmittance of deposited GZO thin films at visible wavelengths between 400 and 700 nm . Indicative of an increase in the band gap was a shift to the blue of the light absorption edge at 380 nm, which occurred when the sputter working pressure was increased. The Tauc plots [222] of GZO thin films are displayed in Figure 4.37b to provide supporting evidence for the concept. Tauc's plot obtained by using the formula (Eq. 4.4) to determine the optical band gap values of all samples.Plotting of $(\alpha h\nu)^2$ versus photon energy, hν and extrapolating the lines from the curves to determine the intercept with the hν axis [266, 267], gives optical band gap values of all samples.

For Ar flow rates of 10 sccm, 20 sccm, and 30 sccm, the optical band gaps were determined to be 3.13 eV, 3.23 eV, and 3.33 eV, respectively. The variation of optical band gaps can be well described by Burstein-Moss effect [268–270], related with the Eq. [4.7]:

$$\triangle E_g = \frac{h^2}{8m^*}\left(\frac{3n}{\pi}\right)^{2/3} \tag{4.7}$$

where,

n = carrier concentrations

m^* = effective mass of electrons Donor electrons reside in higher states above the bottom of the conduction band in severely doped n-type semiconductors such as GZO. This is due to the fact that the expression is mostly connected to carrier concentrations. According to Pauli's exclusion principle, optical transitions must be vertical since the energy levels cannot be occupied twice. This necessitates that optical transitions must be vertical. In order to reach higher energy states in the conduction band, valence electrons require a greater amount of energy [266, 271]. The optical band gap of GZO films widened as a direct consequence of this. The wide optical band gap of TCOs helped to reduce the amount of optical loss and improve the solar cell's overall optical utilization efficiency. As a consequence of this, the transparent conductive film with a large band gap proved to be a superior candidate for the electrodes of solar cells.

4.5.2.2. Urbach energy

Urbach energy, E_u plays a very crucial role in the process of identifying solutions to band tailing issues caused by structural disorder, phonons, excitons, and contaminants. Urbach tail refers to the absorption edge that lies below the exponentially increasing energy gap [227]. The E_u is described within the framework of Einstein's model, and it is feasible to reduce it to an empirical formula stated by [228] and illustrated by Eq. 4.5. In a literature [229], the procedures for calculating the numerical values of Urbach energy are also described in depth. For samples GZO-10, GZO-20, and GZO-30, the Urbach energy of deposited GZO thin films were determined to be 176 meV, 300 meV, and 153 meV, respectively. Figure 4.37c depicts the changes of E_u with Ar flow rates along with optical band gaps in GZO thin films . Significant band tailing problems were detected in the film at middle Ar flow rates of 20 sccm in this study.

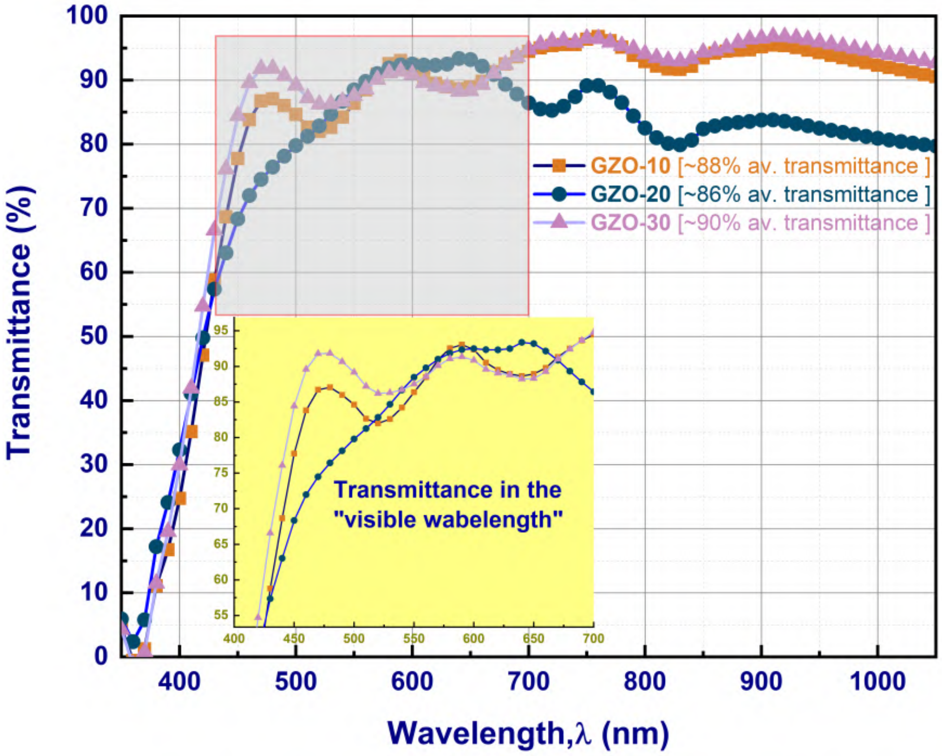
Transmittance (%)
Wavelength,λ (nm)
GZO-10 [~88% av. transmittance]
GZO-20 [~86% av. transmittance]
GZO-30 [~90% av. transmittance]
Transmittance in the "visible wabelength"
0
10
20
30
40
50
60
70
80
90
100
400
500
600
700
800
900
1000
400
450
500
550
600
650
700
55
60
65
70
75
80
85
90
95

(a)

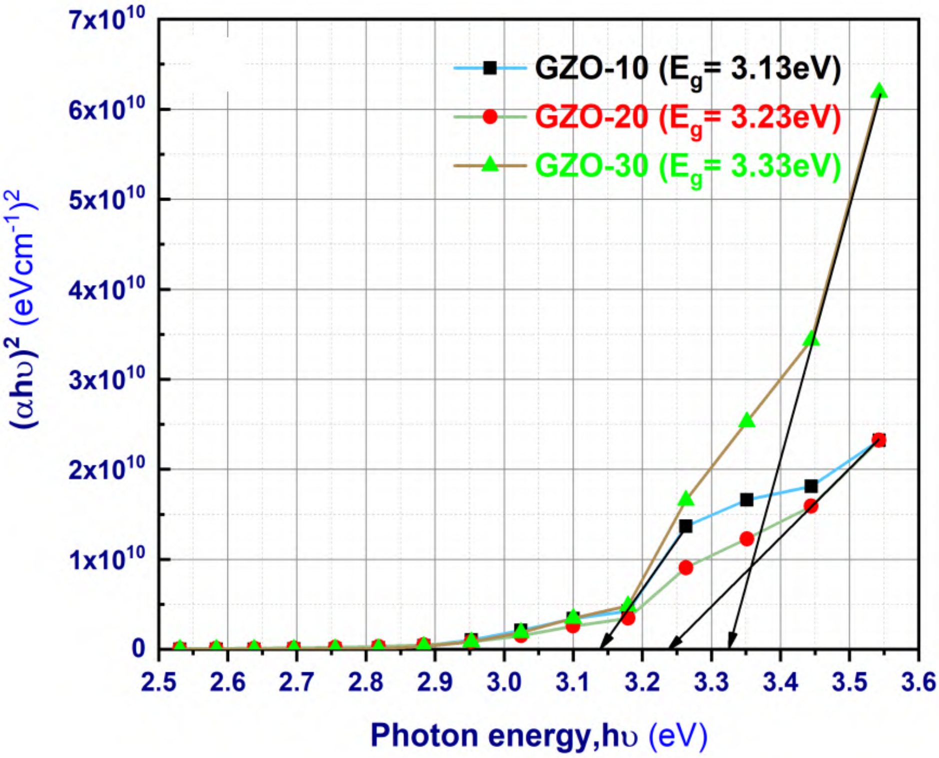
(αhυ)² (eVcm⁻¹)²
Photon energy,hυ (eV)
GZO-10 (Eg= 3.13eV)
GZO-20 (Eg= 3.23eV)
GZO-30 (Eg= 3.33eV)
0
1x10¹⁰
2x10¹⁰
3x10¹⁰
4x10¹⁰
5x10¹⁰
6x10¹⁰
7x10¹⁰
2.5
2.6
2.7
2.8
2.9
3.0
3.1
3.2
3.3
3.4
3.5
3.6

(b)

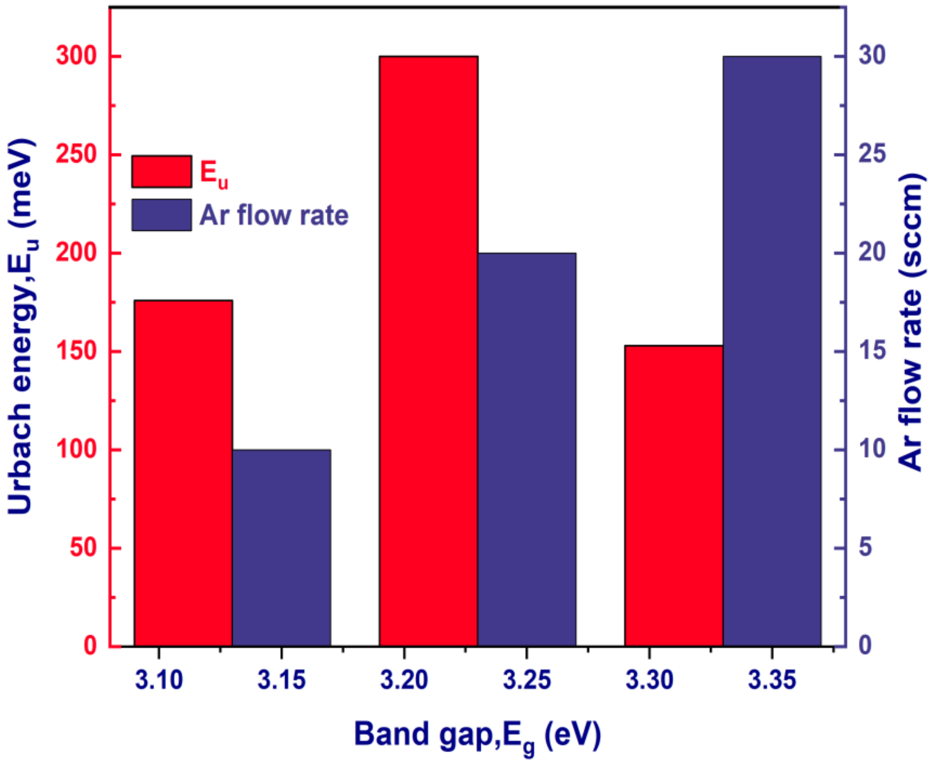

(c)

Figure 4.37: The variation of transmittance (a), optical band gaps (b), and associated band tailing issues (c) for GZO-10, GZO-20, and GZO-30 samples

4.5.2.3. Optical constants

The refractive index and other dispersion characteristics play a crucial role in the determination of the electronic properties of semiconductor materials; hence, they are the most significant design parameters [272] . Consequently, it is important to investigate the influence of sputtering working pressures on optical constants.

The complex index of refraction, $\boldsymbol{n}$, of a non-magnetic material is connected to the complex dielectric constant, $\boldsymbol{\varepsilon_r}$, by a relation Eq. [4.8], which is a consequence of Maxwell's equations. According to Eq. [4.9] and Eq. [4.10], these complex values may be decomposed into frequency-dependent real and imaginary components.

$$\boldsymbol{n} = \sqrt{\boldsymbol{\varepsilon_r}} \tag{4.8}$$

$$\boldsymbol{n} = n + jk \tag{4.9}$$

$$\boldsymbol{\varepsilon_r} = \varepsilon_1 + j\varepsilon_2 \tag{4.10}$$

where,

n = real part of the complex index of refraction

k = imaginary part of the complex index of refraction, known as extinction coefficient

ε_1 = real part of complex dielectric constant

ε_2 = imaginary part of complex dielectric constant

The loss factor, $\tan\delta$ can be expressed by the Eq. [4.11].

$$\tan\delta = \left(\frac{\varepsilon_2}{\varepsilon_1}\right) \tag{4.11}$$

In optical investigations, n and k are calculated directly from transmittance, reflectance, and absorption coefficients as probed by UV-Vis NIR spectroscopy. In practice, n is initially computed using the equations Eq. [4.12] and Eq. [4.13] as proposed by the Swanepoel technique [273] in the medium and weak absorption region of transmission spectra as a function of incident photon wavelengths. Then, k is computed using Eq. [4.14]. After determining the values of n and k, dielectric constants are determined by equating real and imaginary components using Eq. [4.8]. The found relations are represented by Eq. [4.15] and Eq. [4.16].

$$n = \left[N + \left(N^2 - s^2\right)^{1/2}\right]^{1/2} \tag{4.12}$$

where,

$$N = 2s\frac{T_M - T_m}{T_M T_m} + \frac{s^2+1}{2} \tag{4.13}$$

T_M and T_m are the maxima and minima of the transmission envelopes' peak of the samples under considerations and s is the index of refraction of SLG substrate and we used a value of 1.52 throughout our calculations.

$$k = \left(\frac{\lambda\alpha}{4\pi}\right) \tag{4.14}$$

$$\varepsilon_1 = n^2 - k^2 \tag{4.15}$$

$$\varepsilon_2 = 2nk \tag{4.16}$$

4.5.2.4. *Complex refractive index*

The refractive index of a material depends on the scattering of photons within it. It can be the consequence of electron-photon, phonon-photon, and other scattering processes, such as

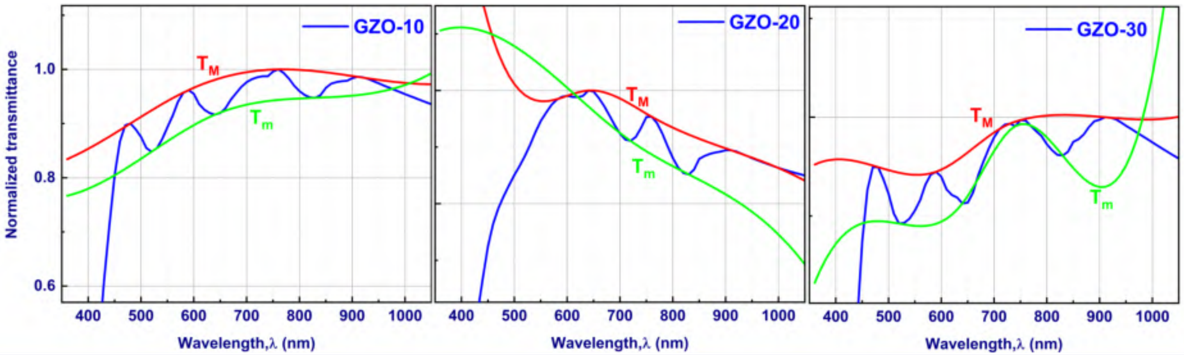

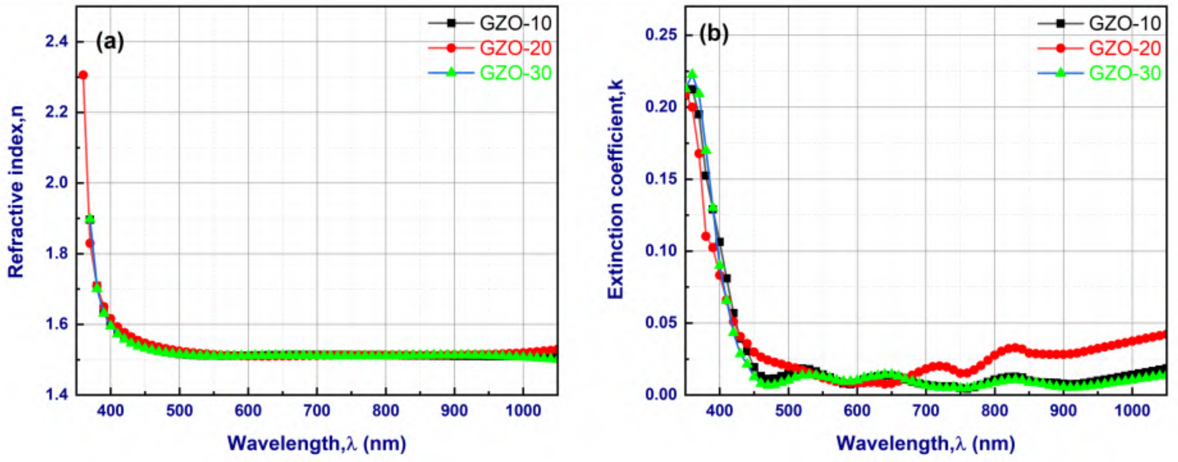

Figure 4.38: The variation of: (a) refractive index,n (b) extinction coefficient,k. (With incident λ_{photon} for the samples GZO-10, GZO-20, and GZO-30.)

traps and irregularities, which can be considered scattering centers. Photons can go through a material with less scattering if the refractive index is lowered. Therefore, the value of transmission must grow as the refractive index decreases. Figure 4.38(a) and Figure 4.38(b) depict the fluctuation of the real and imaginary parts of the complex refractive index as a function of sputtering working pressure with respect to incident photon wavelengths. For samples GZO-10 and GZO-30, the n and k were found to be nearly stable at 1.52 and 0.008 for all sputtering working pressures and 500-1000 nm wavelengths. GZO-20 sample's extinction coefficient,k rose in the near infrared range (800 nm and above) as an exception. This rise is a result of the direct electronic transition near the absorption edge area, which decreases the absorption coefficient. However, this rise in k may also be connected with an increase in defects in the films [274].

4.5.2.5. *Complex dielectric permittivity*

The complex dielectric function depicts how the optical characteristics of a material depend on the wavelength of incoming light. Figure 4.39a and Figure 4.39b depict the fluctuation of the real and imaginary components of the complex dielectric constant as a function of sputtering working pressure with regard to incoming photon energy, respectively. The real component of the dielectric constant, ε_1, remains constant at 2.28 for all sputtering working pressures up to 2.5 eV in photon energy. After that, ε_1 grew steadily to 5.3 for the GZO-20 sample and 3.56 for the GZO-10 and GZO-30 samples at 3.4 eV photon energy, respectively. Almost same patterns are seen for the imaginary portion, ε_2 except for the transition that occurred at 3.75 eV. As the sputtering working pressure increased, the charge carrier mobility and hopping rate increased, resulting in a rise in dielectric polarization and hence dielectric constants.

Figure 4.39c illustrates the relationship between dielectric loss, tan δ, and incoming photon energy at various sputtering working pressures. As a result of the rising nature of ε_1 and ε_2 with increasing photon energy, as discussed above, the tan δ is likewise shown to grow with increasing sputter working pressures at higher photon energies.

4.5.2.6. *Optical conductivity*

The optical conductivity, σ_{opt} is an important criterion for determining the electronic state in materials, and it is directly dependent on the absorption coefficient as well as the refractive index. σ_{opt} can be calculated using the Eq. [4.17].

$$\sigma_{opt} = \left(\frac{\alpha c_0}{4\pi}\right) = \left(\frac{\alpha n c}{4\pi}\right) \tag{4.17}$$

where, c_0 = speed of light in vacuum
c = speed of light through the sample

The fluctuation of σ_{opt} with incoming photon energy for the three studied samples is depicted in Figure 4.40. It can be observed that σ_{opt} rises as photon energy increases. In addition, it is noticed that the optical conductivity follows the same pattern as the refractive index as the wavelength increases. After 2.75 eV, the σ_{opt} was observed to grow significantly. This is because the absorption coefficient has increased significantly. Similar outcomes have been reported in [275].

4.5.2.7. *Electrical properties*

In addition to optical qualities, the carrier transport capacity of transparent electrodes is also a good contributing factor in determining the solar cell efficiency. In order to explore the

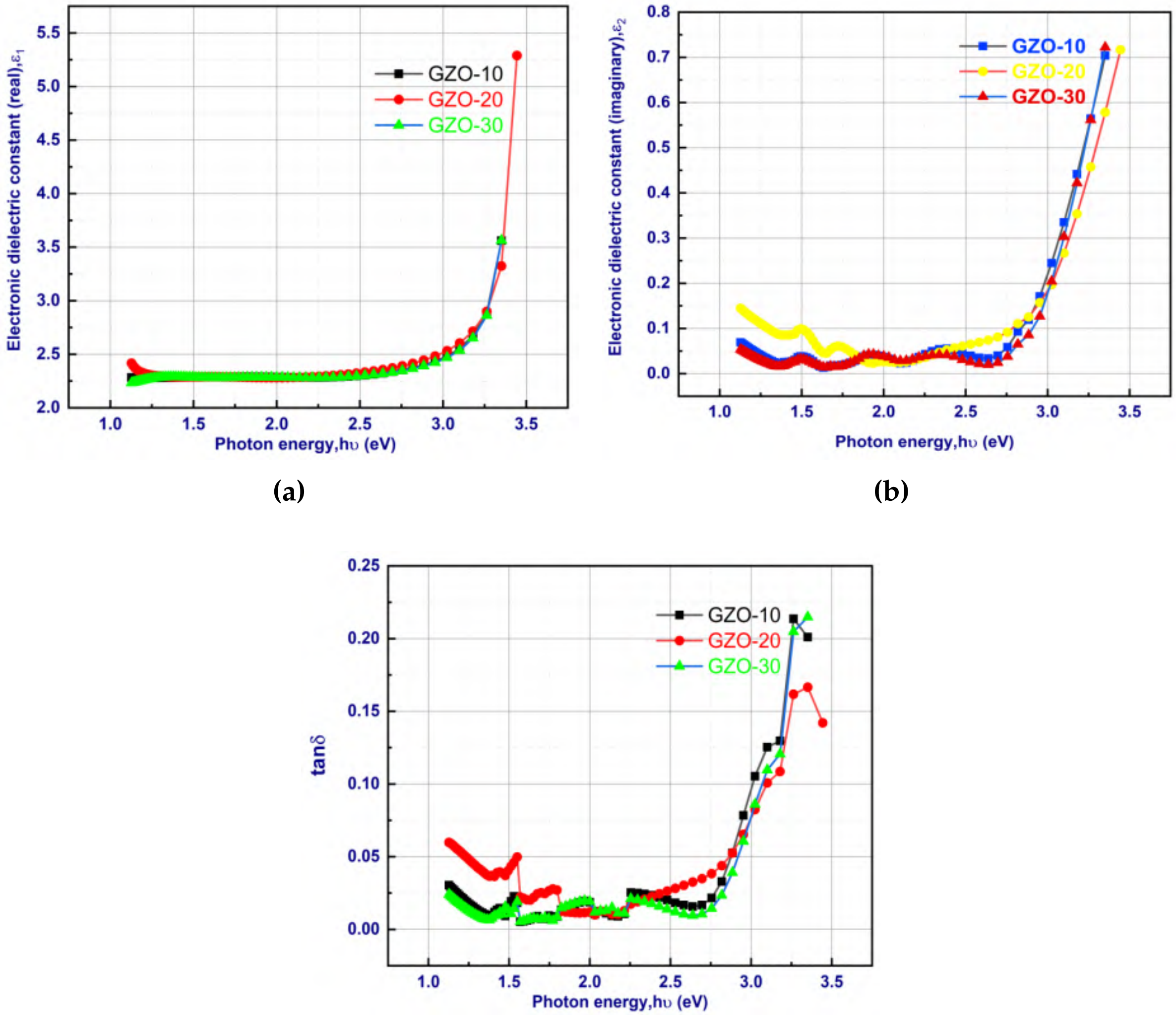

(a) **(b)**

(c)

Figure 4.39: The variation of: (a) ε_1, (b) ε_2, (c)loss factor,tan δ (With incident photon energy)

effect of Ar flow rate on the electrical characteristics of GZO thin films, Figure 4.41 depicts the fluctuation of electron carrier concentration,n carrier mobility, μ_n, and resistivity, ρ of GZO films at various Ar flow rates. Figure 4.41 also demonstrates that the n dropped as the Ar flow rate grew from 10 to 20 sccm and subsequently marginally increased as the Ar flow rate climbed to 30 sccm. Consequently, the Burstein-Moss effect may be assumed to be valid in our study's high sputter working pressure regime with Ar flow rates (20-30 sccm). One of the causes for the reduction in mobility is the dispersion of carriers at grain boundaries. Moreover, when the flow velocity of Ar rose, a larger density of ionized impurities led to a stronger scattering of carriers, which ultimately produced a loss in mobility [276].

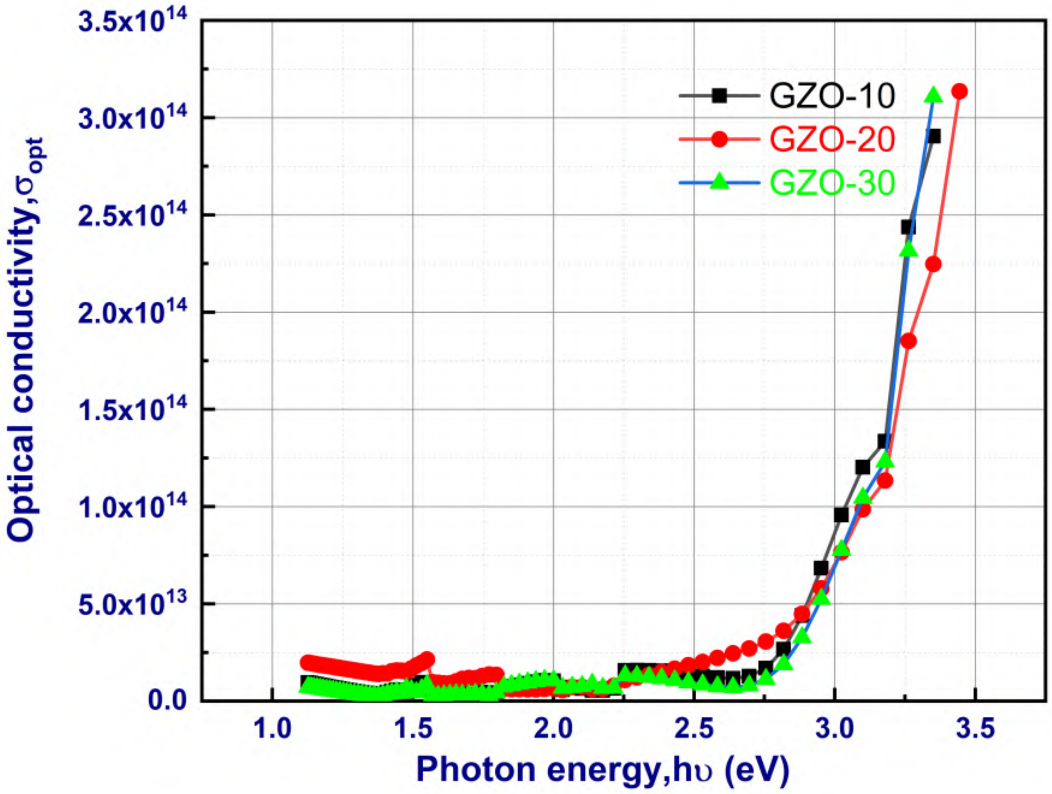

Figure 4.40: The fluctuation of optical conductivity, σ_{opt} with incoming photon energy for the samples GZO-10, GZO-20, and GZO-30

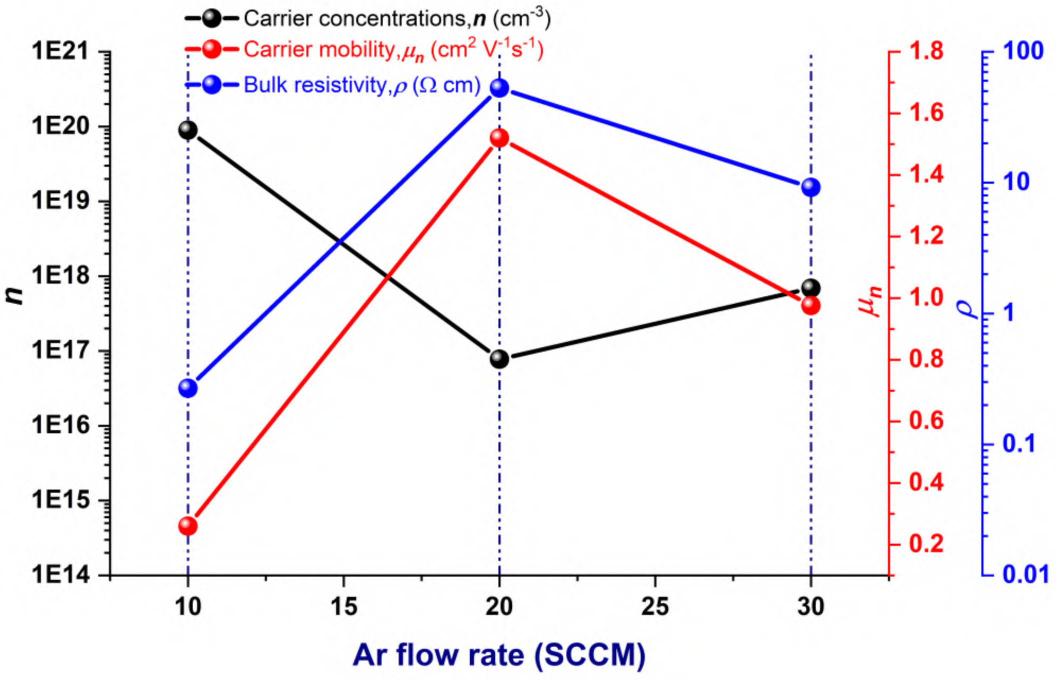

Figure 4.41: Variation of electron carrier concentration (n), carrier mobility (μ_n), and resistivity (ρ) of GZO thin films at various Ar flow rates of 10 sccm, 20 sccm, and 30 sccm

The expression for, the resistivity ρ, is Eq. [4.18].

$$\rho = \frac{1}{nq\mu} \tag{4.18}$$

Thus, it is evident that carrier concentration and mobility have a direct effect on film resistivity. The minimum resistivity was 2.69 × 10^{-1} Ω.cm at a 10 sccm Ar flow rate.

It is well established that the resistivity of a polycrystalline conducting film, such as GZO, is influenced by film thickness [277]. Evidently, the resistivity was highly dependent on the value of working pressure when the RF power density was held constant (2.5 W/cm^2 in our study). As deposition rate tends to decrease as sputtering working pressure increases, at a fixed deposition period (60 minutes in our study), the fabricated GZO films were observed to have decreasing thicknesses.

4.5.2.8. Figure of merit

The transmittance of GZO thin films rises as their thickness decreases. Therefore, resistance and transmittance should have an optimal value in order for the film to function optimally. Haacke [278] established the Figure of Merit (FOM) for evaluating the performance of TCO as given in Eq. [4.19], where T is the transmittance and R_{sh} denotes the sheet resistance of the films. According to Haacke, $x = 10$ is the best option since it simplifies numerical computations for FOM (ϕ_{TC}) in practice. According to Eq. [4.20], the sheet resistance, R_{sh}, is linked to the bulk resistivity, ρ and the film thickness, t. The GZO-10 sample has the greatest average FOM of 6.36 ×10^{-5} Ω^{-1}.

$$\phi_{TC} = \left(\frac{T^x}{R_{sh}}\right) \tag{4.19}$$

$$R_{sh} = \left(\frac{1}{\rho t}\right) \tag{4.20}$$

Table 4.24: Electrical properties of GZO thin films along with FOM

Sample	**t**	ρ	R_{sh}	n	μ_n	T^{10}/R_{sh}	**Rank**
GZO-10	473	0.269	5.68×10^{3}	8.94×10^{19}	0.260	6.36×10^{-5}	1
GZO-20	237	52.8	2.23×10^{6}	8.00×10^{16}	1.52	7.24×10^{-8}	3
GZO-30	158	9.19	5.82×10^{5}	7.00×10^{17}	0.976	8.02×10^{-7}	2

t = Thickness (nm)
ρ = Bulk resistivity (Ω.cm)
R_{sh} = Sheet resistance (Ω)
n = Carrier concentrations (cm^{-3})
μ_n = Carrier mobility (cm^2/Vs)
FOM = Figure of Merit

4.6. Chapter summary

The experiments presented in this chapter used a variety of characterization approaches to acquire a better understanding of the fundamental physical properties of thin-films and solar cells that rely on pure sulfide CZTS absorbers. SCAPS-1D simulation tool was used for numerical study. The method used to create CZTS thin films using RF magnetron sputtering is essentially a two-phase process that includes precursor deposition and high-temperature annealing with elemental sulfur. When the films were subjected to a deposition temperature of 500°C, their optoelectronic and microstructural properties were found to be superior. While the traditional optimal annealing temperature is normally 550°C, the highest temperature setting capabilities of our sputtering machine produced equivalent results. According to the experimental results, the open-circuit voltage observed in the presence of a CdS buffer layer deposited using the CBD approach was 350 mV. Making an ohmic contact grid is challengin. J_{sc} could not be determined, may be because the contacts have a high resistance.

According to the findings of a study on Ge-alloyed CZTS thin film, the insertion of Ge can effectively reduce the concerns of band gap variations and band tailing. This, in turn, reduces the V_{oc} deficit and improves the overall performance of the device. The main finding of the study suggests that films composed of alloyed CZTGS with varying concentrations of x exhibited a significant improvement in their structural and optical properties. A limitation of this study is that more precise control of the co-sputtering process and increasing the range of

x would be better.

This study filled a knowledge gap by introducing (Cd,Mg) codoping in CZTS via a sol-gel spin coating technique. The main finding of the study was that CZCMTS-1 with x = 0.29, y = 0.11, i.e. 40% partial substitution of Zn, substantially reduced Cd concentrations (compared to prior study) without sacrificing favorable features and crystal structure. A simple TFSC constructed in a superstrate structure shown an improvement in PCE. Furthermore, CZCMTS-1/CdS band alignment revealed "cliff-like" CBO with -0.12 eV, which was consistent with earlier research. The V_{oc} deficiency was lowered by 23% (around 335 mV). The goal of this codoping technique was not to chase PCE, but rather to identify rational photovoltaic behavior after successful doping as simulation, which was performed effectively. Poor PCE as a direct result of lower values of J_{sc} and FF could be attributed to a non-ohmic contact grid, a high value of series resistance, and a low value of shunt resistance. While the superstrate constructed device is really well-suited for controlling material composition, it becomes less appropriate when subjected to high temperature treatment. The aforementioned approach might be similarly employed in the context of substrate structure devices to enhance photovoltaic characteristics. Additionally, dimethyl sulfoxide (DMSO) was employed as a solvent in the sol-gel spin coating procedure, resulting in a surface that exhibited roughness, as indicated by the analysis of 3D profilometry. The utilization of an alternative solvent, which is both non-toxic and non-hazardous, apart from dimethyl sulfoxide (DMSO), has the potential to enhance the current state of affairs and exert an influence on the overall efficiency of the photovoltaic (PV) system.

Another finding reveals that using the successive ionic layer adsorption and reaction (SILAR) approach during ZnS deposition results in the creation of a distinct "spike-like" conduction band offset (CBO) with CZTS absorber. The value of CBO measured using the ZnS buffer is +0.75 eV, which is slightly higher than the value indicated in the literature. Precise composition control during deposition may lower the value.

Films were produced in a final investigation on window layer by altering the Ar flow rates (i.e. working pressures) in an RF magnetron sputtering system. It is easier to employ a single target GZO instead of ZnO and Ga_2O_3 co-sputtering, and precise composition control is achievable. At room temperature deposition, samples deposited with 10 scccm Ar flow rates rated first due to their lowest bulk (0.269 Ω.cm), sheet resistance (5.68103 Ω), and maximum carrier concentrations (8.94×10^{19} cm^{-3}) values.

Chapter 5: CONCLUSIONS

This chapter attempts to provide a comprehensive summary of the research results in connection to the research goals and questions, and to discuss their worth and contribution. Additionally, this study will critically assess the constraints inherent in the research design and put forward potential avenues for future investigation.

5.1. Conclusions

Thin-film photovoltaics have emerged as a promising area of research due to their potential to serve as a renewable and environmentally sustainable source of electricity production. It is anticipated that this field will continue to be actively pursued in the foreseeable future. However, prior to making any progress towards the commercialization of technologies like CZTS and its alloys, it is imperative to address several challenges. The current challenges related to CZTS primarily pertain to fundamental aspects. The primary focus in assessing the feasibility of this technology is to address the problem of inadequate PCE. The suboptimal performance of CZTS thin film device can be accredited to recombination in deep acceptor type defects and V_{oc} deficit. This research aimed to investigate on CZTS absorber layer, buffer layer, window layer, and CZTS TFSC, employing RF magnetron sputtering and sol-gel spin coating techniques.

This research employed various characterization techniques to acquire a deeper understanding of the fundamental physical properties of thin-films and solar cells that rely on pure sulfide CZTS absorber. SCAPS-1D simulation tools were also utilized in certain numerical investigations.

Adopting an alternative process done at 500°C substrate temperature, the CZTS absorber layer was achieved with the bandgap of 1.5 eV and V_{oc} of 350 mV from a rudimentary CZTS TFSC device, which verifies the acceptability of the subsequent high-temperature annealing step avoidance. The study was limited by the inability to measure short-circuit current density due to poor formation of grid contacts.

Newly adopted co-sputtering approach for Ge-alloyed CZTS thin films showed improved morphology, crystallite size, microstrain, and dislocation density at $x = 0.38$, which is important for high-efficiency TFSC. The presence of secondary phases in Ge-alloyed samples has been detected. Two tetragonal secondary phases Cu_2GeS_3 and Cu_2SnS_3 were detected in Ge-alloyed sample.

The current research endeavor entailed an examination of the characteristics of co-doped (Cd,Mg) CZTS thin films and superstrate structured TFSCs. This research concerns the analysis of band alignments in co-doped CZTS films and conventional CdS heterointerfaces. The veracity of both claims was verified via simulation. The hypothesis posited that the inclusion of Mg would lead to a reduction in the levels of Cd in the doped specimen, while retaining the advantages of Cd as the sole substitute. It has been observed that Cadmium (Cd) and Magnesium (Mg) can serve as viable substitutes for Zinc (Zn) at the site of Kesterite Copper Zinc Tin Sulfide (CZTS) on an isoelectronic level. The primary outcome of the study reveals that the joint substitution of Cd and Mg led to an enhancement in power conversion efficiency, which was achieved by partially substituting 40% of Zn cation. A reduction of 23% V_{oc} deficit was observed. Furthermore, a CBO resembling a cliff-shape was achieved, exhibiting a minimum energy level of 0.12 eV. One possible drawback of this work is that it might benefit from replication using a device built with a standard substrate structure.

For the alternative buffer layer and its fabrication process, ZnS thin films by SILAR technique may be able to functionally replace the CdS buffer layer, with preferable spike-like CBO. This is in contrast to the conventional CBD method employed in the fabrication of CdS buffer layer.

The proposition to replace AZO with GZO as a window layer was founded on the latter's remarkable film transmittance, which stands at approximately 88%, and its bulk resistivity of 0.269 Ω.cm. These characteristics were achieved using an Ar sputtering gas flow rate of 10 sccm.

5.2. Recommendation for future research

One aspect of this study elucidates the impact of co-doping CZTS absorber layer with (Cd, Mg) on the PCE and V_{oc} deficit of basic superstrate-structured TFSCs. However, research into CZTS TFSCs with a substrate structure is also essential.

The present study investigates a co-doping approach involving Cd and Mg dual atoms targeting the cationic site (Zn) of CZTS to mitigate the incidence of Cu_{Zn} antisites. Further investigation is warranted into the utilization of this approach in conjunction with co-doping involving Ag for the purpose of introducing a partial cation substitution of Cu-atom.

This research employed XPS to examine the band alignment occurring at the interface of the heterojunction, specifically between the co-doped absorber and CdS. Enhancement of the precision of this study could be achieved through the utilization of advanced methodologies such as UPS in combination with XPS.

The CZTS and ZnS exhibit a small lattice mismatch, leading to a favorable "spike-like" CBO when utilizing the SILAR method. In light of the toxicity presented by CdS in CZTS solar cells, ZnS has been recommended as a safe replacement. Accurate manipulation of the composition of the film is imperative to achieve the necessary spike-like band alignment within the 0 to 0.4 eV range. As the obtained value did not fall within the specified parameters.

Appendix A: Supplementary data

A.1. Parameters used in numerical simulation

A.2. Thickness measurements

A.3. XPS survey spectra

Table A.1: SCAPS input data

Material properties	**Symbol**
Band gap (eV)	E_g
Electron affinity (eV)	χ_e
Relative dielectric permittivity	ε_r
Conduction band effective density of states (1/cm^3)	N_c
Valence band effective density of states (1/cm^3)	N_v
Electron mobility (cm^2/Vs)	μ_n
Hole mobility (cm^2/Vs)	μ_p
Acceptor concentration (1/cm^3)	N_A
Donar concentration (1/cm^3)	N_D
Absorption coefficient (1/cm)	α

Table A.2: Layer properties

Parameters			**Layers**		
	ZnO:Al	**i-ZnO**	**ZnS**	**CdS**	**CZTS**
Thickness [μm]	0.45	0.05	0.05	0.05	1.0
Bandgap E_g [eV]	3.3	3.3	3.6	2.4	1.45
Electron affinity χ [eV]	4.6	4.55	4.4	4.5	4.5
Relative dielectric permittivity ε_r [eV]	9	8.12	9	10	10
Conduction band effective density of states N_C [cm^{-3}]	2.2×10^{18}	4.1×10^{18}	3.0×10^{18}	2.8×10^{19}	2.2×10^{18}
Valence band effective density of states N_V [cm^{-3}]	1.8×10^{19}	8.2×10^{19}	1.8×10^{19}	2.4×10^{18}	1.8×10^{19}
Electron themal velocity [cm/s]	1×10^{7}	1×10^{7}	1×10^{7}	1×10^{7}	1×10^{7}
Hole themal velocity [cm/s]	1×10^{7}	1×10^{7}	1×10^{7}	1×10^{7}	1×10^{7}
Electron mobility μ_n [cm^2/V.s]	1×10^{2}	1×10^{2}	1×10^{2}	3.5×10^{2}	1×10^{2}
Hole mobility μ_p [cm^2/V.s]	2.5×10^{1}	2.0×10^{1}	2.5×10^{1}	5.0×10^{1}	2.5×10^{1}
Donor density N_D [cm^{-3}]	1.0×10^{18}	1.0×10^{10}	1.1×10^{17}	1.0×10^{17}	0
Acceptor density N_A [cm^{-3}]	0	0	0	0	1.0×10^{17}
Absorption coefficient α [cm^{-1}]	SCAPS	SCAPS	Experimental	Experimental	Experimental

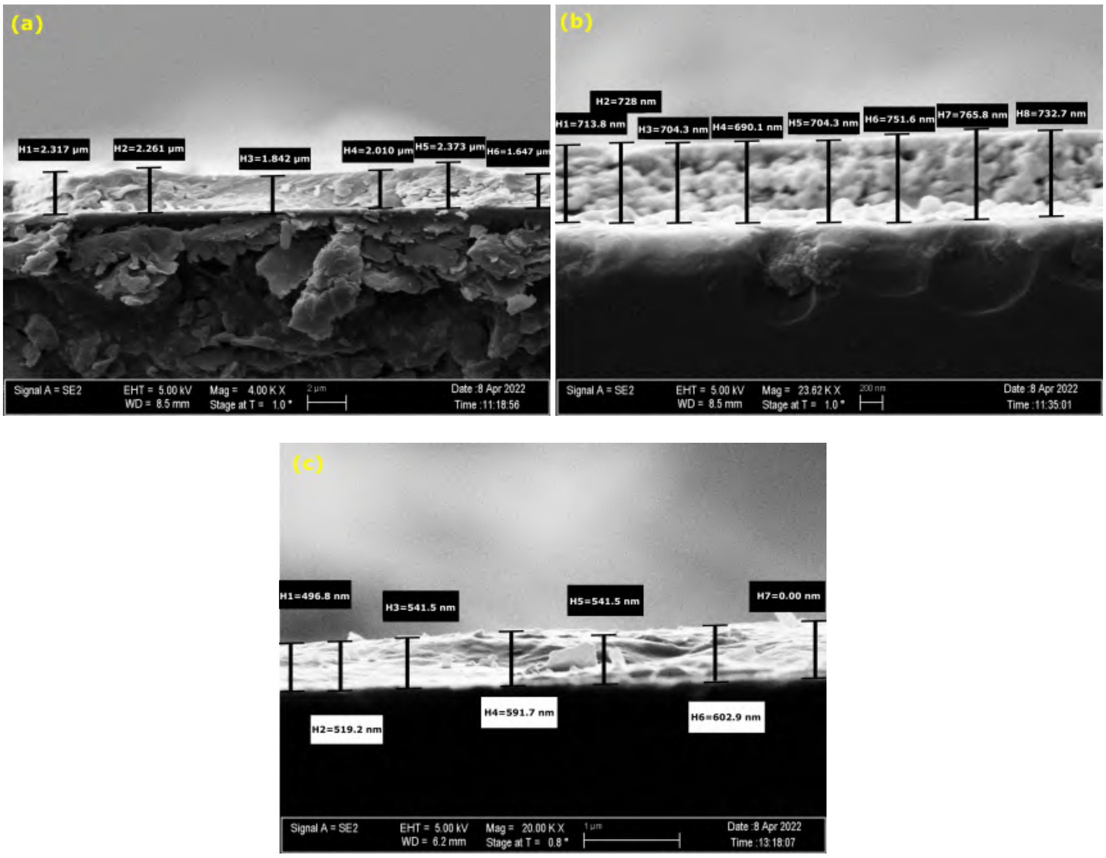

Figure A.1: Thickness measurements: (a) C-00 (b) C-Cd and (c) C-Mg

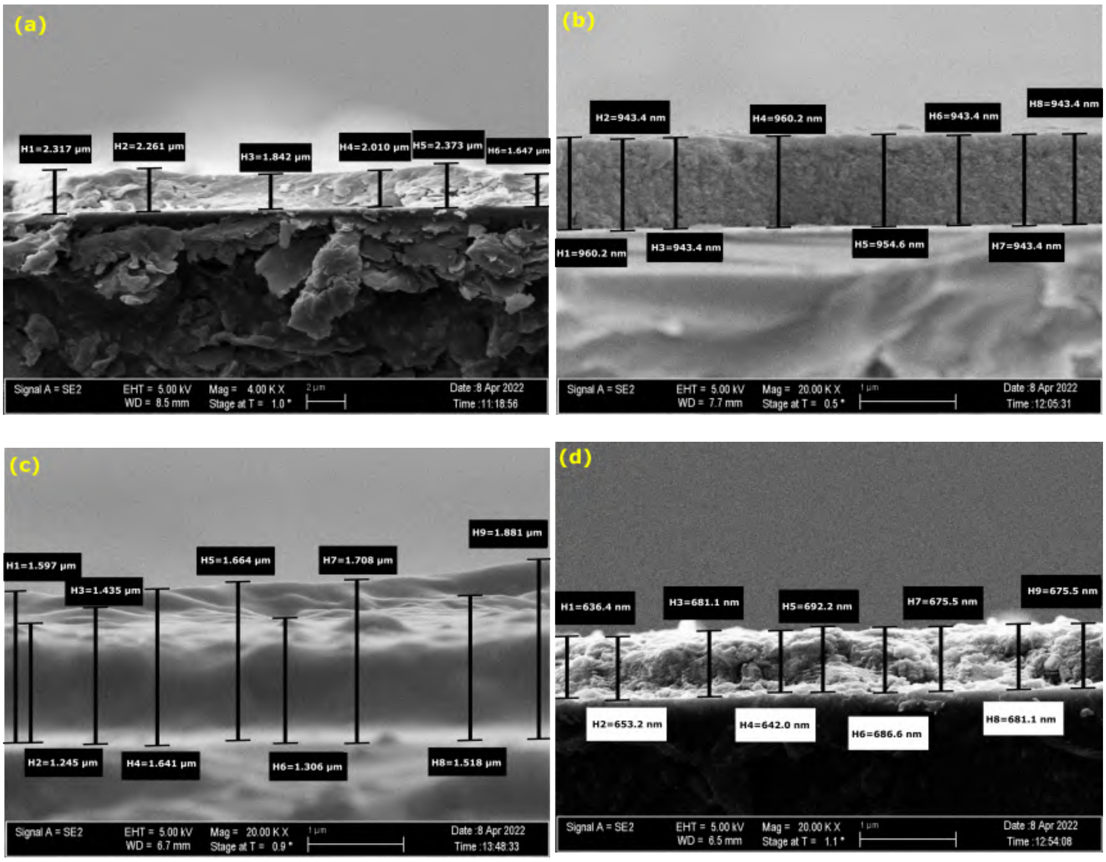

Figure A.2: Thickness measurements: (a) CZTS-0 (b) CZCMTS-1 (c) CZCMTS-2 and (d) CZCMTS-3

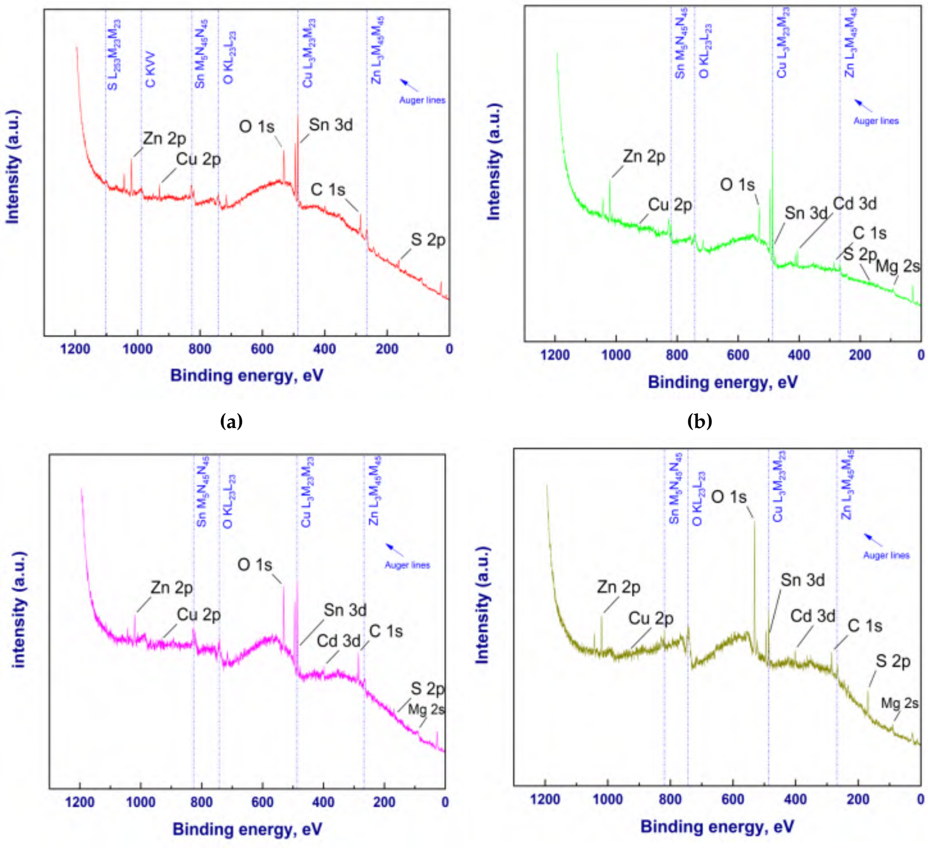

(a)

(b)

(c)

(d)

Figure A.3: Survey spectra: (a) CZTS-0 (b) CZCMTS-1 (c) CZCMTS-2 and (d) CZCMTS-3

Bibliography

[1] H. Katagiri, N. Sasaguchi, S. Hando, S. Hoshino, J. Ohashi, and T. Yokota, "Preparation and evaluation of Cu_2ZnSnS_4 thin films by sulfurization of E-B evaporated precursors," *Solar Energy Materials and Solar Cells.*, vol. 49, p. 2094, Dec. 1997.

[2] W. Shockley and H. J. Queisser, "Detailed balance limit of efficiency of p-n jun.ction solar cells," *Journal of Applied Physics*, vol. 32, pp. 510–519, Jun. 1961.

[3] H. Katagiri, K. Jimbo, M. Tahara, H. Araki, and K. Oishi, "The Influence of the Composition Ratio on CZTS-based Thin Film Solar Cells," in *MRS Online Proceedings Library*, Aug. 2009, p. 1165.

[4] S. Chen, J.-H. Yang, X. G. Gong, A. Walsh, and S.-H. Wei, "Intrinsic point defects and complexes in the quaternary kesterite semiconductor Cu_2ZnSnS_4," *Phys. Rev. B*, vol. 81, p. 245204, Jun. 2010.

[5] Y. E. Romanyuk, S. G. Haass, S. Giraldo, M. Placidi, D. Tiwari, D. J. Fermin, X. Hao, H. Xin, T. Schnabel, M. Kauk-Kuusik, P. Pistor, S. Lie, and L. H. Wong, "Doping and alloying of kesterites," *Journal of Physics: Energy*, vol. 1, p. 044004, Aug. 2019.

[6] S. Chen, X. G. Gong, A. Walsh, and S.-H. Wei, "Defect physics of the kesterite thin-film solar cell absorber Cu_2ZnSnS_4," *Appl. Phys. Lett.*, vol. 96, p. 21902, Jan. 2010.

[7] W. Bao, Sachuronggui, and F.-Y. Qiu, "Band offsets engineering at $Cd_xZn_{1-x}S/Cu_2ZnSnS_4$ heterointerface," *Chinese Physics B*, vol. 25, p. 127102, Oct. 2016.

[8] J. J. Scragg, T. Ericson, X. Fontané, V. Izquierdo-Roca, A. Pérez-Rodríguez, T. Kubart, M. Edoff, and C. Platzer-Björkman, "Rapid annealing of reactively sputtered precursors for Cu_2ZnSnS_4 solar cells," *Progress in Photovoltaics: Research and Applications*, vol. 22, pp. 10–17, Jul. 2014.

[9] S. K. Wallace, D. B. Mitzi, and A. Walsh, "The Steady Rise of Kesterite Solar Cells," *ACS Energy Letters*, vol. 2, pp. 776–779, Mar. 2017.

[10] T. Gokmen, O. Gunawan, T. K. Todorov, and D. B. Mitzi, "Band tailing and efficiency limitation in kesterite solar cells," *Applied Physics Letters*, vol. 103, p. 103506, Sep. 2013.

[11] S. Siebentritt and S. Schorr, "Kesterites—a challenging material for solar cells," *Progress in Photovoltaics: Research and Applications*, vol. 20, pp. 512–519, Feb. 2012.

[12] A. Nagoya, R. Asahi, and G. Kresse, "First-principles study of Cu_2ZnSnS_4 and the related band offsets for photovoltaic applications," *Journal of Physics: Condensed Matter*, vol. 23, p. 404203, Sep. 2011.

[13] A. Ritscher, M. Hoelzel, and M. Lerch, "The order-disorder transition in Cu_2ZnSnS_4 – A neutron scattering investigation," *Journal of Solid State Chemistry*, vol. 238, pp. 68–73, Jun. 2016.

[14] G. Rey, A. Redinger, J. Sendler, T. P. Weiss, M. Thevenin, M. Guennou, B. El Adib, and S. Siebentritt, “The band gap of $Cu_2ZnSnSe_4$: Effect of order-disorder,” *Applied Physics Letters*, vol. 105, p. 112106, Sep. 2014.

[15] M. Kumar, A. Dubey, N. Adhikari, S. Venkatesan, and Q. Qiao, “Strategic review of secondary phases, defects and defect-complexes in kesterite CZTS–Se solar cells,” *Energy Environ. Sci.*, vol. 8, pp. 3134–3159, Aug. 2015.

[16] Z. Su, J. M. R. Tan, X. Li, X. Zeng, S. K. Batabyal, and L. H. Wong, “Cation Substitution of Solution-Processed Cu_2ZnSnS_4 Thin Film Solar Cell with over 9% Efficiency,” *Advanced Energy Materials*, vol. 5, p. 1500682, Jul. 2015.

[17] M. Courel, A. Martinez-Ayala, T. Sanchez, E. Regalado-Perez, I. M. De Los Santos, N. Mathews, and X. Mathew, “Impact of Cd concentrations on the physical properties of $Cu_2(Cd_xZn_{1-x})SnS_4$ thin films,” *Superlattices Microstruct.*, vol. 122, p. 324–335, Oct. 2018.

[18] J. C. Slater, “Atomic radii in crystals,” *The Journal of Chemical Physics*, vol. 41, pp. 3199–3204, Jul. 1964.

[19] B. Shin, O. Gunawan, Y. Zhu, N. A. Bojarczuk, S. J. Chey, and S. Guha, “Thin film solar cell with 8.4% power conversion efficiency using an earth-abundant Cu_2ZnSnS_4 absorber,” *Progress in Photovoltaics: Research and Applications*, vol. 21, pp. 72–76, Nov. 2013.

[20] M. A. Green, K. Emery, Y. Hishikawa, W. Warta, E. D. Dunlop, D. H. Levi, and A. W. Y. Ho-Baillie, “Solar cell efficiency tables (version 49),” *Progress in Photovoltaics: Research and Applications*, vol. 25, pp. 3–13, Nov. 2017.

[21] D. Herrmann, P. Kratzert, S. Weeke, M. Zimmer, J. Djordjevic-Reiss, R. Hunger, P. Lindberg, E. Wallin, O. Lundberg, and L. Stolt, “CIGS module manufacturing with high deposition rates and efficiencies,” in *2014 IEEE 40th Photovoltaic Specialist Conference (PVSC)*, 2014, pp. 2775–2777.

[22] P. Jackson, R. Wuerz, D. Hariskos, E. Lotter, W. Witte, and M. Powalla, “Effects of heavy alkali elements in $Cu(In,Ga)Se_2$ solar cells with efficiencies up to 22.6%,” *physica status solidi (RRL) – Rapid Research Letters*, vol. 10, pp. 583–586, Jul. 2016.

[23] C. J. Chen, *Physics of Solar Energy*. ISBN: 978-0-470-64780-6: Wiley, 2011.

[24] Jean *et al.*, “ Pathways for solar photovoltaics,” *Energy Environ. Sci.*, vol. 8, pp. 1200–1219, Feb. 2015.

[25] NREL. (2021) Best Research-Cell Efficiency Chart. Golden, United States: The National Renewable Energy Laboratory. [Online]. Available: https://www.nrel.gov/pv/cell-efficiency.html

[26] A. Walsh, S. Chen, S.-H. Wei, and X.-G. Gong, “Kesterite thin-film solar cells: Advances in materials modelling of Cu_2ZnSnS_4,” *Advanced Energy Materials.*, vol. 2, pp. 400–409, Mar. 2012.

[27] H. Zhou, W.-C. Hsu, H.-S. Duan, B. Bob, W. Yang, T.-B. Song, C.-J. Hsu, and Y. Yang, “CZTS nanocrystals: a promising approach for next generation thin film photovoltaics,” *Energy Environ. Sci.*, vol. 6, pp. 2822–2838, Jul. 2013.

[28] K. Ito, *Copper Zinc Tin Sulphide-based Thin Film Solar Cells*. ISBN: 978-1-118-43785-8: Wiley, 2007.

[29] C. Yan, J. Huang, K. Sun, S. Johnston, Y. Zhang, H. Sun, A. Pu, M. He, F. Liu, K. Eder, L. Yang, J. M. Cairney, N. J. Ekins-Daukes, Z. Hameiri, J. A. Stride, S. Chen, M. A. Green, and X. Hao, "Cu_2ZnSnS_4 solar cells with over 10% power conversion efficiency enabled by heterojunction heat treatment," *Nature Energy.*, vol. 3, pp. 764–772, Jul. 2018.

[30] J. Li, Y. Huang, J. Huang, G. Liang, Y. Zhang, G. Rey, F. Guo, Z. Su, H. Zhu, L. Cai, K. Sun, Y. Sun, F. Liu, S. Chen, X. Hao, Y. Mai, and M. A. Green, "Defect control for 12.5% efficiency $Cu_2ZnSnSe_4$ Kesterite thin-film solar cells by Engineering of local chemical environment," *Advanced Materials.*, vol. 32, p. 2005268, Nov. 2020.

[31] R. Nitsche, D. Sargent, and P. Wild, "Crystal growth of quaternary 1_2246_4 chalcogenides by iodine vapor transport," *Advanced Materials.*, vol. 1, pp. 52–53, Jan. 1967.

[32] K. Ito and T. Nakazawa, "Electrical and optical properties of Stannite-type quaternary semiconductor thin films," *Japanese Journal of Applied Physics.*, vol. 27, p. 2094, Nov. 1988.

[33] T. Friedlmeier, N. Wieser, T. Walter, H. Dittrich, and S. H., "Heterojunctions based on Cu_2ZnSnS_4 and $Cu_2ZnSnSe_4$ thin films," in *Proceedings of the 14th European Conference of Photovoltaic Science and Engineering and Exhibition.*, Barcelona, Spain: European Photovoltaic Solar Energy Conference, 1997.

[34] H. Katagiri, "Cu_2ZnSnS_4 thin film solar cells," *Thin Solid Films*, vol. 480-481, pp. 426–432, Jun. 2005.

[35] K. Jimbo, R. Kimura, T. Kamimura, S. Yamada, W. S. Maw, H. Araki, K. Oishi, and H. Katagiri, "Cu_2ZnSnS_4-type thin film solar cells using abundant materials," *Thin Solid Films*, vol. 515, pp. 5997–5999, May 2007.

[36] H. Katagiri, K. Jimbo, S. Yamada, T. Kamimura, W. S. Maw, T. Fukano, T. Ito, and T. Motohiro, "Enhanced conversion efficiencies of Cu_2ZnSnS_4-based thin film solar cells by using preferential etching technique," *Applied Physics Express*, vol. 1, p. 041201, Apr. 2008.

[37] D. Barkhouse, O. Gunawan, T. Gokmen, T. Todorov, and D. Mitzi, "Device characteristics of a 10.1% hydrazine-processed $Cu_2ZnSn(S,Se)_4$ solar cell," *Progress in Photovoltaics: Research and Applications*, vol. 20, pp. 6–11, Jan. 2012.

[38] H. Xin, J. K. Katahara, I. L. Braly, and H. W. Hillhouse, "8% Efficient $Cu_2ZnSn(S,Se)_4$ Solar Cells from Redox Equilibrated Simple Precursors in DMSO," *Adv. Energy Mater.*, vol. 4, p. 1301650, Aug. 2014.

[39] W. Wang, M. T. Winkler, O. Gunawan, T. Gokmen, T. K. Todorov, Y. Zhu, and D. B. Mitzi, "Device characteristics of CZTSSe thin-film solar cells with 12.6% efficiency," *Advanced Energy Materials*, vol. 4, p. 1301465, Nov. 2014.

[40] K.-J. Yang, D.-H. Son, S.-J. Sung, J.-H. Sim, Y.-I. Kim, S.-N. Park, D.-H. Jeon, J. Kim, D.-K. Hwang, C.-W. Jeon, D. Nam, H. Cheong, J.-K. Kang, and D.-H. Kim, "A bandgap-graded CZTSSe solar cell with 12.3% efficiency," *Journal of Materials Chemistry A*, vol. 4, pp. 10 151–10 158, Apr. 2016.

[41] D.-H. Son, S.-H. Kim, S.-Y. Kim, Y.-I. Kim, J.-H. Sim, S.-N. Park, D.-H. Jeon, D.-K. Hwang, S.-J. Sung, J.-K. Kang, K.-J. Yang, and D.-H. Kim, "Effect of solid-H_2S gas reactions on CZTSSe thin film growth and photovoltaic properties of a 12.62% efficiency device," *Journal of Materials Chemistry A*, vol. 7, pp. 25 279–25 289, Sep. 2019.

[42] Z. Su, G. Liang, P. Fan, J. Luo, Z. Zheng, Z. Xie, W. Wang, S. Chen, J. Hu, Y. Wei, C. Yan, J. Huang, X. Hao, and F. Liu, “Device post annealing enabling over 12% efficient solution-processed Cu_2ZnSnS_4 solar cells with Cd^{2+} substitution,” *Advanced Materials*, vol. 32, p. 2000121, Jul. 2020.

[43] Y. Du, S. Wang, Q. Tian, Y. Zhao, X. Chang, H. Xiao, Y. Deng, S. Chen, S. Wu, and S. F. Liu, “Defect Engineering in Earth-abundant $Cu_2ZnSn(S,Se)_4$ photovoltaic materials via Ga^{3+}-doping for over 12% efficient solar cells,” *Advanced Functional Materials*, vol. 31, p. 2010325, Feb. 2021.

[44] Y. Gong, R. Qiu, C. Niu, J. Fu, E. Jedlicka, R. Giridharagopal, Q. Zhu, Y. Zhou, W. Yan, S. Yu, J. Jiang, S. Wu, D. S. Ginger, W. Huang, and H. Xin, “Ag incorporation with controlled grain growth enables 12.5% efficient Kesterite solar cell with open circuit voltage reached 64.2% Shockley–Queisser limit,” *Advanced Functional Materials*, vol. 31, p. 2101927, Jun. 2021.

[45] S. Schorr, G. Gurieva, M. Guc, M. Dimitrievska, A. Pérez-Rodríguez, V. Izquierdo-Roca, C. S. Schnohr, J. Kim, W. Jo, and J. M. Merino, “Point defects, compositional fluctuations, and secondary phases in non-stoichiometric kesterites,” *Journal of Physics: Energy*, vol. 2, p. 012002, Dec. 2019.

[46] S. Schorr, H.-J. Hoebler, and M. Tovar, “A neutron diffraction study of the stannite-kesterite solid solution series,” *European Journal of Mineralogy*, vol. 19, pp. 65–73, Jan. 2007.

[47] G. M. Ford, Q. Guo, R. Agrawal, and H. W. Hillhouse, “Earth abundant element $Cu_2Zn(Sn_{1-x}Ge_x)S_4$ nanocrystals for tunable band gap solar cells: 6.8% Efficient device fabrication,” *Mater. Res. Soc. Symp. Proc.*, vol. 1165, pp. 125–136, Aug. 2010.

[48] S. Schorr, “The crystal structure of kesterite type compounds: A neutron and X-ray diffraction study,” *Solar Energy Materials and Solar Cells*, vol. 95, pp. 1482–1488, Jun. 2011.

[49] S. Chen, X.G. Gong, A. Walsh, and S.-H. Wei, “Crystal and electronic band structure of Cu_2ZnSnX_4 (X=S and Se) photovoltaic absorbers: First-principles insights,” *Applied Physics Letters*, vol. 94, p. 041903, Jan. 2009.

[50] S. Chen, A. Walsh, Y. Luo, J.-H. Yang, X. G. Gong, and S.-H. Wei, “Wurtzite-derived polytypes of kesterite and stannite quaternary chalcogenide semiconductors,” *Phys. Rev. B*, vol. 82, p. 195203, Nov. 2010.

[51] S. Chen, X. G. Gong, A. Walsh, and S.-H. Wei, “Electronic structure and stability of quaternary chalcogenide semiconductors derived from cation cross-substitution of II-VI and I-III-VI compounds,” *Phys. Rev. B*, vol. 79, p. 165211, Apr. 2009.

[52] C. Persson, “Electronic and optical properties of Cu_2ZnSnS_4 and $Cu_2ZnSnSe_4$,” *Journal of Applied Physics*, vol. 107, no. 5, p. 053710, 2010.

[53] S. Schorr, “Structural aspects of adamantine like multinary chalcogenides,” *Thin Solid Films*, vol. 515, pp. 5985–5991, May 2007.

[54] J. Paier, R. Asahi, A. Nagoya, and G. Kresse, “Cu_2ZnSnS_4 as a potential photovoltaic material: A hybrid Hartree-Fock density functional theory study,” *Phys. Rev. B*, vol. 79, p. 115126, Mar. 2009.

[55] I. Repins, C. Beall, N. Vora, C. DeHart, D. Kuciauskas, P. Dippo, B. To, J. Mann, W.-C. Hsu, A. Goodrich, and R. Noufi, “Co-evaporated $Cu_2ZnSnSe_4$ films and devices,” *Solar Energy Materials and Solar Cells*, vol. 101, pp. 154–159, Jun. 2012.

[56] K. Tanaka, Y. Fukui, N. Moritake, and H. Uchiki, “Chemical composition dependence of morphological and optical properties of Cu_2ZnSnS_4 thin films deposited by sol–gel sulfurization and Cu_2ZnSnS_4 thin film solar cell efficiency,” *Solar Energy Materials and Solar Cells*, vol. 95, pp. 838–842, Mar. 2011.

[57] R. Haight, A. Barkhouse, O. Gunawan, B. Shin, M. Copel, M. Hopstaken, and D. B. Mitzi, “Band alignment at the $Cu_2ZnSn(S_xSe_{1-x})_4/CdS$ interface,” *Applied Physics Letters*, vol. 98, p. 253502, Jun. 2011.

[58] S. Chen, A. Walsh, X.-G. Gong, and S.-H. Wei, “Classification of Lattice Defects in the Kesterite Cu_2ZnSnS_4 and $Cu_2ZnSnSe_4$ Earth-Abundant Solar Cell Absorbers,” *Advanced Materials*, vol. 25, pp. 1522–1539, Feb. 2013.

[59] H. Katagiri, K. Jimbo, W. S. Maw, K. Oishi, M. Yamazaki, H. Araki, and A. Takeuchi, “Development of CZTS-based thin film solar cells,” *Thin Solid Films.*, vol. 517, pp. 2455–2460, Feb. 2009.

[60] D. Mitzi, O. Gunawan, T. Todorov, K. Wang, and S. Guha, “The path towards a high-performance solution-processed kesterite solar cell,” *Solar Energy Materials and Solar Cells.*, vol. 95, pp. 1421–1436, Jun. 2011.

[61] T. K. Todorov, K. B. Reuter, and D. B. Mitzi, “High-Efficiency Solar Cell with Earth-Abundant Liquid-Processed Absorber,” *Advanced Materials*, vol. 22, pp. E156–E159, May 2010.

[62] K. Sun, C. Yan, F. Liu, J. Huang, F. Zhou, J. A. Stride, M. Green, and X. Hao, “Over 9% Efficient Kesterite Cu_2ZnSnS_4 Solar Cell Fabricated by Using $Zn_{1-x}Cd_xS$ Buffer Layer,” *Advanced Energy Materials*, vol. 6, p. 1600046, Apr. 2016.

[63] K. Sun, J. Huang, C. Yan, A. Pu, F. Liu, H. Sun, X. Liu, Z. Fang, J. A. Stride, M. Green, and X. Hao, “Self-assembled Nanometer-Scale ZnS Structure at the CZTS/ZnCdS Heterointerface for High-Efficiency Wide Band Gap Cu_2ZnSnS_4 Solar Cells,” *Chemistry of Materials*, vol. 30, pp. 4008–4016, May 2018.

[64] S. Siebentritt, “Why are kesterite solar cells not 20% efficient?” *Thin Solid Films*, vol. 535, pp. 1–4, May 2013.

[65] D. M. Berg, R. Djemour, L. Gütay, G. Zoppi, S. Siebentritt, and P. J. Dale, “Thin film solar cells based on the ternary compound Cu_2SnS_3,” *Thin Solid Films*, vol. 520, pp. 6291–6294, Jul. 2012.

[66] G. Marcano, C. Rincón, L. M. de Chalbaud, D. B. Bracho, and G. S. Pérez, “Crystal growth and structure, electrical, and optical characterization of the semiconductor Cu_2SnSe_3,” *Journal of Applied Physics*, vol. 90, pp. 1847–1853, Aug. 2001.

[67] P. Yu and M. Cardona, *Fundamentals of Semiconductors. 4th ed.* Berlin, Heidelberg, Germany: Springer, 2010.

[68] Y.-T. Lin, J.-B. Shi, Y.-C. Chen, C.-J. Chen, and P.-F. Wu, “Synthesis and characterization of Tin Disulfide (SnS_2) nanowires,” *Nanoscale Research Letters*, vol. 7, p. 694, Apr. 2009.

[69] Florinel Sava and Adam Lőrinczi and Mihai A. Popescu and Gabriel Socol and Emanuel Axente and Ion N. Mihailescu and Magdalena Nistor, "Amorphous $SnSe_2$ films," *Journal of Optoelectronics and Advanced Materials*, vol. 8, pp. 1367–1371, Aug. 2006.

[70] J. Vidal, S. Lany, M. d'Avezac, A. Zunger, A. Zakutayev, J. Francis, and J. Tate, "Band-structure, optical properties, and defect physics of the photovoltaic semiconductor SnS," *Applied Physics Letters*, vol. 100, p. 032104, Jan. 2012.

[71] P. Sinsermsuksakul, J. Heo, W. Noh, A. S. Hock, and R. G. Gordon, "Atomic Layer Deposition of Tin Monosulfide Thin Films," *Advanced Energy Materials*, vol. 1, pp. 1116–1125, Sep. 2011.

[72] M. A. Franzman, C. W. Schlenker, M. E. Thompson, and R. L. Brutchey, "Solution-Phase Synthesis of SnSe Nanocrystals for Use in Solar Cells," *Journal of the American Chemical Society*, vol. 132, pp. 4060–4061, Mar. 2010.

[73] G. Liu, T. Schulmeyer, J. Brötz, A. Klein, and W. Jaegermann, "Interface properties and band alignment of Cu_2S/CdS thin film solar cells," *Thin Solid Films*, vol. 431-432, pp. 477–482, May 2003.

[74] S. Kashida, W. Shimosaka, M. Mori, and D. Yoshimura, "Valence band photoemission study of the copper chalcogenide compounds, Cu_2S, Cu_2Se and Cu_2Te," *Journal of Physics and Chemistry of Solids*, vol. 64, pp. 2357–2363, Dec. 2003.

[75] J. Timo Wätjen, J. Engman, M. Edoff, and C. Platzer-Björkman, "Direct evidence of current blocking by ZnSe in $Cu_2ZnSnSe_4$ solar cells," *Applied Physics Letters*, vol. 100, p. 173510, Apr. 2012.

[76] A. Redinger, M. Mousel, M. H. Wolter, N. Valle, and S. Siebentritt, "Influence of S/Se ratio on series resistance and on dominant recombination pathway in $Cu_2ZnSn(SSe)_4$ thin film solar cells," *Thin Solid Films*, vol. 535, pp. 291–295, May 2013.

[77] K. Sun, C. Yan, J. Huang, F. Liu, J. Li, H. Sun, Y. Zhang, X. Cui, A. Wang, Z. Fang, J. Cong, Y. Lai, M. A. Green, and X. Hao, "Beyond 10% efficiency Cu_2ZnSnS_4 solar cells enabled by modifying the heterojunction interface chemistry," *J. Mater. Chem. A*, vol. 7, pp. 27 289–27 296, Nov. 2019.

[78] M. Mousel, A. Redinger, R. Djemour, M. Arasimowicz, N. Valle, P. Dale, and S. Siebentritt, "HCl and Br_2-MeOH etching of $Cu_2ZnSnSe_4$ polycrystalline absorbers," *Thin Solid Films*, vol. 535, pp. 83–87, May 2013.

[79] A. Nagoya, R. Asahi, R. Wahl, and G. Kresse, "Defect formation and phase stability of Cu_2ZnSnS_4 photovoltaic material," *Phys. Rev. B*, vol. 81, p. 113202, Mar. 2010.

[80] H. Katagiri, K. Saitoh, T. Washio, H. Shinohara, T. Kurumadani, and S. Miyajima, " Development of thin film solar cell based on Cu_2ZnSnS_4 thin films," *Solar Energy Materials and Solar Cells*, vol. 65, pp. 141–148, Jan. 2001.

[81] N. Nakayama and K. Ito, "Sprayed films of stannite Cu_2ZnSnS_4," *Applied Surface Science*, vol. 92, pp. 171–175, Feb. 1996.

[82] T. Tanaka, T. Nagatomo, D. Kawasaki, M. Nishio, Q. Guo, A. Wakahara, A. Yoshida, and H. Ogawa, "Preparation of Cu_2ZnSnS_4 thin films by hybrid sputtering," *Journal of Physics and Chemistry of Solids*, vol. 66, pp. 1978–1981, Nov. 2005.

[83] J. J. Scragg, P. J. Dale, L. M. Peter, G. Zoppi, and I. Forbes, "New routes to sustainable photovoltaics: evaluation of Cu_2ZnSnS_4 as an alternative absorber material," *physica status solidi (b)*, vol. 245, pp. 1772–1778, Aug. 2008.

[84] K. Hönes, E. Zscherpel, J. Scragg, and S. Siebentritt, "Shallow defects in Cu_2ZnSnS_4," *Physica B: Condensed Matter*, vol. 404, pp. 4949–4952, Dec. 2009.

[85] X. Cui, K. Sun, J. Huang, J. S. Yun, C.-Y. Lee, C. Yan, H. Sun, Y. Zhang, C. Xue, K. Eder, L. Yang, J. M. Cairney, J. Seidel, N. J. Ekins-Daukes, M. Green, B. Hoex, and X. Hao, "Cd-Free Cu_2ZnSnS_4 solar cell with an efficiency greater than 10% enabled by Al_2O_3 passivation layers," *Energy Environ. Sci.*, vol. 12, pp. 2751–2764, Jul. 2019.

[86] A. Cazzaniga, A. Crovetto, C. Yan, K. Sun, X. Hao, J. Ramis Estelrich, S. Canulescu, E. Stamate, N. Pryds, O. Hansen, and J. Schou, "Ultra-thin Cu_2ZnSnS_4 solar cell by pulsed laser deposition," *Solar Energy Materials and Solar Cells*, vol. 166, pp. 91–99, Jul. 2017.

[87] S. Ahmed, K. Reuter, O. Gunawan, L. Guo, L. Romankiw, and H. Deligianni, "A high efficiency electrodeposited Cu_2ZnSnS_4 solar cell," *Advanced Energy Materials*, vol. 2, pp. 253–259, Nov. 2012.

[88] Q. Guo, G. M. Ford, W.-C. Yang, B. C. Walker, E. A. Stach, H. W. Hillhouse, and R. Agrawal, "Fabrication of 7.2% Efficient CZTSSe Solar Cells Using CZTS Nanocrystals," *Journal of the American Chemical Society*, vol. 132, pp. 17 384–17 386, Nov. 2010.

[89] A. Wangperawong, J. King, S. Herron, B. Tran, K. Pangan-Okimoto, and S. Bent, "Aqueous bath process for deposition of Cu_2ZnSnS_4 photovoltaic absorbers," *Thin Solid Films*, vol. 519, pp. 2488–2492, Feb. 2011.

[90] K. Sun, A. Wang, Z. Su, F. Liu, and X. Hao, "Enhancing the performance of Cu_2ZnSnS_4 solar cell fabricated via successive ionic layer adsorption and reaction method by optimizing the annealing process," *Solar Energy*, vol. 220, pp. 204–210, May 2021.

[91] Z. Zhou, Y. Wang, D. Xu, and Y. Zhang, "Fabrication of Cu_2ZnSnS_4 screen printed layers for solar cells," *Solar Energy Materials and Solar Cells*, vol. 94, pp. 2042–2045, Dec. 2010.

[92] M. T. Winkler, W. Wang, O. Gunawan, H. J. Hovel, T. K. Todorov, and D. B. Mitzi, "Optical designs that improve the efficiency of $Cu_2ZnSn(S,Se)_4$ solar cells," *Energy Environ. Sci.*, vol. 7, pp. 1029–1036, Oct. 2014.

[93] A. Chirilă, S. Buecheler, F. Pianezzi, P. Bloesch, C. Gretener, A. R. Uhl, C. Fella, L. Kranz, J. Perrenoud, S. Seyrling, R. Verma, S. Nishiwaki, Y. E. Romanyuk, G. Bilger, and A. N. Tiwari, "Highly efficient $Cu(In,Ga)Se_2$ solar cells grown on flexible polymer films," *Nature Materials*, vol. 10, pp. 857–861, Sep. 2011.

[94] Y.-F. Qi, D.-X. Kou, W.-H. Zhou, Z.-J. Zhou, Q.-W. Tian, Y.-N. Meng, X.-S. Liu, Z.-L. Du, and S.-X. Wu, "Engineering of interface band bending and defects elimination via a Ag-graded active layer for efficient $(Cu,Ag)_2ZnSn(S,Se)_4$ solar cells," *Energy Environ. Sci.*, vol. 10, pp. 2401–2410, Sep. 2017.

[95] C. Yan, K. Sun, J. Huang, S. Johnston, F. Liu, B. P. Veettil, K. Sun, A. Pu, F. Zhou, J. A. Stride, M. A. Green, and X. Hao, "Beyond 11% Efficient Sulfide Kesterite $Cu_2Zn_xCd_{1-x}SnS_4$ Solar Cell: Effects of Cadmium Alloying," *ACS Energy Letters*, vol. 2, pp. 930–936, Apr. 2017.

[96] C. J. Hages, S. Levcenco, C. K. Miskin, J. H. Alsmeier, D. Abou-Ras, R. G. Wilks, M. Bär, T. Unold, and R. Agrawal, “Improved performance of Ge-alloyed CZTGeSSe thin-film solar cells through control of elemental losses,” *Progress in Photovoltaics: Research and Applications*, vol. 23, pp. 376–384, Dec. 2015.

[97] J. J. S. Scragg, L. Choubrac, A. Lafond, T. Ericson, and C. Platzer-Björkman, “A low-temperature order-disorder transition in Cu_2ZnSnS_4 thin films,” *Applied Physics Letters*, vol. 104, p. 041911, Jan. 2014.

[98] Y. Gong, Y. Zhang, Q. Zhu, Y. Zhou, R. Qiu, C. Niu, W. Yan, W. Huang, and H. Xin, “Identifying the origin of the Voc deficit of kesterite solar cells from the two grain growth mechanisms induced by Sn^{2+} and Sn^{4+} precursors in DMSO solution,” *Energy Environ. Sci.*, vol. 14, pp. 2369–2380, Feb. 2021.

[99] K.-J. Yang, S. Kim, S.-Y. Kim, K. Ahn, D.-H. Son, S.-H. Kim, S.-J. Lee, Y.-I. Kim, S.-N. Park, S.-J. Sung, D.-H. Kim, T. Enkhbat, J. Kim, C.-W. Jeon, and J.-K. Kang, “Flexible $Cu_2ZnSn(S,Se)_4$ solar cells with over 10% efficiency and methods of enlarging the cell area,” *Nature Communications*, vol. 10, p. 2959, Jul. 2019.

[100] T. Ericson, J. J. Scragg, A. Hultqvist, J. T. Wätjen, P. Szaniawski, T. Törndahl, and C. Platzer-Björkman, “Zn(O,S) Buffer Layers and Thickness Variations of CdS Buffer for Cu_2ZnSnS_4 Solar Cells,” *IEEE Journal of Photovoltaics*, vol. 4, pp. 465–469, Jan. 2014.

[101] J. K. Larsen, F. Larsson, T. Törndahl, N. Saini, L. Riekehr, Y. Ren, A. Biswal, D. Hauschild, L. Weinhardt, C. Heske, and C. Platzer-Björkman, “Cadmium Free Cu_2ZnSnS_4 Solar Cells with 9.7% Efficiency,” *Advanced Energy Materials*, vol. 9, p. 1900439, Apr. 2019.

[102] Z.-K. Yuan, S. Chen, H. Xiang, X.-G. Gong, A. Walsh, J.-S. Park, I. Repins, and S.-H. Wei, “Engineering Solar Cell Absorbers by Exploring the Band Alignment and Defect Disparity: The Case of Cu- and Ag-Based Kesterite Compounds,” *Advanced Functional Materials*, vol. 25, pp. 6733–6743, Oct. 2015.

[103] H. Sun, K. Sun, J. Huang, C. Yan, F. Liu, J. Park, A. Pu, J. A. Stride, M. A. Green, and X. Hao, “Efficiency Enhancement of Kesterite Cu_2ZnSnS_4 Solar Cells via Solution-Processed Ultrathin Tin Oxide Intermediate Layer at Absorber/Buffer Interface,” *ACS Applied Energy Materials*, vol. 1, pp. 154–160, Dec. 2018.

[104] T. J. Huang, X. Yin, G. Qi, and H. Gong, “CZTS-based materials and interfaces and their effects on the performance of thin film solar cells,” *physica status solidi (RRL) – Rapid Research Letters*, vol. 08, pp. 735–762, Jul. 2014.

[105] K. F. Tai, O. Gunawan, M. Kuwahara, S. Chen, S. G. Mhaisalkar, C. H. A. Huan, and D. B. Mitzi, “Fill Factor Losses in $Cu_2ZnSn(S_xSe_{1-x})_4$ Solar Cells: Insights from Physical and Electrical Characterization of Devices and Exfoliated Films,” *Advanced Energy Materials*, vol. 6, p. 1501609, Nov. 2016.

[106] J. J. Scragg, T. Kubart, J. T. Wätjen, T. Ericson, M. K. Linnarsson, and C. Platzer-Björkman, “Effects of Back Contact Instability on Cu_2ZnSnS_4 Devices and Processes,” *Chemistry of Materials*, vol. 25, pp. 3162–3171, Jul. 2013.

[107] F. Liu, J. Huang, K. Sun, C. Yan, Y. Shen, J. Park, A. Pu, F. Zhou, X. Liu, J. A. Stride, M. A. Green, and X. Hao, “Beyond 8% ultrathin kesterite Cu_2ZnSnS_4 solar cells by interface reaction route controlling and self-organized nanopattern at the back contact,” *NPG Asia Materials*, vol. 9, pp. e401–e401, Jul. 2017.

[108] Mamta, K. K. Maurya, and V. N. Singh, “Comparison of Various Thin-Film-Based Absorber Materials: A Viable Approach for Next-Generation Solar Cells,” *Coatings*, vol. 12, p. 405, Mar. 2022.

[109] S. Giraldo, M. Neuschitzer, T. Thersleff, S. López-Marino, Y. Sánchez, H. Xie, M. Colina, M. Placidi, P. Pistor, V. Izquierdo-Roca, K. Leifer, A. Pérez-Rodríguez, and E. Saucedo, “Large Efficiency Improvement in $Cu_2ZnSnSe_4$ Solar Cells by Introducing a Superficial Ge Nanolayer,” *Advanced Energy Materials*, vol. 5, p. 1501070, Aug. 2015.

[110] C. Yan, F. Liu, K. Sun, N. Song, J. A. Stride, F. Zhou, X. Hao, and M. Green, “Boosting the efficiency of pure sulfide CZTS solar cells using the In/Cd-based hybrid buffers,” *Solar Energy Materials and Solar Cells*, vol. 144, pp. 700–706, Jan. 2016.

[111] S. Kim, J.-S. Park, S. Hood, and A. Walsh, “Lone-pair effect on carrier capture in Cu_2ZnSnS_4 solar cells,” *J. Mater. Chem. A*, vol. 7, pp. 2686–2693, Jan. 2019.

[112] I. Kim, K. Kim, Y. Oh, K. Woo, G. Cao, S. Jeong, and J. Moon, “Bandgap-Graded $Cu_2Zn(Sn_{1-x}Ge_x)S_4$ Thin-Film Solar Cells Derived from Metal Chalcogenide Complex Ligand Capped Nanocrystals,” *Chemistry of Materials*, vol. 26, pp. 3957–3965, Jun. 2014.

[113] S. Kim, K. M. Kim, H. Tampo, H. Shibata, and S. Niki, “Improvement of voltage deficit of Ge-incorporated kesterite solar cell with 12.3% conversion efficiency,” *Applied Physics Express*, vol. 9, p. 102301, Sep. 2016.

[114] M. Neuschitzer, Y. Sanchez, S. López-Marino, H. Xie, A. Fairbrother, M. Placidi, S. Haass, V. Izquierdo-Roca, A. Perez-Rodriguez, and E. Saucedo, “Optimization of CdS buffer layer for high-performance $Cu_2ZnSnSe_4$ solar cells and the effects of light soaking: elimination of crossover and red kink,” *Progress in Photovoltaics: Research and Applications*, vol. 23, pp. 1660–1667, Jan. 2015.

[115] D. B. Khadka and J. H. Kim, “Band gap engineering of alloyed $Cu_2ZnGe_xSn_{1-x}Q_4$ (Q = S,Se) films for solar cell,” *J. Phys. Chem. C*, vol. 119, pp. 1706–1713, Jan. 2015.

[116] E. Garcia-Llamas, J. Merino, R. Serna, X. Fontané, I. Victorov, A. Pérez-Rodríguez, M. León, I. Bodnar, V. Izquierdo-Roca, and R. Caballero, “Wide band-gap tuning $Cu_2Zn(Sn_{1-x}Ge_x)S_4$ single crystals: Optical and vibrational properties,” *Solar Energy Materials and Solar Cells*, vol. 158, pp. 147–153, Dec. 2016.

[117] Q. Shu, J.-H. Yang, S. Chen, B. Huang, H. Xiang, X.-G. Gong, and S.-H. Wei, “$Cu_2Zn(Sn,Ge)Se_4$ and $Cu_2Zn(Sn,Si)Se_4$ alloys as photovoltaic materials: Structural and electronic properties,” *Phys. Rev. B*, vol. 87, p. 115208, Mar. 2013.

[118] M. Grossberg, K. Timmo, T. Raadik, E. Kärber, V. Mikli, and J. Krustok, “Study of structural and optoelectronic properties of $Cu_2Zn(Sn_{1-x}Ge_x)Se_4$ (x=0 to 1) alloy compounds,” *Thin Solid Films*, vol. 582, pp. 176–179, May 2015.

[119] S. Kang, R. Sharma, J. K. Sim, and C. R. Lee, “Band gap engineering of tandem structured CIGS compound absorption layer fabricated by sputtering and selenization,” *J. Alloys Compd.*, vol. 563, pp. 207–215, Jun. 2013.

[120] D. Kuciauskas, J. V. Li, M. A. Contreras, J. Pankow, P. Dippo, M. Young, L. M. Mansfield, R. Noufi, and D. Levi, “Charge carrier dynamics and recombination in graded band gap $CuIn_{1-x}Ga_xSe_2$ polycrystalline thin-film photovoltaic solar cell absorbers,” *Journal of Applied Physics*, vol. 114, p. 154505, Oct. 2013.

[121] F. Li, Z. Xia, and Q. Liu, "Insight into the Controlled Synthesis of $Cu_2Zn(Ge,Sn)S_4$ Nanoparticles with Selective Grain Size," *The Journal of Physical Chemistry C*, vol. 120, pp. 16 969–16 976, Jul. 2016.

[122] J. Chen, W. Li, C. Yan, S. Huang, and X. Hao, "Studies of compositional dependent $Cu_2Zn(Ge_xSn_{1-x})S_4$ thin films prepared by sulfurizing sputtered metallic precursors," *J. Alloys Compd.*, vol. 621, pp. 154–161, Feb. 2015.

[123] S. Goktas and A. Goktas, "A comparative study on recent progress in efficient ZnO based nanocomposite and heterojunction photocatalysts: A review," *J. Alloys Compd.*, vol. 863, p. 158734, Mar. 2021.

[124] Q. Guo, H. W. Hillhouse, and R. Agrawal, "Synthesis of Cu_2ZnSnS_4 nanocrystal ink and its use for solar cells," *J. Am. Chem. Soc.*, vol. 131, pp. 11 672–11 673, Aug. 2009.

[125] M. Y. Yeh, P. H. Lei, S. H. Lin, and C. D. Yang, "Copper-Zinc-Tin-Sulfur thin film using spin-coating technology," *Materials (Basel).*, vol. 9, p. 526, Jul. 2016.

[126] N. K. Youn *et al.*, "Cu_2ZnSnS_4 solar cells with a single spin-coated absorber layer prepared via a simple sol-gel route," *Int. J. Energy Res.*, vol. 40, pp. 662–669, Apr. 2016.

[127] Y. Fang, J. R. Dilworth, M. Pepper, and P. P. Edwards, "Investigations of the optical and electronic effects of silicon and indium co-doping on ZnO thin films deposited by spray pyrolysis," *Zeitschrift fur Naturforsch. - Sect. B J. Chem. Sci.*, vol. 75, pp. 23–32, Feb. 2020.

[128] A. Goktas, A. Tumbul, Z. Aba, and M. Durgun, "Mg doping levels and annealing temperature induced structural, optical and electrical properties of highly c-axis oriented ZnO:Mg thin films and Al/ZnO:Mg/p-Si/Al heterojunction diode," *Thin Solid Films*, vol. 680, pp. 20–30, May 2019.

[129] A. Tumbul, F. Aslan, S. Demirozu, A. Goktas, A. Kilic, M. Durgun, and M. Z. Zarbali, "Solution processed boron doped ZnO thin films: Influence of different boron complexes," *Mater. Res. Express*, vol. 6, Mar. 2019.

[130] A. Goktas, F. Aslan, A. Tumbul, and S. H. Gunduz, "Tuning of structural, optical and dielectric constants by various transition metal doping in ZnO:T_M (T_M=Mn, Co, Fe) nanostructured thin films: A comparative study," *Ceram. Int.*, vol. 43, pp. 704–713, Jan. 2017.

[131] A. Goktas, "High-quality solution-based Co and Cu co-doped ZnO nanocrystalline thin films: Comparison of the effects of air and argon annealing environments," *J. Alloys Compd.*, vol. 735, pp. 2038–2045, Feb. 2018.

[132] H. Xin, J. K. Katahara,I. L. Braly and H. W. Hillhouse, "Lithium-Doping Inverts the Nanoscale Electric Field at the Grain Boundaries in $Cu_2ZnSn(S,Se)_4$ and Increases Photovoltaic Efficiency," *Phys. Chem. Chem. Phys.*, vol. 17, pp. 23 859–23 866, Aug. 2015.

[133] Y. E. Romanyuk, S. Schorr, and A. N. Tiwari, "Recent Trends in Direct Solution Coating of Kesterite Absorber Layers in Solar Cells," *Sol. Energy Mater. Sol. Cells*, vol. 119, pp. 181–189, Aug. 2013.

[134] L. Wang, Z. Chen, J. Lin, S. Tang, S. Ye, Y. Liu, and X. Yang, "Recent progress in substrate-type and superstrate-type thin-film solar cells," *Nanomaterials*, vol. 9, p. 1312, Sep. 2019.

[135] J. Wu, J. Tang, and D. Chen, "Review of recent progress in solid-state dye-sensitized and perovskite-sensitized solar cells," *Energy & Environmental Science*, vol. 9, pp. 578–601, Mar. 2016.

[136] K. L. Chopra, P. D. Paulson, and V. Dutta, "Thin-film solar cells: An overview," *Progress in Photovoltaics: Research and Applications*, vol. 12, pp. 69–92, Feb. 2004.

[137] J. M. Raulot, C. Domain, and J. F. Guillemoles, "Ab initio investigation of potential indium and gallium free chalcopyrite compounds for photovoltaic application," *J. Phys. Chem. Solids*, vol. 66, pp. 2019–2023, Nov. 2005.

[138] A. Ibraheam, Y. Al-Douri, U. Hashim, M. Ghezzar, A. Addou, and W. K. Ahmed, "Cadmium effect on optical properties of $Cu_2Zn_xCd_{1-x}SnS_4$ quinternary alloys nanostructures," *Solar Energy*, vol. 114, pp. 39–50, Apr. 2015.

[139] A. S. Ibraheam, Y. Al-Douri, S. C. B. Gopinath, and U. Hashim, "A novel quinternary alloy ($Cu_2Zn_xCd_{1-x}SnS_4$) nanostructured sensor for biomedical diagnosis," *Materials Research Express*, vol. 3, p. 085022, Aug. 2016.

[140] A. S. Ibraheam, Y. Al-Douri, C. H. Voon, K. L. Foo, N. Azizah, S. C. B. Gopinath, M. Ameri, and S. S. Ibrahim, "Surface functionalized $Cu_2Zn_{1-x}Cd_xSnS_4$ quinternary alloyed nanostructure for DNA sensing," *Applied Physics A*, vol. 123, p. 200, Mar. 2017.

[141] Q. Zhang, H. Deng, L. Chen, L. Yu, J. Tao, L. Sun, P. Yang, and J. Chu, "Cation substitution induced structural transition, band gap engineering and grain growth of $Cu_2Cd_xZn_{1-x}SnS_4$ thin films," *Journal of Alloys and Compounds*, vol. 695, pp. 482–488, Feb. 2017.

[142] L. Meng, B. Yao, Y. Li, Z. Ding, Z. Xiao, K. Liu, and G. Wang, "Significantly enhancing back contact adhesion and improving stability of $Cu_2(Zn,Cd)Sn(S,Se)_4$ solar cell by a rational carbon doping strategy," *Journal of Alloys and Compounds*, vol. 710, pp. 403–408, Jul. 2017.

[143] J. Fu, Q. Tian, Z. Zhou, D. Kou, Y. Meng, W. Zhou, and S. Wu, "Improving the Performance of Solution-Processed $Cu_2ZnSn(S,Se)_4$ Photovoltaic Materials by Cd^{2+} Substitution," *Chemistry of Materials*, vol. 28, pp. 5821–5828, Jul. 2016.

[144] A. S. Ibraheam, Y. Al-Douri, N. Z. Al-Hazeem, U. Hashim, D. Prakash, and K. D. Verma, "Effect of Cadmium Concentration on Structural, Optical, and Electrical Properties of $Cu_2Zn_{1-x}Cd_xSnS_4$ Quinternary Alloy Nanofibres, Synthesized by Electrospinning Technique," *Journal of Nanomaterials*, vol. 2016, p. 7314714, Mar. 2016.

[145] T. Maeda, S. Nakamura, and T. Wada, "First-Principles Study on Cd Doping in Cu_2ZnSnS_4 and $Cu_2ZnSnSe_4$," *Japanese Journal of Applied Physics*, vol. 51, p. 10NC11, Oct. 2012.

[146] S. R. Rondiya, Y. A. Jadhav, A. Živković, S. B. Jathar, G. K. Rahane, R. W. Cross, A. V. Rokade, R. S. Devan, S. Kolekar, R. L. Hoye, H. N. Ghosh, N. H. de Leeuw, S. R. Jadkar, and N. Y. Dzade, "Solution-processed Cd-substituted CZTS nanocrystals for sensitized liquid junction solar cells," *Journal of Alloys and Compounds*, vol. 890, p. 161575, Jan. 2022.

[147] H. Luan, B. Yao, Y. Li, R. Liu, Z. Ding, Z. Zhang, H. Zhao, and L. Zhang, "Mechanism of enhanced power conversion efficiency of $Cu_2ZnSn(S,Se)_4$ solar cell by cadmium surface diffusion doping," *Journal of Alloys and Compounds*, vol. 876, p. 160160, Sep. 2021.

[148] Y. Wang, R. Hao, J. Guo, X. Li, S. Fang, H. Liu, and S. Sun, “Effect of Mg doping on Cu_2ZnSnS_4 solar cells prepared by DMF-based solution method,” *Optical Materials*, vol. 117, p. 111211, Jul. 2021.

[149] Y. Sui, Y. Zhang, D. Jiang, W. He, Z. Wang, F. Wang, B. Yao, and L. Yang, “Investigation of optimum Mg doping content and annealing parameters of $Cu_2Mg_xZn_{1-x}SnS_4$ thin films for solar cells,” *Nanomaterials*, vol. 9, pp. 1–13, Jun. 2019.

[150] A. Crovetto and O. Hansen, “What is the band alignment of $Cu_2ZnSn(S,Se)_4$ solar cells?” *Solar Energy Materials and Solar Cells*, vol. 169, pp. 177–194, Sep. 2017.

[151] N. Terada, S. Yoshimoto, K. Chochi, T. Fukuyama, M. Mitsunaga, H. Tampo, H. Shibata, K. Matsubara, S. Niki, N. Sakai, T. Katou, and H. Sugimoto, “Characterization of electronic structure of $Cu_2ZnSn(S_xSe_{1-x})_4$ absorber layer and $CdS/Cu_2ZnSn(S_xSe_{1-x})_4$ interfaces by in-situ photoemission and inverse photoemission spectroscopies,” *Thin Solid Films*, vol. 582, pp. 166–170, May 2015.

[152] M. Gloeckler and J. Sites, “Efficiency limitations for wide-band-gap chalcopyrite solar cells,” *Thin Solid Films*, vol. 480-481, pp. 241–245, Jun. 2005.

[153] P. A. Nwofe, “Deposition and Characterisation of SnS Thin Films for Application in Photovoltaic Solar Cell Devices,” Ph.D. dissertation, University of Northumbria at Newcastle, United Kingdom, Oct. 2013. [Online]. Available: https://www.proquest.com/openview/e285e09737e11a2513886de4ad82337e/1?pq-origsite=gscholar&cbl=51922

[154] M. L. N. Palsgaard, A. Crovetto, T. Gunst, T. Markussen, O. Hansen, K. Stokbro, and M. Brandbyge, “Semiconductor band alignment from first principles: A new nonequilibrium Green’s function method applied to the CZTSe/CdS interface for photovoltaics,” in *2016 International Conference on Simulation of Semiconductor Processes and Devices (SISPAD)*, 2016, pp. 377–380.

[155] M. Bär, B.-A. Schubert, B. Marsen, R. G. Wilks, S. Pookpanratana, M. Blum, S. Krause, T. Unold, W. Yang, L. Weinhardt, C. Heske, and H.-W. Schock, “Cliff-like conduction band offset and KCN-induced recombination barrier enhancement at the CdS/Cu_2ZnSnS_4 thin-film solar cell heterojunction,” *Applied Physics Letters*, vol. 99, p. 222105, Nov. 2011.

[156] S. Tajima, K. Kataoka, N. Takahashi, Y. Kimoto, T. Fukano, M. Hasegawa, and H. Hazama, “Direct measurement of band offset at the interface between CdS and Cu_2ZnSnS_4 using hard X-ray photoelectron spectroscopy,” *Applied Physics Letters*, vol. 103, p. 243906, Dec. 2013.

[157] C. Yan, F. Liu, N. Song, B. K. Ng, J. A. Stride, A. Tadich, and X. Hao, “Band alignments of different buffer layers (CdS, Zn(O,S), and In_2S_3) on Cu_2ZnSnS_4,” *Applied Physics Letters*, vol. 104, p. 173901, Apr. 2014.

[158] J. Li, Q. Du, W. Liu, G. Jiang, X. Feng, W. Zhang, J. Zhu, and C. Zhu, “The band offset at CdS/Cu_2ZnSnS_4 heterojunction interface,” *Electronic Materials Letters*, vol. 8, pp. 365–367, Aug. 2012.

[159] A. Santoni, F. Biccari, C. Malerba, M. Valentini, R. Chierchia, and A. Mittiga, “Valence band offset at the CdS/Cu_2ZnSnS_4 interface probed by x-ray photoelectron spectroscopy,” *Journal of Physics D: Applied Physics*, vol. 46, p. 175101, Apr. 2013.

[160] S. Huang, W. Luo, and Z. Zou, “Band positions and photoelectrochemical properties of Cu_2ZnSnS_4 thin films by the ultrasonic spray pyrolysis method,” *Journal of Physics D: Applied Physics*, vol. 46, p. 235108, May 2013.

[161] J. Li, M. Wei, Q. Du, W. Liu, G. Jiang, and C. Zhu, “The band alignment at $CdS/Cu_2ZnSnSe_4$ heterojunction interface,” *Surface and Interface Analysis*, vol. 45, pp. 682–684, Jul. 2013.

[162] T. Kato, H. Hiroi, N. Sakai, and H. Sugimoto, “Buffer/absorber interface study on Cu_2ZnSnS_4 and $Cu_2ZnSnSe_4$ based solar cells: band alignment and its impact on the solar cell performance,” in *28th European Photovoltaic Solar Energy Conference and Exhibition,WIP*, Oct. 2013, p. 2125–2127.

[163] H. Hiroi, N. Sakai, T. Kato, and H. Sugimoto, “High voltage Cu_2ZnSnS_4 submodules by hybrid buffer layer,” in *2013 IEEE 39th Photovoltaic Specialists Conference (PVSC)*, Feb. 2013, pp. 0863–0866.

[164] Z.-Y. Dong, Y.-F. Li, B. Yao, Z.-H. Ding, G. Yang, R. Deng, X. Fang, Z.-P. Wei, and L. Liu, “An experimental and first-principles study on band alignments at interfaces of $Cu_2ZnSnS_4/CdS/ZnO$ heterojunctions,” *Journal of Physics D: Applied Physics*, vol. 47, p. 075304, Jan. 2014.

[165] M. Than Htay, R. Fujimura, R. Hasuike, K. Takei, N. Momose, Y. Hashimoto, and K. Ito, “Effect of ultrasonically generated water vapor treatment on the Cu_2ZnSnS_4/CdS heterojunction-based photovoltaic cells,” *Solar Energy Materials and Solar Cells*, vol. 157, pp. 765–776, Dec. 2016.

[166] H.-J. Chen, S.-W. Fu, S.-H. Wu, T.-C. Tsai, H.-T. Wu, and C.-F. Shih, “Structural and photoelectron spectroscopic studies of band alignment at the Cu_2ZnSnS_4/CdS heterojunction with slight Ni doping in Cu_2ZnSnS_4,” *Journal of Physics D: Applied Physics*, vol. 49, p. 335102, Jul. 2016.

[167] K. Kataoka, S. Tajima, M. Umehara, N. Takahashi, N. Isomura, K. Kitazumi, and Y. Kimoto, “Band slope in CdS layer of $ZnO{:}Ga/CdS/Cu_2ZnSnS_4$ photovoltaic cells revealed by hard X-ray photoelectron spectroscopy,” *Applied Physics Letters*, vol. 109, p. 203902, Nov. 2016.

[168] K. Sardashti, R. Haight, T. Gokmen, W. Wang, L.-Y. Chang, D. B. Mitzi, and A. C. Kummel, “Impact of Nanoscale Elemental Distribution in High-Performance Kesterite Solar Cells,” *Advanced Energy Materials*, vol. 5, p. 1402180, Mar. 2015.

[169] Y. Udaka, S. Takaki, K. Isowaki, T. Nagai, K. M. Kim, S. Kim, H. Tampo, H. Shibata, K. Matsubara, S. Niki, N. Sakai, T. Kato, H. Sugimoto, and N. Terada, “Electronic structure of $Cu_2ZnSn(S_xSe_{1-x})_4$ surface and $CdS/Cu_2ZnSn(S_xSe_{1-x})_4$ interface,” *physica status solidi c*, vol. 14, p. 1600178, Apr. 2017.

[170] S. Chen, A. Walsh, J.-H. Yang, X. G. Gong, L. Sun, P.-X. Yang, J.-H. Chu, and S.-H. Wei, “Compositional dependence of structural and electronic properties of $Cu_2ZnSn(S,Se)_4$ alloys for thin film solar cells,” *Phys. Rev. B*, vol. 83, p. 125201, Mar. 2011.

[171] W. Bao and M. Ichimura, “Prediction of the Band Offsets at the CdS/Cu_2ZnSnS_4 Interface Based on the First-Principles Calculation,” *Japanese Journal of Applied Physics*, vol. 51, p. 10NC31, Oct. 2012.

[172] W. Bao and M. Ichimura, “First-Principles Study on Influences of Crystal Structure and Orientation on Band Offsets at the CdS/Cu_2ZnSnS_4 Interface,” *International Journal of Photoenergy*, vol. 2012, p. 619812, Dec. 2012.

[173] A. Crovetto, M. L. N. Palsgaard, T. Gunst, T. Markussen, K. Stokbro, M. Brandbyge, and O. Hansen, “Interface band gap narrowing behind open circuit voltage losses in Cu_2ZnSnS_4 solar cells,” *Applied Physics Letters*, vol. 110, p. 083903, Feb. 2017.

[174] A. Crovetto, C. Yan, B. Iandolo, F. Zhou, J. Stride, J. Schou, X. Hao, and O. Hansen, “Lattice-matched Cu_2ZnSnS_4/CeO_2 solar cell with open circuit voltage boost,” *Applied Physics Letters*, vol. 109, p. 233904, Dec. 2016.

[175] A. N. L. (.gov). (2013) Lattice Constants and Crystal Structures of some Semiconductors and Other Materials. [Online]. Available: https://7id.xray.aps.anl.gov/calculators/crystal_lattice_parameters.html

[176] J.-J. Chen, B. P. Gila, M. Hlad, A. Gerger, F. Ren, C. R. Abernathy, and S. J. Pearton, “Determination of MgO/GaN heterojunction band offsets by x-ray photoelectron spectroscopy,” *Applied Physics Letters*, vol. 88, p. 042113, Jan. 2006.

[177] M. J. Lee, J. Lim, J. Bang, W. Lee, and J. M. Myoung, “Effect of the thickness and hydrogen treatment on the properties of Ga-doped ZnO transparent conductive films,” *Applied Surface Science*, vol. 255, no. 5, pp. 3195–3200, Jan. 2009.

[178] E. S. Tüzemen, H. Kavak, and R. Esen, “Influence of oxygen pressure of ZnO/glass substrate produced by pulsed filtered cathodic vacuum arc deposition,” *Physica B: Condensed Matter*, vol. 390, no. 1, pp. 366–372, Jul. 2007.

[179] W. J. Jeong, S. K. Kim, and G. C. Park, “Preparation and characteristic of ZnO thin film with high and low resistivity for an application of solar cell,” *Thin Solid Films*, vol. 506–507, pp. 180–183, Jun. 2006.

[180] J. W. Lim, S. J. Yun, and J. H. Kim, “Optical and Electrical Properties of $Ti_xSi_{1-x}O_y$ Films,” *ETRI J.*, vol. 31, no. 6, pp. 675–679, Dec. 2011.

[181] I. Baia, M. Quintela, L. Mendes, P. Nunes, and R. Martins, “Performances exhibited by large area ITO layers produced by r.f. magnetron sputtering,” *Thin Solid Films*, vol. 337, no. 1, pp. 171–175, Oct. 1998.

[182] F.-H. Wang, C.-C. Huang, C.-F. Yang, and H.-T. Tzeng, “Optical and Electrical Properties of the Different Magnetron Sputter Power 300°C Deposited -ZnO Thin Films and Applications in p-i-n -Si:H Thin-Film Solar Cells,” *Int. J. Photoenergy*, vol. 2013, pp. 1–7, Nov. 2013.

[183] E. Commission. (2011) Restriction of Hazardous Substances in Electrical and Electronic Equipment (RoHS). [Online]. Available: https://ec.europa.eu/environment/topics/waste-and-recycling/rohs-directive_en#eclinpage-622

[184] E. Commission. (2011) Critical Raw Materials. [Online]. Available: https://single-market-economy.ec.europa.eu/sectors/raw-materials/areas-specific-interest/critical-raw-materials_en

[185] S. Chen, G. Carraro, D. Barreca, A. Sapelkin, W. Chen, X. Huang, Q. Cheng, F. Zhang, and R. Binions, “Aerosol assisted chemical vapour deposition of Ga-doped ZnO films for

energy efficient glazing: effects of doping concentration on the film growth behaviour and opto-electronic properties," *J. Mater. Chem. A*, vol. 3, no. 24, pp. 13 039–13 049, Jun. 2015.

[186] M. Caglar, S. Ilican, Y. Caglar, and F. Yakuphanoglu, "Electrical conductivity and optical properties of ZnO nanostructured thin film," *Appl. Surf. Sci.*, vol. 255, no. 8, pp. 4491–4496, Apr. 2009.

[187] L. Wu and et al., "First-principles study of doping effect on the phase transition of zinc oxide with transition metal doped," *J. Alloys Compd.*, vol. 541, pp. 250–255, Jan. 2012.

[188] O. Bechambi, A. Touati, S. Sayadi, and W. Najjar, "Effect of cerium doping on the textural, structural and optical properties of zinc oxide: Role of cerium and hydrogen peroxide to enhance the photocatalytic degradation of endocrine disrupting compounds," *Mater. Sci. Semicond. Process.*, vol. 39, pp. 807–816, May 2015.

[189] E. Muchuweni, T. S. Sathiaraj, and H. Nyakotyo, "Effect of gallium doping on the structural, optical and electrical properties of zinc oxide thin films prepared by spray pyrolysis," *Ceram. Int.*, vol. 42, no. 8, pp. 10 066–10 070, Jun. 2016.

[190] S. A. A. Wahab, K. A. Matori, S. H. A. Aziz, M. H. M. Zaid, M. M. A. Kechik, A. Z. K. Azman, R. E. M. Khaidir, M. Z. A. Khiri, and N. Effendy, "Effect of ZnO on the phase transformation and optical properties of silicate glass frits using rice husk ash as a SiO_2 source," *J. Mater. Res. Technol.*, vol. 9, no. 5, pp. 11 013–11 021, Sep. 2020.

[191] I. Ali, A. E.-H. B. Kashyout, M. Tayel, H. S. Hassan, and M. Rizk, "Ruthenium (Ru) doped zinc oxide nanostructure-based radio frequency identification (RFID) gas sensors for NH_3 detection," *J. Mater. Res. Technol.*, vol. 9, no. 6, pp. 15 693–15 704, Nov. 2020.

[192] Z. Cai, K.-K. Kim, and S. Park, "Room temperature detection of NO_2 gas under UV irradiation based on Au nanoparticle-decorated porous ZnO nanowires," *J. Mater. Res. Technol.*, vol. 9, no. 6, pp. 16 289–16 302, Nov. 2020.

[193] M. B. A. Bashir, M. F. Mohd Sabri, S. M. Said, Y. Miyazaki, I. A. Badruddin, D. A. Ameer Shnawah, E. Y. Salih, S. Abushousha, and M. H. Elsheikh, "Enhancement of thermoelectric properties of Co_4Sb_{12} Skutterudite by Al and La double filling," *J. Solid State Chem.*, vol. 284, p. 121205, Oct. 2020.

[194] T. Minami, "Transparent conducting oxide semiconductors for transparent electrodes," *Semiconductor Science and Technology*, vol. 20, no. 4, pp. S35–S44, Mar. 2005.

[195] H. Yoon, K. Lee, T. Lee, B. Cheong, D. Choi, D. Kim, and W. Kim, "Properties of fluorine doped ZnO thin films deposited by magnetron sputtering," *Sol. Energy Mater. Sol. Cells*, vol. 92, pp. 1366–1372, Dec. 2008.

[196] V. Assunção, E. Fortunato, A. Marques, H. Águas, I. Ferreira, M. Costa, and R. Martins, "Influence of the deposition pressure on the properties of transparent and conductive ZnO:Ga thin-film produced by rf sputtering at room temperature," *Thin Solid Films*, vol. 427, pp. 401–405, May 2003.

[197] S. Kim, W. I. Lee, E.-H. Lee, S. K. Hwang, and C. Lee, "Dependence of the resistivity and the transmittance of sputter-deposited Ga-doped ZnO films on oxygen partial pressure and sputtering temperature," *J. Mater. Sci.*, vol. 42, pp. 4845–4849, Jun. 2007.

[198] F. S. Khalid and R. Awang, “Effect of deposition times on structure of Ga-doped ZnO thin films as humidity sensor,” in *THE 2014 UKM FST POSTGRADUATE COLLOQUIUM: Proceedings of the Universiti Kebangsaan Malaysia, Faculty of Science and Technology 2014 Postgraduate Colloquium*, 2014, pp. 14–19.

[199] X. Yu, D. Li, Y. Wang, X. Li, C. Li, and Y. Zhou, “Effects of sputtering power on the properties of ZnO:Ga films deposited by r.f. magnetron-sputtering at low temperature,” *J. Cryst. Growth*, vol. 274, pp. 474–479, Feb. 2005.

[200] C. H. Huang, D. Y. Chen, and C. Y. Hsu, “Influence of deposition parameters and annealing treatment on the properties of GZO films grown using rf magnetron sputtering,” *Ceram. Int.*, vol. 38, pp. 1057–1063, Mar. 2012.

[201] T. P. Rao, M. C. S. Kumar, and N. S. Hussain, “Effects of thickness and atmospheric annealing on structural, electrical and optical properties of GZO thin films by spray pyrolysis,” *J. Alloys Compd.*, vol. 541, pp. 495–504, Apr. 2012.

[202] J. Hu and R. G. Gordon, “Textured aluminum-doped zinc oxide thin films from atmospheric pressure chemical-vapor deposition,” *J. Appl. Phys.*, vol. 71, pp. 880–890, Jan. 1992.

[203] K. Y. Cheong, N. Muti, and S. R. Ramanan, “Electrical and optical studies of ZnO:Ga thin films fabricated via the sol–gel technique,” *Thin Solid Films*, vol. 410, pp. 142–146, Nov. 2002.

[204] G. Hirata, J. McKittrick, T. Cheeks, J. Siqueiros, J. Diaz, O. Contreras, and O. Lopez, “Synthesis and optelectronic characterization of gallium doped zinc oxide transparent electrodes,” *Thin Solid Films*, vol. 288, pp. 29–31, Jan. 2005.

[205] H. Kato, M. Sano, K. Miyamoto, and T. Yao, “Growth and characterization of Ga-doped ZnO layers on a-plane sapphire substrates grown by molecular beam epitaxy,” *J. Cryst. Growth*, vol. 237–239, pp. 538–543, Feb. 2002.

[206] M. Burgelman and J. Poortmans, “SCAPS: a new self-consistent approach to optical and electrical simulation of thin-film solar cells,” *Solar Energy Materials and Solar Cells*, vol. 48, pp. 221–230, Nov. 1997.

[207] M. A. Contreras, M. J. Romero, B. To, F. Hasoon, R. Noufi, S. Ward, and K. Ramanathan, “Optimization of CBD CdS process in high-efficiency Cu(In,Ga)Se_2-based solar cells,” *Thin Solid Films*, vol. 403-404, pp. 204–211, Feb. 2002.

[208] A. K. Sen Gupta, A. Adnan, S. Bhattacharjee, N. K. Das, M. A. Matin, and M. Quamruzzaman, “SnapFib: An easy build Arduino based tabletop prototype for thin film deposition by Successive Ionic Layer Adsorption and Reaction method,” *HardwareX*, vol. 12, p. e00347, Oct. 2022.

[209] R. Pandiyan, Z. Oulad Elhmaidi, Z. Sekkat, M. Abd-lefdil, and M. A. El Khakani, “Reconstructing the energy band electronic structure of pulsed laser deposited CZTS thin films intended for solar cell absorber applications,” *Applied Surface Science*, vol. 396, pp. 1562–1570, Feb. 2017.

[210] E. A. Kraut, R. W. Grant, J. R. Waldrop, and S. P. Kowalczyk, “Precise Determination of the Valence-Band Edge in X-Ray Photoemission Spectra: Application to Measurement of Semiconductor Interface Potentials,” *Phys. Rev. Lett.*, vol. 44, pp. 1620–1623, Jun. 1980.

[211] A. Tumbul, F. Aslan, A. Goktas, M. Z. Zarbali, and A. Kilic, "Highly stable ethanol-based Cu_2ZnSnS_4 (CZTS) low-cost thin film absorber: Effect of solution aging," *Mater. Chem. Phys.*, vol. 258, p. 123997, Jan. 2021.

[212] H. Xie, M. Dimitrievska, X. Fontané, Y. Sánchez, S. López-Marino, V. Izquierdo-Roca, V. Bermúdez, A. Pérez-Rodríguez, and E. Saucedo, "Formation and impact of secondary phases in Cu-poor Zn-rich $Cu_2ZnSn(S_{1-y}Se_y)$ ($0 \leq y \leq 1$) based solar cells," *Sol. Energy Mater. Sol. Cells*, vol. 140, p. 289–298, Sep. 2015.

[213] G. K. Williamson and W. H. Hall, "X-ray line broadening from filed aluminium and wolfram," *Acta Metall.*, vol. 1, pp. 22–31, Jan. 1939.

[214] G. K. Williamson and R. E. Smallman, "Dislocation densities in some annealed and cold-worked metals from measurements on the X-ray Debye-Scherrer spectrum," *Philos. Mag.*, vol. 1, pp. 34–36, Aug. 1956.

[215] Y. B. K. Kumar, D. Nagamalleswari, and G. S. Babu, "Deposition of Cu_2ZnSnS_4 thin film at different solution flow rates," *Phys. B Condens. Matter*, vol. 645, p. 414263, Nov. 2022.

[216] F. Aslan and A. Tumbul, "Non-vacuum processed Cu_2ZnSnS_4 thin films: Influence of copper precursor on structural, optical and morphological properties," *J. Alloys Compd.*, vol. 612, pp. 1–4, Jun. 2014.

[217] F. Mikailzade *et al.*, "Structural, optical and magnetic characterization of nanorod-shaped polycrystalline $Zn_{1-x}Mn_xO$ films synthesized using sol–gel technique," *Appl. Phys. A*, vol. 126, p. 768, Sep. 2020.

[218] D. M. Berg, "Kesterite Equilibrium Reaction and the Discrimination of Secondary Phases from Cu_2ZnSnS_4," Ph.D. dissertation, University of Luxembourg, Luxembourg city, Luxembourg, Jan. 2012. [Online]. Available: https://orbilu.uni.lu/handle/10993/15414

[219] X. Fontane *et al.*, "In-depth resolved Raman scattering analysis for the identification of secondary phases: Characterization of Cu_2ZnSnS_4 layers for solar cell applications," *Appl. Phys. Lett.*, vol. 98, p. 181905, May 2011.

[220] S. Tombolato, "CZTS(e) thin films grown by chemical methods for PV application," Ph.D. dissertation, University of Milano, Bicocca, Mar. 2015. [Online]. Available: https://boa.unimib.it/bitstream/10281/77923/1/phd_unimib_067972.pdf

[221] D. B. Khadka and J. Kim, "Study of structural and optical properties of kesterite Cu_2ZnGeX_4 (X = S,Se) thin films synthesized by chemical spray pyrolysis," *CrystEngComm*, vol. 15, p. 10500–10509, Nov. 2013.

[222] J. Tauc, "Optical properties and electronic structure of amorphous Ge and Si," *Materials Research Bulletin*, vol. 3, pp. 37–46, Oct. 1968.

[223] L. Nie, S. Liu, Y. Chai, and R. Yuan, "Spray pyrolysis deposition and photoresponse of Cu_2CdSnS_4 thin films," *J. Anal. Appl. Pyrolysis*, vol. 112, pp. 363–368, Mar. 2015.

[224] A. Tumbul, A. Goktas, M. Z. Zarbali, and F. Aslan, "Structural, morphological and optical properties of the vacuum-free processed CZTS thin film absorbers," *Mater. Res. Express*, vol. 5, p. 66408, Jun. 2018.

[225] M. C. Benachour, R. Bensaha, and R. Moreno, “Annealing duration influence on dip-coated CZTS thin films properties obtained by sol-gel method,” *Optik (Stuttg).*, vol. 187, pp. 1–8, Jun. 2019.

[226] A. Jafari-Rad and H. Kafashan, “Preparation and characterization of electrochemically deposited nanostructured Ti-doped ZnS thin films,” *Ceram. Int.*, vol. 45, p. 21413–21422, Dec. 2019.

[227] R. C. Rai, “Analysis of the Urbach tails in absorption spectra of undoped ZnO thin films,” *J. Appl. Phys.*, vol. 113, p. 153508, Apr. 2013.

[228] Y. Natsume, H. Sakata, and T. Hirayama, “Low-temperature electrical conductivity and optical absorption edge of ZnO films prepared by chemical vapour deposition,” *Physica Status Solidi (a)*, vol. 148, pp. 485–495, Apr. 1995.

[229] A. K. Sen Gupta, E. M. K. I. Ahamed, M. Quamruzzaman, M. A. Matin, K. S. Rahaman, and N. Amin, “Consequence on Optical Properties of ZnS Thin-Film Deposited by RF Magnetron Sputtering with Varying Substrate Temperatures,” in *2020 47th IEEE Photovoltaic Specialists Conference (PVSC))*, Jun. 2020, p. 2646–2648.

[230] Y. Ono, A. Bungo, T. Noji, Y. Koike, and T. Kajitani, “MEM analysis on electron density distribution of superconductors, $Pb_2Sr_2Y_{0.90}Sr_{0.10}Cu_3O_8$, $Pb_2Sr_2Y_{1-x}Ca_xCu_3O_8$ (x=0.25 and 0.41) and $Pb_2Sr_2Ho_{0.64}Ca_{0.36}Cu_3O_8$,” *Materials Transactions*, vol. 39, pp. 562–569, May 1998.

[231] M. Takata, M. Yamada, Y. Kubota, and M. Sakata, “High Resolution X-Ray Powder Diffraction by the Combination of Synchrotron Radiation and Imaging Plate to Observe Electron Distribution by the Maximum Entropy Method,” *Advances in X-Ray Analysis*, vol. 35, pp. 85–90, Mar. 2019.

[232] S. Israel, R. Saravanan, N. Srinivasan, and R. Rajaram, “High Resolution X-Ray Powder Diffraction by the Combination of Synchrotron Radiation and Imaging Plate to Observe Electron Distribution by the Maximum Entropy Method,” *Journal of Physics and Chemistry of Solids*, vol. 64, pp. 43–49, Jan. 2003.

[233] R. Saravanan *et al.*, “Electron density distribution in GaAs using MEM,” *Journal of Physics and Chemistry of Solids*, vol. 64, pp. 51–58, Jan. 2003.

[234] H. Kafashan, “Structural characterizations of pure SnS and In-doped SnS thin films using isotropic and anisotropic models,” *Mater. Res. Express*, vol. 5, p. 46417, Apr. 2018.

[235] H. Ahmoum, P. Chelvanathan, M. Su’ait, M. Boughrara, G. Li, A. H. Al-Waeli, K. Sopian, M. Kerouad, and N. Amin, “Impact of preheating environment on microstructural and optoelectronic properties of Cu_2ZnSnS_4 (CZTS) thin films deposited by spin-coating,” *Superlattices Microstruct.*, vol. 140, p. 106452, Apr. 2020.

[236] J. Tao, J. Liu, J. He, K. Zhang, J. Jiang, L. Sun, P. Yang, and J. Chu, “Synthesis and characterization of Cu_2ZnSnS_4 thin films by the sulfurization of co-electrodeposited Cu-Zn-Sn-S precursor layers for solar cell applications,” *RSC Adv.*, vol. 4, p. 23977–23984, May 2014.

[237] Y. Lin, S. Ikeda, W. Septina, Y. Kawasaki, T. Harada, and M. Matsumura, “Mechanistic aspects of preheating effects of electrodeposited metallic precursors on structural and photovoltaic properties of Cu_2ZnSnS_4 thin films,” *Sol. Energy Mater. Sol. Cells*, vol. 120, p. 218–225, Jan. 2014.

[238] P. A. Fernandes, P. M. P. Salome, and A. F. D. Cunha, "A study of ternary Cu_2SnS_3 and Cu_3SnS_4 thin films prepared by sulfurizing stacked metal precursors," *J. Phys. D. Appl. Phys.*, vol. 43, p. 215403, May 2010.

[239] P. Fernandes, P. Salomé, and A. da Cunha, "Study of polycrystalline Cu_2ZnSnS_4 films by Raman scattering," *J. Alloys Compd.*, vol. 509, p. 7600–7606, Jul. 2011.

[240] D. M. Berg, R. Djemour, L. Gütay, S. Siebentritt, P. J. Dale, X. Fontane, V. Izquierdo-Roca, and A. Pérez-Rodriguez, "Raman analysis of monoclinic Cu_2SnS_3 thin films," *Appl. Phys. Lett.*, vol. 100, p. 192103, May 2012.

[241] L. Sun, J. He, H. Kong, F. Yue, P. Yang, and J. Chu, "Structure, composition and optical properties of Cu_2ZnSnS_4 thin films deposited by Pulsed Laser Deposition method," *Sol. Energy Mater. Sol. Cells*, vol. 95, p. 2907–2913, Oct. 2011.

[242] A. Moholkar, S. Shinde, G. Agawane, S. Jo, K. Rajpure, P. Patil, C. Bhosale, and J. Kim, "Studies of compositional dependent CZTS thin film solar cells by pulsed laser deposition technique: An attempt to improve the efficiency," *J. Alloys Compd.*, vol. 544, p. 145–151, Dec. 2012.

[243] A. Alasvand and H. Kafashan, "Comprehensive physical studies on nanostructured Zn-doped CdSe thin films," *J. Alloys Compd.*, vol. 789, p. 108–118, Jun. 2019.

[244] A. Goudarzi, G. M. Aval, R. Sahraei, and H. Ahmadpoor, "Ammonia-free chemical bath deposition of nanocrystalline ZnS thin film buffer layer for solar cells," *Thin Solid Films*, vol. 516, p. 4953–4957, Jun. 2008.

[245] M. Öztaş, M. Bedir, A. Necmeddin Yazici, E. Vural Kafadar, and H. Toktamış, "Characterization of copper-doped sprayed ZnS thin films," *Phys. B Condens. Matter*, vol. 381, pp. 40–46, May 2006.

[246] D. Seo and S. Lim, "Effect of sulfur and copper amounts in sol-gel precursor solution on the growth, crystal properties, and optical properties of Cu_2ZnSnS_4 films," *J. Mater. Sci. Mater. Electron.*, vol. 24, p. 3756–3763, Oct. 2013.

[247] H. Kafashan, R. Ebrahimi-Kahrizsangi, F. Jamali-Sheini, and R. Yousefi, "Effect of Al doping on the structural and optical properties of electrodeposited SnS thin films," *Phys. Status Solidi Appl. Mater. Sci.*, vol. 213, p. 1302–1308, Jan. 2016.

[248] S. Thanikaikarasan, K. Sundaram, T. Mahalingam, S. Velumani, and J.-K. Rhee, "Electrodeposition and characterization of Fe doped CdSe thin films from aqueous solution," *Mater. Sci. Eng. B Solid-State Mater. Adv. Technol.*, vol. 174, pp. 242–248, Oct. 2010.

[249] M. P. Suryawanshi, G. L. Agawane, S. M. Bhosale, S. W. Shin, P. S. Patil, J. H. Kim, and A. V. Moholkar, "CZTS based thin film solar cells: A status review," *Mater. Technol.*, vol. 28, pp. 98–109, Nov. 2013.

[250] M. Tsega and D.-H. Kuo, "The performance of the donor and acceptor doping in the Cu-rich $Cu_2ZnSnSe_4$ bulks with different Zn/Sn ratios," *Solid State Commun.*, vol. 164, pp. 42–46, Jun. 2013.

[251] G. Gurieva, M. Dimitrievska, S. Zander, A. Pérez-Rodríguez, V. Izquierdo-Roca, and S. Schorr, "Structural characterisation of $Cu_{2.04}Zn_{0.91}Sn_{1.05}S_{2.08}Se_{1.92}$," *physica status solidi c*, vol. 12, pp. 588–591, Apr. 2015.

[252] R. Gunder, J. A. Márquez-Prieto, G. Gurieva, T. Unold, and S. Schorr, “Structural characterization of off-stoichiometric kesterite-type $Cu_2ZnGeSe_4$ compound semiconductors: from cation distribution to intrinsic point defect density,” *CrystEngComm*, vol. 20, pp. 1491–1498, Jan. 2018.

[253] L. E. Valle Rios, K. Neldner, G. Gurieva, and S. Schorr, “Existence of off-stoichiometric single phase kesterite,” *Journal of Alloys and Compounds*, vol. 657, pp. 408–413, Feb. 2016.

[254] G. Gurieva, L. E. Valle Rios, A. Franz, P. Whitfield, and S. Schorr, “Intrinsic point defects in off-stoichiometric $Cu_2ZnSnSe_4$: A neutron diffraction study,” *Journal of Applied Physics*, vol. 123, p. 161519, Oct. 2018.

[255] A. Lafond, L. Choubrac, C. Guillot-Deudon, P. Deniard, and S. Jobic, “Crystal Structures of Photovoltaic Chalcogenides, an Intricate Puzzle to Solve: the Cases of CIGSe and CZTS Materials,” *Zeitschrift für anorganische und allgemeine Chemie*, vol. 638, pp. 2571–2577, Aug. 2012.

[256] M. Souli, R. Engazou, L. Ajili, and N. Kamoun-Turki, “Physical properties evolution of sprayed Cu_2MgSnS_4 thin films with growth parameters and vacuum annealing,” *Superlattices and Microstructures*, vol. 147, p. 106711, Nov. 2020.

[257] M. G. Faraj and K. Ibrahim, “Optical and Structural Properties of Thermally Evaporated Zinc Oxide Thin Films on Polyethylene Terephthalate Substrates,” *International Journal of Polymer Science*, vol. 2011, p. 302843, Dec. 2011.

[258] A. V. der Drift, “A Principle Governing Growth Orientation in Vapour-Deposited Layers,” *Physics*, 2014.

[259] S.-U. Jen, H. Sun, H.-P. Chiang, S.-C. Chen, J.-Y. Chen, and X. Wang, “Optoelectronic Properties and the Electrical Stability of Ga-Doped ZnO Thin Films Prepared via Radio Frequency Sputtering,” *Materials*, vol. 9, p. 987, Apr. 2016.

[260] R. D. Shannon, “Revised effective ionic radii and systematic studies of interatomic distances in halides and chalcogenides,” *Acta Crystallographica Section A*, vol. 32, pp. 751–767, Sep. 1976.

[261] Fang-HsingWang, C.-C. Huang, C.-F. Yang, and H.-T. Tzeng, “Optical and Electrical Properties of the Different Magnetron Sputter Power 300°C Deposited Ga_2O_3-ZnO Thin Films and Applications in p-i-n α-Si:H Thin-Film Solar Cells,” *Physics*, 2013.

[262] X. Li, Y. Wang, W. Liu, G. Jiang, and C. Zhu, “Study of oxygen vacancies influence on the lattice parameter in ZnO thin film,” *Materials Letters*, vol. 85, pp. 25–28, Oct. 2012.

[263] G. Fang, D. Li, and B.-L. Yao, “Effect of Vacuum Annealing on the Properties of Transparent Conductive AZO Thin Films Prepared by DC Magnetron Sputtering,” *physica status solidi (a)*, vol. 193, pp. 139–152, Jun. 2002.

[264] H.-B. Zhou, H.-Y. Zhang, L.-W. Han, and J.-C. Han, “Effects of sputtering power on the properties of Al-doped ZnO films deposited on amorphous silicon films substrate,” *Superlattices and Microstructures*, vol. 64, pp. 563–568, Dec. 2013.

[265] D. K. Kim, “Characteristics of Ga doped ZnO Thin Films Deposited by RF Magnetron Sputtering with Base Pressure,” *Applied Science and Convergence Technology*, vol. 28, pp. 13–15, Jan. 2019.

[266] V. Kumar, R. Singh, L. Purohit, and R. Mehra, "Structural, Transport and Optical Properties of Boron-doped Zinc Oxide Nanocrystalline," *Journal of Materials Science & Technology*, vol. 27, pp. 481–488, Jul. 2011.

[267] Q. Huang, Y. Wang, S. Wang, D. Zhang, Y. Zhao, and X. Zhang, "Transparent conductive ZnO:B films deposited by magnetron sputtering," *Thin Solid Films*, vol. 520, pp. 5960–5964, Jul. 2012.

[268] X. Zeng, X. Wen, X. Sun, W. Liao, and Y. Wen, "Boron-doped zinc oxide thin films grown by metal organic chemical vapor deposition for bifacial a-si:h/c-si heterojunction solar cells," *Thin Solid Films*, vol. 605, pp. 257–262, Apr. 2016.

[269] E. Burstein, "Anomalous Optical Absorption Limit in InSb," *Phys. Rev.*, vol. 93, pp. 632–633, Feb. 1954.

[270] T. S. Moss, "The Interpretation of the Properties of Indium Antimonide," *Proceedings of the Physical Society. Section B*, vol. 67, p. 775, Oct. 1954.

[271] L.-H. Wong and Y.-S. Lai, "Characterization of boron-doped ZnO thin films prepared by magnetron sputtering with (100-x)ZnO-xB_2O_3 ceramic targets," *Thin Solid Films*, vol. 583, pp. 205–211, May 2015.

[272] F. Urbach, "The Long-Wavelength Edge of Photographic Sensitivity and of the Electronic Absorption of Solids," *Phys. Rev.*, vol. 92, pp. 1324–1324, Dec. 1953.

[273] R. Swanepoel, "Determination of the thickness and optical constants of amorphous silicon," *Journal of Physics E: Scientific Instruments*, vol. 16, p. 1214, Dec. 1983.

[274] E. M. Bouabdalli, M. El Jouad, T. Garmim, S. Touhtouh, A. Louardi, M. Monkade, and B. Hartiti, "Preparation and Characterization of Nickel and Aluminum-Codoped SnO_2 Thin Films for Optoelectronic Applications," *International Journal of Photoenergy*, vol. 2021, p. 5556441, Sep. 2021.

[275] M. El-Bana and S. Fouad, "Opto-electrical characterisation of $As_{33}Se_{67-x}Sn_x$ thin films," *Journal of Alloys and Compounds*, vol. 695, pp. 1532–1538, Feb. 2017.

[276] X. Chen, B. Xu, J. Xue, Y. Zhao, C. Wei, J. Sun, Y. Wang, X. Zhang, and X. Geng, "Boron-doped zinc oxide thin films for large-area solar cells grown by metal organic chemical vapor deposition," *Thin Solid Films*, vol. 515, pp. 3753–3759, Feb. 2007.

[277] J. K. Kim, S. J. Yun, J. M. Lee, and J. Wook Lim, "Effect of rf-power density on the resistivity of Ga-doped ZnO film deposited by rf-magnetron sputter deposition technique," *Current Applied Physics*, vol. 10, pp. S451–S454, May 2010.

[278] G. Haacke, "New figure of merit for transparent conductors," *Journal of Applied Physics*, vol. 47, pp. 4086–4089, Aug. 1976.